



HAL
open science

spatiotemporal study of spin-crossover materials : electro-elastic modelling in bistable nanomaterials

Yogendra Singh

► **To cite this version:**

Yogendra Singh. spatiotemporal study of spin-crossover materials : electro-elastic modelling in bistable nanomaterials. Statistical Mechanics [cond-mat.stat-mech]. Université Paris-Saclay, 2021. English. NNT : 2021UPAST078 . tel-03613540

HAL Id: tel-03613540

<https://theses.hal.science/tel-03613540>

Submitted on 18 Mar 2022

HAL is a multi-disciplinary open access archive for the deposit and dissemination of scientific research documents, whether they are published or not. The documents may come from teaching and research institutions in France or abroad, or from public or private research centers.

L'archive ouverte pluridisciplinaire **HAL**, est destinée au dépôt et à la diffusion de documents scientifiques de niveau recherche, publiés ou non, émanant des établissements d'enseignement et de recherche français ou étrangers, des laboratoires publics ou privés.

Etude Spatio-temporelle de Matériaux à
transition de spin : modélisation électro-
élastique dans des nanomatériaux
bistables.

*Spatiotemporal study of Spin-Crossover
materials: Electro-elastic Modelling in bistable
Nanomaterials*

Thèse de doctorat de l'université Paris-Saclay

École doctorale n° 573, Interfaces : matériaux, systèmes, usages

Spécialité de doctorat : Physique

Unité de recherche : Université Paris-Saclay, UVSQ, CNRS, GEMaC, 78000, France.

Référent : Université de Versailles -Saint-Quentin-en-Yvelines

**Thèse présentée et soutenue à Paris-Saclay,
le 06/07/2021, par**

Yogendra SINGH

Composition du Jury

Yann GARCIA

Professeur, Université catholique de
Louvain

Président

Hung The DIEP

Professeur, Cergy Paris University

Rapporteur & Examineur

Smail TRIKI

Professeur, Université de Bretagne
Occidentale

Rapporteur & Examineur

Sebastien PILLET

Chercheur, Université de Lorraine

Examineur

Jorge LINARES

Professeur, UVSQ

Examineur

Isabelle MAURIN

Chercheur, Institut Néel

Examineur

Direction de la thèse

Kamel BOUKHEDDAEN

Professeur, UVSQ

Directeur de thèse

Titre : Etude Spatio-temporelle de Matériaux à transition de spin : modélisation électro-élastique dans des nanomatériaux bistables.

Mots clés : Transitions de phases, Transition de spin, Nanostructures/particules (Coeur-coquille), Effets spatio-temporels, Magnétoélasticité, Interactions élastiques, Méthode Monte Carlo.

Résumé : Cette thèse est dédiée à la modélisation et à l'étude des comportements longue portée et des effets spatiotemporels accompagnant la transition de spin dans systèmes hystérétiques, le plus souvent pilotés par des phénomènes de frustration élastique. L'étude de différents systèmes à transition de spin (cœur-coquille, MEMS/NEMS) pour différentes formes géométriques durant leur transition thermo-induite a été conduite en introduisant la frustration élastique dans une myriade de possibilités. Parmi ces dernières, il y a les systèmes cœur/coquille ayant différents champs de ligands, ou différents désaccords de paramètres de mailles dans le cœur et la coquille dans les phases HS et/ou LS, ainsi que le cas de cristaux contraints mécaniquement.

Tous ces systèmes ont la particularité de présenter des transitions du premier ordre où nos études ont montré l'existence de différents mécanismes à travers lesquels les propriétés magnétiques (électroniques) et élastiques sont altérées. Nous avons pu révéler les effets physiques du changement de l'épaisseur de la coquille et sa conséquence sur les effets élastiques (contrainte-déformation, pression) dans la nanostructure commutable. Une méthode analytique permettant de calculer simplement la moyenne de la distance entre proches voisins, dont les résultats sont en parfait accord avec les simulations MC, est aussi proposée.

En outre, l'effet du désaccord de paramètre de maille entre le cœur et la coquille a été étudié pour les deux états de spins, HS et LS. Celui-ci a d'ailleurs montré des comportements riches et variés, tels que l'apparition de structures HS/LS labyrinthiques, les dilatations et les contractions de la nanostructure au-delà des valeurs des paramètres de maille à l'équilibre, des transitions thermiques multi-étapes et des transitions réentrantes sur la fraction HS ainsi que sur le paramètre de réseau. L'ensemble de ces résultats a été étudié et hiérarchisé. Ce type de comportement, spécifique aux réseaux nanostructuré ainsi que la dissociation entre les synergies des

interactions électro-élastiques de la nanostructure cœur-coquille est ici attribuée à l'existence d'une frustration dynamique induite dans les états HS et LS, qui de notre point de vue mériterait d'être approfondie dans de futurs travaux.

Un autre type de systèmes à transition de spins étudié dans cette thèse est celui lié aux micro/nano-systèmes électromécaniques (MEMS/NEMS). Cette partie est centrée sur l'analyse théorique des aptitudes des systèmes à transition de spin en tant que commutateurs électro-élastiques. Ainsi, nous avons étendu nos modèles à l'étude des changements mécaniques à l'échelle macroscopique d'un cristal bistable doublement encastré. Le but est sa réaction à la dilatation en volume accompagnant le passage LS vers HS. Ces investigations ont mis en évidence de nombreuses observations intéressantes au regard de la flexion du cristal lors de sa transition, de sa longueur totale, de sa dynamique spatio-temporelle, de l'organisation des états de spin et de sa relation avec la distribution spatiale de l'énergie élastique. Les nouvelles perspectives acquises à travers cette étude prospective est un premier pas ouvrant la voie à des études plus réalistes à 3D.

Tous ces résultats originaux ont été obtenus en utilisant un modèle spatiotemporel basé sur une description électro-élastique du phénomène de la transition de spin, incluant à la fois les degrés de liberté de spin et de distorsion. Ces études ont été conduites avec l'objectif de répondre à des questions fondamentales liées à la température de transition des systèmes à transition de spin, à leur comportement hystérétique, aux conditions d'apparition des transitions multi-étapes, et aux effets de stimuli externes ou internes divers et variés, tels que les contraintes mécaniques imposées, le désaccord de paramètres de maille, et aux différences de champs de ligand notamment dans les systèmes cœur coquille.

Title: Spatiotemporal study of Spin-Crossover materials: Electro-elastic Modelling in bistable Nanomaterials

Keywords: Phase-transitions, Spin-transition, Nano-structure/particles (Core-Shell), Spatio-temporal effects, Magneto-elasticity, Elastic interactions, Monte-Carlo method.

Abstract: This thesis work is devoted to the modelling and study of long-range behaviours and spatiotemporal effects occurring during thermal hysteresis primarily due to frustration driven phase transitions in Spin-Crossover (SCO) systems. The study of different Spin-Crossover systems (Core-Shell, MEMS/NEMS) with different geometric forms during their thermo-induced spin transition have been conducted, by introducing frustration in myriad of ways: having different ligand fields for core and shell entities and thus different transition temperatures, through lattice mismatch in High Spin (HS) or Low Spin (LS) state of shell lattice with respect to that of core lattice, or by simply clamping the single-crystal SCO in LS or HS state.

All of these systems exhibit first-order phase transition where investigations showed different mechanisms through which magnetic (electronic) and elastic properties are altered. We have been able to reveal the effects of variation of shell width, the mechanism through which elastic properties (stress-strain, pressure) are being distributed throughout the core-shell architecture and the ways it affects the magnetic behaviour of the SCO nanoparticle. An analytical method for calculating the average nearest neighbour distances is also presented, which almost perfectly agrees with the Monte-Carlo simulation.

Furthermore, the effect of lattice mismatch in both LS and HS states of the shell lattice has been studied, and the origins of rich varieties of interesting behaviours regarding the nanostructure have been explained. Factors governing the appearance of labyrinth-like structures (domains) of HS and LS state, contraction or expansion of the nanostructure beyond the equilibrium lattice parameters, multistep, re-entrant phase transitions of HS fraction and lattice spacing have been studied and summarised.

This type of behavior is impossible to obtain on a simple lattice.

This disassociation between the synergies of the electronic and elastic coupling of the core-shell nanostructure due to the dynamically induced frustration in HS or LS state is very intriguing and would require further attention in future works. Another SCO system studied in this thesis is related to Micro/Nano-electro-mechanical systems (MEMS/NEMS). This part is focused on understanding actuating capabilities of the SCO system, to theoretically model the behavior of electronic and mechanic properties of SCO molecular switches, thereby contributing to the design of better micro/nano-electromechanical systems. Thus, we extend our previous theoretical work, and use microscopic electro-elastic model to explain non-negligible changes in the doubly clamped SCO beams due to stress generated through thermal expansion or contraction. Several interesting observations regarding the bending, average "crystal" length, spatio-temporal dynamics of the HS fraction, elastic energy distribution, and relaxation curves related to the stable states of the system have been discussed. The additional insight gained through this study will be a fundamental step toward the explanation of the effect of fixed edges on the structural and thermal properties of the crystal, and thus will be very helpful in modelling this behavior for the 3D lattice.

All of these original results are obtained using a spatiotemporal model based on the description of the spin-crossover problem as an electro-elastic model, combining both electronic and lattice distortion degrees of freedom. These studies are conducted in order to answer some fundamental problems related to transition temperature, multistep transitions, effect of various external factors such as clamping, lattice mismatch and ligand field differences related to the SCO materials.

Acknowledgment

Writing this thesis was among some of the hardest things I have done in my life, and among all of the pages, these are the hardest to write. For these, I had to go through hard questions first, "How to thank someone enough?", especially those who have been so instrumental in realization of the dream, to express and convey it in a way that it can get across as intended, and with the same fervor, if that is not daunting enough, to do it just through words (which I am not good at), is certainly beyond my competence. But in spite of that, I would like to give it a try, and in order to do so, I would again shamelessly ask your help. Although, I would hope that, on its own, the gratitude conveyed through these words will settle (in you), where it has originated from (in me). I suspect that they (words) may feel bit light, hollow, or ritualistic in character, but I would still request you to let them gravitate towards/sink in till they hit the bottom, for I can assure you that is exactly where they had originated from, i.e., bottom of my heart.

Firstly, I would like to thank all the members of the jury for agreeing to evaluate this work. As it is said "To err is human, and to correct gently is humane", I would like to thank, both the reviewers Professor Hung T. DIEP and Professor Smail TRIKI, for agreeing to review this work, and for their kind words and encouragement, and all the jury members Professor Yann GARCIA, Professor Jorge LINARES, Dr. Isabelle Maurin, and Dr. Sebastien Pillet, for agreeing to evaluate this work. I am very delighted and honored to have you all as a part of this jury.

I would also like to thank Professor Seji MIYASHITA, Nishino MASAMICHI, Jorge LINARES and Hassane OUBOUCHOU, for friendly discussions, guidance, and collaborations, which was very helpful to advance in this field. On the similar note, I would like to thank for all the help and support I was able to get from the team (both Past, and present members), Physics of Switchable Molecular Materials (P2MC). Thank you very much, Mouhamadou SY, Miguel Ángel PÁEZ ESPEJO, Karim AFFES, Houcem FOURATI, Mamadou NDIAYE, Nour El-Islam BELMOURI, Guillaume BOUCHEZ, Ahmed SLIMANI, Killian Babilotte, due to your friendships, encouragements, lively discussions all these years went like a breeze of fresh air, and I was able to learn a lot from all of you.

I would now dare to attempt to thank all of my friends over the years; without them this journey would not have been conceivable. Thank you Shalu RANI for lifting me out of degeneracies consistently (three times in a row now), Sumit KUMAR, Pragya VISHWAKARMA, Karim ICHAR, Rachid ALHIAN, Subramaniam Vaidyanathan your presence here was immense support. I am at loss of words now when it comes to thank you all from the "Second Floor Family", you guys are extremely supportive, loving,

genuine and kindest of human beings, even the hardest of times felt not just bearable, but pleasurable in your company. Thus, thanks to all of you (especially Amrut, Pranav and Pranjali for initiation), for letting me be a part of it, even being miles away from home, your company made it feel very homely. I would also like to thank Ankush, Sonali, Mahima, Nripesh, and Onkar dada, thanks a lot for being there in the hardest of times and no matter what I say here can do justice to your contributions, deepest and sincerest of gratitude to all of you. Of course, there are many more yet to be thanked, but for the concerns of brevity, I would like to thank all of my friends, not just for the sake of saying it, but I have to because I can still feel the warmth of that gentle push on my back, the helping hand, which all of you extended, because of which this journey could possibly take this course.

I would also like to thank all the institutions which have been part of this journey, Universite Paris-Saclay (UVSQ), and laboratory Group of Condensed Matter Studies (GEMaC) for welcoming me here in FRANCE, and providing me with this opportunity of immense importance to me. I would also like to thank, teachers and professors from the previous institution, who prepared me for this undertaking. Thanks to VNIT, Delhi University, and my Schools, for I was blessed with great teachers while I was there.

Now I would turn to those, whom I don't know where to begin with, thanks to my family and their immense and unaccountable sacrifices, at every turn that I am able to realise something which was deemed unachievable, to begin with. Thanks for your immense love, blessings, and support in each and every way possible. Thanks to my grandmother for the seemingly infinite hope she had in me, to my mom for instilling conviction, morality, and fortitude in me. To my brothers (blessing to me), for giving me a memorable childhood, being my earliest confidant, giving me lessons in justice, and teaching me how to "KEEP CALM...." before that became cool. To my father and grandfather for their immense sacrifices, setting the bar high (leading through their own actions and achievements), for challenging me to achieve the best and nothing less. To my sister for her love and teaching me "how to dream" and making me taste "rainbows". To Twinkle for her immense support, love, and for always being on my side no matter what adversity may look like, thanks for bearing up with me, thanks for imparting courage during the darkest of hours. Thanks to all of you for picking me up from my lowest, and giving me another chance to re-build myself, again and again.....and again.

Thanks to all of you from the bottom of my heart.

Only now I can begin to express my deepest and sincerest of gratitude, to the person, without whose support, and efforts, all of this would not be possible at all. I am highly grateful to Professor Kamel BOUKHEDDADEN for extending me a very warm welcome,

and opportunity to work alongside his team, for his kindness, permanent support and availability. It was a great learning opportunity to work with you. Not only did I learn about the subject in hand, but also something about every other aspect of life. I could literally feel all the passion (contagious in nature) he carries around, which he keeps sprinkling on us from time to time, through his conduct. I am very grateful to you for the knowledge you have imparted and engraved in me throughout the duration of my thesis. For all of those lessons and discussions in physics, philosophy and life. I hope, I can pick some of your traits, your curiosity, zeal, and much more importantly, the focus, and detail through which meaningful investigations are conducted. Thanks for teaching all of that through conduct, and through exercise that everything meaningful has to be derived through efforts. Words fail to describe how grateful I am to you for having me always helped, supported and guided in all situations. I am highly grateful for the patience bestowed, motivation imparted, enthusiasm, and immense knowledge shared. Your guidance helped me during every aspect of this thesis (research, publications, presentations and writing).

To be succinct and suffice, I could not have imagined having a better advisor and mentor for myself.

Table of Contents

General Introduction

Chapter 1

1.1 Introduction	18
1.2 Metal complexes and Ligand field theory: Overview	19
1.2.1 Crystal Field Theory	20
1.2.2 Molecular orbital theory	23
1.2.3 Ligand Field Theory	26
1.3 What is Spin Crossover: Historical Overview.....	29
1.4 On thermodynamics of spin-crossover systems.....	33
1.4.1 Entropy driven spin-crossover	34
1.4.1 Mixed spin phases and co-operativity.....	38
1.5 Models and methods used to predict the spin crossover behaviour.....	42
1.5.1 Modelling: Overview.....	42
1.5.1 Models used to characterize Spin Crossover Systems	43
1.5.1.1 Ising model: Wajnflasz and Pick approach	46
1.5.1.2 Slichter and Drickamer model.....	48
1.5.1.3 Domain model: Sorai and Seki	49
1.5.1.4 Ising models	51
1.5.1.5. Elastic models.....	53
1.6. Methods used to solve the Ising – like model	56
1.6.1. Overview:.....	56
1.6.2 Monte Carlo Methods	57
1.6.2.1. Choice of Boundary Conditions	57
1.6.2.2. Monte Carlo Metropolis.....	57
1.7 How to switch “ON” and “OFF” Molecular Switches: A brief review of various stimuli-based responses in SCO.....	60
1.7.1 Temperature	60
1.7.2 Pressure driven spin-crossover	60
1.7.3 Electric field.....	62
1.7.4 Magnetic field.....	62

1.7.5 Light induced spin-crossover	62
1.7.6 X-rays	63
1.7.7 Chemical stimuli	63
1.8 Detection and Applications	64
1.8.1 Detection of the Spin Crossover	64
1.8.1.1 Magnetic Susceptibility Measurements	64
1.8.1.2 Mossbauer Spectroscopy	65
1.8.1.3 Crystallography	65
1.8.1.4 Heat Capacity Measurements	66
1.8.1.5 Vibrational Spectroscopy	66
1.8.1.6 Optical Microscopy Measurements	67
1.8.1.7 Refractive Index Change	69
1.8.1.8 Electrical Measurements	69
1.8.2 EMERGING APPLICATIONS USING MOLECULAR SPIN CROSSOVER COMPOUNDS	70
1.8.2.1 Molecular electronics or Spintronics	70
1.8.2.2 Spin Crossover in Nanoparticles, Thin Films and Nanocomposites	72
1.8.2.3 Actuators (MEMS/NEMS)	73
References: -	74
 <i>Chapter 2</i>	
2.1 Introduction	91
2.2 Core–Shell Spin Crossover	93
2.2.1 Experimental observations	94
2.2.2 Theoretical observations	97
2.3 The Model	102
2.4 Results and Discussions	106
2.4.1 Thermal Properties of the uncoated core	106
2.4.2 Case of active core and shell spin-crossover nanoparticles	109
2.4.3 Electronic properties of the SCO nanocomposite	111
2.4.4 Mechanical properties of the SCO nanocomposite	113
2.4.5 Analytical expressions of the relaxed lattice parameters	116
2.4.6 Spatial distribution of the HS fraction	119
2.4.7 Elastic energy and spatiotemporal behavior of the nanocomposite at the transition	122
2.5 Conclusion	124

References: -	127
----------------------------	------------

Chapter 3

3.1 Introduction	135
-------------------------------	------------

3.2 The Model	137
----------------------------	------------

3.2.1 Technical details of Monte Carlo simulations	141
---	------------

3.3 Results and discussion	142
---	------------

3.3.1 Thermal behavior of uncoated core and hollow shell	142
---	------------

3.3.2 Case of spin-crossover nanostructure with active core and shell	143
--	------------

3.3.2.1 Effect of the core-shell lattice parameter misfit in HS state on the whole system.....	144
--	-----

3.3.2.2 Thermal properties of shell and core components	146
---	-----

3.3.2.3 Spatial distribution of the HS fraction and evidence of labyrinth formation inside the core	151
---	-----

3.3.2.4 Spatial profiles of the lattice bond lengths	153
--	-----

3.3.2.5 Lattice distortion and spatial distribution of elastic stresses	155
---	-----

3.3.2.6 Effect of the core-shell lattice parameter misfit in HS state on the whole system.....	159
--	-----

3.3.2.7 Thermal properties of shell and core components	161
---	-----

3.3.2.8 Spatial distribution of the HS fraction and evidence of labyrinth formation inside the core	166
---	-----

3.3.2.9 Lattice distortion and spatial distribution of elastic stresses	167
---	-----

3.3.2.10 Centre of mass	170
-------------------------------	-----

3.4 Conclusion	171
-----------------------------	------------

References: -	173
----------------------------	------------

Chapter 4

4.1 Introduction	176
-------------------------------	------------

4.2 Hamiltonian	179
------------------------------	------------

4.3 Results and discussion	181
---	------------

4.3.1 Boundaries effects	181
---------------------------------------	------------

4.3.1.1 Thermo-induced spin transition.....	181
---	-----

4.3.1.2 Spatiotemporal aspects.....	183
-------------------------------------	-----

4.3.2 Size effects	186
---------------------------------	------------

4.3.2.1 Length effects of crystal	186
---	-----

4.3.2.2 Thickness effects of crystal	190
--	-----

4.3.3 Relaxation Dynamics.....	193
---------------------------------------	------------

4.4 Conclusion	195
-----------------------------	------------

References:-	197
---------------------------	------------

Chapter 5

5.1 General Conclusion	201
5.1.1 Chapter 2.....	202
5.1.2 Chapter 3.....	203
5.1.3 Chapter 4.....	204
5.2 Perspectives	205
5.2.1 Thermal and mechanical properties of a 3-dimensional SCO crystal in elastically bounded media:.....	205
5.2.2 Core-Shell Architecture:	206
5.2.3 Metal-organic framework Spin Crossover materials:	207
5.2.3.1 Description of the model:	208

General Introduction

At the Crossroads of Nobels: Spin-Crossover

Vacuum tubes were hailed as the key to industrialization in the early 20th century. The invention (John Bardeen, Walter Brattain, and William Shockley) of the transistor (Nobel 1956) caused a tectonic shift in technological advancement, and the development of vacuum tubes became obsolete. Indeed we have come a long way from there thanks to pioneering work (Jack S. Kilby, Zhores I. Alferov and Herbert Kroemer) in information and communication technology (Nobel 2000), at least 10^{18} operations per second is expected to be performed by the first “exascale” computer in 2019. Despite being the size of ten tennis courts, the computer’s electronic components will be as tiny as feasible. 333 million transistors per square millimeter are expected in the latest processors; this corresponds to an area of 2 nanometers for each transistor on the chip.

But will that be it? Or can we downsize even further?

Over the years, it has been observed that the miniaturization of traditional electronics components is reaching its limit, not only because of manufacturing technological reasons but also because when a system achieves a minimal critical dimension, the physical phenomena driven by nanoscale material topology are typically substantially different. As a result, a bottom-up method is becoming more competitive in comparison to a top-down strategy, thus paving the way for a new research area centered on the development and study of “molecular systems”. This concept necessitates a thorough knowledge, manipulation, and good optimization of chemical and physical properties of various materials. We will need to shrink from microchips to the nanoscale in order to fit more information into fewer spaces; currently, the goal is to reach the molecular level. A renewed interest in building devices using molecular-scale components is being spurred on by the desire for even deeper downsizing of silicon-based electronics.

In a wide array of disciplines, illuminating research is laying the groundwork for the impending technological revolution. The development (Alan Heeger, Alan MacDiarmid, and Hideki Shirakawa) of electrically conductive polymer (Nobel 2000) could be considered as the first significant step toward more challenging molecular-scale electronics. Indeed, advances in designing and synthesis (Jean-Pierre Sauvage, Sir J. Fraser Stoddart and Bernard L. Feringa) of molecular machines (Nobel 2016) can help us in answering the previously asked question (How small can you make machinery?).

“In terms of development, the molecular motor is at about the same stage as the electric motor was in the 1830s when researchers proudly displayed various spinning cranks and wheels in their laboratories without having any idea that they

would lead to washing machines, fans and food processors. So, 32 years after Feynman's visionary lecture, we can still only guess at the thrilling developments ahead of us. However, we have a definite answer to his initial question: How small can you make machinery? At least 1,000 times thinner than a strand of hair." (Taken from Popular Information provided by The Nobel Prize foundation 2016)

Simultaneously breakthroughs of fundamental importance in both chemistry (Nobel 1998, 2007, 2010, 2013) and physics (Nobel 1977, 1982, 1991) are not to be forgotten. From an experimental point of view, palladium-catalyzed cross couplings in organic synthesis (Richard F. Heck, Ei-ichi Negishi, and Akira Suzuki) have been of immense importance in developing organic light-emitting diodes (OLEDs). They have applications in the synthesis of ligands and catalysts. At the same time, from the theory side, investigations of the electronic structure of magnetic and disordered systems (Philip Warren Anderson, Sir Nevill Francis Mott, and John Hasbrouck Van Vleck) contributed immensely to current technical development, particularly in electronics. In particular, Van Vleck, termed "the father of modern magnetism", was the first to develop the crystal field theory and the ligand field theory. His work was also instrumental in understanding the Jahn-Teller effect (Hermann Arthur Jahn and Edward Teller predicted it in the 1930s) in greater detail and in realizing its experimental importance.

Similarly, work done in the theory of critical phenomena (Kenneth G. Wilson) and order phenomena (Pierre-Gilles de Gennes) at the phase transition, by building on the work done by L. Landau and L. Onsager, gave a complete theoretical description of the behaviour close to the critical point and also gave methods to calculate the crucial quantities numerically. Wilson's analysis showed that sufficiently close to the critical point, most of the system's variables become redundant. Two numbers essentially determine the critical phenomena: the dimensionality of the system and the dimensionality of a critical quantity called the "order parameter", a quantity introduced already in Landau's theory. This is a concrete example of the impact of broad generalization. According to this theory, a large number of completely unrelated systems can exhibit the same behavior when they are close to the critical point. Wilson's theory was backed up by solid evidence derived from fundamental concepts. There have been numerous advances in the understanding of polymer order phenomena since De Gennes's study was first published, which are based on general physical principles of phase transition. De Gennes's has shown that there is a surprising amount of generality in the mathematical concepts used to describe phase transitions in seemingly disparate physical systems such as magnets, superconductors, liquid crystals, and polymer solutions. While these are some examples in pure theoretical research, they were of great relevance when it comes to creating a more solid foundation for the technical utilization of systems (materials).

On equal footing is the work done in the direction of developing methods and theories, which in practice revolutionised the way in which science is conducted

by adding computations as another dimension (or tool) in the hands of theoreticians and experimentalists. Experimental techniques are increasingly frequently supplemented by computer-based simulations. They've been created and polished for decades, making it possible to study matter's structure and property behavior up close. It was Walter Kohn's theoretical contributions that laid the foundations for current Density-functional theory, while John Pople's computational approaches and enhancements allowed chemists to apply quantum chemical methods, revitalizing interest in the field. Innovative multiscale models have been developed (Martin Karplus, Michael Levitt, and Arieh Warshel) and are now standard laboratory tools for chemists. This means that chemists now spend just as much time in front of their computers as they do in the laboratory. Molecular biology, medicine, and geology all rely on these quantum chemistry procedures that were once uncommon but are now practically universal in inorganic chemistry.

While these methods were predominantly to bridge the gap between classical and quantum mechanical nature to solve many-body problems, another class of methods that can take into account a combination between classical/statistical/quantum mechanical nature are Monte Carlo methods. As a general class of computational techniques, Monte Carlo methods and experiments use repeated random sampling and randomization to tackle problems that might be deterministic. Even though the early pioneers like Stanislaw Ulam, John von Neumann, Enrico Fermi, and Nicholas Metropolis have their names attached to it, the field has been graced by numerous more luminaries from various fields who have made significant contributions as well. As a result, these methods have gone a long way since they were first created in the 1940s to examine physics-related problems (particularly neutron diffusion). Now their applicability transcends across disciplines, ranging from Natural science (Physics, Chemistry, Biology), Mathematics, Informatics (Artificial Intelligence) to Social Science (Economics, Finance, Business) and what not! Simulations are so realistic that they predict the outcome of conventional experiments.

The point of laying over this historical context is to exemplify that the current advancement should not be seen in isolation in one particular domain but as an amalgamation of both minor and major improvements in various fields. Also, to instil confidence that the objective in question is not an exercise of "castle-building in the air"; instead, it has a solid underlying foundation formed over years of research and technological progress. Even though it's yet unclear what the next-generation "core element/material" (i.e., bronze, iron, steel, silicon) will be for modern industrial civilisation, but one thing's for sure: it'll be at the atomic/molecular scale. MOLETRONICS (molecular electronics) deals with assembling molecular electronic components and utilizing molecules as the building blocks. By piling molecules three-dimensionally, the overall efficiency of the system might be significantly improved. Molecular electronic devices are capable of exhibiting virtually unlimited capability.

Thus, we are at a point in time where we can safely presume that rather than delving in “If’s?”, it might be more fruitful to reach “How ?” and “When ?”. In coming years culmination of multiple other breath-taking breakthroughs in various domains would be required to envision this future. And indeed, we can see, the field of molecular electronics is teeming with results, rationalizations, and speculations. Reports of passive molecular electronics devices, such as tunnel junctions and rectifiers, as well as of active devices, for example, single-molecule transistors and molecular switch tunnel junctions, have withstood scientific scrutiny. Simple molecular electronic devices usually consist of organic molecules sandwiched between conducting electrodes. Liquid-crystal displays, conducting polymers, organic light-emitting screens, and electrophotography’s photoreceptors are examples of recent successes. In addition, other products such as organic photovoltaic devices, organic superconductors, chemical sensors, electronic nasal sensors, solid-state coolants are rapidly evolving. One of the most popular research topics is exploring molecular-scale technologies that could one day replace silicon-based electronics altogether.

Impressive progress in increasingly sophisticated technologies has led to tremendous improvements in instrumentations and novel analytical techniques. These developments have impacted and encouraged the expansion of new scientific explorations in many different fields, and it is nowadays possible to observe, investigate and control phenomena at the ultrasmall and ultrafast scales. In 1988, the discovery of the giant magnetoresistance (GMR) by Albert Fert and Peter Andreas Grünberg (Nobel 2007) opened a new area of research in spintronics. While, the extraction (Andre Geim and Konstantin Novoselov) of the first two-dimensional material, Graphene (Nobel 2010), revolutionised the field of Nano-materials and electronics. Since then, there have been literally hundreds of other examples of functional two-dimensional materials demonstrating an extensive range of characteristics and functionalities. Both of these discoveries set the tone in which the functionalities of this regime would be viewed and exploited in future applications. Thus, considerable research is going on to use the flexibility in electronic spin properties and the small size of the individual molecular building blocks to fabricate electronic components. When employed as building blocks for memory and logic components, organic molecules outperform bulk silicon; as flexible thin films, they can be easily manufactured and have a high switching speed potential with minimal power requirements.

The use of organic molecules to manipulate the spin of the electrons and enhance spin-dependent transport through molecules opened a way towards a new kind of spintronics called molecular spintronics. This is one of the main reasons for the growing interest in using organic molecules in spintronic devices. The molecule’s spin transport and magnetoresistance are primarily influenced by modifying the molecular density of states (DOS) at the metal-organic interface. In this context, studies (Gerhard Ertl) conducted to understand chemical processes on solid surfaces (Nobel 2007) laid the methodological foundations for an entire field of

research (surface chemistry). This field aims to observe how individual layers of atoms and molecules behave on the extremely pure surface of a metal. Ertl's painstaking and systematic investigation conducted created a methodology for surface chemistry. With his painstaking precision and remarkable ability to refine difficulties, the outstanding realism of his results is attributable to the fact that it has laid the groundwork for how different experimental approaches can be employed to create an all-encompassing picture of a surface reaction.

The recent developments in the field of organic spintronics show the possibility of creating efficient spintronic devices with different types of organic molecules. While these previous mentions constitute the essence of scientific trend and impressing achievements being made continuously while pushing back its frontiers toward smaller scales. For instance, it is astonishing the accuracy with which it is possible to control a single atomic layer deposition or to develop artificial molecular machines designed to perform work under an appropriate external stimulus. Similar efforts that were set to bring in a revolution in chemistry and related sciences was targeted at ultrafast scales. The pioneering work conducted to study transition states of chemical reactions (Ahmed H. Zewail) gave birth to a research area called femtochemistry (Nobel 1999), which spurred further interests in the investigation of elementary processes at the ultra-small and ultra-fast time scales. Applications range from how catalysts function and how molecular electronic components must be designed to the most delicate mechanisms in life processes and how the medicines of the future should be produced.

The active control of a molecule spin constitutes one of the biggest hurdles in molecular spintronics. The enduring fascination with the control of matter properties and applied functionalities has resulted in a frenzy of research on matter transformations, which are typically governed by varying macroscopic parameters such as temperature, pressure, electric or magnetic field. Till now, spin manipulation has been done by the alteration of the molecular structure either by chemical doping or by external stimulation. However, the use of light as a control parameter has been more and more preferred in the different disciplines of science. New emerging fields makes it now possible to understand and control the properties of molecules and solids by light. The light-control of molecular transformation found applications in various areas, from technological applications to biological systems and medicine (biocompatible chromophores for drug delivery and cancer cure).

Nevertheless, the opportunity to drive Photo-Induced Phase Transition (PIPT) in solid-state physics founds general excitement in impacting the macroscopic state of materials with light pulses. Innovating new spin-based technologies require the capacity to control and modify the molecular spin in a reversible manner. A promising approach would be to use multifunctional molecules. For example, a spin-active molecule that can change its spin state by external excitations, e.g., temperature, light, electric field etc., can be used as a spacer layer. But in all the

cases, a detailed understanding of the physics of the interfaces of the molecules is mandatory to go further.

This discussion was vital as it sets the periphery of our context and domains in which we will view the available systems (i.e., complexes, materials, molecules, etc.), their dimensionality (0D, 1D, 2D, 3D), and functionality (Spintronics, devices/switches, magnetic/electronic/elastic, optical, etc.). Somewhere within the periphery of this discussion, we might find the solution, which might help us envision the prospects or update them.

One such example which we will discuss in this context are our “shy” (changes colour), “heavyweights” (heavy metals), Spin-Crossover (SCO) materials/molecules/complexes, they certainly “punch above their weight” (multiple functionalities, and applications), as a prominent molecular class, and are well known “Sci-magnets”, both literally (diamagnetic and paramagnetic states), and figuratively (have admirers (researchers) across disciplines (Physics, Chemistry, Biology, Geology...)). Not to forget, they are very “down to earth” (effects in earth’s lower mantle) and easy to please (controlled by various stimuli: temperature, light, pressure, magnetic or electric fields,...).

Spin-Crossover (SCO) complexes comprise a transition metal ion that can be switched between a low-spin (LS) and a high-spin (HS) state by external stimuli such as temperature, light, pressure, magnetic or electric fields. The two arrangements may result in different conductances, but the switchable spin of the metal ion has a significant potential for molecular spintronics. The SCO feature is connected to a sensitive energy balance between the HS and LS states associated with molecular conformational changes. Preserving this fragile truce for SCO molecules adsorbed onto surfaces necessitates careful regulation of the molecule’s interaction with the nearby electrodes in order to assure the SCO property.

Switchable molecules have recently attracted a lot of interest as molecular machines and actuators because of the potential they hold. So that the molecules may generate useful work in an efficient manner, they must be integrated and interfaced with their surroundings so that they can be connected to an external source of energy. The energy is then transduced by the molecules and can be controlled. SCO complexes are very well known to exhibit volume transition accompanying the spin or electronic transition. Therefore SCO complexes can be seen flexing their “molecular muscles” in this arena too, and further investigations will establish “How hard a punch it can throw?”.

Another significant area where SCO complexes can be revolutionary is, magnetic memory domain; being a very crucial part of computer technology, it is not shrinking at the same rate as its processing counterparts. So far, the state of the art technology will store one bit of data in about a dozen magnetic grains, each of which is about 3nm in size (while the state of the art transistors has been downsized to 2 nm). As computing becomes quicker and more powerful, memory is becoming a bottleneck.

A single molecule can be utilized to store information via a nanoscale molecular switch. Albeit the switching process can be monitored electrically as a change in the conductance of the molecule, incorporating spin functionality to molecular switches is a critical notion for creating molecular spintronic devices. One might very well ask, is it possible to imprint binary data on a magnetic molecule with a diameter of less than 1nm, replacing the existing solid magnetic grains? Until recently, this appeared to be science fiction, but that's about to change. The single-molecule magnet (SMM) is a result of advances in various domains of physics and chemistry. A single-molecule magnet can be thought of as a paramagnet the size of a single molecule. In general, SMMs are coordination complexes containing unpaired electrons that may transition between two opposed orientations of their magnetic moment, providing magnetic bi-stability below a specific 'blocking temperature'. The concept is that one molecule at a time will be addressed for data storage applications in the future. SCO complexes can lead the way in this category too as for Fe (II) complexes the LS state is diamagnetic in nature while the HS state is paramagnetic, not just that since the transition could be controlled through various stimuli, they very well enrich the prospects of SMM devices.

It's important to remember that all the aforementioned "molecular boulevards" (molecular elec-/spin-tronics, memories, devices, and machines) are still being paved. For this reason, further research is needed to fully understand the physics at play. Only if its development is founded on sound scientific results that have been tried and tested at each stage will molecular avenues evolve into a powerful technology. A thorough understanding of various regulating mechanisms, as well as the development of procedures for manufacturing reliable devices and assuring their resilience, are required for these goals to be achieved. Because of this, the future generation of technologies will most likely include hybrid devices that integrate molecular and electronic components. Experimental verification and controlled device manufacture are two main challenges in moletronics. Molecular devices must be robustly modeled in order to close the gap between their synthesis and implementation in solid-state molecular devices. Improved electrical functionality and innovative multifunctional compounds can be developed by accurately predicting material behavior. In spite of the difficulty of experimentally verifying and simulating molecular devices, significant advances have been made in this area.

An overview of the PhD project's context and purpose.

New technological applications necessitate the creation of switchable materials. However, little is known about the mechanisms that take place throughout the process of switching. This investigation is complicated even further by the presence of multi-scale features in molecular materials. SCO materials are fascinating as prototypes in this context. With a discussion of the potential uses for such components, this thesis presents an in-depth description of SCO based switchable molecular complexes in the form of core-shell nanocomposite and actuator. We emphasise new breakthroughs and present a brief history of accomplishments in the field of molecular devices.

There were numerous unanswered questions at the start of this PhD regarding the ability to construct multistep transitions. What role does structure-property relation play for a SCO system? What are the key parameters governing the switching? What impact do various forms of frustration have on the switching mechanism? How do the various degrees of freedom react and their corresponding timescales? What role do other degrees of freedom related to symmetry and ordering play? Does this mean that new paths for the development of composite materials can be explored? Can strain engineering be used to uncover or improve new functionalities?

This thesis attempts to explain the variety of empirically observed bulk characteristics and behaviors in SCO systems. We developed structure-property links, inferred the processes of multistep transitions, and described why and how intermolecular interactions play a role using a simple, yet elegant elastic model. New emergent traits and behaviors were also predicted, particularly for the core-shell architectural design. In Chapters 2 and 3, we illustrate that this model can be utilized to predict and explain various observations made during experimental core-shell heterostructure transitions. We demonstrate clear structure-property relations that explain these results in terms of competition and cooperation by changing various misfit parameters or simply adjusting the core to shell entities ratio.

In Chapter 4, we suggest using elastic models to investigate a new system called "molecular actuators." Grasping and forecasting the behavior of these materials is crucial for optimal operation, and a detailed understanding of structure-property correlations are required. Various research has been undertaken over the last 35 years to determine the stress profile of these devices. However, the effect of surface stresses on device rigidity is still poorly understood, and a controlled, quantitative measurement of surface effects and stress on cantilever stiffness with

commensurate theoretical interpretation remains out of reach. The purpose of this chapter is to theoretically comprehend the electronic and mechanical properties of SCO molecular switches, hence leading to the creation of improved microelectromechanical systems (MEMS). As a result, we extend our prior theoretical work by employing a microscopic electro-elastic model to describe non-negligible changes in doubly clamped SCO beams caused by stress generated by thermal expansion or contraction. This study's further knowledge will be a critical step toward explaining the effect of fixed edges on the structural and thermal properties of the crystal.

In Chapter 5, we shall discuss the research's future prospects. As a result, this PhD thesis aims to open up new avenues for the development of new hybrid materials or devices by leveraging the current understanding of fundamental physical processes.

Chapter 1.

Introduction to Spin-Crossover Systems

1.1 Introduction

In the solid-state, the local molecular distortions caused by the metal ions changing spin state couple to the long-range elastic interactions, which can lead to first-order transitions with hysteresis, indicating significant interactions between the metal centres. Consequently, over recent years, Spin Crossover (SCO) systems have emerged as both an experimental and theoretical playground of bulk properties. On the applied side, they are among the main class of switching materials. The unique functionality of SCO systems, getting triggered by different external stimuli [1]–[5], makes them highly sought after for their numerous applications as smart molecular devices, including reversible high-density memory, multi-bit electronics, quantum bits, optical displays and nanoscale sensing and various technological applications [6]–[15]. Moreover, the spin state switching phenomena have considerable importance in biological systems such as metalloproteins; isopenicillin N-synthase, deoxyhemerythin and ribonucleotide reductase [16] or geology [17]. Spin Crossover switchable magnetic materials have several advantages comparing with conventional magnets since most of them change the color and can be tailor-made; thus, they provide a unique tool for fine-tuning the physical properties. On the fundamental side, the remarkable chemical versatility and variability of these systems allows for the manipulation of both the local chemistry and molecular structure to produce a diverse range of bulk properties and behaviours.

So, this chapter treats the basic knowledge necessary to understand SCO materials. It begins with a brief discussion about coordination chemistry and various theories, which will be helpful in explaining the SCO. Next, we move on to general historical introduction of SCO materials and then continues with an overview of SCO phenomena. Then we discuss about various models developed with significant emphasis on the techniques and the model we are going to use in this thesis in order to encapsulate and portray the entire picture of the various phenomena occurring across the variety of SCO systems. Additionally, a brief review of the mode influence of external stimuli on SCO behavior is provided, and multiple detection techniques and applications are discussed succinctly.

1.2 Metal complexes and Ligand field theory: Overview

Coordination complexes typically consist of a central transition metal ion (a metal with a partially filled d-shell), surrounded by several ligands. A ligand can be any atom, ion or molecule usually, with one or more lone electron pairs. The bond between the metal and ligands is a coordinate covalent or dative bond; a bond formed from the donation of two electrons from the same atom. Usually, with the ligand as the electron donor. Depending on whether one or many of the atoms in the ligand form a coordination covalent bond with the metal, the ligand is said to be either monodentate (one bond) or polydentate (many bonds)

The chemistry of coordination complexes is usually dominated by the s- and p-orbitals of the ligands and the d- orbitals of the metal. This limits number of bonding and non-bonding electrons pairs to nine (five d-orbitals, three p-orbitals, one s-orbital). Consequently, the number of coordination bonds is limited to the number of empty s-, p- and d- orbitals. Although uncommon, f-orbitals can sometimes contribute to bonding, resulting in coordination complexes with more than nine ligands. The arrangement of ligands depends on the type of metal and the type, symmetry and position of the ligands. However, typically for transition metals, only the bonding electron pairs contribute to the molecular geometry. This results in complexes having a regular geometry that depends only on the number of coordination bonds (the coordination number).

The presence of the ligands has a large influence on the structural, spectral and magnetic properties of the complex. For example, coordination complexes have a remarkable diversity of colours that arise from electronic transitions that are either d-d transitions or charge transfer bands. d-d transitions occur as a result of an electronic transition between d-orbitals, and charge transfer bands arise from the transfer of charge between the metal and ligands. Since the ligands are predominantly s- and p-orbitals, the d-d transitions must occur as a result of the splitting of the d-orbitals of the metal. This splitting has a significant effect on the magnetic properties of the complex.

There are a host of theories that attempt to explain the influence of the ligands on the metal: crystal field theory, molecular orbital theory and valence bond theory. Interestingly, each of these theories correctly depicts certain aspects of a more complete approach. The current incarnation of this “more complete theory” is ligand field theory. However, ligand field theory is quite abstract by nature and does not lend itself to intuition. Instead, we will begin by applying a combination of crystal field theory (in Section 1.2.1) and molecular orbital theory (in Section 1.2.2) to explain both the electrostatic and covalent nature of the bonding. We will then go on to explain the basics of Ligand field theory in Section 1.2.3.

1.2.1 Crystal Field Theory

The chemistry of transition metal complexes is driven by the valence d-orbitals of the transition metal cations. In the free atom, all d orbitals are degenerate, and they have the same energy. When ligands are added, the atomic d orbitals interact with the s and p orbitals (typically) of the ligands relevant to the symmetry at hand, and they form molecular orbitals. Crystal field theory (CFT) was first developed to explain the influence of the ligands on the d-orbitals of a transition metal ion. CFT is predicated on the idea that metal–ligand interactions are entirely electrostatic. Despite the fact that this assumption is manifestly false for many complexes, such as those containing neutral ligands like CO, CFT allows chemists to describe many of the features of transition-metal complexes with reasonable precision. Consequently, CFT is typically only applicable when ligands are negatively charged ions or molecules with lone electron pairs. In these cases, the electrostatic field (formally, crystal field) generated by the ligands can be approximated by a set of point charges or dipoles. Where negative ions are replaced by negative point charges and molecules with lone electron pairs are replaced by dipoles. Since the symmetry of the crystal field will be lower than the symmetry of the d-orbitals, the presence of the ligands will break the symmetry of the d-orbitals. Consequently, electrons occupying orbitals with lobes closer to the surrounding charges will experience a greater electrostatic force, resulting in a splitting of the orbitals, Δ , relative to the average distance between the orbital lobes and the surrounding point charges or dipoles, see Fig. 1.1. Where Δ measures the influence of the ligands on the d-orbitals of the central metal ion.

An octahedral structure of six negative charges modifies the d orbital energies of a transition metal ion. Keep in mind that the five degenerate d orbitals are initially degenerate (have the same energy). The d orbitals will remain degenerate if six negative charges are distributed uniformly across the surface of a sphere. Still, their energy will be increased due to repulsive electrostatic interactions between the spherical shell of negative charge and electrons in the d orbitals (Figure 1a). Adding six negative charges to the vertices of an octahedron does not change the average energy of the d orbitals, but it does eliminate their degeneracy: the five d orbitals are divided into two groups whose energies depend on their orientations. As shown in Figure 1b, the d_{z^2} and $d_{x^2-y^2}$ orbitals point directly at the six negative charges located on the x, y, and z axes. An electron in these two orbitals (collectively referred to as e_g orbitals) will have a higher energy than it will be for a spherical distribution of negative charge because of the increased electrostatic repulsions. In contrast, the other three d orbitals (d_{xy} , d_{xz} , and d_{yz} , collectively called the t_{2g} orbitals) are all oriented at a 45° angle to the coordinate axes, so they point between the six negative charges. An electron in any of these three orbitals has lower energy than a spherical distribution of negative charge.

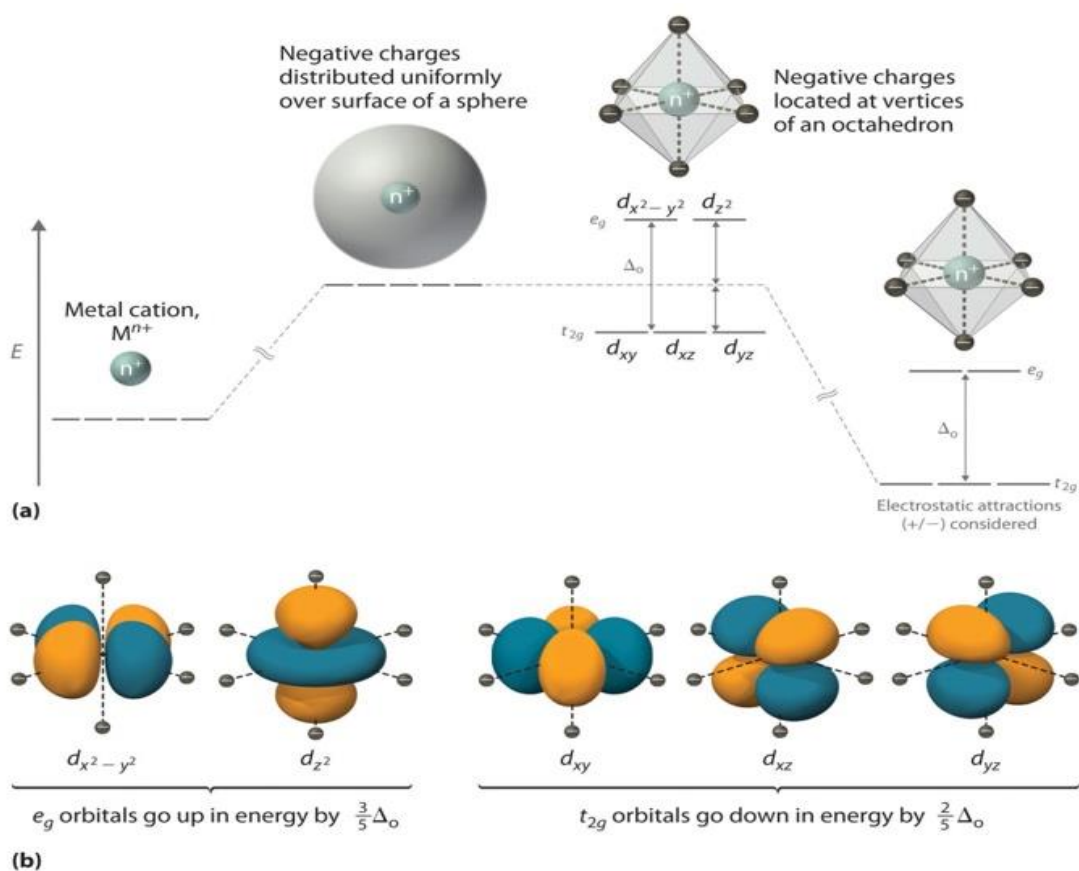


Figure 1.1 The five d Orbitals are split into two sets with different energies due to an octahedral arrangement of six negative charges around a metal ion. (a) Applying a uniform charge of -6 to a spherical surface surrounding a metal ion increases the energy of all five d orbitals due to electrostatic repulsions, but the five d orbitals remain degenerate. Placing a charge of -1 at each vertex of an octahedron causes the d orbitals to split into two groups with different energies: the $d_{x^2-y^2}$ and d_{z^2} orbitals increase in energy, while the d_{xy} , d_{xz} , and d_{yz} orbitals decrease in energy. The average energy of the five d orbitals is the same as for a spherical distribution of a -6 charge, however. Attractive electrostatic interactions between the negatively charged ligands and the positively charged metal ion (far right) decrease the energy of all five d orbitals but do not affect the orbital splittings. (b) The two e_g orbitals (left) point directly at the six negatively charged ligands, increasing their energy compared to a spherical negative charge distribution. In contrast, the three t_{2g} orbitals (right) point between the negatively charged ligands, lowering their energy compared to a spherical charge distribution. Adapted from [18].

Symmetry arguments show that the presence of the surrounding point charges splits the d-orbitals into e_g and t_{2g} orbital sets. The difference in energy between the two sets of d orbitals is called the crystal field splitting energy (Δ), Consequently, Δ can be calculated from taking the energy difference between an electron in an e_g and t_{2g} orbital.

$$\Delta_{oct} = E(e_g) - E(t_{2g}) \quad (1)$$

where oct is an abbreviation for octahedral. As we will see, the magnitude of the splitting is determined by the charge on the metal ion, the metal's position in the periodic table, and the nature of the ligands. It is important to note that splitting the d orbitals in a crystal field has no effect on the total energy of the five d orbitals: the two e_g orbitals increase in energy by $0.6 \Delta_{oct}$, whereas the three t_{2g} orbitals decrease in energy by $0.4 \Delta_{oct}$. Thus, the total change in energy is

$$2(0.6 \Delta_{oct}) + 3(-0.4 \Delta_{oct}) = 0 \quad (2)$$

As a result, the t_{2g} orbitals are stabilised while the e_g orbitals are destabilised. The spin-pairing energy (P) is the increase in energy caused by the addition of an electron to an already occupied orbital. A high-spin configuration occurs when the Δ_{oct} is less than P, which results in complexes with the maximum number of unpaired electrons possible. Conversely, a low-spin configuration occurs when the Δ_{oct} is greater than P, which produces complexes with the minimum number of unpaired electrons possible. Strong-field ligands interact strongly with the d orbitals of the metal ions and give a large Δ_{oct} , whereas weak-field ligands interact weakly and give a smaller Δ_{oct} . The magnitude of Δ_{oct} dictates whether a complex with four, five, six, or seven d electrons is high spin or low spin, which affects its magnetic properties, structure, and reactivity. As we noted, the magnitude of Δ_{oct} depends on three factors: the charge on the metal ion, the principal quantum number of the metal (and thus its location in the periodic table), and the nature of the ligand.

The experimentally observed order of the crystal field splitting energies produced by different ligands is called the spectrochemical series, shown here in order of decreasing Δ_{oct} :

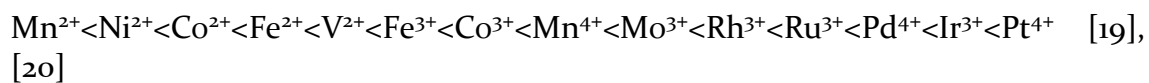
strong field ligands {CO \approx CN⁻}
> intermediate field ligands {NO⁻² > phen > en > NH₃ > SCN⁻
> H₂O > oxalate²⁻}
> weak field ligands {OH⁻ > F > acetate⁻ > Cl⁻ > Br⁻ > I⁻}

In general, halogens are weak ligands (a small value of Δ_{oct}), water has a medium strength, ammonia has much higher strength, and the strong bonding ligands of cyanide and carbon monoxide have a very strong bonding strength. The size of the splitting will also depend on the nature of the metal. The following factors will play a role in the size of Δ_{oct} :

Δ_{oct} increases with increasing oxidation number of the metal. This is due to the smaller size of the ion, which results in shorter metal-to-ligand distances and, as a result, a larger ligand field.

Δ_{oct} increases as you go down a group. This is due to the better bonding ability of expanded shells using the 4d or 5d orbitals.

The results of these trends are summarized in the list below. The smallest values of Δ_{oct} occur with the +2 ions, with increasing values observed for higher charged ions which are in the series below.



In general, since CFT neglects the finite size of the atomic orbitals and the covalent nature of the bonding, its successes are limited to explaining d-d transitions in systems where CFT is appropriate. A full explanation of the spectral and magnetic properties of coordination complexes requires both treatment of the electrostatic and covalent nature of the bonding.

1.2.2 Molecular orbital theory

Molecular orbital theory (MOT) was developed as a way of explaining covalent bonding in molecules. In MOT, the electrons are not assigned to individual atoms but “molecular orbitals” that are delocalized over the molecule. More accurately, MOT approximates the many-electron wave function as a product of single electron wavefunctions called molecular orbitals. Each molecular orbital can be thought of as an average field of nuclei and electrons. Essentially, MOT has the same theoretical foundation as the Hartree-Fock method [21]. Consequently, MOT is most accurate for molecules with strong covalent bonding. The molecular orbitals can be classified as either bonding, anti-bonding or non-bonding. Bonding and anti-bonding molecular orbitals are created from the superposition of atomic orbitals with similar energy and the same symmetry; one from the constructive interference (bonding) and one from destructively interference (anti-bonding) of the atomic orbitals (see Fig. 1.2). The anti-bonding orbitals are usually distinguished by an asterisk, for example e_g^* . The atomic orbitals that do not have a symmetric counterpart are called non-bonding orbitals.

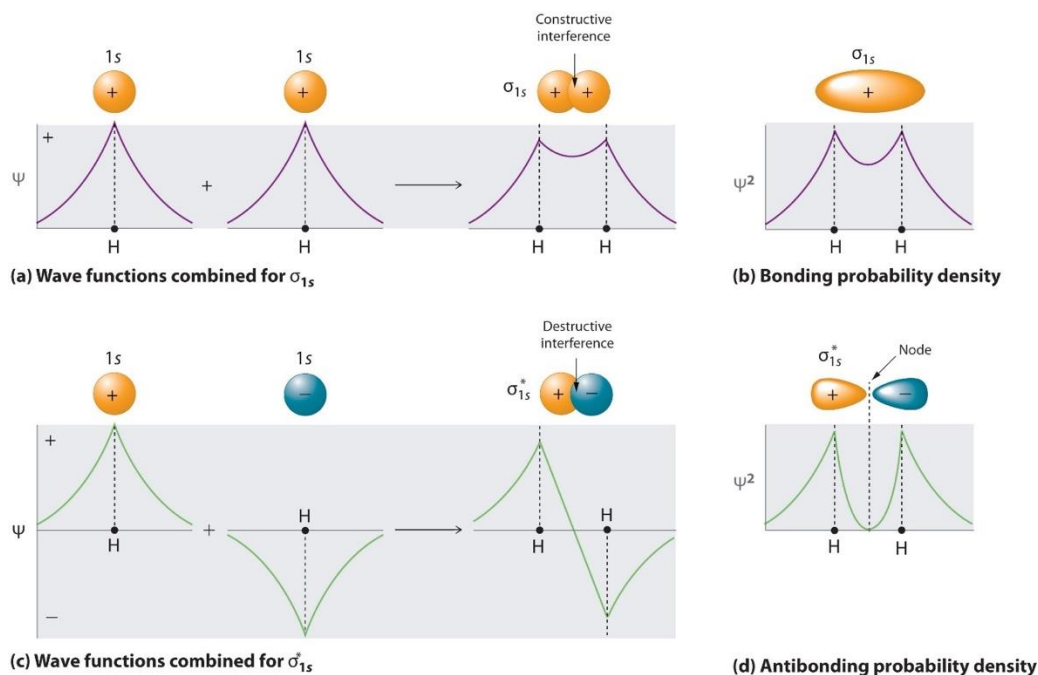


Figure 1. 2 Molecular Orbitals for the H₂ Molecule. (a) This diagram shows the formation of a bonding σ_{1s} molecular orbital for H₂ as the sum of the wave functions (Ψ) of two H 1s atomic orbitals. (b) This plot of the square of the wave function (Ψ^2) for the bonding σ_{1s} molecular orbital illustrates the increased electron probability density between the two hydrogen nuclei. (The probability density is proportional to the square of the wave function.) (c) This diagram shows the formation of an antibonding σ_{1s}^* molecular orbital for H₂ as the difference of the wave functions (Ψ) of two H 1s atomic orbitals. (d) This plot of the square of the wave function (Ψ^2) for the σ_{1s}^* antibonding molecular orbital illustrates the node corresponding to zero electron probability density between the two hydrogen nuclei. Adapted from [22].

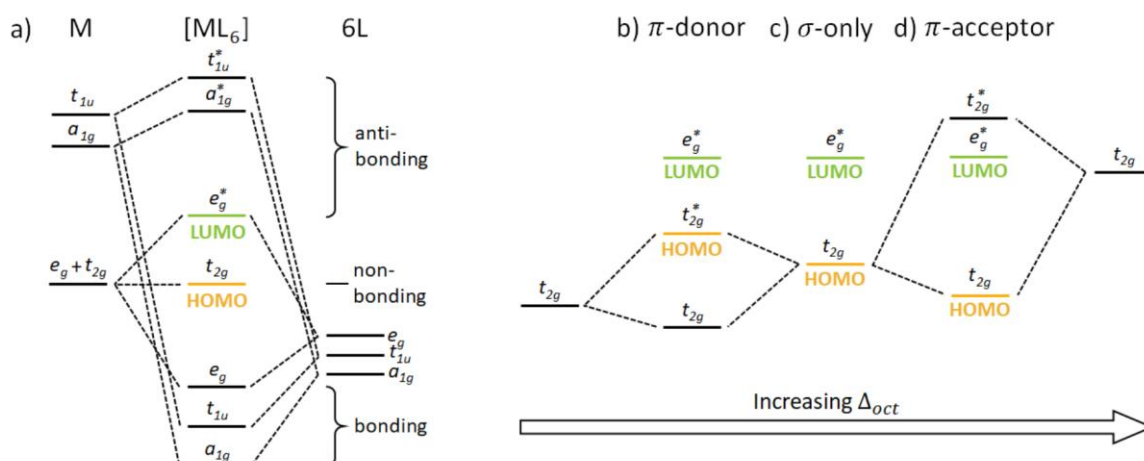


Figure 1. 3 Molecular orbital energy level diagrams for ML₆, showing (a) the influence of σ -bonding and (b-d) π -bonding on the molecular orbitals. The energy difference between the highest occupied molecular orbital (HOMO) and lowest unoccupied molecular orbital (LUMO) strongly depends on the type and strength of the π -bonding, decreasing for stronger (b) π -donation and increasing for stronger (d) π -acceptance. Adapted from [23]

For bonding orbitals, the constructive interference of the atomic orbitals will result in an increase in the concentration of the electron density in the region between the nuclei (see Fig. 1.2b). The increased electron density will attract the atoms closer together, strengthening the bond between the atoms and increasing the molecular stability. Whereas, for anti-bonding orbitals, the destructive interference of the atomic orbitals will decrease the electron density in the inter-nuclei regime and shift it further away from nuclei (see Fig. 1.2d). This decrease in the electron density increases the Coulomb repulsion between the atoms, pushing them away from each other, weakening the bond between them, and decreasing the molecular stability. Evidently, specific physical properties like the strength, length and stability of the metal-ligand bond will depend on the population of the bonding and anti-bonding orbitals. Typically, this can be quantified by the bond order

$$\text{bond} = \frac{N_{BO} - N_{ABO}}{2}, \quad (3)$$

where N_x is the population of electrons in the bonding ($x = BO$) and antibonding ($x = ABO$) orbitals. The bond order indicates the number of free electron pairs and more loosely corresponds to the strength of the bond between electrons. The stronger the electronic interactions are, the more tightly held together the molecules are. And thus, a shorter metal-ligand bond distance and higher molecular stability.

In the MOT description of octahedral molecular complexes, there is a host of different bonding, anti-bonding and non-bonding orbitals (see Fig. 1.3a). For a perfectly octahedral molecular complex, MOT arrives at the same conclusion as CFT. The highest occupied molecular orbitals (HOMO) will be the t_{2g} orbital set and the lowest unoccupied molecular orbitals (LUMO) will be the e_g orbital set. However, in the MOT description, the e_g and t_{2g} orbitals are formed from the bonding between the metal and ligands. The stability of t_{2g} orbitals depend strongly on the nature of the σ^- and π^- bonding (see Fig. 1.3b-d). σ^- bonding being the strongest type of bond formed from the head-on overlap of atomic orbitals. And, π^- bonding being typically weaker, formed from the side-on overlap of atomic orbitals. In the absence of any π^- bonding, the t_{2g} orbitals will be non-bonding (see Fig. 1.3c). Whereas, if the π^- bonding orbitals of the ligand have similar energy and the same symmetry as the non-bonding t_{2g} orbitals, then either the metal or ligand will donate an electron pair to form a π^- bond. When the ligand donates the electron pair, it is referred to as π^- donation, and when the metal donates the electron pair, it is referred to as π^- acceptance. This bond splits the non-bonding t_{2g} orbitals into bonding t_{2g} and anti-bonding t_{2g}^* orbitals.

Depending on whether the ligands are π -donors (see Fig. 1.3b) or π -acceptors (see Fig. 1.3d), the HOMO will be either the t_{2g}^* or t_{2g} orbital sets, respectively. Since the t_{2g}^* orbitals will have higher energy than the non-bonding t_{2g} orbitals, π^- donation will decrease Δ_{oct} (see Fig. 1.3b), and π -acceptance will increase Δ_{oct} (see Fig. 1.3d).

1.2.3 Ligand Field Theory

Ligand field theory (LFT) was initially developed as a means of combining CFT and MOT to produce a complete version of MOT that includes electrostatic repulsions. It is a purely microscopic description of coordination complexes that take into account electron-electron interactions among the d electrons as well as metal-ligand bonding and electrostatic repulsion.

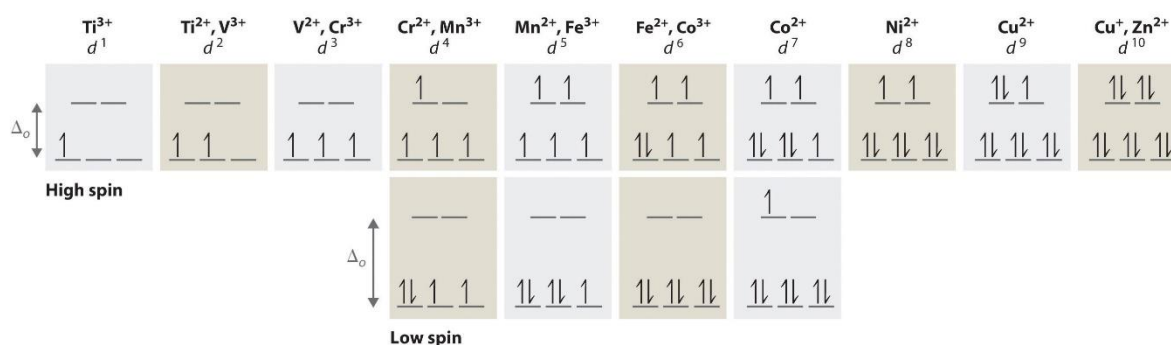


Figure 1. 4 The Possible Electron Configurations for Octahedral d^n Transition-Metal Complexes ($n = 1-10$). Two different configurations are possible for octahedral complexes of metals with d_4 , d_5 , d_6 , and d_7 configurations; the magnitude of $\Delta_{oct} \sim 10Dq$ determines which configuration is observed. Depending on the strength of orbital splitting, $10Dq$, and spin pairing energy, P , the e_g^* ($10Dq > P$ (*High Spin*)) and t_{2g} ($10Dq < P$ (*Low Spin*)) orbitals of an octahedral molecular complex with $d^4 - d^7$ can be filled according to either (a) Hund's rule; maximise the spin multiplicity or (b) the aufbau principle; fill the orbitals in order of increasing stability, maximising the spin multiplicity of each [18].

The coordination number of the resulting metal complex and the ligand structural arrangement depends on various parameters, the most important being the number of electrons in the d orbitals of the metal ion, the presence of double-bonds and the relative sizes of the ligands and the metal ion: early and big transition metals, smaller ligands and few double bonds favor high coordination numbers. The presence of polydentate ligands, unequal bond lengths, spin-orbit coupling or structural distortions such as Jahn-teller distortions will slightly and sometimes dramatically lift the degeneracy of the orbitals [21]. The symmetry of the complex can range from the rare linear and trigonal planar geometries for respectively two and three-fold coordination to tri-capped trigonal prismatic for nine-fold coordination or even icosahedral geometries for some lanthanide and actinide complexes. Of course, one must keep in mind that these represent limiting

geometries: if all the ligands are different, asymmetrical steric repulsion and electrostatic interaction will distort the structure. The Jahn-Teller effect [24], [25] occurring in orbital nonlinear spatially degenerate molecules (most often of octahedral geometries) can also modify the structure, as in their case reducing the symmetry of the complex lifts a degeneracy in the electrons orbitals, reducing the energy of the complex. More geometries can be found in the book by Y. Jean [20].

A qualitative approach that can be used for octahedral metal complexes can be explained through these diagrams: We've already discussed two of them in (Fig. 1.3). Only sigma bonding is examined in the first diagram (Fig. 1.3a), which depicts the combination of metal 3d, 4s, and 4p orbitals with occupied ligand group orbitals (using one orbital from each ligand). The metal electrons would then be fed into the, t_{2g} and e_g^* molecular orbitals, which is identical to the CFT model except that the, e_g orbital is now e_g^* . The ligand π orbitals are full and at lower energy than the metal t_{2g} in the second plot (Fig. 1.3b) for scenario B. This causes a decrease in the size of $\Delta \sim 10Dq$. The ligand π orbitals in instance C are vacant and have higher energy than the metal t_{2g} . The size of $\Delta \sim 10Dq$ increases as a result of this.

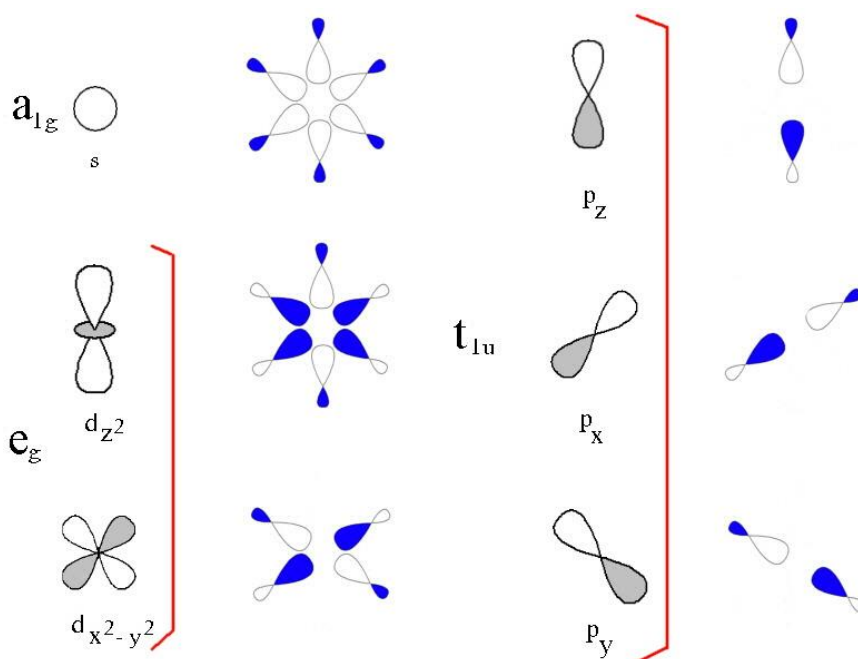


Figure 1.5 The ligand group orbitals that would have the proper symmetry to overlap with the 3d, 4s, and 4p metal ion atomic orbitals are displayed alongside them. The symmetry adapted linear combination of ligand orbitals are generated by taking 6 sigma orbitals from the ligands, designated as $\sigma_x, \sigma_{-x}, \sigma_y, \sigma_{-y}, \sigma_z, \sigma_{-z}$ and then combining them to make 6 ligand group orbitals. (labelled a_{1g}, e_g, t_{1u}) [26]

Metal ion atomic orbitals for 3d, 4s and 4p, are shown in Fig. 1.5, along with the orbitals of the ligand group that would be required to produce the correct

symmetry to be able to overlap with them. Complexes with strong π -acceptance are filled according to Hund's rule; maximise the spin multiplicity. Whereas complexes with strong π -donation are filled according to the aufbau principle; fill each orbital set in order of decreasing stability, maximising the spin multiplicity of each. We can illustrate this phenomenon by considering two energy scales: Δ and P the energy required for an electron to form an electron pair. If $\Delta > P$, the electrons will preferentially form electron pairs instead of occupying higher energy orbitals. Whereas, if $\Delta < P$, it becomes preferable for the electrons to occupy higher energy orbitals instead of forming electron pairs. Depending on the number of d electrons, the different regimes correspond to either the same or different spin-states, see Fig. 1.4. For an octahedral molecular complex with $d^4 - d^7$, shown in Fig. 1.4, the ground state can be either the high-spin (HS) state if $\Delta < P$ or the low-spin (LS) state if $\Delta > P$. The HS state is filled according to Hund's first rule, and the LS state is filled according to aufbau filling principle.

In LFT, the nd orbitals of a transition metal ion, in a perfectly octahedral complex, are split into e_g^* and t_{2g} orbital sets. The orbital splitting between the e_g^* and t_{2g} orbital sets is referred to as the ligand field splitting parameter $10Dq$. The value of the ligand field, the crystal field splitting energy, is often noted as $10Dq$ "differential quanta" instead of Δ to distinguish LFT from CFT and MOT, where Dq is a semiempirical parameter related to the crystal force field. The strength $10Dq$ depends on the nature of the metal ion and the nature and symmetry of the surrounding ligands. In particular, the strength of $10Dq$ depends on the relative population of the bonding and anti-bonding orbitals (bond order) and the metal-ligand bond distance. The former is a consequence of the metal-ligand bonding, while the latter is predominantly a consequence of electrostatic repulsion. More explicitly $10Dq \propto r_{M-L}^{-n}$, where r_{M-L} is the metal-ligand bond length and $n \in 5,6$ [27].

This relationship highlights an important structure-property relationship for spin-crossover systems; spin crossovers (SCO/SC) and spin transitions (ST) are most commonly observed in complexes with the most prominent structural differences between the HS and LS states. We can illustrate this by considering the ratio

$$\frac{10Dq^{LS}}{10Dq^{HS}} = \left(\frac{r_{HS}}{r_{LS}}\right)^n \quad (1.3)$$

An increase in r_{HS}/r_{LS} leads to an increase in $\frac{10Dq^{LS}}{10Dq^{HS}}$. In turn, this leads to a more extensive regime in which spin crossovers and spin transitions can occur. In general, since the HS state has a higher population of anti-bonding orbitals than the LS state, the HS state will have a higher bond length, spin multiplicity, lower bond strength, and molecular stability. A secondary effect of this is a dramatic increase in the entropy of the HS state over the LS state. Evidently, the higher spin and orbital multiplicity of the HS state will result in a higher overall electronic entropy than the LS state. Less obviously, the lower molecular stability in the HS state is associated with a softening of the vibrational modes and a dramatic

increase in the vibrational entropy [9], [28].

For complexes in the $\Delta^{HS} < p < \Delta^{LS}$ region, the significant differences in bond length and entropy between the HS and LS states allow small external perturbations to drive a spin-crossover or spin transition [27]. There are hundreds of known complexes that meet this criterion [27]. Most commonly, the molecular geometry is (near) octahedral with a central Fe^{2+} , Fe^{3+} , or Co^{2+} ion, or less commonly the central metal is Co^{3+} , Cr^{2+} , Mn^{2+} , or Mn^{3+} [9], [27]. There are numerous possible ligands for the more common metals ions that can result in a spin-crossover and spin transition [9].

1.3 What is Spin Crossover: Historical Overview

The SCO phenomenon was discovered by L. Cambi and L. Szego in the early 1930s while studying the magnetic susceptibility of $Fe(III)$ compounds [29]. The preliminary explanation for this unusual magnetic behavior (i.e., ST) was thermal equilibrium between two different magnetic isomers. Three years later, this phenomenon was discovered in $Fe(II)$ [30]–[32] compounds. Since then, many SCO materials with an electronic $3d^4 - 3d^7$ configuration have been discovered with other metals such as: $Co(II)(3d^7)$ [33], [34], $Mn(III)(3d^5)$ [35]–[38], $Mn(II)(3d^4)$ [39], $Cr(II)(3d^4)$ [40]–[42], and $Co(III)(3d^6)$ [43], [44]. Furthermore, many SCO materials are now produced synthetically due to industrial requirements [30], [45].

The term "Spin Crossover" was coined for the first time in 1964 [46] to refer to the spin change. Because of the way the $3d$ orbitals split in the octahedral ligand field, two distinct electronic configuration states can be distinguished: a diamagnetic low-spin (LS) state, which corresponds to the maximum spin pairing configuration, and a paramagnetic high-spin (HS) state, which is achieved when the given ion has the maximum multiplicity. The study of the required electronic properties for a molecule to be switchable is the first step in understanding the SCO phenomenon. The molecular energy spectrum must first be determined. However, the complicated electronic structure of a SCO molecule prevents analytical solutions to Schrödinger's equation from being obtained. First principle and quantum chemical calculations adapted for SCO molecules have been intensively developed over the last few decades, and success in the simulation of molecular vibrational properties has been realized [47]. The systematic prediction of the ground state and the precise estimation of the ground energy level, on the other hand, remains a challenge. As a result, more simplified approaches are required. In this regard, crystal field and ligand field theories discussed in the previous sections are extremely useful for qualitatively describing the SCO electronic structure and spin conversion phenomenon [43].

A spin-crossover complex's general structure consists of a central transition metal atom (e.g., Fe, Co, etc.) surrounded by ligands formed by various organic groups.

The presence of ligands in a transition metal complex modifies the electronic and magnetic properties of the central metal atom to comprehend the structure, electronic, and magnetic properties of the transition metal complex to a certain extent, the ligand field theory (LFT) can predict this modification. The central transition metals in most spin-crossover molecules have an octahedral coordination geometry (i.e., 6 metal–ligand bonds) with electronic configurations ranging from d^4 to d^7 . As we have discussed in the previous section at the molecular level, two major effects compete: on the one hand, electrons tend to occupy d orbitals (Hund's rule) due to exchange coupling. Electrons, on the other hand, tend to fill the t_{2g} level, which is the lowest energy level. As a result of these antagonistic effects, there are two possible ground states depending on the strength of the ligand field, which is strongly spin state dependent in contrast to the electron pairing energy P , which is almost insensitive to spin state.

In this section, we will look closely at the case of $Fe(II)$ -complexes in which the d -orbital is partially filled with six d electrons. The $3d$ orbitals in a $Fe(II)$ compound are divided into two subsets [48], [49]. The first subset consists of three t_{2g} orbitals (d_{xy} , d_{yz} , d_{zx}), while the second subset consists of the remaining two e_g orbitals ($d_{x^2-y^2}$, d_{z^2}). The complex's spin state will be determined by the placement of the electrons in the e_g and t_{2g} orbitals. The orbitals are shown in Fig. 1.1a. Depending on the system's conditions (i.e., ligand field strength), the system balance can be skewed toward one of two states: the LS state or the HS state. If the spin-pairing energy (P) (derived from electron-electron repulsion) is greater than the ligand field strength ($10Dq$), the electrons will first occupy the five d -orbitals singly according to Hund's rule, and then the sixth electron will pair with the first d -orbital (Fig. 1.4). This configuration leaves the system with four unpaired d -electrons and changes the complex's net spin to $S = 2$. This is the paramagnetic high-spin (HS) ground state ${}^5T_{2g}(t_{2g}^4 e_g^2)$ (Fig. 1.4). If the spin-pairing energy (P) is less than the ligand field strength ($10Dq$), the electrons will no longer follow the Hund's law, and electrons will pair and occupy the lowest energy d -orbitals (t_{2g}) twice. In accordance with Pauli's principle, the orbitals will take an anti-parallel configuration; as a result, the diamagnetic low-spin (LS) ground state ${}^1A_{1g}(t_{2g}^6 e_g^0)$ has a net spin $S = 0$ (Fig. 1.4).

When the ligand field force is of the same order of magnitude as the electron pairing energy, any small external perturbation can reversibly switch the molecule from one spin state to the other in a reversible manner. This phenomenon is known as spin crossover (SCO/SC), spin equilibrium, spin conversion, or spin transition (ST).

Through the Russel-Saunders coupling scheme, the complex's different spin states are represented by ${}^{(2S+1)}L_J$ (where $(2S + 1)$: the spin multiplicity, J : the total angular momentum quantum number, and L : the total orbital quantum number in spectroscopic notation). The energies of the corresponding states are calculated as a function of the electron-electron repulsion Racah parameters (B, C).

According to Tanabe Sugano's diagram, the range of ligand field values for which a SCO can be observed is limited.

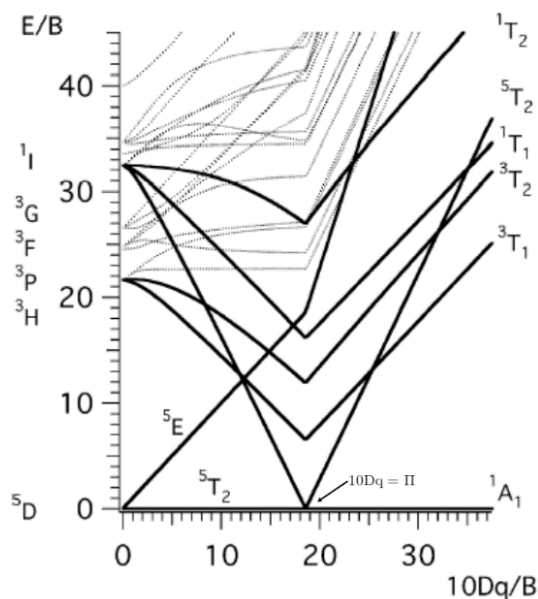


Figure 1. 6 Tanabe-Sugano diagram for the transition metal ions having the electronic configuration d^6 in an octahedral molecular geometry, showing only the relevant low lying energy states. The energy of the excited states (in the unit of Racah parameter B) has been plotted as a function of the ligand-field strength ($10Dq$) (also in the unit of Racah parameter B). The energy levels show a sharp discontinuity at $10Dq = 20B = P$, in which the lowest energy state changes from the ${}^5T_{2g}$ (HS) (for $10Dq < 20B(P)$) state to the ${}^1A_{1g}$ (LS) (for $10Dq > 20B(P)$) state [50].

The Tanabe-Sugano diagram depicts the splitting of metal ion electronic states in the presence of an octahedral ligand field. The Tanabe-Sugano diagram of the $Fe(II)$ transition metal ion (electronic configuration d^6) is shown in Fig. 1.6, where the energy of the different ligand-field states is plotted as a function of the ligand field strength ($10Dq$) in Racah parameter B units. The ground state of a free metal ion without a ligand field is $5D$ ($e_g + t_{2g}$). When the ligand field enters the picture, the free ion ground state splits into an excited state (5E) and the HS ground state (${}^5T_{2g}$) ($t_{2g}^4 e_g^2$). With $10Dq$ greater than the pairing energy (P), the ground state transitions from the HS (${}^5T_{2g}$) to the LS (${}^1A_{1g}$). The transition to the ground state occurs at the energy where $10Dq$ equals P . If the $10Dq$ energy in some $Fe(II)$ -complexes is close to the pairing energy; then external stimuli can cause ligand state switching. The Tanabe-Sugano diagram in Fig. 1.6 also shows the possible transition to the other excited states and estimates the energy required for the transition.

Furthermore, this distribution across all t_{2g} and e_g orbitals causes the first direct "consequence" of this electronic configuration change upon LS to HS conversion is an increase in metal-ligand distances of around 10%, corresponding to a 25% increase in octahedron volume (Fig. 1.12). This variation suggests significant

differences in vibration modes, as determined by IR and Raman spectroscopy measurements (Fig. 1.7). For example, stretching vibrational modes $\nu(\text{FeN})$ are greater in the LS state than in the HS state in a FeN_6 octahedron, with a typical ratio $\nu^{\text{LS}}\text{FeN}/\nu^{\text{HS}}\text{FeN}$ ranging from 1.1 to 1.9 [51].

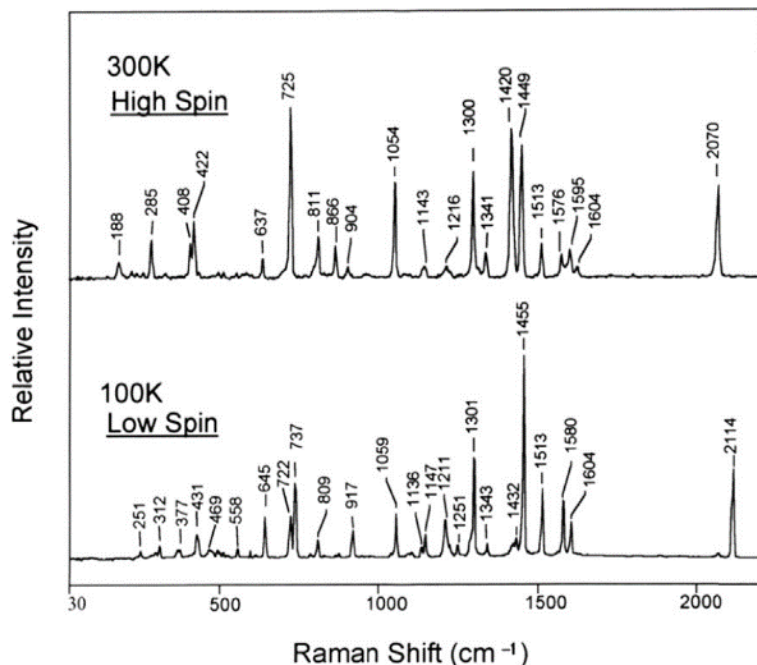


Figure 1. 7 Raman spectra of $\text{Fe}(\text{phen})_2(\text{NCS})_2$ in the HS state (300 K) and LS state (100 K). In the range $< 600 \text{ cm}^{-1}$ where the entropy values are maximized, the average of vibrational modes are $\nu_{\text{av,HS}} = 298 \text{ cm}^{-1}$ and $\nu_{\text{av,LS}} = 393 \text{ cm}^{-1}$ in the HS and LS states, respectively, leading to a ratio $\nu_{\text{av,HS}}/\nu_{\text{av,LS}} \sim 1.3$. [51]

We can gain a further understanding of what happens at $10Dq = P$ by considering the adiabatic potential energy surfaces for the HS and LS states, shown in Fig. 1.8. Here we have assumed that the vibronic modes for each electronic state can be approximated as a simple harmonic oscillator

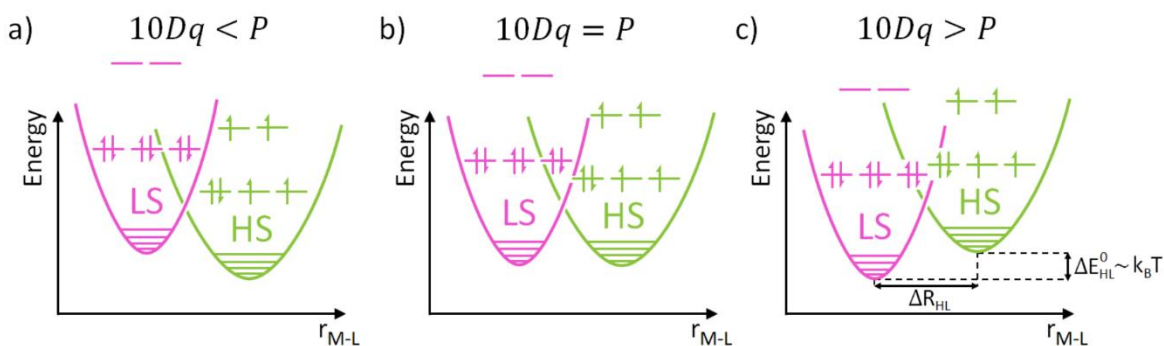


Figure 1. 8 Energy level diagram showing the lowest vibronic levels of adiabatic potential wells of the LS and HS states of an octahedral SCO complex as the ratio of $10Dq$ and P is varied. The

potential energy of the HS and LS states are represented as a function of the metal-ligand distance. (Figure extracted from [23])

Based on Fig. 1.8, the condition for the thermal occupation of the higher energy spin-state (spin-crossover) becomes clear: When the difference between the zero-point energies of the two spin states is of the same order of magnitude as the thermal energy, that $\Delta E = E_0^{HS} - E_0^{LS} \approx k_B T$, thermo-induced spin conversion is possible. However, this definition requires some refinement since it does not account for the entropy differences between the spin-states. The zero-point energy in SCO compounds is the sum of electronic and vibrational contributions. Except for a few rare SCO compounds [52]–[55], the LS state has the lowest zero-point energy and thus is the ground state at zero temperature (Fig. 1.8). Due to the larger electronic and vibrational entropy of the HS state over the LS state, the HS will remain energetically favourable at all temperatures if it is the ground state. Whereas, if the ground state is LS, then there exists a critical temperature at which the HS state becomes energetically favourable, and a spin-crossover or spin transition can occur. This shift is caused by entropic contributions, which are stronger in the HS state than in the LS state. Indeed, the entropy difference has two origins: electronic origins due to increased spin multiplicity (and, to a lesser extent, orbital momentum) in the HS state, and particularly a vibrational origin due to lower vibrational frequencies [56]. This transition can occur as a result of changes in temperature, pressure, light irradiation, external fields and chemical environment when $\Delta E_{HL}^0 \sim T\Delta S$. It is widely assumed that the SCO is an entropy-driven phase conversion.

The thermodynamic picture of the spin crossover phenomenon will be discussed in the following section.

1.4 On thermodynamics of spin-crossover systems

Fundamental elements of spin-crossover (SCO) mechanisms are discussed using macroscopic – mesoscopic techniques and considerations of ligand/crystal field theory, thermodynamics, and modeling of the thermoinduced spin transition in the solid-state. When SCO molecules interact with their surroundings, the spin conversion phenomenon can be explained using axiomatic thermodynamic principles. In the first step, an isothermal and isobaric ensemble (N, P, T) of N non-interacting (isolated) SCO molecules in contact with a thermal bath T is considered with a possible control of the external pressure P . The spin conversion can be viewed as a thermal equilibrium between two phases at constant pressure. For such experimental conditions, the relevant state function is Gibbs energy $G = H - TS$, where H and S represent the system's enthalpy and entropy, respectively. The Gibbs energy difference between the HS and LS phases describes the system's thermodynamic properties:

$$\Delta G = \Delta H - T\Delta S \quad (1.4)$$

where $\Delta H = H_{HS} - H_{LS}$ is the enthalpy variation [57] and $\Delta S = S_{HS} - S_{LS}$ is the system's entropy variation. We can define the equilibrium temperature $T_{1/2}$ as the temperature at which the proportions of HS and LS molecules are the same as when $\Delta G = 0$:

$$T_{1/2} = \frac{\Delta H}{\Delta S} \quad (1.5)$$

According to Eq. 1.5, when $T < T_{1/2}$, the enthalpic term is dominant, and the LS state is favored, whereas when $T > T_{1/2}$, the entropic term becomes dominant and the HS state is favored, thus justifying the term "entropy-driven conversion phase."

1.4.1 Entropy driven spin-crossover

Consider the various contributions to enthalpy and entropy variations. ΔH is divided into two parts: a temperature-independent electronic part called ΔH_{el} and a vibrational part called ΔH_{vib} . Similarly, ΔS can be arbitrarily divided into various contributions to the statistical disorder:

$$\Delta S = \Delta S_{el} + \Delta S_{vib} + \Delta S_{trans} + \Delta S_{rot} \quad (1.6)$$

The two final terms, ΔS_{trans} and ΔS_{rot} , correspond to the entropy variation due to translation and rotation, respectively, and are mostly ignored in the solid state. The first term, $\Delta S_{el} = \Delta S_{orb} + \Delta S_{spin}$, represents the electronic entropy variation and arises from the difference in degeneracy (orbital and spin momenta) between the HS and LS electronic states:

$$\Delta S_{orb} = R[\ln(2L + 1)_{HS} - \ln(2L + 1)_{LS}] \quad (1.7)$$

and

$$\Delta S_{spin} = R[\ln(2S + 1)_{HS} - \ln(2S + 1)_{LS}] \quad (1.8)$$

where R is the perfect gas constant. L and S are, respectively, the total orbital and total spin momenta of the spin state. The contribution of spin degeneracy comes from the change in state degeneracy caused by the change in spin multiplicity as the system transitions from LS (HS) to HS (LS).

In the ideal situation of a SCO $Fe(II)$ complex with perfect octahedral symmetry, we have $\Delta S_s = R \ln(5) = 13.38 \text{ J mol}^{-1} \text{ K}^{-1}$ and $\Delta S_{orb} = R \ln(3) = 9.13 \text{ J mol}^{-1} \text{ K}^{-1}$. In practice, there is no orbital degeneracy; the orbital momentum is "blocked" to $L = 0$ as the local symmetry of the $Fe(II)$ is usually lower due to Jahn-Teller distortion; thus, the orbital contribution to the entropy change is usually neglected.

Thus, the main contribution to ΔS_{el} is the change in entropy caused by spin degeneracy, which can be expressed as:

$$\Delta S_{el} = R[\ln(2S + 1)_{HS} - \ln(2S + 1)_{LS}] \quad (1.9)$$

So, the change in entropy for *Fe(II)*-centered spin-crossover molecules in octahedral geometry with $s = 2$ as HS and $S = 0$ as LS is $\Delta S_{el} = R \ln(5/1) = 13.38 \text{ J mol}^{-1} \text{ K}^{-1}$ [58]. Temperature has no effect on electronic entropy, which favors the HS state. Vibrational entropy variation is the second term ΔS_{vib} (vibrational entropy) depends only on variation of intramolecular modes between the HS and LS states in the case of isolated molecules. In solid states the contribution to intermolecular vibrations must be added although it is often considered less important than intramolecular. Although, intermolecular and intramolecular vibrational contributions are difficult to distinguish as they are usually linked with each other. Vibratory entropy may be expressed as follows (see Ref. [55] for further analysis):

$$S_{vib}(T) = R \sum_{\lambda} \left(-\ln[1 - e^{-hv_{\lambda}/k_B T}] + \frac{hv_{\lambda}}{k_B T} \frac{1}{\exp(hv_{\lambda}/k_B T)} \right) \quad (1.10)$$

where the sum $\sum \lambda$ runs overall vibration modes. A convenient hypothesis is the low-frequency approximation ($hv \ll k_B T$), in which case Eq. 1.10 becomes

$$S_{vib} = -R \sum_{\lambda} \left(\ln \frac{hv_{\lambda}}{k_B T} \right) \quad (1.11)$$

The vibrational contribution to the entropy change can be expressed in terms of the entropy of an ensemble of harmonic oscillators

$$\Delta S_{vib} = S_{vib}^{HS} - S_{vib}^{LS} = R \sum_{\lambda=1}^{15} \ln(v_{\lambda}^{LS}/v_{\lambda}^{HS}) = 15 R \ln(\langle v_{\lambda}^{LS} \rangle / \langle v_{\lambda}^{HS} \rangle) \quad (1.12)$$

Considering a perfect octahedron ($\lambda = 15$ molecular vibrational modes) and taking $\langle v_{\lambda}^{LS} \rangle / \langle v_{\lambda}^{HS} \rangle = 1.3$ (Fig. 1.7), we obtain $\Delta S_{vib} = 32.7 \text{ J mol}^{-1} \text{ K}^{-1}$ in agreement with the experimental measurements [51].

When there is a spin crossover, the lengths of the metal-ligand bonds change, resulting in different stretching frequencies. Changed phonon modes are responsible for the vibrational component of overall entropy change. In most spin-crossover complexes, the vibrational contribution is the predominant contributor to the total entropy change [58].

There is a very least contribution to the entropy change due to the rotational degree of freedom of the complexes [59]. This can be calculated semi-classically as

$$\Delta S_{rot} = R \ln(z_{rot} + 3/2) \quad (1.13)$$

where $z_{rot} = \left(\frac{\sqrt{2}}{\pi}\right)^3 \left(\frac{\sqrt{\pi}}{\sigma}\right) (k_B T)^{3/2} (J_1 J_2 J_3)^{1/2}$ and J_i are the moments of inertia, and σ is the symmetry number. The value of σ is 2 for C_2 symmetry and 1 for C_1 symmetry. The typical value of the entropy change due to rotation is of the order

of $1 J.mol^{-1}.K^{-1}$ [58].

This means that the vibrational contribution, and to a lesser extent the electronic contribution, account for the majority of the entropy change in thermal spin crossover. Both ΔH and ΔS are positive in a spin-crossover transition[59][60]. The variation in Gibbs free energy can be rewritten as-

$$\Delta G(T, p) = \Delta H \left(1 - \frac{T\Delta S}{\Delta H}\right) = \Delta H \left(1 - \frac{T}{T_{1/2}}\right) \quad (1.14)$$

(In this case, we define a temperature $T_{1/2} = \frac{\Delta H}{\Delta S}$ at which $\Delta G = 0$. At this temperature ($T_{1/2}$), the Gibbs free energy for both spin states is equal, and they have an equal probability of being populated.

This temperature is known as the transition temperature. The adiabatic potentials of the HS and LS states of a *Fe(II)* spin-crossover complex as a function of the totally symmetric metal-ligand stretching distance ($r(Fe - L)$) are shown in Fig. 1.18.

Thermal spin-crossover requires a zero-point energy difference between the HS and LS states (ΔE_{HL}^0 i.e., ΔG) in the order of thermal energy $k_B T$. At $T = 0 K$, $\Delta G = \Delta H$ (from eq. 3.16), and thus the LS state is thermodynamically superior to the HS state (because $\Delta H > 0$). In general, at temperatures below $T_{1/2}$, the LS state is preferred (because $\Delta G > 0$), while at temperatures above $T_{1/2}$, the HS state is preferred (because $\Delta G < 0$). During thermal spin-crossover, the metal-ligand bond length abruptly changes, causing the ligand field strength to change. The ligand field strength ratio in the LS and HS states is given by Eq. 1.3 $\left[\frac{10Dq^{LS}}{10Dq^{HS}} = \left(\frac{r_{HS}}{r_{LS}}\right)^n\right]$ where n is between 5 and 6. Because r_{HS} is greater than r_{LS} , the ligand field strength decreases abruptly in the transition from LS to HS. The main driving force in this transition process is the change in entropy (ΔS), which modifies the value of (ΔG). As a result, thermal spin crossover is referred to as an entropy-driven phenomenon.

We can draw two important conclusions from this result. First, the HS state has higher vibrational entropy, which is then favored at high temperatures. This means that the vibrational contribution, and to a lesser extent the electronic contribution, account for the majority of the entropy change in thermal spin-crossover. In general, the entropy variation ΔS ranges from 40 to 80 $J mol^{-1}K^{-1}$ in comparison to $\Delta S_{el} = 13.38 J mol^{-1}K^{-1}$. All of these thermodynamic quantities can be extracted from calorimetric measurements [59], [61], [62] (Fig. 1.9), whereas vibrational properties can be evaluated using Raman and infrared spectroscopies [51], [63], [64].

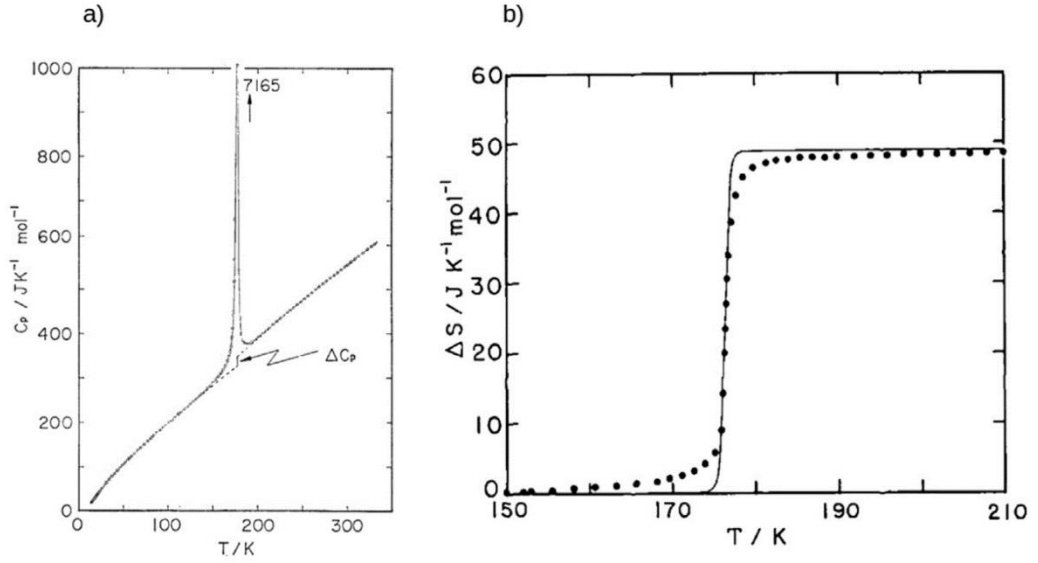


Figure 1.9 (a) Temperature dependence of the heat capacity of $[Fe(phen)_2(NCS)_2]$ crystal. ΔC_p corresponds to the discontinuity associated with the spin transition. (b) Temperature dependence of entropy variation of the same compound (full black circles). Straight line corresponds to a fit using the so-called domain model [59].

Considering N noninteracting molecules, N_{HS} are in the HS state, then we can define the HS fraction $n_{HS} = N_{HS} / N$, which is erroneously referred to as the order parameter of the spin transition. The Gibbs energy of a SCO system can be expressed as

$$G = n_{HS}G_{HS} + (1 - n_{HS})G_{LS} - TS_{mix} \quad (1.14)$$

Due to the vast number of possibilities for distributing N_{HS} molecules in the HS state across N molecules, the mixing entropy equates to a loss of statistical information for the system. Mixing entropy can be written as in the thermodynamic limit.

$$S_{mix} = -k_B N [n_{HS} \ln(n_{HS}) + (1 - n_{HS}) \ln(1 - n_{HS})] \quad (1.15)$$

The equilibrium condition corresponds to

$$\left(\frac{\partial G}{\partial n_{HS}} \right)_{T,p} = 0 \quad (1.16)$$

It is then possible to follow the thermal evolution of the HS fraction (Fig. 1.10):

$$T = \frac{\Delta H}{R \ln \left(\frac{1 - n_{HS}}{n_{HS}} \right) + \Delta S} \quad (1.17)$$

Using the expression $\Delta s = R \ln \Omega$ for the entropy change, where Ω is the effective degeneracy, expression (1.17) can be rewritten as $\ln \frac{n_{HS}}{1 - n_{HS}} = \Omega e^{-\Delta H/RT}$.

This leads to the Arrhenius law $\ln \frac{n_{HS}}{1-n_{HS}} = \ln \Omega - \Delta H / RT$

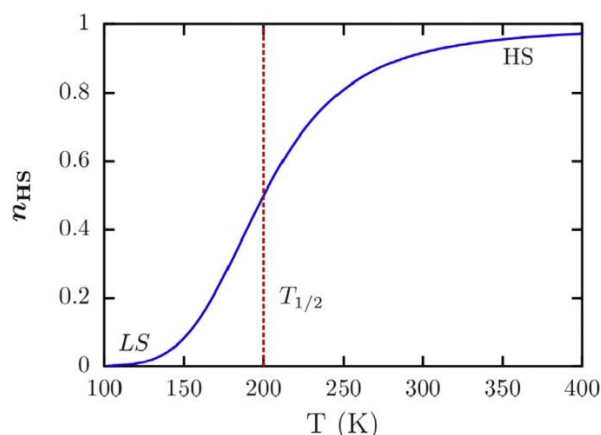


Figure 1.10 Thermal evolution of the HS fraction n_{HS} (blue line) in the case of noninteracting SCO molecules. The equilibrium temperature $T_{1/2}$,

The only way to see a steady spin transfer from the LS to the HS state in non-interacting SCO molecules is to raise the temperature. The emission or absorption of a latent heat whose existence is totally determined by interactions between SCO molecules is directly related to the occurrence of rapid first-order transitions with bi-stability occurrences.

1.4.1 Mixed spin phases and co-operativity

In the previous section, we assumed that there is no mixed phase of the molecules in HS and LS states. We saw in the previous section that when there is a spin-crossover, the volume of the molecule changes. When considering molecules in a crystal, however, an additional entropy term must be added to the expression of Gibbs free energy to account for the coexistence of HS and LS. Generally, the volume of the HS molecule is greater than that of the LS molecule; a spin transition of a molecule at a given position can induce a transition to a nearby molecule via elastic interaction when they are in a crystal. This elastic interaction causes internal pressure in the crystal, causing the spin-crossover transition to grow inside the crystal. This is commonly referred to as cooperativity.

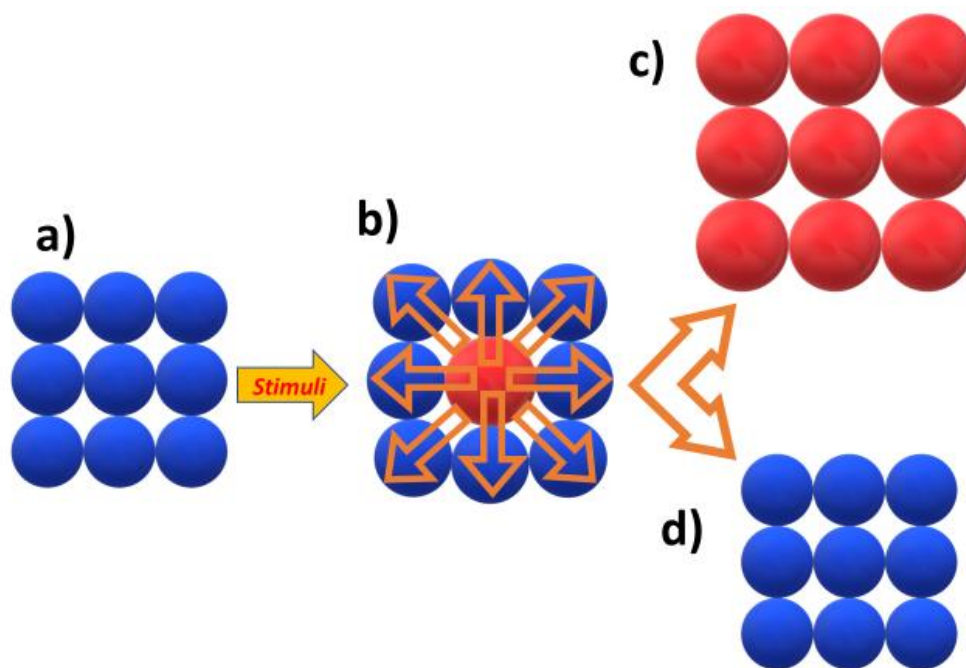


Figure 1.11 Simplified representation of collective mechanisms in the case of a highly cooperative SCO compound a) Molecules in the LS state. b) The central molecule transits towards the HS state, which implies a lattice deformation, and the molecule wants to expand (arrows). As a result, c) either the neighbors transit towards the HS state or d) the molecule returns to the LS state

Cooperative behavior is one of the distinctive characteristics of spin transition in SCO materials, and it relies on the interactions between SCO centers to produce a macroscopic effect. However, the medium used by this cooperativity, namely the nature of the interactions between SCO molecules, can change from one system to the other. The various theoretical models of spin transition also consider different origins [65], but they can be combined to improve the predictions when the need arises [65], [66]. The spin transition itself can be considered either as a random event where the HS and LS molecules are dispersed regularly in the solid (Fig. 1.11), like in the original model used by Slichter and Drickamer (inhomogeneous, process controlled by nucleation), or as a domain growth where the HS and LS molecules form domains. The mean size of these domains provides insights into the cooperativity of the molecule, an approach pioneered by Sorai et al. [59], [67] (homogeneous, process controlled by propagation). Both of these models we will discuss in detail in the coming sections. The different spin transition triggers mentioned in part 1.7 can favor one of those two types of transitions. For example, the light-induced excited spin state trapping (LIESST) excitation effect is considered to be intrinsically inhomogeneous, [68], [69] and non-cooperative process.

The cooperative interactions between the metal ions are a result of elastic interactions [9], [28], [70]. The “elastic” interaction arises from the volume change concomitant to the spin transition. The local structural distortions caused by metal

ions changing spin-state creates a local elastic strain that couples to the long-range elastic interactions (acoustic phonons), generating a build-up of stress over the material [70]. The molecules are considered as spheres that interact with each other through the elastic medium and is comparable to a phase transition in a mean-field approach. Strong cooperative interactions typically occur when there is a direct covalent interaction between the metal ions, a large structural difference between the spin-states and the lattice and chemical environment is flexible enough to accommodate the molecular distortions [10]. How the structural changes occur on the molecular level does not seem to matter, for example, whether the change occurs as a result of an increase in metal-ligand distance or ligand distortion [10]. Typically, while the local molecular distortions are usually totally symmetric, the structural distortions of the lattice can either involve the expanding or contracting of the lattice or a significant spatial rearrangement of the metal ions as the transition occurs [70].

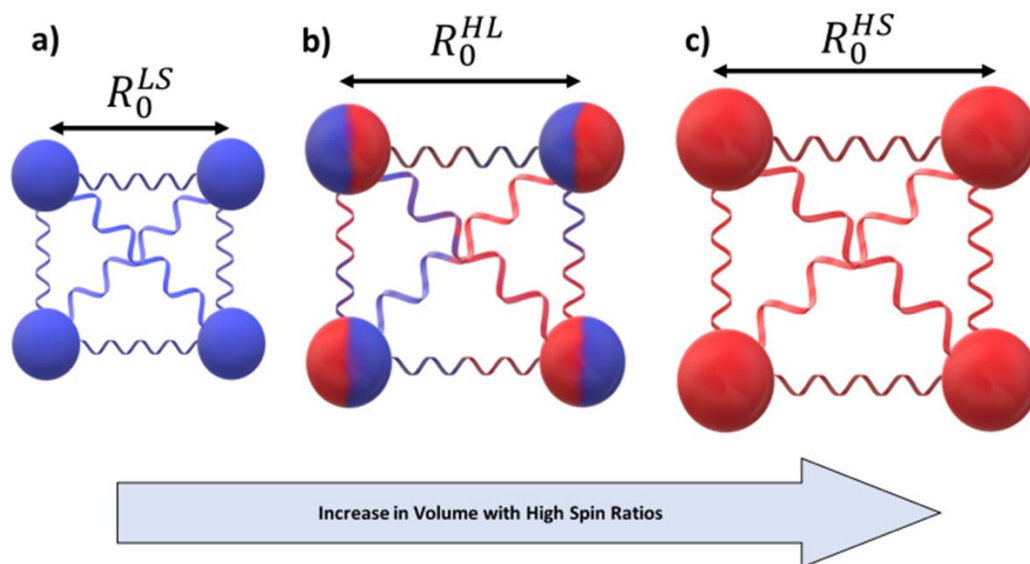


Figure 1. 12 Changes in electronic configuration leads to LS to HS conversion and results in an increase in metal-ligand distances of around 10%, corresponding to a 25% increase in octahedron volume. Where (a) R_0^{LS} , (b) R_0^{HL} and (c) R_0^{HS} corresponds to distance between nearest-neighbor metal center and relative n_{HS} fraction ranging from 0 – 1.

This forms the basis of the Spiering model [71]. It can be compared to an internal “pressure” exerted by each molecule on its neighbors [72], [73]. According to Kepenekian et al., electrostatic interaction from polarization of the metal centers play a primary role in the hysteresis of the spin transition of Fe(II) SCO molecules [74]. This approach has the advantage that it makes cooperativity dependent on the Madelung field of the molecule, which facilitates the predictions. Less is known about the role played by the intermolecular interactions in determining the cooperative behaviour. “Weak” bonds were also a traditional focus of the community [75], [76] in the context of cooperativity. They include notably π - π stacking, hydrogen bonds [77], [78], sulfur bonds, Van-der-Waals interactions the

presence of guest molecules [79], solvent atoms [80] and anions [81] and metallophilic interactions [76] have been shown to strongly modify the collective SCO behaviours [70].

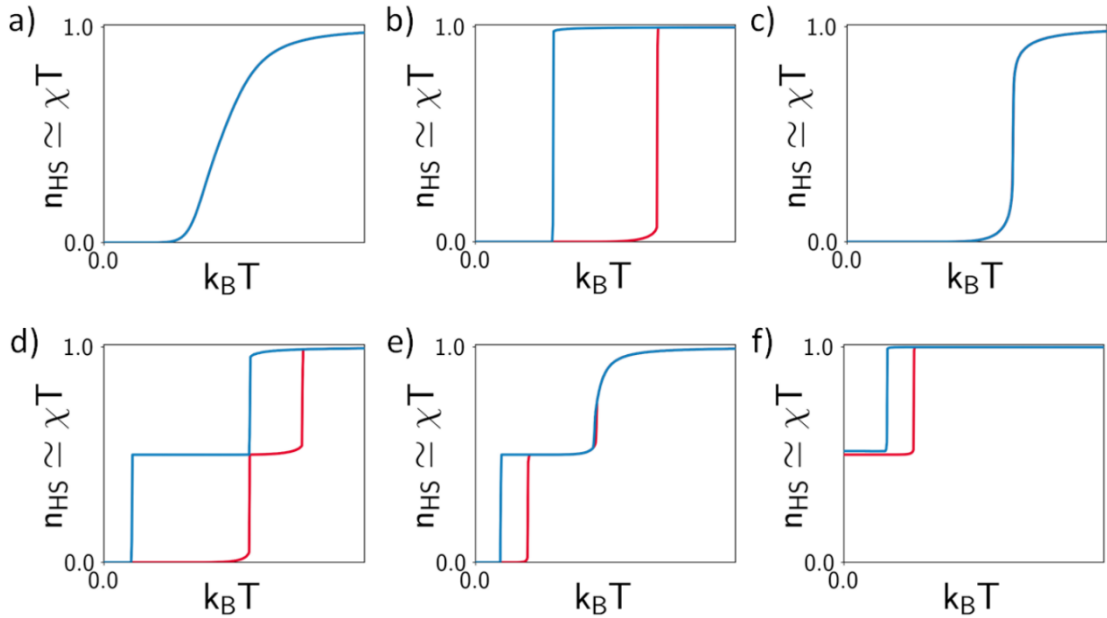


Figure 1.13 Heating (red) and cooling (blue) SCO curves (the fraction of high spins, n_{HS} , vs. temperature, T) for (a) a crossover, (b) a one-step transition with hysteresis, (c) a continuous crossover, (d) a two-step transition with two first-order transitions, (e) a two-step transition with one first and one second-order transition and (f) an incomplete one-step transition with hysteresis [23].

Plotting n_{HS} as a function of temperature is a good measure of the cooperativity – the extent to which the electronic and structural changes of a transition metal ion are propagated throughout the lattice. The cooperativity is usually measured by plotting χ_T vs T . Typically, the plot of χ_T vs T is referred to as the SCO or spin-transition curve. The most commonly reported SCO curves are either crossovers (Fig. 1.13a) or first-order transitions (Fig. 1.13b). Although, in general, SCO curves can also be continuous (Fig. 1.13c), a multi-step process with many transitions (Fig. 1.13d-e) or incomplete (Fig. 1.13f) [82]. An incomplete SCO curve refers to a SCO system with a low-temperature ground state with $n_{HS} \neq 0$ or a high-temperature phase $n_{HS} \neq 1$. Incomplete transitions and multi-step transitions often display antiferroelastic ordering of spin-states (see Fig. 1.13f). A detailed review of multi-step transitions due to changes in SCO environment, frustration, and instabilities (nanocomposite) reported in experiments on SCO materials and frameworks is given in Chapter 2 and 3, also see Refs.[83]–[86]. For example, Murphy et al. [79] showed that changing the number and type of guest molecules changed the number of reported transitions from one-step to two and three- step. Although in general, any changes to the structural properties of the atomic architecture, including changes in polymorphism [87], can alter the bulk properties and

behaviours [70]. Very little is known about the role spin-spin interactions play in determining the bulk properties and behaviours of spin-crossover systems. Estimates of the strength of these interactions for tetra- and decanuclear molecular materials range from 4–6 K [88], two orders of magnitude lower than estimates of the strength of the elastic interactions 100 – 400 K [89]. Consequently, the effects of spin-spin interactions are typically ignored in the temperature regimes where spin-crossover occurs.

Finally, since the cooperative behavior of SCO relies on inter-molecular interactions, it can be tuned by the addition of external molecules/solvents and/or metal dilution, by replacing the central Fe with other metals [90]. It is widely known that dilution in solution severely restricts cooperativity [91], but a less severe effect can be reached by including solvent molecules in the crystalline lattice [92]. Another way is to dilute the SCO compound in a polymer matrix [93]. These methods allow the individual study and tuning of the various cooperative interactions mentioned previously. For further studies in the field of SCO theoretical calculations, one can consult the reviews by Boča [65], [66] and Enachescu [94].

Deriving structure-property relations and determining the mechanisms that govern them has become one of the great challenges of the SCO community. Overcoming this challenge would allow for the rational design of SCO systems with enhanced applications and novel bulk properties and behaviours. Taking into account the complex interaction mechanism between SCO molecules, in contrast to the basic thermodynamic approaches describing the SCO phenomenon of isolated molecules, necessitates the introduction of phenomenological parameters whose links to measurable experimental quantities are not always straightforward. These parameters mean that collective behavior mechanisms are drastically simplified in their solid-state. A summary of several macroscopic/thermodynamic models which simulate interacting SCO compounds is provided in the following section.

1.5 Models and methods used to predict the spin crossover behaviour

1.5.1 Modelling: Overview

A model is an idealization [95] of a real-world behavior based on various physical or mathematical approximations. A model's overarching goal is to simulate real-world behaviors while retaining the fundamental aspects of the theory. Theoretical treatments of models do not always present perfect physical realizations. In these cases, the only way to test an estimated theoretical solution is to compare it to data obtained through computer simulation [96]. There are physical systems today that are so complex that they cannot be studied within the framework of a theoretical

treatment, and only simulations can determine the properties of this system. If the simulation results differ from the experimental results, an innovative reconsideration must be defined. Even if simulations do not always provide a better understanding of behavior, their main advantage remains the ability to separate and isolate various physical effects. Given that the real world contains plethora of materials and understanding the ubiquitous behavior of these materials remains a challenge because a variety of factors must be studied (i.e., shape, size, entropy, flexibility, etc). In the case of simplified models, simulations can 'turn off' or 'turn on' the special effects produced by ubiquitous behavior, and thus the precise consequences of each contributing cause are determined.

Concerning the simulations' purpose, we would like to emphasize that the simulations are not just to provide a better 'curve fitting' to experimental results than the analytic theory. It is hoped that simulations will provide a complete understanding of the physical properties and mechanisms that cause an observed phenomenon [97].

1.5.1 Models used to characterize Spin Crossover Systems

First and foremost, in this section, we will present and describe some models [4] that have been used to characterize spin transition materials. Many mathematicians, physicists, and chemists have worked hard over the last century to develop models and materials that can accurately predict what is happening in our system [98]. Over time, experimental data influenced theoretical studies and vice versa, resulting in a partial understanding of the mechanism underlying different complex spin transition behaviors. The chronologic order will be used to classify the mathematical models used to characterize the spin transition compounds because it is more practical and easier for the reader to understand the models that stayed on the "base" of developing other models. In the following lines, we want to make a brief description of the models that have been previously developed to explain the macroscopic evolution of the fraction (which is the number of molecules which are in HS state) under different external perturbations such as: temperature, pressure, etc. We must start from the quantum origin [99]–[111] or from the thermodynamical hypotheses [112]–[117] for each mathematical model.

The Wajnflasz - Pick model, developed in the early 1970s, was the first to introduce the concept of intermolecular interaction capable of qualitatively simulating spin transition phenomena [103]. They presupposed that each metal center is a four-level system (two ionic radii each having two spins states). A fictitious spin ($\sigma = \pm 1$) was introduced to characterize each spin state. An Ising type coupling term between neighboring centers describes the interaction between ionic centers. The Hamiltonian is solved, In the mean-field approximation. The nature of the interaction term, which is not entirely justified, is the model's main limitation. However, this model was the first to predict continuous and discontinuous spin

transitions for interaction parameters greater than $k_{\beta}T_{1/2}$ (where $T_{1/2}$ is the spin state's switching temperature).

Bari and Sivardière [101] continued this work two years later, in 1972. They demonstrated and clarified some physical aspects that were overlooked in the Wajnflasz model. In fact, they demonstrated the relationship between the transition temperature and the intensity of ion interaction in their work. The primary goal of this model is to determine the partition function (Z), which allows the determination of all physical macroscopic parameters. Wajnflasz and Pick's 1970 model and Bari and Sivardière's 1972 model explained the process of first-order phase transition, which occurs between the low spin (LS) and high spin (HS) states; behaviour also obtained experimentally in octahedral complexes. In comparison to the models that will be discussed in this paper, both of the models presented above have a significant disadvantage: the entropy of the system is influenced by the degeneracy of the two states (LS and HS states), and the system does not exhibit a variation in entropy near the transition point, which is a critical issue[118].

The Slichter and Drickamer model[119], developed in the same year as Bari and Sivardière's model, is one of the main macroscopic models that accounts for intermolecular interactions. Slichter and Drickamer propose use of an external pressure perturbation factor to describe the spin transition phenomenon in this model. The application of pressure provided the foundation for many macroscopic models that attempt to specify the origin of interactions. Another intriguing feature of this model is that each molecule state is dependent on the neighbouring molecule states via the intermolecular interaction term " J ". When this model was applied to some SCO materials, a discontinuous spin transition or a spin transition with hysteresis was obtained.

Sorai and Seki [99] took a different approach in 1974, proposing an alternative thermodynamics model. They assumed that molecules in the same spin state are organized into domains. They calculate the critical size of the spin domain using calorimetric measurements and calorimetric data. This model is currently limited because it cannot reproduce a hysteretic transition.

Zimmermann and König [102] proposed a model in 1977 that makes the vibration mode more explicit. While discussing this model, it is essential to note that the molar entropy increase upon spin conversion ΔS is quantitatively accounted for, and the intermolecular interactions are introduced via an Ising-like Hamiltonian. The Bragg-Williams approximation was used to solve this Hamiltonian.

Concerning the vibration mode, it has been assumed in this model that it follows the Debye model, regardless of its character, which may be intra or inter molecular. Another point worth mentioning in Zimmermann's article is that he demonstrated the formal equivalence between two-level models treated in the mean-field approximation and macroscopic two states (LS and HS states) models based on

regular solution thermodynamics.

Another significant step forward in model development occurred in 1979, when Kambara [120] used ligand field theory to demonstrate that the spin transition from the LS to the HS state is induced by the Jahn-Teller coupling. This coupling is caused by the difference in d electrons and a local distortion of Fe^{II} complexes used in the random phase approximation and solved with mean field equations. Within this model, a discontinuous LS-HS spin transition was observed, which was influenced by temperature, magnetic field, or pressure [121]. Gütlich et al. [113] proposed an extended Sorai and Seki model in 1979, establishing the link between the thermodynamic model and experimental results. They included calorimetric data on the thermal dependence of the HS fraction in this extended model. The first approach to the truly physical origins of cooperation was proposed in 1981 [113] by Onishi and Sugano, and in 1982 [116] by Spiering et al. As we've seen, the spin transition is accompanied by a volume change. This change will generate a stress field, which will spread throughout the network due to its elasticity. To address this issue, the authors envisioned molecules as hard spheres (i.e., isotropic) inserted in an elastic medium. These spheres were treated as if they were point defects. In 1984, Edwards and Purcell [122] proposed a new model in which a material is thought to be formed by chains of molecules. Only the molecules in the chains interact with one another, while the chains do not. Bousseksou et al. proposed a new approach to a two-level model in the 1990s [123], [124]. They believe that the ratio of degeneracies $deg \left(deg = \frac{deg_{HS}}{deg_{LS}} \right)$ of two states is much larger than the spin degeneracy. Such degeneration results from the change of entropy during the spin state transition. This new hypothesis allows for more precise adjustment of data from experimental calorimetric measurements. The Everett model [30], used by König et al. [125], [126] to characterize the major and minor hysteresis loops, and the Preisach model [127]–[129], used to fit hysteretic experimental data, are the other two models used to characterize spin transition materials.

Over time, it was discovered that the Ising model is the simplest to apply in SCO studies. In addition, some models based on elastic properties have been proposed. In this case, we can distinguish between the two approaches. Boukheddaden et al. [130] and Enachescu et al. [131], [132] proposed the first approach. This model is based on the realistic idea that the difference in molecular volumes between the two states (LS and HS) causes elastic interactions and causes molecules in the system to shift during the transition.

The second approach is that of Nasser et al. [107], [133]. The uniqueness of the current model stems from the Hamiltonian's simple structure, in which the elastic constant connecting two SC units depends on their electronic states. Until now, the atom phonon coupling model has been studied using the mean-field method or Monte Carlo simulations for chain and square lattice systems.[100], [104]–[106][134]–[139] present a wide range of behavioral characteristics of spin transition compounds that were reproduced.

1.5.1.1 Ising model: Wajnflasz and Pick approach

Ising's model was first suggested by Wilhelm Lenz in 1920 [140] then studied by Ernst Ising [141] in his thesis on the study of one-dimensional magnetic systems, the results of which were published in 1925 [142]. Originally developed to study magnetic systems on a regular network, its simplicity has made it very popular, and we find adaptations in all areas of statistical physics. Important Developments due in particular to the works of Onsager and Kaufman [143]–[145] and of Yang and Lee [146], [147] allowed simulation in the description of phase transitions. Use of mean-field variational theories [148] Bethe-Peierls [149], or CVM (Cluster Variational Method) [150], [151] also led to important developments which have structured the statistical physics of interactive systems. For spin transition systems, the Hamiltonian proposed by Wajnflasz and Pick (WP) is written as:

$$H = \Delta_0 \sum_1^N s_i - J \sum_{\langle i,j \rangle} s_i s_j \quad (1.18)$$

where $s = \pm 1$ is the fictitious spin state where $s = +1$ and $s = -1$ are associated with the HS and LS states respectively, Δ_0 is the energy of the ligand field acting on the isolated molecule and J the strength of interactions. The first sum traverses the N molecules of the system and the second sum over the pairs $\langle i, j \rangle$ traverses all the pairs of close neighbors in the network. This sum is rewritten as $\sum_{\langle i,j \rangle} = \frac{1}{2} \sum_i \sum_j^q$, where q is the number of neighbors of molecule i . To obtain analytical expressions allowing us to study the thermodynamics of this model, we simply use the mean field approximation. It's important to point out here that this approximation, although rough, allows us to qualitatively find most of the thermodynamic properties. It is therefore very often a useful prerequisite for Monte-Carlo calculation, for example. We develop the product of fictitious spins as

$$S_i S_j = m^2 + m(\delta S_i + \delta S_j) + \delta S_i \times \delta S_j = -m^2 + m(S_i + S_j) + \delta S_i \delta S_j \quad (1.19)$$

where $m = \langle s_i \rangle$, the fluctuations $\delta S_i \delta S_j$ are neglected in the mean-field approximation, which allows us to rewrite the Hamiltonian

$$H_{MF} = \Delta_0 \sum_i^N s_i + J m^2 N q / 2 - J m q \sum_i S_i \quad (1.20)$$

The partition function in the canonical set of this Hamiltonian, taking into account g_{hs} degeneracies for state $s = +1$ and g_{ls} for state $s = -1$, is written as,

$$Z_{MF} = e^{-\beta J m^2 N q / 2} \prod_i (g_{HS} e^{-\beta(\Delta_0 - J m q)} + g_{LS} e^{\beta(\Delta_0 - J m q)}) \quad (1.21)$$

$$Z_{MF} = g_{LS}^{1/2} e^{-\beta J m^2 N q / 2} (2 \cos h[\beta(\Delta_0 - k_B T \ln g / 2 - J m q)])^N \quad (1.22)$$

where $\beta = \frac{1}{k_B T}$. Free energy is then given for

$$F = -k_B T \ln Z_{MF} \quad (1.23)$$

The mean value of the fictitious spin is then easily obtained by minimizing the free energy $\frac{\partial F}{\partial m} = 0$, which leads to the self-consistent equation

$$m = \tanh[\beta(\Delta_0 - k_B T \ln g/2 - Jmq)] \quad (1.24)$$

By rewriting the temperature, T , as a function of the fictitious magnetization m , we obtain,

$$T = \frac{2qJm - \Delta_0}{k_B \ln\left(\frac{1+m}{1-m}\right) - k_B \ln g/2} \quad (1.25)$$

which gives us the value of the transition temperature for $m = 0$:

$$T_{eq} = 2\Delta_0 / k_B \ln g \quad (1.26)$$

J. Wajnflasz and R. Pick pioneered the application of this model in spin transition research in 1970-71 [152], [153]. Wajnflasz warns the reader in his early theoretical work that the interaction between spin transition ions is not of magnetic origin. As stated in the article, the use of Ising's model is thus a simplification, which explains the many subsequent developments attempting to model the interactions between the molecules of spin transition compounds in a more realistic manner.

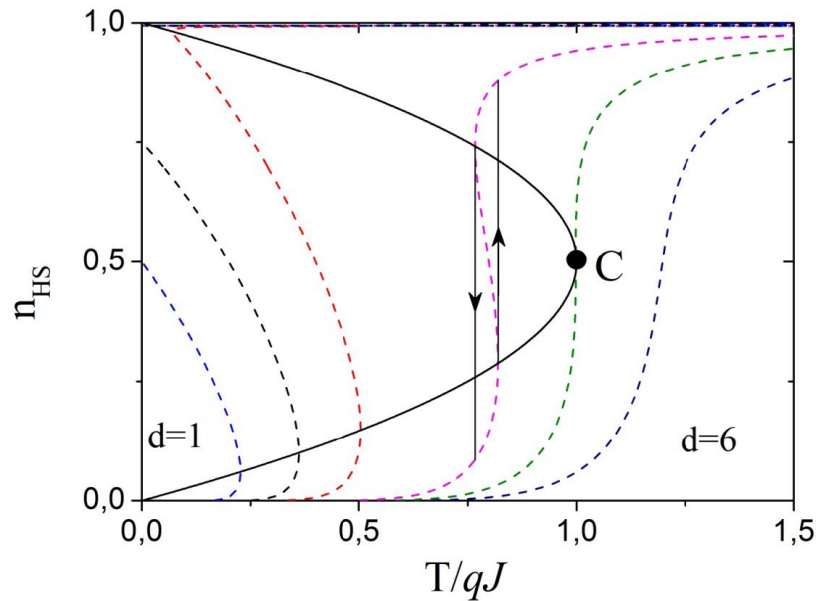


Figure 1.14 Thermal behavior in reduced coordinates calculated from equation (1.25) for $g = 150$ and the values of $d = \Delta_0/qJ = 1, 2, 3, 4, 5$ and 6 in the mean field approximation. The point C obtained for $d_c = \Delta_0/qJ = \ln g \sim 5.01$ is the critical point. Hence for $d < d_c$ there is no longer any first order transition. The solid line is the spinodal curve. Adapted from reference [154]

1.5.1.2 Slichter and Drickamer model

In 1972, Slichter and Drickamer[119] proposed a mean-field model which illustrates different types of spin transition observed in solids. They supposed that a solid is formed by a mixture of LS and HS states. If we define the n_{LS} and n_{HS} spin fraction corresponding to LS or HS states, the entropy of the system can be written as:

$$G = n_{LS}G_{LS} + n_{HS}G_{HS} - TS_{mix} + \Gamma n_{HS}(1 - n_{HS}) \quad (1.27)$$

Where, Γ = the intermolecular interaction;

$$S_{mix} = -R(n_{LS} \ln(n_{LS}) + n_{HS} \ln(n_{HS})) \quad (1.28)$$

If we consider the origin energy G_{BS} as: $G_{BS} = 0$ and $\Delta G = G_{BS} = \Delta H - T\Delta S$ (where $\Delta H = H_{HS} - H_{LS}$ is the difference of enthalpy and $\Delta S = S_{HS} - S_{LS}$ is the difference of entropy during the transition); the eq. (1.27) can be written as follows:

$$G = n_{HS}\Delta H + \Gamma n_{HS}(1 - n_{HS}) - RT \left[(1 - n_{HS})\ln(1 - n_{HS}) + n_{HS} \ln n_{HS} + n_{HS} \frac{\Delta S}{R} \right] \quad (1.29)$$

The equilibrium condition of the system, $\left(\frac{\Delta G}{\Delta n_{HS}} \right)_{T,P}$ gives the possibility to write the temperature (T) in function of high spin fraction n_{HS} as:

$$T = \frac{\Delta H + \Gamma(1 - 2n_{HS})}{R \ln\left(\frac{1 - n_{HS}}{n_{HS}}\right) + \Delta S} \quad (1.30)$$

Again, we can easily write this expression into the form of special Arrhenius $\ln\left(\frac{n_s}{1 - n_y}\right) = \ln \Omega - \left(\frac{\Delta H + \Gamma(1 - 2n_{HS})}{RT}\right)$. We recall that when we have defined the transition temperature as $T_{1/2} = \Delta H / \Delta S$ at which the proportion of HS and LS are equal, no cooperativity was considered. If we consider no cooperativity, then the thermal spin crossover follows smooth Gibbs-Boltzmann statistics. As soon as cooperativity comes into play, the transition is more abrupt than without cooperativity. The threshold between second-order and first-order phase transition is given by $\Gamma = 2RT_{1/2}$ which is fulfilled for $(dT / dx_{HS})_{HS=0.5} = 0$. When $\Gamma < 2RT_{1/2}$ then the inter-molecular interaction is fragile, and the transition is smooth without any hysteresis (with no cooperativity). The transition is abrupt as $\Gamma = 2RT_{1/2}$. At $\Gamma > 2RT_{1/2}$, the transition is even more abrupt and is consisting of two extrema points which can be interpreted as the opening of the thermal hysteresis. The inclusion of the cooperative term by Slichter and Drickamer [119] in the thermodynamic model helps a better understanding of the thermal SCO processes. The nucleation of domains and evolution of the phase boundaries due to cooperativity in SCO complexes in solid form during thermal spin crossover is a fascinating phenomenon to study.

If we consider $\Gamma = 0$, the expression of n_{HS} dependent on the temperature can be written as:

$$n_{HS} = \frac{\exp(\Delta S/R)}{\exp(\Delta S/R) + \exp(\Delta H/RT)} \quad (1.31)$$

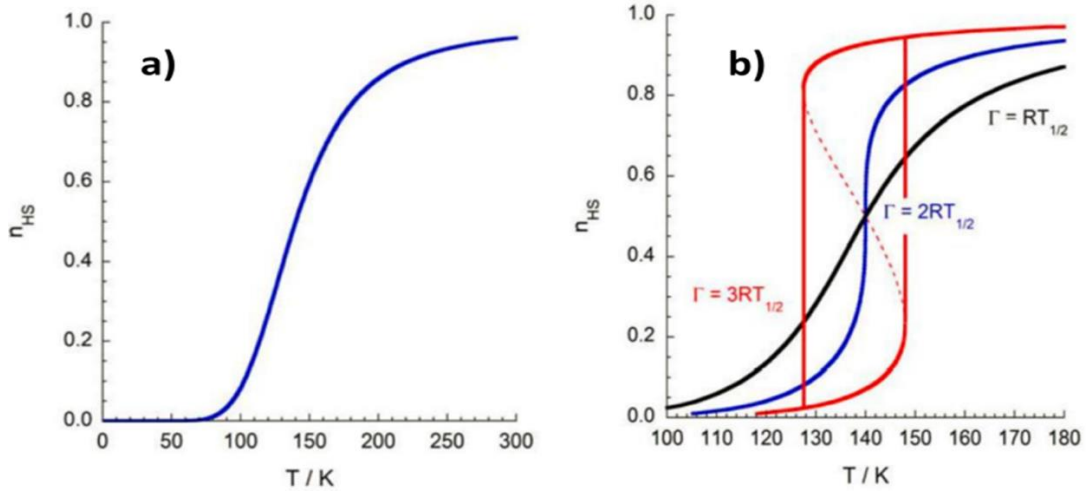


Figure 1. 15 (a) Fraction of HS-state molecules n_{HS} as function of temperature, ($\Delta H = 7kJ.mol^{-1}$, and $\Delta S = 50 J.K^{-1}.mol^{-1}$). (b) Fraction of HS-state molecules n_{HS} as function of temperature, ($\Delta H = 7kJ.mol^{-1}$ and $\Delta S = 50 J.K^{-1}.mol^{-1}$) [46].

In the Fig. 1.15a, because the intermolecular interaction is zero, there will be a gradual transition. If the intermolecular interaction is different from zero, there will be different types of transition in function of the interaction strength (Fig. 1.15b).

1.5.1.3 Domain model: Sorai and Seki

Sorai and Seki [99] take as a starting point the hypothesis that the population of the centers HS and LS is not distributed randomly but is concentrated in domains, thus the name domain model attributed to this approach. In this case, too, the authors employ macroscopic thermodynamics to linearize the Gibbs free energy:

$$G = N(G_{HS}n_{HS} + LS(1 - n_{HS})) - TS_{mix} \quad (1.32)$$

where the mixing entropy is S_{mix} for the No domains of size n is written:

$$S_{mix} = k_B \ln \frac{N_0!}{(n_{HS}N_0)!(1-n_{HS})N_0!} \quad (1.33)$$

$$S_{mix} = -k_B N_0 ((1 - n_{HS}) \ln(1 - n_{HS}) + n_{HS} \ln n_{HS}) \quad (1.34)$$

As in the case of the Bari and Sivardière model, we can determine the stationary states by minimizing the free energy with respect to the order parameter, that is, $\left. \frac{\partial G}{\partial n_{HS}} \right|_T = 0$ and $N = nN_0$, which leads to

$$n_{HS} = \frac{1}{1 + \exp\left(\frac{n\Delta G}{k_B T}\right)} \quad (1.35)$$

To establish the value of N_0 , the heat capacity is calculated, which leads to,

$$C_p = \frac{\partial}{\partial T} (n_{HS}H_{HS} + (1 - n_{HS})H_{LS}) \quad (1.36)$$

$$= n_{HS}C_{p,HS} + (1 - n_{HS})C_{p,LS} + \frac{(H_{HS} - H_{LS})^2 \exp(\Delta G/N_0 k_B T)}{N_0 k_B T^2 (1 + \exp(\Delta G/N_0 k_B T))^2} \quad (1.37)$$

At the transition temperature, $T_{1/2}$, the free energy of the two phases HS and LS are equal, so we have $\Delta G = 0$, which allows us to calculate

$$N_0 = \frac{(H_{HS} - H_{LS})^2}{4k_B T_{1/2}^2 [C_p(\max) - 0.5(C_{p,HS} + C_{p,LS})]} \quad (1.38)$$

An example of the fit of the experimental specific heat curve is shown in Fig. 1.16

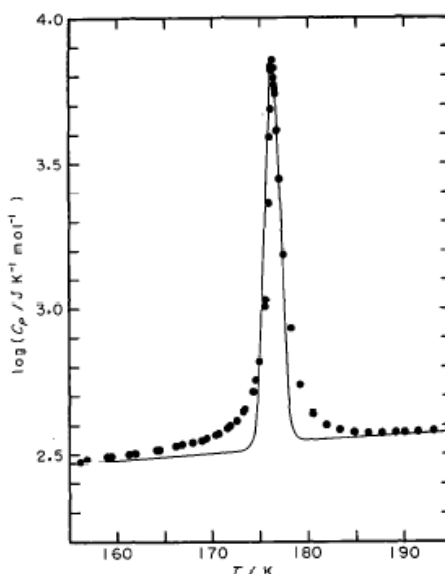


Figure 1. 16 Heat capacity for a spin transition compound $[Fe(phen)_2(NCS)_2]$ The circles are experimental data, and the solid line is the solution of equation 1.37. Adapted from reference [99].

The use of this model has resulted in the assumption that as the number of molecules increases, the transition becomes more abrupt (Fig. 1.17). Despite the fact that this model cannot reproduce a hysteretic transition, it does have some advantages in terms of solid structure. It should be noted that the domain structure

hypothesis implies the existence of intermolecular interactions that facilitate the spin transition even if no interaction is explicitly introduced in the free energy expression. Temperature [155][48] or light [156], [157] induced an LS-HS transition, according to X-ray diffraction measurements on a single crystal.

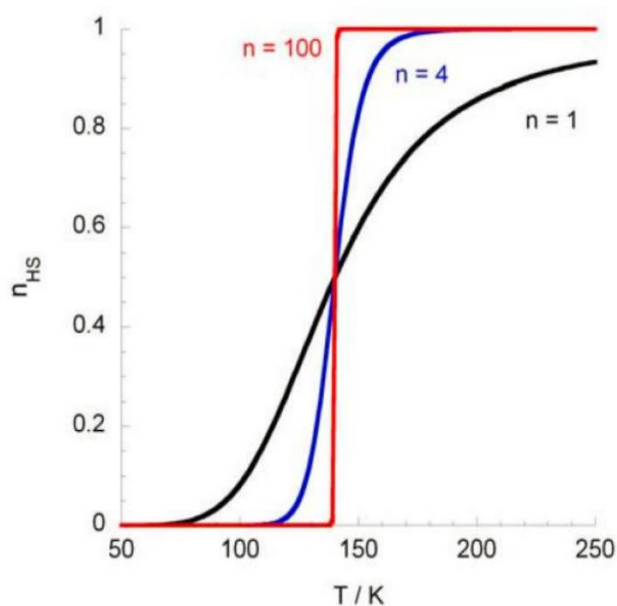


Figure 1.17 Fraction of HS-state molecules n_{HS} as function of temperature ($\Delta H = 7 \text{ kJ} \cdot \text{mol}^{-1}$ and $T_c = 140 \text{ K}$) [158]

It is important to note that the different models presented are all isomorphic to the Ising type model in its mean-field version, as demonstrated by Nishino et al. [159]

1.5.1.4 Ising models

1.5.1.4.1 Ising with short-range interactions:

Despite its apparent simplicity [160]–[163], the Ising model's mathematical structure is difficult, if not impossible, to solve exactly for the 2D [164] and 3D [165] systems. Because it is simple and allows one to understand many features of phase transitions, the Ising models are now the most widely used basis for quantitative interpretation of the SCO phenomenon. This model could be thought of as an extension of the Wajnflasz and Pick model. The Ising model is applicable to a variety of crystallographic systems, including 3D (three-dimensional lattices) [166], [167], 2D (two-dimensional lattices) [168], [169], and 1D (one-dimensional lattice) [166], [170], [171]. In order to study the behavior of SCO compounds, an Ising-like model is often used by associating to each molecule a fictitious spin operator σ with eigenvalues $\sigma = +1$ corresponding to the HS state and $\sigma = -1$ for the LS state. The two molecular states are usually degenerated and from this purpose the degeneracies by g_{HS} and g_{LS} , respectively are denoted. In order to associate non-degenerated states to the fictitious spin a temperature dependent “field” can be introduced in the Ising-type Hamiltonian which takes into account the original

state degeneracies. Thus, for non-interacting molecules, the associated effective Hamiltonian can be written as follows:

$$H = -h_{is} \sum_{i=1}^N \sigma_i \quad (1.39)$$

With,

$$h_{is} = -\frac{\Delta}{2} + \frac{k_B T}{2} \ln\left(\frac{g_{HS}}{g_{LS}}\right) \quad (1.40)$$

Where N is the number of molecules (spins) in the system, k_B is Boltzmann constant, while T is the temperature. $T_0 = \Delta / [k_B \ln(g_{HS} / g_{LS})]$ is known as equilibrium temperature for the system. It is apparent that negative spin values are expected at low temperature, $T < T_0$, where the energy difference between the states is dominant in the effective field formula. For high temperatures, positive spin values are expected since their higher degeneracy is higher, and the right term becomes dominant.

For interacting molecules, the Ising exchange-type is usually considered, as

$$H = -h_{is} \sum_{i=1}^N \sigma_i - J \sum_{\langle i,j \rangle} \sigma_i \sigma_j$$

Where $\langle i, j \rangle$, denotes that the sites i , and j are adjacent neighbors, the second sum takes into account the strength of the nearest neighbors interaction, which is denoted by J . The Wajnflasz model is with a temperature dependent field and a short-range interaction given in (13). The critical temperature at which phase transition occurs for the purely Ising ferromagnetic model formed by the last term in Hamiltonian [107] with J positive is denoted by T_C .

If the equilibrium temperature for the non-interacting model (T_0) is larger than this critical temperature (T_C) the system (13) has a gradual spin transition from LS state to HS state generated by the variation of temperature. If ($T_0 < T_C$) the spin transition is discontinuous associated to a first-order phase transition.

1.5.1.4.2. Ising model with short and long-range interactions: Ising –like model:

However, no phase transition can be theoretically obtained for such systems in one dimension ($T_0 = 0$), although they have been experimentally observed in SCO molecular chains. In order to resolve this inconsistency, long-range interactions between molecules have been considered in various forms [108] [117]. Here, it is considered that long-range interactions act on each spin as a uniform field proportional to the average spin $\langle \sigma \rangle$ of the system while the proportionality constant is denoted by G . The long-range interaction mimics the elastic interaction among molecules. In fact the long-range interactions, in spin crossover solids, originate from the molecular volume expansion or decompression over all the crystal [117]. In crystals, a volume change of only some molecules is

accompanied by an internal pressure which replicate at the surface of the crystal. This pressure acts on all molecules of the crystal with the same strength [172] even if they are at different distances. The former is treated by one-dimensional nearest neighbor coupling, and the latter is taken into account as a mean-field approximation though a temperature-dependent term which takes the form of an external “field”.

So is adopted the following Ising Hamiltonian:

$$H_{sys} = \frac{\Delta - k_B T \ln g}{2} \sum_{i=1}^N \sigma_i - G \langle \sigma \rangle \sum_{i=1}^N \sigma_i - J \sum_{i=1}^{N-1} \sigma_i \sigma_{i+1} \quad (1.40)$$

The Ising model is not difficult to solve in the 1D dimension if we apply the following techniques: matrix transfer, series expansions, and the renormalization group. For the 2D and 3D systems, no exact solution has been found until now. For these systems, Monte Carlo Metropolis [168] [173], [174] Monte Carlo Arrhenius [170] [175] Monte Carlo entropic sampling [170][176], [177], Molecular Dynamics [178], [179] represent good choices.

The general Ising Hamiltonian for SCO is given by:

$$H_{sys} = \frac{\Delta - k_B T \ln g}{2} \sum_{i=1}^N \sigma_i - G \langle \sigma \rangle \sum_{i=1}^N \sigma_i - J \sum_{\langle i,j \rangle} \sigma_i \sigma_j \quad (1.41)$$

1.5.1.5. Elastic models

In recent years the growth in computing power assisted the researchers in employing the use of stochastics methods like Monte-Carlo Metropolis to solve the Hamiltonians of theoretical models without linearizing them. More sophisticated microscopic models were therefore developed by adding the elastic nature of interactions reserved until now to macroscopic or mesoscopic models. To describe the mechanisms of the spin transition, one must take into account structural aspects. The difference in the volume of the molecules between the HS and LS states suggests different rigidities of the lattice in the two states which must be considered in the elastic constants. These novel class of cooperative SCO models based on the so-called ball and spring concept [180], largely reuse the Ising type model by changing the interaction by an elastic potential. This innovative theoretical description of SCO materials, using this model starts from the idea: when a molecule switches from one state to the other (i.e., LS to HS or HS to LS), its volume varies (Fig. 1.11 and 1.12). This variation will produce, at first, an instantaneous force in the springs connecting the switching molecule with its closest neighbors. This force will determine the shift in position of these neighbors and subsequently of all molecules in the system. From this point of view, they are therefore similar to compressible Ising models. In general, the Hamiltonian of the system is written as:

$$H = \Delta_{eff} \sum_i^N S_i + \sum_{\langle i,j \rangle} V(r_{ij}, s_i, s_j) \quad (1.42)$$

Where $r_{ij} = \|\vec{r}_i - \vec{r}_j\|$ is the distance between neighboring molecules and $\Delta_{eff} = (\Delta_0 - k_B T \ln g) / 2$. Here, the potential $V(r_{ij}, s_i, s_j)$ can have different possible forms. The model of Nicolazzi et al. [168] assumes a Lennard-Jones type anharmonic interaction, at the origin of the expansion thermal crystal; the other models use a harmonic potential [181] which accounts for also elastic effects and abrupt volume change of the system at the transition phase but other models also treat the molecule as an elastic oscillator interacting with a crystal lattice modeled via anharmonic potentials, or other. The potential describes the interaction with nearby neighbors as dependent on the state of spin. However, the elastic interaction produces long-range effects during relaxation network mechanics. This gives a richness and a complexity that does not exist in the model Ising type. The distances, r_{ij} , can be treated by the Monte-Carlo method also [179] or by molecular dynamics [182]. The Monte-Carlo Metropolis method for positions is equivalent to the method of MC for spin state. We go through all the molecules and we propose a different position, we then calculate the probability of the two states (current and proposed) and we accept or reject the new position accordingly. The biggest difference is that the state value of spin is a discrete variable with two possible eigenvalues $s = \pm 1$ and the position of the molecules \vec{r} is a continuous variable. To propose a new position, we draw a perturbation of the position between $\delta\vec{r} \in (-d\vec{r}, d\vec{r})$, or $d\vec{r}$ is the greatest possible perturbation for a single step of the MC method. The probability of passing is then,

$$P(s_i, s_j, \vec{r}_i, \vec{r}_j \rightarrow s_i, s_j, \vec{r}_i + \delta\vec{r}, \vec{r}_j) = \frac{e^{-\beta H(s_i, s_j, \vec{r}_i + \delta\vec{r}, \vec{r}_j)}}{e^{-\beta H(s_i, s_j, \vec{r}_i, \vec{r}_j)}}$$

These models with this type of digital resolution allow us to observe the spatiotemporal aspects and the change in volume as can be seen in Fig. 1.18

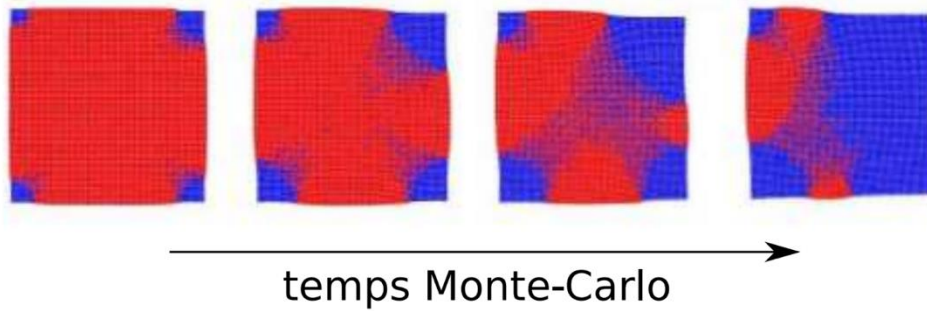


Figure 1. 18 Results showing the elastic behavior of a spin transition system during transition (adapted from reference [183])

This stochastic method has the advantage of bringing into play the temperature of the system and therefore to take into account position fluctuations, to determine the state of the network but the calculation of probability using the exponential is very costly in terms of computation, especially that the mechanical relaxation of the network takes a large number of MC (Monte-Carlo) steps. The deterministic

method for calculating the positions of molecules consists in solving the Newton's equations for a system subjected to viscous friction. The force produced by the potential due to neighbors is

$$\vec{F}_i = -\vec{\nabla}V(s_i, s_j, \vec{r}_i, \vec{r}_j) \quad (1.44)$$

Positions are recalculated between MC steps for spin state in order to mechanically relax the network. Solvable using Monte Carlo procedure [175][184], [185] or Molecular Dynamics [182] simulations, the elastic model have been used for the first time to study HS-LS relaxation processes[186], [187]. The advantage of this method is a significant performance gain in computing time but also the possibility of knowing the speed of molecules. This gives access to the study of shock waves and precursor phenomena of the spin transition. In the recent years the elastic model has been continuously adapted for the study of the light-induced hysteresis phenomenon [187], or the study of the evolution of clusters during the thermal transition [188]. Furthermore, the elastic model has also been helpful in showing the role of impurities during the Spin transition process [184], the domain wall propagation[189], the deformation field and local stress propagation [179], or in the study of core-shell systems [190].

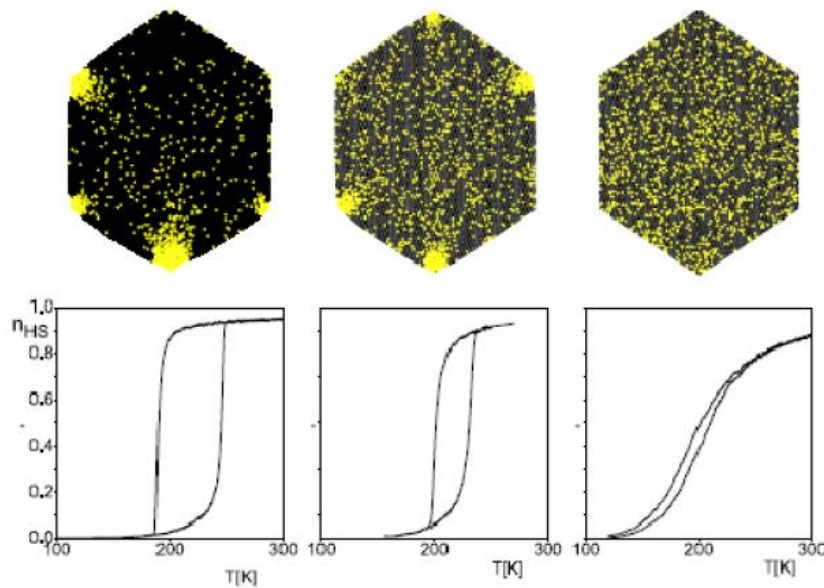


Figure 1. 19 Network configurations corresponding to 15% of molecules in the LS state (yellow color) for different interaction values with the corresponding hysteresis cycles. [65]

1.6. Methods used to solve the Ising – like model

1.6.1. Overview:

The growing popularity of new programming languages and tools [191], [192] has increased the demand for complex and powerful computational solutions, and its application of speculating in different fields has excellent benefits [193]–[195]. Nowadays, “computer simulations” have evolved into a complementary third division that complements the two traditional approaches (i.e., theoretical and experimental part). Researchers from various fields (such as natural sciences, engineering, social-sciences, finance, business, and so on) can now illustrate and present results in new, innovative ways, thanks to computer simulations. In physics, it is well known that the analytical theory's results are only precise in a few very exceptional cases and that in almost all other cases, approximations are required to facilitate valid results.

Even when there are models that do not have exact solutions (for example, the two- and three-dimensional Ising models in an applied field), computer simulations allow the correctness of the approximations made in the analytical treatment of these models to be verified. Similarly, the information provided by experiments contains some inaccuracies. For example, depending on the impurities in the material, the measurements yield varying and sometimes contradictory results. Considering the preceding examples, we can conclude that simulations serve as a link between experiment and theory, providing decisive outcomes to physical problems. It is now recognized that computer simulation methods are valid scientific approaches that contribute significantly to our understanding of nature [138].

Over the previous half-century, phase transitions in a wide range of statistical physics models have been extensively revised. From a theoretical standpoint, this has resulted in an expansion of simple models whose primary purpose is to look for and capture the fundamental qualitative characteristics of a natural system [98]. A wide range of analytical techniques has been developed to determine the phase behavior of these models. These approaches have recently been gradually supplemented by computer simulations [97]. Once the partition function is known, statistical mechanics demonstrates that the calculations of thermodynamic properties can be evaluated. However, the partition function is defined as the sum of all the microstates of a system and, in most cases (except in small systems), cannot be estimated due to a large number of microstates. We should also mention that an exact listing of the partition function is impossible. Knowing the difficult way of precisely solving Hamiltonian systems, Monte Carlo (MC) simulations are frequently used as a tool to obtain information about the thermodynamic properties of these systems. MC methods have proven to be very flexible and powerful routines for studying the phase transition problem in statistical physics.

In this section, we review the traditional MC simulation methods, which allow us to understand the behaviour of the SCO systems. We wish to emphasize that our methods presentation is only meant to be an introduction to our research work, and a more detailed treatment of these methods are accessible in the specialized literature.

1.6.2 Monte Carlo Methods

1.6.2.1. Choice of Boundary Conditions

The importance of comprehending complex systems has been recognized in a variety of fields. In simulations, depending on the structure and geometry to be modeled, periodic boundary conditions (PBCs) or open boundary conditions (OPBs) can be used (also known as free boundary conditions -FBCs). Furthermore, because the goal of the simulations is to achieve or complete the experimental work, there are combinations of OBCs and PBCs (i.e. APBCs). One example of where OBCs may be used successfully in place of PBCs is in the study of sample surface effects.

OBCs considerations have become very common in almost all studies in recent years, owing to the fact that the miniaturization of materials and devices has become a priority axe in research. Because simulations are applied to limited systems, the manner in which the lattice's "edges" or boundaries are considered is essential. OBCs are a type of boundary condition in which there is no connection between the end of a row and any other row on the lattice. In this case, the spins at the end of a row cannot see any neighbors on their path. These OBCs not only introduce finite-size smearing but also surface and corner effects as a result of the "dangling bonds" at the atoms' edges. Furthermore, when studying surface or corner behavior, OBC considerations are critical. OBCs may be more reasonable in some cases (for example, when modeling the behavior of nano-systems or grains), but the properties of systems with OBCs change more frequently than the properties of unlimited systems. In thin films modeling it's used a combination between PBCs and OBCs. These conditions are used in the study of various phenomena, e.g. wetting, interface localization delocalization transitions, surface induced ordering and disordering, etc.

A final example of conditions used in modeling SCO systems is the so-called "Edge effects" conditions. The edge atoms in this system [Figure 3.6d] are fixed in the HS state. The goal of fixing edge atoms in the HS state is to simulate polymeric-matrix roll (in which SCO can be embedded) and to understand incomplete spin-transition behaviour [97][168][171][190][196].

1.6.2.2. Monte Carlo Metropolis

More than 70 years ago, Metropolis [197] introduced the Monte Carlo method [185],

which is now used in a variety of fields. The canonical ensemble was used in the early simulations to approximate the average of physical size values given by Gibbs law. Using a Markov chain in the following form: x_0, x_1, \dots, x_n , where a configuration, x_{i+1} , depends only on an immediate previous configuration x_i , the transition probability of obtaining x_{i+1} from x_i is given by $p(x_{i+1}|x_i)$.

For example, if it is desired to compute magnetization of the system, there must be taken the configurations of the spins, where the Boltzmann factor $e^{-\omega/k_B T}$ has the highest value (a peak). The probability of the energy for a particular configuration is equivalent to $e^{-\omega/k_B T}$, which means that the acceptance of a configuration of the Markov chain, is weighted by a frequency proportional to the Boltzmann factor. The accepted configurations are then averaged to obtain an equilibrium property using an appropriate switching probability from one configuration to another. However, because time is not an explicit variable, this method of determining different physical properties of systems has drawbacks.

Markov chains, in general, provide a discrete series of steps for a finite set of states $\{N\}$. An N-state Ising model, for example, has 2^N possible states, and the transition probability is chosen to facilitate the Boltzmann distribution $P(x) \approx \exp(-W(x) / k_B T)$. Assuming we have free energy, when a spin is turned from S_i to $-S_i$, we should admit a move with a probability, because we want to be close to the ground state all the time. In contrast to an energy decrease, the Monte Carlo approach samples a set of molecular states with increasing energy states that vary with temperature. The very high energy states, on the other hand, will make only minor contributions to the system's stability because as the system's energy increases, the Boltzmann term decreases. In contrast to molecular dynamics, Monte Carlo allows for a larger jump in system optimization. Furthermore, for each step, we can have different steps for rotations, translations, internal coordinates, and optimization. The process of molecular dynamics is rather deterministic. Except for the Langevin algorithm, there is no randomness in the calculations because everything is determined at the start, and we can then leave the system to progress.

The sampling algorithms' operation can be summarized as follows: After using a random number generator or a regular algorithm to move a spin (i.e., the program starts with all the spins in $-S_i$ and then switches the spins from $-S_i(Ls)$ to $S_i(HS)$, one by one), the energy of the new configuration can be calculated. If this energy is less than that of the previous configuration, the novel configuration is accepted. In the opposite case, if the energy of the new configuration is greater than the energy of the previous configuration, the Metropolis algorithm can decide whether or not to keep the new configuration.

The probability ($P(x) = e^{-\omega/k_B T}$) that the new configuration to be retained depends on the Boltzmann factor and of a random number R (randomly chosen from the $\{0, 1\}$ interval). If the value of P is inferior to the value of R , the new configuration is accepted. Otherwise, the new configuration will be refused and

the former configuration is again submitted to another elementary perturbation. All the selected configurations are progressively built and fashioned as a Markov chain. It is a usual technique to search in the conformational space. The obtained structures can become the initial point for a novel minimization.

As presented in the above discussion, the Metropolis algorithm can be designed in the following way:

Firstly, the system's initial spins configuration is generated at random or based on the user's preferences. Then the initial configuration's energy is calculated. Secondly, by reversing a single spin, a new configuration is generated (proposed). Then energy for the new configuration is calculated. The energy difference, (ΔW), between the initial and new configurations is calculated and analysed as follows:

If $\Delta W < 0$ the new configuration is accepted. If $\Delta W > 0$ then, the program chooses a random number R with uniform probability over the $[0, 1]$ interval.

If $e^{-\omega/k_B T} < R$, the new configuration is accepted.

If $e^{-\omega/k_B T} > R$, the previous configuration is kept and the algorithm is restarted beginning with the first step.

Other Monte Carlo methods which are popular for studying complex system are Monte Carlo Entropic Sampling, and Monte Carlo Arrhenius. Although we won't go into detail of these methods for brevity concerns and review them very briefly. Monte Carlo entropic sampling (MCES) is based on a system probability distribution and depends on the system entropy [93]. MC methods haven't allowed the access of some configurations of the system and, in this way, didn't display the whole spectrum distribution. The origin of this behavior boils down to high-energy barriers that connect two configurations because the barrier is a function of several parameters such as energy gap, temperature, the strength of interactions, Lee [93] introduced an equivalent method of Berg's multicanonical method [94], in which these parameters as mentioned earlier have no influence. This new method, called entropic sampling, builds the distribution of states by using the system's entropy of the. In this way, a uniform probability distribution can be obtained. Before starting a discussion about the Arrhenius algorithm, we must recall the Arrhenius equation. It is well known that in the case of a chemical reaction between two reactant molecules, there must be a low amount of energy called activation energy (E_a) in order to become possible, the effective collisions between them. The Arrhenius algorithm uses a probability in order to pass from the HS state to the LS state or vice-versa [173] [175] [185] [198].

1.7 How to switch “ON” and “OFF” Molecular Switches: A brief review of various stimuli-based responses in SCO.

Before we move on to the application part, it is crucial to understand what other factors can affect or are used to govern the SCO process. As other requirements are necessary because the temperature is insufficient for a good characterization of the recording materials. To be a good recording material, the compounds must have two states: LS and HS, both of which must be stable and easily detectable. Another vital factor to consider is that the transition must occur near room temperature and be abrupt with hysteresis [199] [200]. The width of the hysteresis loop varies depending on the application. A large hysteresis loop width ($> 40\text{K}$) is required for data storage, whereas for sensor devices, a linear dependence of the n_{HS} as function of the external stimulus is required because the user must be informed about the change of a parameter (i.e., pressure, temperature) instantly [201]. Only if these elements are present will the system be able to provide accurate and precise information.

Now we will discuss briefly various factors or stimuli which could be optimised in order to harness the SCO material potential.

1.7.1 Temperature

Temperature [202]–[204] is the most commonly used external factor to trigger the transition from an LS to an HS state or vice versa. Different types of behaviors can be distinguished by the interaction strength between the molecules and their types in the SCO compounds ranging from spin-conversion to a multistep spin transition. Depending on the temperature variation, in SCO compounds, various ST behaviours can be observed including: Abrupt Transition with or without hysteresis [205]; Complete or incomplete transition [196] [168] [190] at high or low temperature; Two-step [170] [167] [169] or multi-steps [166] [171] transition.

1.7.2 Pressure driven spin-crossover

At constant pressure (e.g. atmospheric pressure) and zero temperature, the variation of the enthalpy (ΔH) between the HS and LS states originate from the zero-point energy difference between the potential energy minima of the HS and LS states.

Thermodynamically, the enthalpy (H) of a system is given by $H = U + pV$, where U is the system's internal energy, p is the pressure, and V is the system's volume. When the pressure on the system differs from the atmospheric pressure, the variation of enthalpy can be expressed in terms of the work done by the pressure

($p\Delta V$) and variation of internal energy (ΔU) as:

$$\Delta H = \Delta U + p\Delta V \quad (1.45)$$

where $\Delta V = V_{HS} - V_{LS}$ can be approximated to be pressure independent. $\Delta V > 0$ in most spin-crossover systems (since $V_{HS} > V_{LS}$). With the change in pressure, the variation of metal-ligand bond length and the ligand field strength is negligible compared to the change in $p\Delta V$ value [206], [207]. Since $\Delta V > 0$, thus an increase in pressure increases ΔH also and hence the LS state is favored over the HS phase [208], [209] [210]–[212]. The influence of pressure can even impact the shape of the spin transition itself, as a unit cell contraction increases the number and the strength of intermolecular contacts [209], favoring cooperativity. However, some complexes like $[Fe(PM - PeA)_2(NCS)_2]$ form a new stable phase at high pressure, and this phase has a lower spin transition temperature, which yields an apparent decrease in the spin transition temperature when pressure is applied[93] . Furthermore, it is known that the application of pressure leads mostly to a general reversible behavior of the system, although there are situations when the behavior generated by pressure is irreversible [101-103]. Concerning this factor, the first study was made in 1969 by A.H. Ewald [213] on a series of SCO compounds based on $Co(II)$ in solution.

The application of pressure on liquid or solid complexes has as main effect the change of the compound's fundamental state [214], [215]. Studying compounds, Slichter and Drickamer [119] have shown that the transition between the diamagnetic state and the paramagnetic state can occur, even if the external pressure is not very big and the switching temperature is shifted to higher temperatures with $15 - 20K/Kbar$. The application of an external pressure on a SCO material can also produce the modification of the electronic or the crystallographic structure (Fig. 1.20) [216], [217].

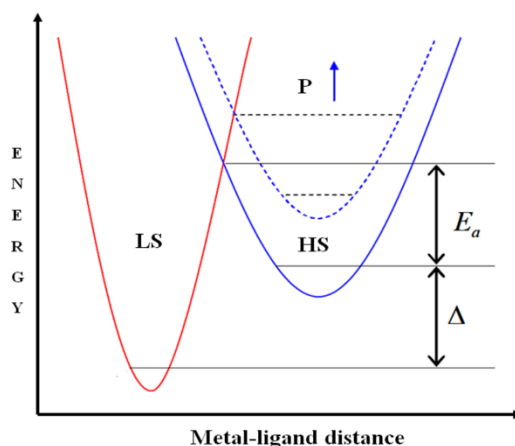


Figure 1. 20 Representation of the molecular configurationally diagram, i.e., a plot of the adiabatic energy versus the distortion coordinate (metal-ligand distance) showing the shift of HS potential well on the application of pressure.

The effect can also depend on the hydrostatic or non-hydrostatic origin of the application of the pressure[212]

1.7.3 Electric field

Electrostatic field control of the spin transition is still an open field. When an electrostatic field is applied to a spin-crossover system, it can drive a spin-crossover via the coupling with the dipole moment present in the molecule or by charging the molecular ligands [218]. In the process of cooperative spin transition electric field can play an important role for some SCO complexes [72], and therefore in the hysteresis, as seen for SCO molecules dispersed in polymeric matrices [219]. Results were obtained with linear junctions[218] and multi-metal complexes [220], but electrostatic field control of the spin state of bulk SCO samples still remains to be seen. One route of spin-crossover using electric field can be feasible with nanometric junctions or STM where appropriate voltages applied to the STM tip can produce enough electric field for the spin transition to occur in a film of SCO complexes.

1.7.4 Magnetic field

In a diamagnetic or paramagnetic system, the magnetization is defined by $\vec{M} = \chi_M \vec{H}$, where χ_M is the magnetic susceptibility and \vec{H} is the external magnetic field. In the presence of the external magnetic field (\vec{H}), the variation of magnetic energy per unit volume is:

$$E_n(H) = -\mu_0 \vec{M} \cdot \vec{H} = -\mu_0 \chi_M H^2 \quad (1.46)$$

Now, in the case of a spin-crossover system, magnetic field control of the spin transition was observed for bulk samples [221]. The magnetic susceptibility of the HS species (χ_M^{HS}) is higher than that of the LS species (χ_M^{LS}) [222][206]. Thus, from equation 1.46 we can observe that the application of an external magnetic field will favor the HS state as it has the minimum magnetic energy, due to Zeeman effect. A significant drawback is that, similar to the pressure stimuli; intense fields have to be used to witness a sizable effect: a shift of only 2K is observed for a 5T field [222]. It is also to be noted that experiments [223] based on the use of pulsed magnetic field (30T), shows shifts of only few kelvins. These experiments also pose serious problems on the type of dynamics of the SCO: adiabatic or isothermal regimes in the triggering of the SCO transition.

1.7.5 Light-induced spin-crossover

Light irradiation can also induce a spin transition in the spin-crossover complexes. McGravey et al.(in the year 1982)[224] were the first to observe a laser-pulse induced transition from LS ($^1A_{1g}$) to HS ($^5T_{2g}$) state on several *Fe(II)* spin

crossover complexes in solution [224]. The relaxation from the metastable HS state to the LS state at around room temperature (with $T_{1/2} \sim RT$) was occurred at the timescale of nanoseconds to microseconds. This discovery opened up new possibilities to trap the spin state of the spin crossover complexes at lower temperatures. This was first done by Decurtins et al. in 1984 [225]. They have observed a light-induced transition from LS state to HS state of a *Fe(II)*SCO complex in solid form at temperatures below 50 K. Below this temperature the complex was trapped in the HS state after the light induced transition and it stayed at this state for few hours. The decay rate was extremely slow and at around 50 K the system relaxed back to the normal LS state from the excited HS state. These experiments showed that at cryogenic temperatures, the spin state of a SCO complex can be trapped in HS state upon light irradiation with very slow relaxation rate [226][227]. They proposed this unknown photophysical phenomenon back at that time as "Light-Induced Excited Spin State Trapping (LIESST)". Since their discovery, a great deal of research has been carried out to study the light-induced switching of the *Fe(II)* SCO complexes in the form of solid, thin films and ultrathin films [228]–[233]. One of the consequences of the LIESST effect was the discovery of LITH phenomenon by A. Desaix et al. in 1998, which is driven by the competition between light and temperature and thus produced non-equilibrium first-order phase transition.

1.7.6 X-rays

The exposure of the soft X-rays to the spin-crossover complexes can give rise to a soft X-ray induced excited spin state trapping (SOXIESST) of the system. This phenomenon, first observed by Collison et al. [234], can be attributed to the similar trapping of the metastable HS state through a cascade of excited states as observed in the case of LIESST effect. An important drawback of this effect is that in some cases the effect might not be reversible. The exposure of the X-ray might permanently damage the molecules or break some of their ligands [234] and hence causing irreversibility of the spin state switching. While the use of X-rays (X-ray diffraction, EXAFS, XANES...) to study SCO molecules and processes have met a lot of success[235]–[243] effect in itself has not received a lot of attention.

1.7.7 Chemical stimuli

Different from the physical triggers reviewed until this point, the chemical stimuli can also be used to switch the spin state of SCO molecules. Since the ligand field determines the spin state of the molecule, it is natural that the nature of the solvent in solutions of SCO molecules impacts the spin state, either directly [244] or by ligand exchange [76,95]. For the first time, the influence of a reversible solvent up to the ST regime has been illustrated for 1D coordination polymer by Garcia et al. [245] for $[Fe(hyertz)_3(3 - nitrophenylsulfonate)_2, 3H_2O(1.3H_2O)]$, with *hyertz* = 4 – (2' – hydroxyethyl) – 1,2,4 – triazole compound. In 2004, a

bistable behavior for some temperatures has been reported by Real et al. [246], [247] as a response generated by cooperative phenomena met in some *Fe(II)* based SCO compounds. A reversible LS-HS spin state change was observed with the uptake of guest molecules. In compounds such as *Fe(pyrazine)Ni(II)(CN)*, *Fe(pyrazine)Pd(II)(CN)*, or *Fe(pyrazine)Pt(II)(CN)*, the HS state presents a yellow color and can be stabilized with a hydroxilic solvent. The LS state has a red-brown color and can be stabilized with CS_2 solvent. In 2009, Kepert et al. [248] reported a guest-dependent spin crossover property for the same Hofmann-type system. Usually, bond-breaking leads to irreversible spin-crossover. Nevertheless, some recent examples of bridged compounds that exhibit a reversible bond-breaking/-making SCO [249] exist. Chemical stimuli are sometimes used in conjunction with physical methods, such as the strategy to alter the ligands by optical stimulus in order to obtain a similar effect as the LIESST but still present at higher temperatures, a promising effect called ligand-driven light-induced spin change [76][226].

Among all these external stimuli for spin crossover, the most studied ones are temperature, pressure, electric field and light.

1.8 Detection and Applications

1.8.1 Detection of the Spin Crossover

The physical characterization of the spin transition in molecular systems is a critical task in the field of scientific research. Regardless of the stimulus used to initiate the spin crossover phenomenon (temperature change, pressure, magnetic field, or light), it can be monitored using a variety of experimental techniques that can reveal the electronic state of the SCO centre directly or indirectly. Indeed, the transition spin is accompanied by various variations in micro- and macroscopic properties, such as the density of electronic states, the magnetic moment, metal-ligand distance, vibrational properties, crystal lattice volume, etc. All these properties mean that the spin transition can be detected by various characterization techniques and involves physicists, chemists, crystallographers, theoreticians, etc. [250]–[254]. The more simple, accurate, and robust these techniques become, the more valuable they are, as many SCO applications rely on the precise detection of phenomena. In this part, we will introduce some experimental techniques allowing the study and investigation of this transition phenomenon spin.

1.8.1.1 Magnetic Susceptibility Measurements

It is one of the most popular characterization techniques for SCO materials. One of the essential properties of spin transition materials is, of course, the magnetization, M , of compounds. When the compound is exposed to a

homogeneous external magnetic field, H , magnetization is then induced in the system. The change from the HS state to the LS state (or vice versa) as a function of temperature is reflected in a variation of the magnetic susceptibility ($\chi_m(T)$) of the material. According to the Curie's law, the product $\chi_m \cdot T$ for a paramagnetic material is constant for all values of temperature T . Hence, if the magnetic susceptibilities at each spin state are not accurately known, the product $\chi_m \cdot T$ vs T is often plotted. This way, any variation of the product will be due to the SCO phenomenon in the material. Several experimental techniques allow this magnetization to be measured, such as the Faraday balance [40] or the SQUID magnetometer [255], [256]. In Fig. 1.21, we represent an example of measurement of the product $\chi_m \cdot T$ according to the temperature of the spin transition compound $\{[Fe(2 - pytrz)_2[Pd(CN)_4]] \cdot 3H_2O\}$ that is studied using this technique, showing an incomplete spin transition with a hysteresis cycle around 161 K [257].

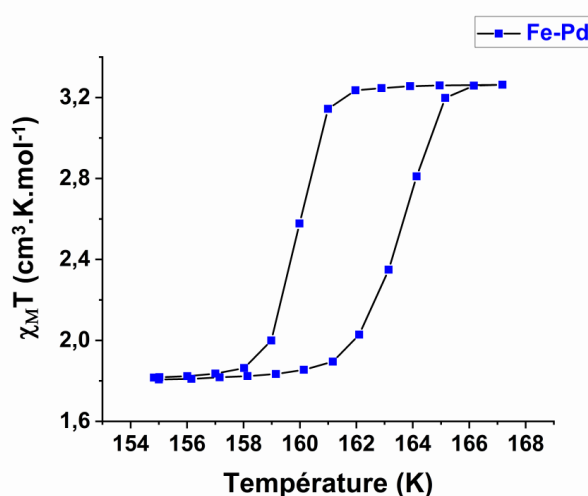


Figure 1. 21 Thermal evolution of the product $\chi_m \cdot T$ for the compound $\{[Fe(2 - pytrz)_2[Pd(CN)_4]] \cdot 3H_2O\}$ [257].

1.8.1.2 Mössbauer Spectroscopy

It is the spectroscopic method of choice for the study of the SCO in Fe based complexes. This type of spectroscopy allows to distinguish the molar fractions of $Fe(II)$ or $Fe(III)$ centers at each spin state. By the same token, this technique provides valuable insights into the local structure of the material around the iron centers and lattice dynamics information.

1.8.1.3 Crystallography

The spin transition is always accompanied by various changes in physical properties due to the variation of the ligand field and the occupation of atomic orbitals. X-ray diffraction techniques can be employed to deduce the structural evolution of the compounds upon the SCO, which can be done as a function of temperature, allowing to characterize the change in the elongations of the metal-

ligand distances between the two spin states, the increase in volume and angular distortions. Additionally, elastic properties such as the bulk moduli can be inferred. In general, these types of observations are widely used in the SCO field in order to establish structure-property correlations. This thermal investigation of X-rays can be performed on powder or a single crystal, making it possible to obtain information on the type of transition (gradual, abrupt ..), the space group and the atomic distances. [258], [259]

1.8.1.4 Heat Capacity Measurements

Thermodynamical parameters such as changes of enthalpy and entropy can be estimated. Differential Scanning Calorimetry (DSC) is an experimental technique used to identify the presence and the nature of phase transitions in solid materials. It makes it possible to determine, for example, the glass transition temperature (T_g), melting and crystallization temperature, enthalpy of reaction, specific heat, oxidative stability and various other physical properties in most materials (plastics, rubber trees, resins, powders, fibers, textiles ...). DSC is about measuring the change in the material's heat capacity as a function of the temperature variation while comparing it by the heat flow. Among the various existing transitions, the transition spin can also be detected using DSC; the typical behavior for a spin transition material corresponds to an endothermic peak in heating of LS towards HS and an exothermic peak in cooling from HS towards LS [260]–[262]. We present the example of the compound $\{[Fe(2 - pytrz)_2[Pd(CN)_4]]\} \cdot 3H_2O$ [257], in Fig. 1.22.

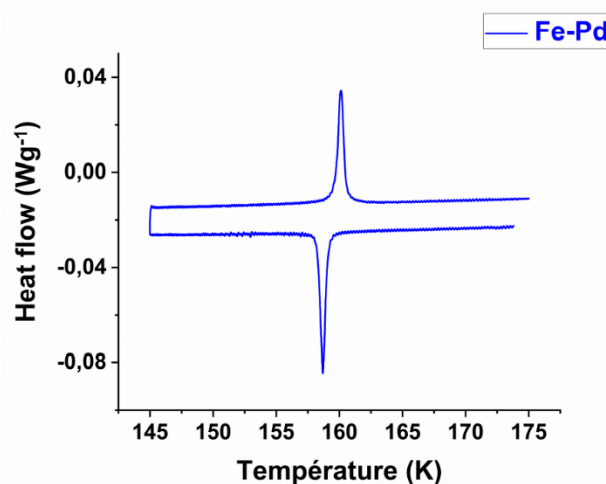


Figure 1. 22 DSC measurements showing the peaks of exo-, and endothermal transformations for the compound $\{[Fe(2 - pytrz)_2[Pd(CN)_4]]\} \cdot 3H_2O$ [257].

1.8.1.5 Vibrational Spectroscopy

The variation of vibration spectra in spin transition materials between the HS and

LS states allow characterization by Raman or infrared spectroscopy [263], [264]. Infrared absorption or Raman spectroscopies are actively used since the frequencies of metal-ligand vibrations, induced by the variation of the Fe-ligand distances at the transition, are of higher energies in the state LS than in the HS state. Currently, these techniques have been extended and coupled to optical microscopes in order to perform localized micro-Raman and micro-IR spectroscopies.

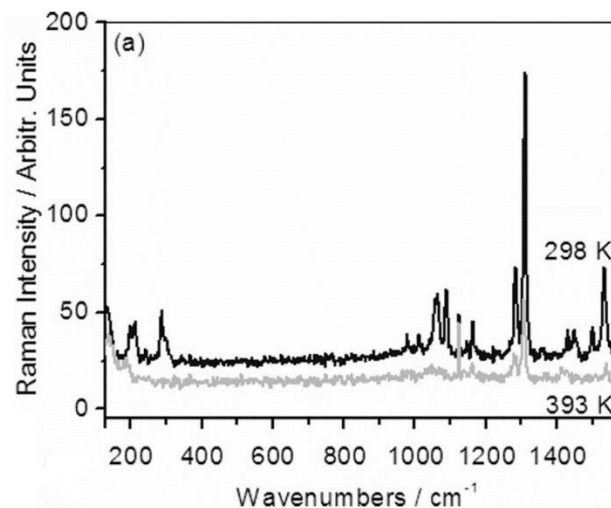


Figure 1. 23 Raman spectrum of particles $[Fe(Htrz)_2(trz)](BF_4) \cdot H_2O$ in the state LS (298 K) and the state HS (393 K) obtained with excitation at 532 nm. Figure adapted from reference [265].

Indeed, Fig. 1.23 shows the example of a Raman spectrum of the compound $[Fe(Htrz)_2(trz)](BF_4) \cdot H_2O$ studied in reference [265]. This compound performs a spin transition with hysteresis cycle at an equilibrium temperature around $T = 358 K$. This spectrum is obtained using an excitation at 532 nm, starting from particles deposited on a glass slide. It was noticed, as the authors have pointed out, that at room temperature $T = 298 K$, (system in LS state) vibrational modes are detected at 200, 214, 287, and 301 cm^{-1} . These bands which constitute the fingerprints of the LS state disappear at high temperature when the system reaches the HS state.

1.8.1.6 Optical Microscopy Measurements

One of the most remarkable properties of spin transition materials is their thermochromism (usually pronounced) due to the change of the electronic configuration of the SCO centers. In fact, the visible UV and IR absorption bands are affected by the spin transition, thus allowing an excellent optical characterization of these materials by optical microscopy [266].

A multitude of physical information can be deduced from the analysis of optical microscopy images like the HS fraction, N_{HS} , allowing us to go back to the nature

of the transition, the propagation speed or speed field of the HS / LS interface, length variations in single crystals between the two phases [267]–[279]. As a result, it is possible to monitor the SCO phenomenon utilizing optical reflectivity absorption spectroscopies. Since the absorbance is closely proportional to the concentration of the colour centres when normalized appropriately, these absorption spectra directly yield the temperature dependence of the molar fraction of the metal ions in the LS or HS states.

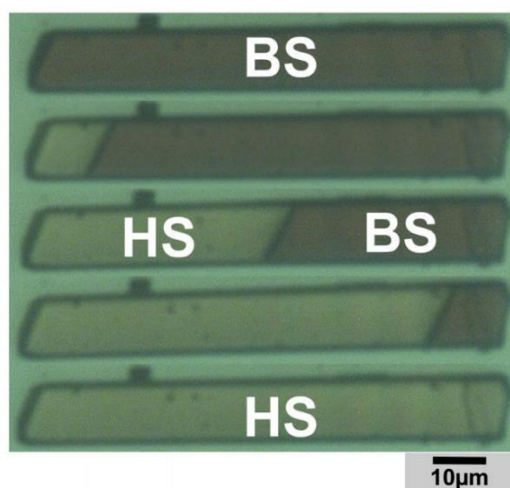


Figure 1. 24 Selection of images of a single crystal of the compound $[Fe(NCSe)(py)_2]_2(m - bpyz)]$ placed under vacuum in a cryostat and illuminated by a light source of $2.47mW$ during the heat-induced transition. The images are taken during the heating phase with a thermal scan of $0.2 Kmin^{-1}$ [280]

In Fig. 1.24, we have represented images of a single crystal of the compound $[Fe(NCSe)(py)_2]_2(m - bpyz)]$ studied as part of Mouhamadou SY's thesis (team P2MC) [24]. These images are obtained through the light microscope and show a first-order phase transition with an HS/LS interface propagation nucleation regime. The crystal appears lighter in the HS state and darker in the LS state. An analysis of the optical density according to the methodology described above makes it possible to go back to the hysteresis cycle of the thermal transition that we have shown in Fig. 1.25.

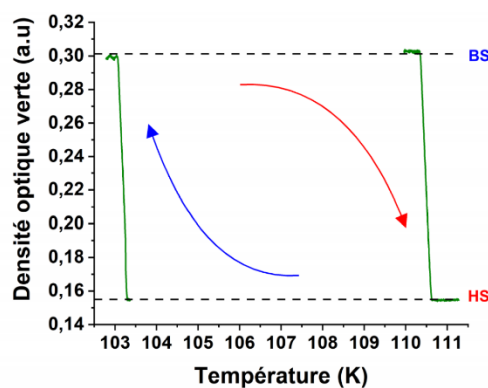


Figure 1. 25 Thermal evolution of the green optical density of a single crystal of the compound $[Fe(NCSe)(py)_2]_2(m - bpypz)$ (Fig. 1.24), showing the hysteresis cycle of the spin transition.

Compared to the magnetic measurements, the optical microscopy studies allow the characterization of the spatiotemporal aspects of the SCO transition on a unique single crystal. The orientation of the interface connects to the crystallographic changes and gives crucial information about the anisotropic character of the structural changes.

1.8.1.7 Refractive Index Change

Spin crossover thin films can be used to modulate the propagation of electromagnetic waves in plasmonic or other types of guided-wave devices. ref. [281] for example of a surface plasmon polariton (SPP) wave. For an appropriate combination of the wavelength, polarization and incidence angle of the exciting light beam, a resonance is observed in the reflectance spectra. This is the so-called “simultaneous wave vector and frequency matching condition”. When the temperature of the multilayer is increased, the spin state of the SCO layer changes from HS to LS, and the associated increase of the refractive index leads to a shift of the resonance to lower angles. This temperature-dependent behavior occurs due to both ordinary thermal expansion of the material as well as due to the SCO phenomenon. [282] However, these two phenomena can be differentiated due to the observed discontinuity of the shift of the minimum of the angular reflectance around the transition temperature of the film.

1.8.1.8 Electrical Measurements

A number of recent papers have been devoted to the study of the transport properties of SCO materials from the single molecule or nanoparticle [218], [283]–[286] to the macroscopic level [287], [288] with promising perspectives in nanoelectronics and spintronics. In particular, the characterization of a single object placed in a “nano-gap” has been complicated. There is always a considerable uncertainty for assessing the real origin of the variations in the electrical current changes measured on the samples as a function of a bias voltage; these could be due to the SCO or other unrelated phenomena. Furthermore, it is not trivial to extrapolate the different physical properties observed on a macroscopic ensemble of (nano) objects to those observed in the single object measurements. There are theoretical calculations in the early stages of development for the description of the electrical transport in SCO materials that will surely provide useful help. For example, it has been observed that the thermal hysteresis loop in the dc electrical conductivity of the compound $[Fe(Htrz)_2(trz)](BF_4)$ is clearly associated to the SCO phenomenon [287]. It was observed that the LS phase of the compound is more conductive than the HS phase due to a lower activation barrier of the LS form. It was shown that the possibility to observe a spin state dependence of the conductivity in the highly insulating SCO materials is very dependent on the interplay between the spin transition temperature and the activation parameters

of the compound. Additionally, it was also demonstrated that by modifying the conditions of the synthesis, it is possible to modify drastically the charge transport behavior of the sample without affecting the SCO properties of the material. In consequence, small variations in the morphology or composition of the measured objects can lead to dramatic changes in the conductance behavior. All these studies reveal the electrical measurements as a promising characterization tool for performing size effect studies of SCO materials

1.8.2 EMERGING APPLICATIONS USING MOLECULAR SPIN CROSSOVER COMPOUNDS

As a result of their importance in the natural world and their potential application as molecular-scale switches, molecules with bistable spin states are widely studied. Different physical-chemical events are involved in molecular switches, and the switching event is usually accompanied by a major rearrangement in the locations of atoms. In this section a review of emerging properties and applications of spin-crossover (SCO) materials in a wide range of technologies, SCO materials and frameworks have been sought after for their many potential applications including molecular electronics [199]–[201], [286], [289]–[293], high-density reversible memory [7], [8], [13], [15], [72], [219], [286] actuators [12], ultrafast nanoscale switches, [13], [15], [72], [219], [286], [294] sensors [13], [219], [286], [295] and displays [8], [13], [15], [72], [219], [286]. Understanding the mechanisms that control the collective behaviours of SCO materials could significantly enhance their potential to be engineered for specific applications.

Nowadays, it is evident that SCO compounds are among the most promising innovative materials. SCO compounds have opened a new branch in the field of material science with significant well-adapted properties, such as room-temperature operating range, chemical stability, short addressing time, low addressing power, and complete reversibility behavior, which represent potential functionalities in the context of upcoming technologies [16]. These remarkable developments in the SCO area have been amplified in the last two decades, thanks to intense theoretical and experimental investigations [17] [29]. Today, research and development are focusing on nanotechnology, and as a result, basic research, as well as, profit-oriented industrial development laboratories' slogan, is "go nano". The study of SCO materials at a reduced scale has become feasible, thereby envisioning fascinating insight into spin transition (ST) phenomena.

1.8.2.1 Molecular electronics or Spintronics

Use of spin-crossover (SCO) complexes as building blocks for molecular spintronics are promising because the spin state of the molecules can be switched reversibly between low spin (LS) and high spin (HS) by external excitations like

temperature, light, pressure, magnetic field [72], [227], [286]. In bulk and thin films, spin transition of different SCO complexes has been documented for such external stimuli [229], [231], [296]. However, for potential application in spintronic devices, the molecules need to retain their spin-crossover properties when deposited on surfaces. More importantly, for a single molecular device application, it has to be preserved at the first molecular layer or even for single molecules in contact with the substrate [297]. SCO transition by means of voltage pulses was possible for single *Fe – phen* spin crossover molecules on *CuN* / *Cu(001)* owing to the weaker hybridization between the molecule and *CuN*. But the switching was not possible for the molecules on bare *Cu(001)* because of the strong coupling between the molecule and *Cu(001)* [297]. In an ultrathin film of another SCO complex [*Fe(bpz)₂(phen)*] the transition has been observed only in the second layer of molecules, the first molecular layer was working as a decoupling layer from the substrate [232]. These studies show that in order to have spin crossover for the single molecules or in a monolayer of molecules on a substrate, the molecule substrate interaction has to be rather weak. Passing a current through a molecule [298], [299] or mechanically stretching or squeezing its ligands [300], [301] can reversibly change its spin-state; a voltage can switch between the two broken symmetry states of an antiferro-elastically ordered chain [302]; and strain can induce the motion of domain walls in ordered phases of SCO materials [303]. These experiments suggest that applying a voltage or strain could also induce motion of the defects somewhat analogous to the current induced motion of skyrmions [304], [305]. Either of these effects would make a valuable resource for spintronic applications. With such a wide range of environment-sensitive properties and spintronic capabilities [306]–[308], it is not surprising that SCO molecules have attracted significant interest from the community.

Thin films and nanoparticles can be patterned to suit the needs of device elaboration in a complementary approach to those developed as described above [309]. It is interesting to note the diversity and the complementarity of the techniques used in this purpose: for example, the combined SAM/lithography technique of Molnár et al. [309] to produce nanoparticles of desired shape and size, or the combined drop-casting/stamp technique of Cavallini et al. [310] to produce 1-D type structures. The use of this latter technique has further allowed them to reproduce CD-patterns with *Fe – phen* on silicon substrates [311] as shown on Fig. 1.26

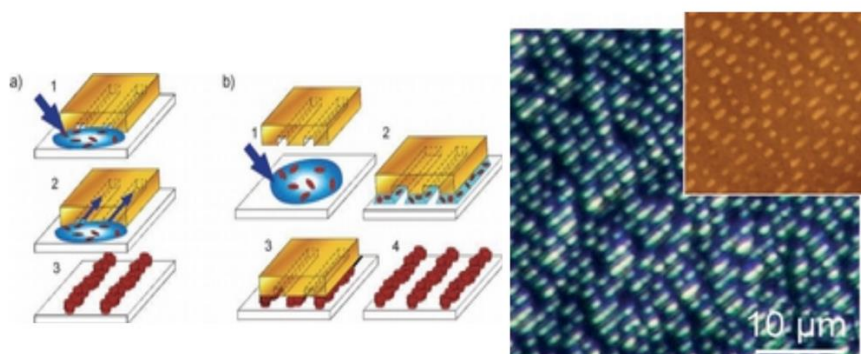


Figure 1.26 Schematic representations of (a) the micro-inject moulding in capillaries process and (b) stamp-lithography controlled wetting process, and on the left optical microscopy (insert AFM, vertical scale 0-80nm) picture of the pattern obtained by this latter process using a CD-pattern mould. Adapted from [31].

1.8.2.2 Spin Crossover in Nanoparticles, Thin Films and Nanocomposites

The appealing properties of thin films [312] or nanoparticles [291], [313]–[320] confer a promising market for industry while simultaneously bridging the gap between the understanding of single molecules and bulk macroscopic materials behaviours. When individual materials and technologies achieve their limits in terms of application needs, new technological strategies are introduced to substitute or turn their value in a different manner. One of the ways to overcome the drawbacks of a given material is attained by making it work in combination with other materials in composites and nanocomposites. This requires obviously a more complex, interdisciplinary approach. Basically, a composite material is defined as a material made from two or more constituents with different properties which, when combined, produce a material with different characteristics from the individual components. Regarding this aim, the manufacture of thin films, nanoparticles and other nano-objects together with a nanoscale understanding of the material properties is of central interest [196], [281], [291], [293], [321]–[327]. The evolution in the understanding of ST at the nanoscale level has been stimulated through instrumental improvements in nanoscale manipulation [292], measurement methods [328]. Simultaneously, a continuous boost in computing power has permitted the modelling of the materials and their properties at the nanoscale level. New attractive progress has been made in the area of SCO complexes with infinite one-, two- or three-dimensional (1D, 2D, 3D) networks, the so-called coordination polymers [329]. The major goals of that approach are to enhance and fine-tune cooperative properties by the strong covalent links between the metallic cores in the polymers.

In recent literature, several highly cooperative polymer systems have been reported displaying hysteretic behaviour (thermal and piezo) even, in some cases, at room temperature. It is generally accepted that the SCO phenomenon depends

on the molecular environment (anion, solvent, packing) [330]. Among the “exotic” SCO nanoparticles system, one can cite the nanoball reported by Duriska et al. [131], a $Fe(II)(NCS)_2 - Cu(I)(Tp^{4-py})(CH_3CN)$ association that exhibit thermally-induced, light-induced, and guest-induced (by complexation with an external, “guest” molecule) spin transition. 1-D nanowires or nanotubes of SCO systems have not been successfully produced [286] before 2012 (although enhanced shape anisotropy by confined growth [331] and patterning of nanocrystals [310], [311] into 1-D-like systems were known), when the first example of the template assembly of a mononuclear SCO molecule into nanowires was reported by Martinho et al. [332]

Some surprising developments have come from an unexpected exchange with biology, as Naik et al. have used a biomembrane to grow $[Fe(ptz)_6](BF_4)_2$ nanocrystals, using it as a natural stencil to transfer the patterns on Si wafers by conformational contact [333]. The practical applications range from moisture sensors [334] to digital displays [335].

1.8.2.3 Actuators (MEMS/NEMS)

Microelectromechanical systems (MEMS) are microscale devices able to transform a mechanical signal into an electrical one and vice-versa. The long-range order of switching molecules results in a collective or cooperative volume shift at the macroscopic level, which can be easily exploited for actuation purposes. The combination of SCO materials and MEMS opens up new possibilities for MEMS actuation as well as the study of SCO mechanical characteristics. Although SCO compounds that act at room temperature are now widely available [336], their deposition on delicate mechanical parts and reliable performance remain a significant issue. The potential of SCO materials as actuators necessitates a thorough understanding of their mechanical properties, as well as, their effective integration into practical devices and appropriate transduction mechanisms. Recently M.D Juarez et al. has been able to achieve MEMS devices in which the SCO molecules are not only used to tune the device mechanical properties but also perform controlled and reversible macroscopic work under ambient conditions [337]–[343].

In the future, nano-systems will provide new opportunities for the selective and sensitive recognition of a wide range of measuring capabilities. Furthermore, the development of new stable and processable compounds as well as a new dedicated procedure have allowed for significant progress, opening up new technological perspectives for SCO compounds and reviving interest in the field. For instance, miniaturized sensors for detecting diverse physical contact such as tiny weights, pressure, radiation (electromagnetic or simple light), and chemical and biological substances may be realized with nano-systems or nano-elements. There is no doubt that the trend is to create nano-systems, and in this context, systems that are superior in energetic efficiency, easily integrable, environmentally friendly, and

cost-efficient. However, these real-world applications have just not yet reached industry, primarily because there are still scientific and technological barriers [235]. The parameter space where bistability can be reached is still too small compared to industrial needs, and triggered effects such as LIESST happen at too low temperatures. It could be a possibility that a pure SCO system might not be able to satisfy all the requirements [344]. However, more exotic systems can be devised to make use of the high sensitivity to the environment of SCO centres, for example, in molecular sensing by guest-dependent SCO in a SCO framework [345]. Research applications, notably in the field of non-linear optics [344], are also considered.

Therefore, this work aims to reduce the gap between the theoretical understanding of the phenomenon and the practical applications.

References: -

- [1] M. M. Turnbull, T. Sugimoto, and L. K. Thompson, *Molecule-Based Magnetic Materials*, vol. 644. Washington, DC: American Chemical Society, 1996.
- [2] J.-F. Létard, P. Guionneau, and L. Goux-Capes, "Towards Spin Crossover Applications," in *Spin Crossover in Transition Metal Compounds III*, vol. 235, Springer-Verlag, 2006, pp. 221–249.
- [3] A. Hauser, "Spin-Crossover Materials. Properties and Applications. Edited by Malcolm A. Halcrow.," *Angew. Chemie Int. Ed.*, vol. 52, no. 40, pp. 10419–10419, Sep. 2013.
- [4] G. Molnár, L. Salmon, W. Nicolazzi, F. Terki, and A. Bousseksou, "Emerging properties and applications of spin crossover nanomaterials," *J. Mater. Chem. C*, vol. 2, no. 8, pp. 1360–1366, Feb. 2014.
- [5] J. Linares, E. Codjovi, and Y. Garcia, "Pressure and temperature spin crossover sensors with optical detection," *Sensors*, vol. 12, no. 4, pp. 4479–4492, Apr. 2012.
- [6] C. M. Jureschi *et al.*, "Pressure sensor via optical detection based on a 1D spin transition coordination polymer," *Sensors (Switzerland)*, vol. 15, no. 2, pp. 2388–2398, Jan. 2015.
- [7] E. Freysz, S. Montant, S. Létard, and J. F. Létard, "Single laser pulse induces spin state transition within the hysteresis loop of an Iron compound," *Chem. Phys. Lett.*, vol. 394, no. 4–6, pp. 318–323, Aug. 2004.
- [8] O. Kahn, J. Kröber, and C. Jay, "Spin Transition Molecular Materials for displays and data recording," *Adv. Mater.*, vol. 4, no. 11, pp. 718–728, Nov. 1992.
- [9] P. Gütllich, Y. Garcia, and H. A. Goodwin, "Spin crossover phenomena in Fe(II) complexes," *Chem. Soc. Rev.*, vol. 29, no. 6, pp. 419–427, Jan. 2000.
- [10] "Spin-Crossover Materials: Properties and Applications | Wiley." [Online]. Available: <https://www.wiley.com/en-us/Spin+Crossover+Materials%3A+Properties+and+Applications-p-9781119998679>. [Accessed: 10-Jun-2021].
- [11] M. Atzori and R. Sessoli, "The Second Quantum Revolution: Role and Challenges of Molecular Chemistry," *Journal of the American Chemical Society*, vol. 141, no. 29. American Chemical Society, pp. 11339–11352, Jul-2019.
- [12] M. Mikolasek *et al.*, "Complete Set of Elastic Moduli of a Spin-Crossover Solid: Spin-State Dependence and Mechanical Actuation," *J. Am. Chem. Soc.*, vol. 140, no. 28, pp. 8970–8979, Jul. 2018.
- [13] O. Kahn and C. J. Martinez, "Spin-transition polymers: From molecular materials toward memory devices," *Science*, vol. 279, no. 5347. American Association for the Advancement of Science, pp. 44–48, Jan-1998.
- [14] A. Bousseksou, G. Molnár, L. Salmon, and W. Nicolazzi, "Molecular spin crossover phenomenon: Recent achievements and prospects," *Chem. Soc. Rev.*, vol. 40, no. 6, pp. 3313–3335, May 2011.
- [15] O. Fouché, J. Degert, G. Jonusauskas, N. Daro, J. F. Létard, and E. Freysz, "Mechanism for optical switching of

- the spin crossover $[\text{Fe}(\text{NH}_2\text{-trz})_3](\text{Br})_2 \cdot 3\text{H}_2\text{O}$ compound at room temperature,” *Phys. Chem. Chem. Phys.*, vol. 12, no. 12, pp. 3044–3052, Mar. 2010.
- [16] “Control of Iron(II) Spin States in 2,2':6',2''- Terpyridine Complexes through Ligand Substitution - Constable - 1999 - Chemistry – A European Journal - Wiley Online Library.” .
- [17] D. Antonangeli *et al.*, “Spin crossover in ferropenicillinase at high pressure: A seismologically transparent transition?,” *Science (80-.)*, vol. 331, no. 6013, pp. 64–67, Jan. 2011.
- [18] “Introduction to Crystal Field Theory - Chemistry LibreTexts.” .
- [19] C. K. Jørgensen, “Absorption spectra of transition group complexes of sulphur-containing ligands,” *J. Inorg. Nucl. Chem.*, vol. 24, no. 12, pp. 1571–1585, Dec. 1962.
- [20] “Les orbitales moléculaires dans les complexes: cours et exercices corrigés - Yves Jean - Google Books.” .
- [21] “Multiplets of Transition-Metal Ions in Crystals - Satoru Sugano - Google Books.” .
- [22] “10.8: Molecular Orbital Theory- Electron Delocalization - Chemistry LibreTexts.” .
- [23] J. A. Cruddas, “Emergent phenomena in spin crossover systems,” The University of Queensland, 2021.
- [24] “Miessler, Fischer & Tarr, Inorganic Chemistry, 5th Edition | Pearson.” .
- [25] I. B. Bersuker, *The Jahn–Teller Effect*, vol. 9780521822. Cambridge University Press, 2006.
- [26] “Ligand Field Theory Fundamentals - Chemistry LibreTexts.” .
- [27] “Spin Crossover in Transition Metal Compounds III | Philipp Gütlich | Springer.” .
- [28] W. Nicolazzi and A. Bousseksou, “Thermodynamical aspects of the spin crossover phenomenon,” *Comptes Rendus Chimie*, vol. 21, no. 12. Elsevier Masson SAS, pp. 1060–1074, Dec-2018.
- [29] M. Bergmann and L. Zervas, “Synthesen mit Glucosamin,” *Berichte der Dtsch. Chem. Gesellschaft (A B Ser.)*, vol. 64, no. 5, pp. 975–980, May 1931.
- [30] E. König, “Nature and dynamics of the spin-state interconversion in metal complexes,” Springer, Berlin, Heidelberg, 1991, pp. 51–152.
- [31] E. König, H. C. Ørsted, and K. Madeja, “S = 1 Ground State in Six-Coordinated Iron(II),” *J. Am. Chem. Soc.*, vol. 88, no. 19, pp. 4528–4529, 1966.
- [32] E. König and K. Madeja, “Unusual Magnetic Behaviour of Some Iron(II)-Bis-(1 10-phenanthroline) Complexes,” 1966.
- [33] K. Heinze, G. Huttner, L. Zsolnai, and P. Schober, “Complexes of Cobalt(II) Chloride with the Tripodal Trisphosphane triphos: Solution Dynamics, Spin-Crossover, Reactivity, and Redox Activity,” *Inorg. Chem.*, vol. 36, no. 24, pp. 5457–5469, 1997.
- [34] J. Faus, M. Julve, F. Lloret, J. A. Real, and J. Sletten, “Dimethylviolatobis(phenanthroline)cobalt(II), a Novel Spin-Crossover Octahedral Co(II) Complex. Synthesis, Crystal Structure and Magnetic Properties of $[\text{Co}(\text{dmvi})(\text{phen})_2]\text{ClO}_4 \cdot 3\text{H}_2\text{O}$,” *Inorg. Chem.*, vol. 33, no. 24, pp. 5535–5540, Nov. 1994.
- [35] H. -J Krokoszinski, C. Santandrea, E. Gmelin, and K. Bärner, “Specific Heat Anomaly Connected with a High-Spin–Low-Spin Transition in Metallic $\text{MnAs}_{1-x}\text{Px}$ Crystals,” *Phys. status solidi*, vol. 113, no. 1, pp. 185–195, Sep. 1982.
- [36] Y. Garcia, O. Kahn, J. P. Ader, A. Buzdin, Y. Meurdesoif, and M. Guillot, “The effect of a magnetic field on the inversion temperature of a spin crossover compound revisited,” *Phys. Lett. Sect. A Gen. At. Solid State Phys.*, vol. 271, no. 1–2, pp. 145–154, Jun. 2000.
- [37] P. G. Sim and E. Sinn, “First Manganese(III) Spin Crossover and First d4 Crossover. Comment on Cytochrome Oxidase,” *J. Am. Chem. Soc.*, vol. 103, no. 1, pp. 241–243, 1981.
- [38] J. Zarembowitch and O. Kahn, “Magnetic properties of some spin-crossover, high-spin, and low-spin cobalt(II) complexes with Schiff bases derived from 3-formylsalicylic acid,” *Inorg. Chem.*, vol. 23, no. 5, pp. 589–593, 1984.
- [39] R. Boča, L. Dlháň, W. Linert, H. Ehrenberg, H. Fuess, and W. Haase, “Ligand sphere-enhanced magnetic anisotropy in cobalt(II) and manganese(II) 2,6-bis-(benzimidazol-2'-yl)-pyridine dichloride,” *Chem. Phys. Lett.*, vol. 307, no. 5–6, pp. 359–366, Jul. 1999.

- [40] M. Sorai, Y. Yumoto, H. Dost M., and L. F. Larkworthy, "Calorimetric study on the spin-crossover phenomenon between 3T₁ and 5E in trans-bis[1,2-bis(diethylphosphino) ethane]diodochromium(II), [CrI₂(depe)₂]," *J. Phys. Chem. Solids*, vol. 54, no. 4, pp. 421–430, Apr. 1993.
- [41] D. M. Halepoto, D. G. L. Holt, L. F. Larkworthy, D. C. Povey, G. W. Smith, and G. J. Leigh, "Spin crossover in chromium(II) complexes," *Polyhedron*, vol. 8, no. 13–14, pp. 1821–1822, Jan. 1989.
- [42] D. M. Halepoto, D. G. L. Holt, L. F. Larkworthy, G. J. Leigh, D. C. Povey, and G. W. Smith, "Spin crossover in chromium(II) complexes and the crystal and molecular structure of the high spin form of bis[1,2-bis(diethylphosphino)ethane]diiodochromium(II)," *J. Chem. Soc. Chem. Commun.*, no. 18, pp. 1322–1323, Jan. 1989.
- [43] A. Hauser, "Ligand Field Theoretical Considerations," in *Adv Polym Sci*, vol. 233, Springer, Berlin, Heidelberg, 2012, pp. 49–58.
- [44] W. Kläui, W. Eberspach, and P. Gülich, "Spin-Crossover Cobalt(III) Complexes: Steric and Electronic Control of Spin State," *Inorg. Chem.*, vol. 26, no. 24, pp. 3977–3982, Dec. 1987.
- [45] S. Benmansour, C. Atmani, F. Setifi, S. Triki, M. Marchivie, and C. J. Gómez-García, "Polynitrile anions as ligands: From magnetic polymeric architectures to spin crossover materials," *Coordination Chemistry Reviews*, vol. 254, no. 13–14, Elsevier, pp. 1468–1478, Jul-2010.
- [46] I. G. R. Ossj, "Anomalous behaviour at the 6 A₁ - 2 T₂ crossover in iron (III) complexes," *Proc. R. Soc. London. Ser. A. Math. Phys. Sci.*, vol. 280, no. 1381, pp. 235–257, Jul. 1964.
- [47] H. Paulsen and A. X. Trautwein, "Density Functional Theory Calculations for Spin Crossover Complexes," in *Spin Crossover in Transition Metal Compounds III*, vol. 235, Springer-Verlag, 2006, pp. 197–219.
- [48] and H. C. O. Kahn, R. Claude, "No Title," *Nouv. J. Chim. J. Chem.*, vol. 167, no. 4, 1980.
- [49] C. J. Humphreys, "Physical chemistry: Electrons seen in orbit," *Nature*, vol. 401, no. 6748, Nature Publishing Group, pp. 21–22, Sep-1999.
- [50] A. Hauser, "Ligand Field Theoretical Considerations," Springer, 2012, pp. 49–58.
- [51] A. Bousseksou *et al.*, "Raman spectroscopy of the high- and low-spin states of the spin crossover complex Fe(phen)₂(NCS)₂: An initial approach to estimation of vibrational contributions to the associated entropy change Dedication to Professor Olivier Kahn, we are very sad that yo," *Chem. Phys. Lett.*, vol. 318, no. 4–5, pp. 409–416, Feb. 2000.
- [52] N. Moliner *et al.*, "Mass effect on the equienergetic high-spin/low-spin states of spin-crossover in 4,4'-bipyridine-bridged iron(II) polymeric compounds: Synthesis, structure, and magnetic, Mössbauer, and theoretical studies," *Inorg. Chem.*, vol. 41, no. 26, pp. 6997–7005, Dec. 2002.
- [53] A. Bousseksou, L. Salmon, F. Varret, and J. P. Tuchagues, "The second example of spin conversion governed by molecular vibrations: A novel ferrous complex resulting from hexacoordination of a Schiff base with an N₄O₂ donor set," *Chem. Phys. Lett.*, vol. 282, no. 2, pp. 209–214, Jan. 1998.
- [54] A. Bousseksou, M. Vereist, H. Constant-Machado, G. Lemerrier, J. P. Tuchagues, and F. Varret, "[FeII(TRIM)₂]F₂, the First Example of Spin Conversion Monitored by Molecular Vibrations," *Inorg. Chem.*, vol. 35, no. 1, pp. 110–115, 1996.
- [55] A. Bousseksou, H. Constant-Machado, and F. Varret, "A Simple Ising-Like Model for Spin Conversion Including Molecular Vibrations," *J. Phys. I*, vol. 5, no. 6, pp. 747–760, Jun. 1995.
- [56] "Multiplets of Transition-Metal Ions in Crystals - 1st Edition."
- [57] L. F. Lindoy and S. E. Livingstone, "Complexes of iron(II), cobalt(II) and nickel(II) with α-diimines and related bidentate ligands," *Coord. Chem. Rev.*, vol. 2, no. 2, pp. 173–193, Sep. 1967.
- [58] G. Brehm, M. Reiher, and S. Schneider, "Estimation of the vibrational contribution to the entropy change associated with the low- to high-spin transition in Fe(phen)₂(NCS)₂ complexes: Results obtained by IR and Raman spectroscopy and DFT calculations," *J. Phys. Chem. A*, vol. 106, no. 50, pp. 12024–12034, Dec. 2002.
- [59] M. Sorai and S. Seki, "Phonon coupled cooperative low-spin 1A₁ high-spin 5T₂ transition in [Fe(phen)₂(NCS)₂] and [Fe(phen)₂(NCSe)₂] crystals," *J. Phys. Chem. Solids*, vol. 35, no. 4, pp. 555–570, Jan. 1974.
- [60] P. Gülich, A. Hauser, and H. Spiering, "Thermal and Optical Switching of Iron(II) Complexes," *Angewandte Chemie International Edition in English*, vol. 33, no. 20, pp. 2024–2054, 02-Nov-1994.
- [61] S. K. Kulshreshtha, R. M. Iyer, E. König, and G. Ritter, "The nature of spin-state transitions in Fe(II)

- complexes," *Chem. Phys. Lett.*, vol. 110, no. 2, pp. 201–204, Sep. 1984.
- [62] S. K. Kulshreshtha and R. M. Iyer, "Nature of the high-spin ($5T_2$) α low-spin ($1A_1$) transition in $[\text{Fe}(\text{bipy})_2(\text{NCS})_2]$," *Chem. Phys. Lett.*, vol. 108, no. 5, pp. 501–504, Jul. 1984.
- [63] N. Moliner *et al.*, "Thermal and optical switching of molecular spin states in the $\{[\text{FeL}(\text{H}_2\text{B}(\text{pz})_2)_2]\}$ spin-crossover system (L = bpy, phen)," *J. Phys. Chem. B*, vol. 106, no. 16, pp. 4276–4283, Apr. 2002.
- [64] G. Molnár *et al.*, "Vibrational spectroscopy of cyanide-bridged, iron(II) spin-crossover coordination polymers: Estimation of vibrational contributions to the entropy change associated with the spin transition," *J. Phys. Chem. B*, vol. 106, no. 38, pp. 9701–9707, Sep. 2002.
- [65] J. Pavlik and R. Boča, "Established static models of spin crossover," *European Journal of Inorganic Chemistry*, vol. 2013, no. 5–6. John Wiley & Sons, Ltd, pp. 697–709, Feb-2013.
- [66] R. Boča and W. Linert, "Is There a Need for New Models of the Spin Crossover?," *Monatshefte für Chemie*, vol. 134, no. 2. Springer, pp. 199–216, Feb-2003.
- [67] T. Nakamoto, Z. C. Tan, and M. Sorai, "Heat capacity of the spin crossover complex $[\text{Fe}(\text{2-pic})_3]\text{Cl}_2 \cdot \text{MeOH}$: A spin crossover phenomenon with weak cooperativity in the solid state," *Inorg. Chem.*, vol. 40, no. 15, pp. 3805–3809, Jul. 2001.
- [68] C. Enachescu, H. Constant-Machado, E. Codjovi, J. Linares, K. Boukheddaden, and F. Varret, "Direct access to the photo-excitation and relaxation terms in photo-switchable solids: Non-linear aspects," *J. Phys. Chem. Solids*, vol. 62, no. 8, pp. 1409–1422, Aug. 2001.
- [69] F. Varret, M. Nogues, and A. Goujon, "Photomagnetic Properties of Some Inorganic Solids," in *Magnetism: Molecules to Materials I*, Wiley-VCH Verlag GmbH & Co. KGaA, 2003, pp. 257–295.
- [70] E. Collet and P. Guionneau, "Structural analysis of spin-crossover materials: From molecules to materials," *Comptes Rendus Chimie*, vol. 21, no. 12. Elsevier Masson SAS, pp. 1133–1151, Dec-2018.
- [71] H. Spiering, "Spin Crossover Transit. Met. Compd. III," *Springer-Verlag*, vol. 235, pp. 171–195.
- [72] M. A. Halcrow, *Spin-Crossover Materials: Properties and Applications*. John Wiley and Sons, 2013.
- [73] A. Hauser, "Cooperative effects on the HS \rightarrow LS relaxation in the $[\text{Fe}(\text{ptz})_6](\text{BF}_4)_2$ spin-crossover system," *Chem. Phys. Lett.*, vol. 192, no. 1, pp. 65–70, Apr. 1992.
- [74] M. Kepenekian, B. Le Guennic, and V. Robert, "Primary role of the electrostatic contributions in a rational growth of hysteresis loop in spin-crossover Fe(II) complexes," *J. Am. Chem. Soc.*, vol. 131, no. 32, pp. 11498–11502, Aug. 2009.
- [75] A. D. Naik, B. Tinant, K. Muffler, J. A. Wolny, V. Schünemann, and Y. Garcia, "Relevance of supramolecular interactions, texture and lattice occupancy in the designer iron(II) spin crossover complexes," *J. Solid State Chem.*, vol. 182, no. 6, pp. 1365–1376, Jun. 2009.
- [76] J. A. Real, A. B. Gaspar, and M. Carmen Muñoz, "Thermal, pressure and light switchable spin-crossover materials," *Dalton Transactions*, no. 12. The Royal Society of Chemistry, pp. 2062–2079, Jun-2005.
- [77] M. Cavallini *et al.*, "Thin Deposits and Patterning of Room-Temperature-Switchable One-Dimensional Spin-Crossover Compounds," vol. 27, pp. 4076–4081, 2011.
- [78] P. Gütllich, H. Köppen, and H. G. Steinhäuser, "Deuterium isotope effect on the high-spin α low-spin transition in deuterated solvates of tris(2-picolylamine) iron(II) chloride," *Chem. Phys. Lett.*, vol. 74, no. 3, pp. 475–480, Sep. 1980.
- [79] M. J. Murphy, K. A. Zenere, F. Ragon, P. D. Southon, C. J. Kepert, and S. M. Neville, "Guest programmable multistep spin crossover in a porous 2-D Hofmann-type material," *J. Am. Chem. Soc.*, vol. 139, no. 3, pp. 1330–1335, Jan. 2017.
- [80] W. Phonsri *et al.*, "Solvent modified spin crossover in an iron(III) complex: Phase changes and an exceptionally wide hysteresis," *Chem. Sci.*, vol. 8, no. 5, pp. 3949–3959, May 2017.
- [81] H. Hagiwara, R. Minoura, T. Udagawa, K. Mibu, and J. Okabayashi, "Alternative Route Triggering Multistep Spin Crossover with Hysteresis in an Iron(II) Family Mediated by Flexible Anion Ordering," *Inorg. Chem.*, vol. 59, no. 14, pp. 9866–9880, Jul. 2020.
- [82] P. Gütllich, Y. Garcia, and H. A. Goodwin, "Spin crossover phenomena in Fe(II) complexes," *Chem. Soc. Rev.*, vol. 29, no. 6, pp. 419–427, Jan. 2000.

- [83] E. Collet and P. Guionneau, "Structural analysis of spin-crossover materials: From molecules to materials," *Comptes Rendus Chimie*, vol. 21, no. 12. Elsevier Masson SAS, pp. 1133–1151, 01-Dec-2018.
- [84] N. Ortega-Villar, M. Muñoz, and J. Real, "Symmetry Breaking in Iron(II) Spin-Crossover Molecular Crystals," *Magnetochemistry*, vol. 2, no. 1, p. 16, Mar. 2016.
- [85] Z. P. Ni *et al.*, "Recent advances in guest effects on spin-crossover behavior in Hofmann-type metal-organic frameworks," *Coordination Chemistry Reviews*, vol. 335. Elsevier B.V., pp. 28–43, 15-Mar-2017.
- [86] "Spin Crossover in Transition Metal Compounds III | Philipp Güttlich | Springer." [Online]. Available: <https://www.springer.com/gp/book/9783540403951>. [Accessed: 11-Jun-2021].
- [87] J. Tao, R. J. Wei, R. Bin Huang, and L. S. Zheng, "Polymorphism in spin-crossover systems," *Chem. Soc. Rev.*, vol. 41, no. 2, pp. 703–737, Jan. 2012.
- [88] C. Desroches *et al.*, "Tetra- and decanuclear iron(II) complexes of thiacalixarene macrocycles: Synthesis, structure, Mössbauer spectroscopy and magnetic properties," *Eur. J. Inorg. Chem.*, vol. 2006, no. 2, pp. 357–365, Jan. 2006.
- [89] J. Cruddas and B. J. Powell, "Structure-property relationships and the mechanisms of multistep transitions in spin crossover materials and frameworks," *Inorg. Chem. Front.*, vol. 7, no. 22, pp. 4424–4437, Nov. 2020.
- [90] N. Paradis, G. Chastanet, and J. F. Létard, "When stable and metastable HS states meet in spin-crossover compounds," *Eur. J. Inorg. Chem.*, vol. 2012, no. 22, pp. 3618–3624, Aug. 2012.
- [91] M. P. Shores, C. M. Klug, and S. R. Fiedler, "Spin-State Switching in Solution," in *Spin-Crossover Materials: Properties and Applications*, John Wiley and Sons, 2013, pp. 281–301.
- [92] N. Sariciftci, U. Lemmer, D. Vacar, and A. Heeger, "Dynamic Orientation of Conjugated Oligomers in Nematic Liquid Crystalline Matrices," *Synth. Met.*, vol. 84, no. 1, pp. 609–610, 1997.
- [93] F. Renz, M. Hasegawa, T. Hoshi, U. El-Ayaan, W. Linert, and Y. Fukuda, "Anisotropic effect after stretching of the spin-crossover compound [Fe(II)(2,6-bis-(benzimidazol-2'-yl)pyridine)₂] (ClO₄)₂ in polyvinylalcohol polymer matrix," *Mol. Cryst. Liq. Cryst. Sci. Technol. Sect. A Mol. Cryst. Liq. Cryst.*, vol. 335, pp. 1243–1252, 1999.
- [94] C. Enachescu, M. Nishino, and S. Miyashita, "Theoretical Descriptions of Spin-Transitions in Bulk Lattices," in *Spin-Crossover Materials: Properties and Applications*, John Wiley and Sons, 2013, pp. 455–474.
- [95] S. Ramasesha, T. V. Ramakrishnan, and C. N. R. Rao, "Models for spin-state transitions in solids," *J. Phys. C Solid State Phys.*, vol. 12, no. 7, pp. 1307–1317, Apr. 1979.
- [96] S. J. Plimpton and J. D. Gale, "Developing community codes for materials modeling," *Current Opinion in Solid State and Materials Science*, vol. 17, no. 6. Elsevier Ltd, pp. 271–276, 01-Dec-2013.
- [97] D. P. Landau and K. Binder, "A Guide to Monte Carlo Simulations in Statistical Physics," 2014.
- [98] J. Pavlik and R. Boča, "Established static models of spin crossover," *European Journal of Inorganic Chemistry*, vol. 2013, no. 5–6. John Wiley & Sons, Ltd, pp. 697–709, 18-Feb-2013.
- [99] M. Sorai and S. Seki, "Phonon coupled cooperative low-spin 1A₁high-spin 5T₂ transition in [Fe(phen)₂(NCS)₂] and [Fe(phen)₂(NCSe)₂] crystals," *J. Phys. Chem. Solids*, vol. 35, no. 4, pp. 555–570, Jan. 1974.
- [100] K. Boukheddaden, "Static and dynamical aspects of a phonon-induced spin-crossover transition - Local equilibrium approach," *Eur. J. Inorg. Chem.*, vol. 2013, no. 5–6, pp. 865–874, Feb. 2013.
- [101] R. A. Bari and J. Sivardière, "Low-spin-high-spin transitions in transition-metal-ion compounds," *Phys. Rev. B*, vol. 5, no. 11, pp. 4466–4471, Jun. 1972.
- [102] R. Zimmermann and E. König, "A model for high-spin/low-spin transitions in solids including the effect of lattice vibrations," *J. Phys. Chem. Solids*, vol. 38, no. 7, pp. 779–788, Jan. 1977.
- [103] J. Wajñflasz, "Etude de la transition „Low Spin”-„High Spin” dans les complexes octaédriques d'ion de transition," *Phys. status solidi*, vol. 40, no. 2, pp. 537–545, Jan. 1970.
- [104] A. M. Apetrei, K. Boukheddaden, and A. Stancu, "Dynamic phase transitions in the one-dimensional spin-phonon coupling model," *Phys. Rev. B - Condens. Matter Mater. Phys.*, vol. 87, no. 1, p. 014302, Jan. 2013.
- [105] J. A. Nasser, L. Chassigne, S. Topçu, J. Linares, and Y. Alayli, "Study of the atom-phonon coupling model for (SC) partition function: First order phase transition for an infinite linear chain," *Eur. Phys. J. B*, vol. 87, no. 3, p. 69, Mar. 2014.

- [106] J. A. Nasser *et al.*, "Two-dimensional atom-phonon coupling model for spin conversion: Role of metastable states," *Eur. Phys. J. B*, vol. 83, no. 2, pp. 115–132, Sep. 2011.
- [107] J. A. Nasser, "First order high-spin/low-spin phase transition induced by acoustic-phonons," *Eur. Phys. J. B*, vol. 21, no. 1, pp. 3–10, May 2001.
- [108] J. Linares, H. Spiering, and F. Varret, "Analytical solution of 1D Ising-like systems modified by weak long range interaction Application to spin crossover compounds," *Eur. Phys. J. B*, vol. 10, no. 2, pp. 271–275, Jul. 1999.
- [109] A. Bousseksou, J. Nasser, J. Linares, K. Boukheddaden, and F. Varret, "Two-Level models for the two-step spin crossovers," *Mol. Cryst. Liq. Cryst. Sci. Technol. Sect. A. Mol. Cryst. Liq. Cryst.*, vol. 234, no. 1, pp. 269–274, 1993.
- [110] A. Bousseksou, J. Nasser, J. Linares, K. Boukheddaden, and F. Varret, "Ising-like model for the two-step spin-crossover," *J. Phys. I*, vol. 2, no. 7, pp. 1381–1403, Jul. 1992.
- [111] T. Kambara, "Theory of high-spin \rightleftharpoons low-spin transitions in transition metal compounds induced by the Jahn-Teller effect," *J. Chem. Phys.*, vol. 70, no. 9, pp. 4199–4206, Jul. 1979.
- [112] R. Zimmermann, "A model for high-spin/low-spin transitions with an interpretation of thermal hysteresis effects," *J. Phys. Chem. Solids*, vol. 44, no. 2, pp. 151–158, Jan. 1983.
- [113] P. Gütlich, H. Köppen, R. Link, and H. G. Steinhäuser, "Interpretation of high spin \rightleftharpoons low spin transition in iron (II) complexes. I. A phenomenological thermodynamic model," *J. Chem. Phys.*, vol. 70, no. 8, pp. 3977–3983, Jul. 1979.
- [114] H. Spiering and N. Willenbacher, "Elastic interaction of high-spin and low-spin complex molecules in spin-crossover compounds. II," *J. Phys. Condens. Matter*, vol. 1, no. 50, pp. 10089–10105, Dec. 1989.
- [115] N. Willenbacher and S. Spiering, "The elastic interaction of high-spin and low-spin complex molecules in spin-crossover compounds," *J. Phys. C Solid State Phys.*, vol. 21, no. 8, pp. 1423–1439, Mar. 1988.
- [116] H. Spiering, E. Meissner, H. Köppen, E. W. Müller, and P. Gütlich, "The effect of the lattice expansion on high spin \rightleftharpoons low spin transitions," *Chem. Phys.*, vol. 68, no. 1–2, pp. 65–71, Jun. 1982.
- [117] S. Ohnishi and S. Sugano, "Strain interaction effects on the high-spin-low-spin transition of transition-metal compounds," *J. Phys. C Solid State Phys.*, vol. 14, no. 1, pp. 39–55, Jan. 1981.
- [118] M. Sorai and S. Seki, "Magnetic Heat Capacity Due to Cooperative Low-Spin $1A_1 \rightleftharpoons$ High-Spin $5T_2$ Transition in $\text{Fe}(\text{phen})_2(\text{NCS})_2$ Crystal," *J. Phys. Soc. Japan*, vol. 33, no. 2, p. 575, Dec. 1972.
- [119] C. P. Slichter and H. G. Drickamer, "Pressure-induced electronic changes in compounds of iron," *J. Chem. Phys.*, vol. 56, no. 5, pp. 2142–2160, Sep. 1972.
- [120] T. Kambara, "The Effect of Iron Concentration on the High-Spin \rightleftharpoons Low-Spin Transitions in Iron Compounds," *J. Phys. Soc. Japan*, vol. 49, no. 5, pp. 1806–1811, Nov. 1980.
- [121] T. Kambara, "Theory of pressure-induced high-spin \rightleftharpoons low-spin transition in compounds of iron," *J. Phys. Soc. Japan*, vol. 50, no. 7, pp. 2257–2264, Nov. 1981.
- [122] K. F. Purcell and M. P. Edwards, "Cooperativity in Thermally Induced Intersystem Crossing in Solids: $\text{Fe}(\text{phen})_2(\text{NCR})_2$, R = BH_3 , BPh_3 , S, Se," *Inorg. Chem.*, vol. 23, no. 17, pp. 2620–2625, 1984.
- [124] A. Bousseksou, H. Constant-Machado, and F. Varret, "A Simple Ising-Like Model for Spin Conversion Including Molecular Vibrations," *J. Phys. I*, vol. 5, no. 6, pp. 747–760, Jun. 1995.
- [125] E. König, H. C. Ørsted, and K. Madeja, "S = 1 Ground State in Six-Coordinated Iron(II)," *J. Am. Chem. Soc.*, vol. 88, no. 19, pp. 4528–4529, 1966.
- [126] E. König and K. Madeja, "Unusual magnetic behaviour of some iron(II)-bis-(1,10-phenanthroline) complexes," *Chem. Commun.*, no. 3, pp. 61–62, Jan. 1966.
- [127] A. Stancu, L. Stoleriu, P. Postolache, and R. Tanasa, "New Preisach model for structured particulate ferromagnetic media," in *Journal of Magnetism and Magnetic Materials*, 2005, vol. 290-291 PART 1, pp. 490–493.
- [128] A. Stancu, B. Negulescu, R. Tanasa, and L. Stoleriu, "Preisach model for systems with asymmetric First order reversal curve (FORC) distribution," OAM-RC, Mar. 2010.
- [129] H. Constant-Machado, A. Stancu, J. Linares, and F. Varret, "Thermal hysteresis loops in spin-crossover compounds analyzed in terms of classical preisach model," *IEEE Trans. Magn.*, vol. 34, no. 4 PART 2, pp.

2213–2219, 1998.

- [130] M. Nishino, K. Boukheddaden, Y. Konishi, and S. Miyashita, “Simple two-dimensional model for the elastic origin of cooperativity among spin states of spin-crossover complexes,” *Phys. Rev. Lett.*, vol. 98, no. 24, p. 247203, Jun. 2007.
- [131] C. Enachescu, L. Stoleriu, A. Stancu, and A. Hauser, “Model for elastic relaxation phenomena in finite 2D hexagonal molecular lattices,” *Phys. Rev. Lett.*, vol. 102, no. 25, p. 257204, Jun. 2009.
- [132] L. Stoleriu, C. Enachescu, A. Stancu, and A. Hauser, “Elastic model for complex hysteretic processes in molecular magnets,” in *IEEE Transactions on Magnetism*, 2008, vol. 44, no. 11 PART 2, pp. 3052–3055.
- [133] J. A. Nasser, “Diluted spin conversion compounds behaviours in the atom-phonon coupling model: Case of not too large dilution : Rrd-Jones potential?,” *Eur. Phys. J. B*, vol. 48, no. 1, pp. 19–27, Nov. 2005.
- [134] A. Gindulescu, A. Rotaru, J. Linares, M. Dimian, and J. Nasser, “Excited metastables electronic spin states in spin crossover compounds studies by atom-phonon coupling model: Gradual and two-step transition cases,” *J. Appl. Phys.*, vol. 107, no. 9, p. 23, May 2010.
- [135] A. Rotaru, A. Carmona, F. Combaud, J. Linares, A. Stancu, and J. Nasser, “Monte Carlo simulations for 1- and 2D spin crossover compounds using the atom-phonon coupling model,” *Polyhedron*, vol. 28, no. 9–10, pp. 1684–1687, Jun. 2009.
- [136] A. Rotaru, J. Linares, E. Codjovi, J. Nasser, and A. Stancu, “Size and pressure effects in the atom-phonon coupling model for spin crossover compounds,” *J. Appl. Phys.*, vol. 103, no. 7, p. 07B908, Feb. 2008.
- [137] A. Rotaru, J. Linares, S. Mordelet, A. Stancu, and J. Nasser, “Re-entrance phase and excited metastable electronic spin states in one-dimensional spin crossover compounds explained by atom-phonon coupling model,” *J. Appl. Phys.*, vol. 106, no. 4, p. 043507, Aug. 2009.
- [138] M. P. Espejo, A. Gndulescu, J. Linares, J. Nasser, and M. Dimian, “Phase diagram of two-dimensional spin crossover systems using the atom-phonon coupling model,” in *Journal of Applied Physics*, 2011, vol. 109, no. 7, p. 07B102.
- [139] A. Gindulescu, A. Rotaru, J. Linares, M. Dimian, and J. Nasser, “Metastable states at low temperature in spin crossover compounds in the framework of the atom-phonon coupling model,” in *Polyhedron*, 2011, vol. 30, no. 18, pp. 3186–3188.
- [140] W. Lenz, “Beitrag zum Verständnis der magnetischen Erscheinungen in festen Körpern,” *Z. Phys.*, vol. 21, pp. 613–615, 1920.
- [141] S. G. Brush, “History of the Lenz-Ising model,” *Rev. Mod. Phys.*, vol. 39, no. 4, pp. 883–893, Oct. 1967.
- [142] E. Ising, “Beitrag zur Theorie des Ferromagnetismus,” *Zeitschrift für Phys.*, vol. 31, no. 1, pp. 253–258, Feb. 1925.
- [143] B. Kaufman and L. Onsager, “Crystal statistics. III. Short-range order in a binary ising lattice,” *Phys. Rev.*, vol. 76, no. 8, pp. 1244–1252, Oct. 1949.
- [144] B. Kaufman, “Crystal statistics. II. Partition function evaluated by spinor analysis,” *Phys. Rev.*, vol. 76, no. 8, pp. 1232–1243, Oct. 1949.
- [145] L. Onsager, “Crystal statistics. I. A two-dimensional model with an order-disorder transition,” *Phys. Rev.*, vol. 65, no. 3–4, pp. 117–149, Feb. 1944.
- [146] T. D. Lee and C. N. Yang, “Statistical theory of equations of state and phase transitions. II. Lattice gas and ising model,” *Phys. Rev.*, vol. 87, no. 3, pp. 410–419, Aug. 1952.
- [147] C. N. Yang and T. D. Lee, “Statistical theory of equations of state and phase transitions. I. Theory of condensation,” *Phys. Rev.*, vol. 87, no. 3, pp. 404–409, Aug. 1952.
- [148] P. Weiss, “No Title,” *J. Phys. Radium*, vol. 6, 1907.
- [149] H. A. B. Ethe, H. H. Wills, and W. L. Bragg, “Statistical theory of superlattices,” *Proc. R. Soc. London. Ser. A - Math. Phys. Sci.*, vol. 150, no. 871, pp. 552–575, Jul. 1935.
- [150] G. Rubin and A. Finel, “Calculation of phase diagrams of ternary systems with cluster-variation- method entropy,” *J. Phys. Condens. Matter*, vol. 5, no. 49, pp. 9105–9120, Dec. 1993.
- [151] R. Kikuchi, “Superposition approximation and natural iteration calculation in cluster-variation method,” *J. Chem. Phys.*, vol. 60, no. 3, pp. 1071–1080, Aug. 1974.

- [152] J. Wajnflasz and R. Pick, "TRANSITIONS « LOW SPIN »-« HIGH SPIN » DANS LES COMPLEXES DE Fe²⁺," *Le J. Phys. Colloq.*, vol. 32, no. C1, pp. C1-91-C1-92, Feb. 1971.
- [153] J. Wajnflasz, "Etude de la transition „Low Spin”-„High Spin” dans les complexes octaédriques d'ion de transition," *Phys. status solidi*, vol. 40, no. 2, pp. 537–545, Jan. 1970.
- [154] K. Boukheddaden, I. Shteto, B. Hôo, and F. Varret, "Dynamical model for spin-crossover solids. I. Relaxation effects in the mean-field approach," *Phys. Rev. B - Condens. Matter Mater. Phys.*, vol. 62, no. 22, pp. 14796–14805, Dec. 2000.
- [155] S. Pillet, V. Legrand, M. Souhassou, and C. Lecomte, "Kinetics of light-induced first-order phase transformation in molecular solids: Fe(btr)₂(NCS)₂·2H₂O," *Phys. Rev. B - Condens. Matter Mater. Phys.*, vol. 74, no. 14, p. 140101, Oct. 2006.
- [156] K. Ichiyanagi *et al.*, "Nature and mechanism of the photoinduced spin transition in [Fe(PM-BiA)₂(NCS)₂]," *Phys. Rev. B - Condens. Matter Mater. Phys.*, vol. 73, no. 6, p. 060408, Feb. 2006.
- [157] N. Huby *et al.*, "Photoinduced spin transition probed by x-ray diffraction," *Phys. Rev. B - Condens. Matter Mater. Phys.*, vol. 69, no. 2, p. 020101, Jan. 2004.
- [158] A. TISSOT, "No Title," *ICMM, Vol. Ph.D, Univ. Paris-Sud 11, Orsay*, 2011.
- [159] M. Nishino, S. Miyashita, and K. Boukheddaden, "Effective interaction range in the spin crossover phenomenon: Wajnflasz and domain models," *J. Chem. Phys.*, vol. 118, no. 10, pp. 4594–4597, Mar. 2003.
- [160] M. Wortis, "Griffiths singularities in the randomly dilute one-dimensional Ising model," *Phys. Rev. B*, vol. 10, no. 11, pp. 4665–4671, Dec. 1974.
- [161] "The Two-Dimensional Ising Model — Barry McCoy, Tai Tsun Wu | Harvard University Press." [Online]. Available: <https://www.hup.harvard.edu/catalog.php?isbn=9780674180758>. [Accessed: 12-Jun-2021].
- [162] J. F. Nagle, "Ising chain with competing interactions," *Phys. Rev. A*, vol. 2, no. 5, pp. 2124–2128, Nov. 1970.
- [163] J. S. Marsh, "Ising-chain statistics," *Phys. Rev.*, vol. 145, no. 1, pp. 251–254, May 1966.
- [164] X. Wu, N. Izmailian, and W. Guo, "Shape-dependent finite-size effect of the critical two-dimensional Ising model on a triangular lattice," *Phys. Rev. E - Stat. Nonlinear, Soft Matter Phys.*, vol. 87, no. 2, p. 022124, Feb. 2013.
- [165] T. Papakonstantinou and A. Malakis, "Critical behavior of the three-dimensional Ising model with anisotropic bond randomness at the ferromagnetic-paramagnetic transition line," *Phys. Rev. E - Stat. Nonlinear, Soft Matter Phys.*, vol. 87, no. 1, p. 012132, Jan. 2013.
- [166] D. Chiruta, J. Linares, M. Dimian, Y. Alayli, and Y. Garcia, "Role of edge atoms in the hysteretic behaviour of 3D spin crossover nanoparticles revealed by an Ising-like model," *Eur. J. Inorg. Chem.*, vol. 2013, no. 29, pp. 5086–5093, Oct. 2013.
- [167] D. Chiruta, J. Linares, Y. Garcia, P. R. Dahoo, and M. Dimian, "Analysis of the hysteretic behaviour of 3D spin crossover compounds by using an ising-like model," *Eur. J. Inorg. Chem.*, vol. 2013, no. 21, pp. 3601–3608, Jul. 2013.
- [168] D. Chiruta, C. M. Jureschi, J. Linares, Y. Garcia, and A. Rotaru, "Lattice architecture effect on the cooperativity of spin transition coordination polymers," *J. Appl. Phys.*, vol. 115, no. 5, p. 053523, Feb. 2014.
- [169] D. Chiruta, J. Linares, P. Richard Dahoo, and M. Dimian, "Influence of pressure and interactions strength on hysteretic behavior in two-dimensional polymeric spin crossover compounds," *Phys. B Condens. Matter*, vol. 435, no. 435, pp. 76–79, Feb. 2014.
- [170] D. Chiruta, J. Linares, P. R. Dahoo, and M. Dimian, "Analysis of long-range interaction effects on phase transitions in two-step spin-crossover chains by using Ising-type systems and Monte Carlo entropic sampling technique," *J. Appl. Phys.*, vol. 112, no. 7, p. 074906, Oct. 2012.
- [171] D. Chiruta, J. Linares, Y. Garcia, M. Dimian, and P. R. Dahoo, "Analysis of multi-step transitions in spin crossover nanochains," *Phys. B Condens. Matter*, vol. 434, no. 1, pp. 134–138, Feb. 2014.
- [172] K. Boukheddaden, "Monte carlo investigations on surface elastic energy of spin-crossover solids: Direct access to image pressure and the eshelby constant," *Phys. Rev. B - Condens. Matter Mater. Phys.*, vol. 88, no. 13, p. 134105, Oct. 2013.
- [173] M. Nishino, K. Boukheddaden, S. Miyashita, and F. Varret, "Arrhenius Monte Carlo study of two-step spin crossover: Equilibrium and relaxation paths," *Phys. Rev. B - Condens. Matter Mater. Phys.*, vol. 68, no. 22,

p. 224402, Dec. 2003.

- [174] J. Linares, J. Nasser, K. Boukheddaden, A. Bousseksou, and F. Varret, "Monte Carlo simulations of spin-crossover transitions using the two-level model. I: Mononuclear single sublattice case," *J. Magn. Magn. Mater.*, vol. 140–144, no. PART 3, pp. 1507–1508, Feb. 1995.
- [175] A. Atitoaie, R. Tanasa, and C. Enachescu, "Size dependent thermal hysteresis in spin crossover nanoparticles reflected within a Monte Carlo based Ising-like model," *J. Magn. Magn. Mater.*, vol. 324, no. 8, pp. 1596–1600, Apr. 2012.
- [176] I. Shteto, J. Linares, and F. Varret, "Monte Carlo entropic sampling for the study of metastable states and relaxation paths," *Phys. Rev. E - Stat. Physics, Plasmas, Fluids, Relat. Interdiscip. Top.*, vol. 56, no. 5, pp. 5128–5137, Nov. 1997.
- [177] J. Linares, C. Enachescu, K. Boukheddaden, and F. Varret, "Monte Carlo entropic sampling applied to spin crossover solids: The squareness of the thermal hysteresis loop," in *Polyhedron*, 2003, vol. 22, no. 14–17, pp. 2453–2456.
- [178] A. Slimani, F. Varret, K. Boukheddaden, D. Garrot, H. Oubouchou, and S. Kaizaki, "Velocity of the high-spin low-spin interface inside the thermal hysteresis loop of a spin-crossover crystal, via photothermal control of the interface motion," *Phys. Rev. Lett.*, vol. 110, no. 8, p. 087208, Feb. 2013.
- [179] A. Slimani, K. Boukheddaden, F. Varret, H. Oubouchou, M. Nishino, and S. Miyashita, "Microscopic spin-distortion model for switchable molecular solids: Spatiotemporal study of the deformation field and local stress at the thermal spin transition," *Phys. Rev. B - Condens. Matter Mater. Phys.*, vol. 87, no. 1, p. 014111, Jan. 2013.
- [180] Y. Konishi, H. Tokoro, M. Nishino, and S. Miyashita, "Monte Carlo simulation of pressure-induced phase transitions in spin-crossover materials," *Phys. Rev. Lett.*, vol. 100, no. 6, Feb. 2008.
- [181] K. Boukheddaden, S. Miyashita, and M. Nishino, "Elastic interaction among transition metals in one-dimensional spin-crossover solids," *Phys. Rev. B - Condens. Matter Mater. Phys.*, vol. 75, no. 9, p. 094112, Mar. 2007.
- [182] M. Nishino, K. Boukheddaden, and S. Miyashita, "Molecular dynamics study of thermal expansion and compression in spin-crossover solids using a microscopic model of elastic interactions," *Phys. Rev. B - Condens. Matter Mater. Phys.*, vol. 79, no. 1, p. 012409, Jan. 2009.
- [183] M. Nishino, C. Enachescu, S. Miyashita, K. Boukheddaden, and F. Varret, "Intrinsic effects of the boundary condition on switching processes in effective long-range interactions originating from local structural change," *Phys. Rev. B - Condens. Matter Mater. Phys.*, vol. 82, no. 2, p. 020409, Jul. 2010.
- [184] C. Enachescu, L. Stoleriu, A. Stancu, and A. Hauser, "Study of the relaxation in diluted spin crossover molecular magnets in the framework of the mechano-elastic model," in *Journal of Applied Physics*, 2011, vol. 109, no. 7, p. 07B111.
- [185] C. Enachescu, M. Nishino, S. Miyashita, L. Stoleriu, and A. Stancu, "Monte carlo metropolis study of cluster evolution in spin-crossover solids within the framework of a mechanoelastic model," *Phys. Rev. B - Condens. Matter Mater. Phys.*, vol. 86, no. 5, p. 054114, Aug. 2012.
- [186] P. Chakraborty, C. Enachescu, and A. Hauser, "Analysis of the Experimental Data for Pure and Diluted $[\text{Fe}_x\text{Zn}_{1-x}(\text{btr})_3](\text{ClO}_4)_2$ Spin-Crossover Solids in the Framework of a Mechanoelastic Model," 2013.
- [187] C. Enachescu, L. Stoleriu, A. Stancu, and A. Hauser, "Competition between photoexcitation and relaxation in spin-crossover complexes in the frame of a mechanoelastic model," *Phys. Rev. B - Condens. Matter Mater. Phys.*, vol. 82, no. 10, p. 104114, Sep. 2010.
- [188] C. Enachescu, M. Nishino, S. Miyashita, A. Hauser, A. Stancu, and L. Stoleriu, "Cluster evolution in spin crossover systems observed in the frame of a mechano-elastic model," *EPL*, vol. 91, no. 2, p. 27003, Jul. 2010.
- [189] M. Nishino, T. Nakada, C. Enachescu, K. Boukheddaden, and S. Miyashita, "Crossover of the roughness exponent for interface growth in systems with long-range interactions due to lattice distortion," *Phys. Rev. B - Condens. Matter Mater. Phys.*, vol. 88, no. 9, p. 094303, Sep. 2013.
- [190] H. Oubouchou, A. Slimani, and K. Boukheddaden, "Interplay between elastic interactions in a core-shell model for spin-crossover nanoparticles," *Phys. Rev. B - Condens. Matter Mater. Phys.*, vol. 87, no. 10, p. 104104, Mar. 2013.
- [191] Y. Komura and Y. Okabe, "CUDA programs for the GPU computing of the Swendsen-Wang multi-cluster spin flip algorithm: 2D and 3D Ising, Potts, and XY models," *Comput. Phys. Commun.*, vol. 185, no. 3, pp. 1038–1043, Mar. 2014.

- [192] "CUDA Fortran for Scientists and Engineers - 1st Edition." [Online]. Available: <https://www.elsevier.com/books/cuda-fortran-for-scientists-and-engineers/ruetsch/978-0-12-416970-8>. [Accessed: 12-Jun-2021].
- [194] "Markov Chains - Gibbs Fields, Monte Carlo Simulation, and Queues | Pierre Bremaud | Springer." [Online]. Available: <https://www.springer.com/gp/book/9780387985091>. [Accessed: 12-Jun-2021].
- [195] "Monte Carlo Calculations in Nuclear Medicine, Second Edition: Applications ... - Google Livres." [Online]. Available: https://books.google.fr/books?hl=fr&lr=&id=KDoeWJpbbOQC&oi=fnd&pg=PP1&ots=I846y7CyAV&sig=Ggw6UXTeD1HiqveZ_9CwzBZD8Kc#v=onepage&q&f=false. [Accessed: 12-Jun-2021].
- [196] A. Muraoka, K. Boukheddaden, J. Linares, and F. Varret, "Two-dimensional Ising-like model with specific edge effects for spin-crossover nanoparticles: A Monte Carlo study," *Phys. Rev. B - Condens. Matter Mater. Phys.*, vol. 84, no. 5, p. 054119, Aug. 2011.
- [197] N. Metropolis, A. W. Rosenbluth, M. N. Rosenbluth, A. H. Teller, and E. Teller, "Equation of state calculations by fast computing machines," *J. Chem. Phys.*, vol. 21, no. 6, pp. 1087–1092, Dec. 1953.
- [198] A. Dobrinescu, C. Enachescu, and A. Stancu, "Ising-like model study of size dependence relaxation in spin crossover complexes," *J. Magn. Magn. Mater.*, vol. 321, no. 24, pp. 4132–4138, Dec. 2009.
- [199] G. Maruccio, R. Cingolani, and R. Rinaldi, "Projecting the nanoworld: Concepts, results and perspectives of molecular electronics," *J. Mater. Chem.*, vol. 14, no. 4, pp. 542–554, Feb. 2004.
- [200] J.-F. Létard, P. Guionneau, and L. Goux-Capes, "Towards Spin Crossover Applications," in *Spin Crossover in Transition Metal Compounds III*, vol. 235, Springer-Verlag, 2006, pp. 221–249.
- [201] J. Linares, E. Codjovi, and Y. Garcia, "Pressure and temperature spin crossover sensors with optical detection," *Sensors*, vol. 12, no. 4, pp. 4479–4492, Apr. 2012.
- [202] E. C. Ellingsworth, B. Turner, and G. Szulczewski, "Thermal conversion of [Fe(phen)₃](SCN)₂ thin films into the spin crossover complex Fe(phen)₂(NCS)₂," *RSC Adv.*, vol. 3, no. 11, pp. 3745–3754, Mar. 2013.
- [203] S. E. Korshunov, "Finite-temperature phase transitions in the quantum fully frustrated transverse-field Ising models," *Phys. Rev. B - Condens. Matter Mater. Phys.*, vol. 86, no. 1, p. 014429, Jul. 2012.
- [204] T. Q. Hung *et al.*, "Room temperature magnetic detection of spin switching in nanosized spin-crossover materials," *Angew. Chemie - Int. Ed.*, vol. 52, no. 4, pp. 1185–1188, Jan. 2013.
- [205] L. Zhang *et al.*, "Abrupt spin transition around room temperature and light induced properties in FeII complexes with N₄O₂ coordination sphere," *Chem. Commun.*, vol. 46, no. 15, pp. 2554–2556, Apr. 2010.
- [206] A. Bouseksou, G. Molnár, and G. Matouzenko, "Switching of molecular spin states in inorganic complexes by temperature, pressure, magnetic field and light: Towards molecular devices," *European Journal of Inorganic Chemistry*, vol. 2004, no. 22. John Wiley & Sons, Ltd, pp. 4353–4369, 19-Nov-2004.
- [207] J. Jęftić, R. Hinek, S. C. Capelli, and A. Hauser, "Cooperativity in the Iron(II) Spin-Crossover Compound Fe(ptz)₆J(PF₆)₂ under the Influence of External Pressure (ptz = 1-n-Propyltetrazole)," *Inorg. Chem.*, vol. 36, no. 14, pp. 3080–3087, 1997.
- [208] P. Gütllich, V. Ksenofontov, and A. B. Gaspar, "Pressure effect studies on spin crossover systems," in *Coordination Chemistry Reviews*, 2005, vol. 249, no. 17-18 SPEC. ISS., pp. 1811–1829.
- [209] T. Granier, B. Gallois, J. Gaultier, J. A. Real, and J. Zarembowitch, "High-Pressure Single-Crystal X-ray Diffraction Study of Two Spin-Crossover Iron(II) Complexes: Fe(Phen)₂(NCS)₂ and Fe(Btz)₂(NCS)₂," *Inorg. Chem.*, vol. 32, no. 23, pp. 5305–5312, 1993.
- [210] A. Bouseksou, G. Molnár, J. P. Tuchagues, N. Menéndez, É. Codjovi, and F. Varret, "Triggering the spin-crossover of Fe(phen)₂(NCS)₂ by a pressure pulse. Pressure and magnetic field induce 'mirror effects,'" *Comptes Rendus Chim.*, vol. 6, no. 3, pp. 329–335, Mar. 2003.
- [211] J. Jęftić, R. Hinek, S. C. Capelli, and A. Hauser, "Cooperativity in the Iron(II) Spin-Crossover Compound Fe(ptz)₆J(PF₆)₂ under the Influence of External Pressure (ptz = 1-n-Propyltetrazole)," *Inorg. Chem.*, vol. 36, no. 14, pp. 3080–3087, 1997.
- [212] V. Ksenofontov, A. B. Gaspar, and P. Gütllich, "Pressure Effect Studies on Spin Crossover and Valence Tautomeric Systems," in *Spin Crossover in Transition Metal Compounds III*, vol. 235, Springer-Verlag, 2006, pp. 23–64.
- [213] A. H. Ewald and E. Sinn, "Pressure in coordination chemistry. II. Antiferromagnetic complexes of copper(II),"

Inorg. Chem., vol. 8, no. 3, pp. 537–539, Mar. 1969.

- [214] M. G. Cowan, J. Olguín, S. Narayanaswamy, J. L. Tallon, and S. Brooker, “Reversible switching of a cobalt complex by thermal, pressure, and electrochemical stimuli: Abrupt, complete, hysteretic spin crossover,” *J. Am. Chem. Soc.*, vol. 134, no. 6, pp. 2892–2894, Feb. 2012.
- [215] A. Bhattacharjee, M. Roy, V. Ksenofontov, J. A. Kitchen, S. Brooker, and P. Gülich, “Pressure effect studies on the spin-transition behavior of a dinuclear iron(II) compound,” *Eur. J. Inorg. Chem.*, vol. 2013, no. 5–6, pp. 843–849, Feb. 2013.
- [216] A. Galet, A. B. Gaspar, M. C. Muñoz, G. Levchenko, and J. A. Real, “Pressure effect and crystal structure reinvestigations on the spin crossover system: [Fe(bt)₂(NCS)₂] (bt = 2,2'-bithiazoline) polymorphs A and B,” *Inorg. Chem.*, vol. 45, no. 24, pp. 9670–9679, Nov. 2006.
- [217] J. Jętic, “Thermal- and pressure-induced spin transition coupled to crystallographic phase transition in some Fe(II) molecular crystals,” *High Press. Res.*, vol. 29, no. 2, pp. 369–376, Jun. 2009.
- [218] V. Meded *et al.*, “Electrical control over the Fe(II) spin crossover in a single molecule: Theory and experiment,” *Phys. Rev. B - Condens. Matter Mater. Phys.*, vol. 83, no. 24, p. 245415, Jun. 2011.
- [219] F. Renz, “Physical and chemical induced spin crossover,” in *Journal of Physics: Conference Series*, 2010, vol. 217, no. 1, p. 12022.
- [220] T. Mahfoud *et al.*, “Electric-field-induced charge-transfer phase transition: A promising approach toward electrically switchable devices,” *J. Am. Chem. Soc.*, vol. 131, no. 41, pp. 15049–15054, Oct. 2009.
- [221] A. Bousseksou *et al.*, “Dynamic triggering of a spin-transition by a pulsed magnetic field,” *Eur. Phys. J. B*, vol. 13, no. 3, pp. 451–456, Feb. 2000.
- [222] Y. Qi, E. W. Müller, H. Spiering, and P. Gülich, “The effect of a magnetic field on the high-spin α low-spin transition in [Fe(phen)₂(NCS)₂],” *Chem. Phys. Lett.*, vol. 101, no. 4–5, pp. 503–505, Oct. 1983.
- [223] A. Bousseksou, F. Varret, M. Goiran, K. Boukheddaden, and J. P. Tuchagues, “The Spin Crossover Phenomenon Under High Magnetic Field,” in *Top Curr Chem*, vol. 235, Springer, Berlin, Heidelberg, 2006, pp. 65–84.
- [224] J. J. McGarvey and I. Lawthers, “Photochemically-induced perturbation of the $1A \rightleftharpoons 5T$ equilibrium in FeII complexes by pulsed laser irradiation in the metal-to-ligand charge-transfer absorption band,” *J. Chem. Soc. Chem. Commun.*, no. 16, pp. 906–907, Jan. 1982.
- [225] S. Decurtins, P. Gülich, C. P. Köhler, H. Spiering, and A. Hauser, “Light-induced excited spin state trapping in a transition-metal complex: The hexa-1-propyltetrazole-iron (II) tetrafluoroborate spin-crossover system,” *Chem. Phys. Lett.*, vol. 105, no. 1, pp. 1–4, Mar. 1984.
- [226] M.-L. Boillot, J. Zarembowitch, and A. Sour, “Ligand-Driven Light-Induced Spin Change (LD-LISC): A Promising Photomagnetic Effect,” *Top Curr Chem*, vol. 234, pp. 261–276, 2004.
- [227] A. Hauser, “Light-Induced Spin Crossover and the High-Spin \rightarrow Low-Spin Relaxation,” in *Top Curr Chem*, vol. 234, Springer, Berlin, Heidelberg, 2012, pp. 155–198.
- [228] R. Bertoni *et al.*, “Elastically driven cooperative response of a molecular material impacted by a laser pulse,” *Nat. Mater.*, vol. 15, no. 6, pp. 606–610, Jun. 2016.
- [229] V. Davesne *et al.*, “Hysteresis and change of transition temperature in thin films of Fe{[Me₂Pyrz]₃BH}₂, a new sublimable spin-crossover molecule,” *J. Chem. Phys.*, vol. 142, no. 19, May 2015.
- [230] B. Warner *et al.*, “Temperature- and light-induced spin crossover observed by X-ray spectroscopy on isolated Fe(II) complexes on gold,” *J. Phys. Chem. Lett.*, vol. 4, no. 9, pp. 1546–1552, May 2013.
- [231] V. Davesne *et al.*, “First glimpse of the soft x-ray induced excited spin-state trapping effect dynamics on spin cross-over molecules,” *J. Chem. Phys.*, vol. 139, no. 7, Aug. 2013.
- [232] T. G. Gopakumar *et al.*, “Spin-crossover complex on Au(111): Structural and electronic differences between mono- and multilayers,” *Chem. - A Eur. J.*, vol. 19, no. 46, pp. 15702–15709, Nov. 2013.
- [233] M. Bernien *et al.*, “Highly Efficient Thermal and Light-Induced Spin-State Switching of an Fe(II) Complex in Direct Contact with a Solid Surface,” *ACS Nano*, vol. 9, no. 9, pp. 8960–8966, Sep. 2015.
- [234] D. Collison *et al.*, “Soft X-ray induced excited spin state trapping and soft X-ray photochemistry at the iron L_{2,3} edge in [Fe(phen)₂(NCS)₂] and [Fe(phen)₂(NCSe)₂] (phen = 1,10-phenanthroline),” *J. Chem. Soc. - Dalt. Trans.*, no. 22, pp. 4371–4376, Nov. 1997.

- [235] K. S. Murray, "The Development of Spin-Crossover Research," in *Spin-Crossover Materials: Properties and Applications*, John Wiley and Sons, 2013, pp. 1–54.
- [236] V. Briois *et al.*, "Full Multiple Scattering and Crystal Field Multiplet Calculations Performed on the Spin Transition FeII(phen)₂(NCS)₂ Complex at the Iron K and L_{2,3} X-ray Absorption Edges," *J. Am. Chem. Soc.*, vol. 117, no. 3, pp. 1019–1026, 1995.
- [237] J. J. Lee *et al.*, "X-ray absorption spectroscopic studies on light-induced excited spin state trapping of an Fe(II) complex," *J. Am. Chem. Soc.*, vol. 122, no. 24, pp. 5742–5747, Jun. 2000.
- [238] A. Cannizzo *et al.*, "Light-induced spin crossover in Fe(II)-based complexes: The full photocycle unraveled by ultrafast optical and X-ray spectroscopies," *Coordination Chemistry Reviews*, vol. 254, no. 21–22. Elsevier, pp. 2677–2686, 01-Nov-2010.
- [239] C. Bressler *et al.*, "Femtosecond XANES study of the light-induced spin crossover dynamics in an iron(II) complex," *Science (80-.)*, vol. 323, no. 5913, pp. 489–492, Jan. 2009.
- [240] N. Kojima, Y. Murakami, T. Komatsu, and T. Yokoyama, "EXAFS study on the spin-crossover system, [Fe(4-NH₂trz)₃](R-SO₃)₂," *Synth. Met.*, vol. 103, no. 1–3, p. 2154, Jun. 1999.
- [241] C. C. Dit Moulin, P. Rudolf, A. M. Flank, and C. Te Chen, "Spin transition evidenced by soft X-ray absorption spectroscopy," *J. Phys. Chem.*, vol. 96, no. 15, pp. 6196–6198, 1992.
- [242] M. Marchivie, "Approche structurale du phénomène de transition de spin par diffraction des rayons X sous contraintes (T, P, h□)." [\[Accessed: 12-Jun-2021\]](#).
- [243] N. V. Bausk, S. B. Érenburg, L. G. Lavrenova, and L. N. Mazalov, "EXAFS study of spin transition effect on the spatial and electronic structure of Fe(II) complexes with triazoles," *J. Struct. Chem.*, vol. 36, no. 6, pp. 925–931, Nov. 1995.
- [244] M. P. Shores, C. M. Klug, and S. R. Fiedler, "Spin-State Switching in Solution," in *Spin-Crossover Materials: Properties and Applications*, John Wiley and Sons, 2013, pp. 281–301.
- [245] Y. Garcia, V. Niel, M. Carmen Muñoz, and J. A. Real, "Spin crossover in 1D, 2D and 3D polymeric fe(II) networks," *Top. Curr. Chem.*, vol. 233, pp. 229–257, 2004.
- [246] J. A. Real, A. B. Gaspar, M. C. Muñoz, P. Gütllich, V. Ksenofontov, and H. Spiering, "Bipyrimidine-bridged dinuclear iron(II) spin crossover compounds," *Top. Curr. Chem.*, vol. 233, pp. 167–193, 2004.
- [247] J. A. Real, A. B. Gaspar, and M. Carmen Muñoz, "Thermal, pressure and light switchable spin-crossover materials," *Dalton Transactions*, no. 12. The Royal Society of Chemistry, pp. 2062–2079, 21-Jun-2005.
- [248] M. B. Duriska *et al.*, "Systematic metal variation and solvent and hydrogen-gas storage in supramolecular nanoballs," *Angew. Chemie - Int. Ed.*, vol. 48, no. 47, pp. 8919–8922, Nov. 2009.
- [249] A. Lindner, M. Menzel, F. Renz, D. G. Kurth, and A. F. Thünemann, "Metallosupramolecular coordination polyelectrolytes investigated by Mössbauer spectroscopy," in *ICAME 2005*, Springer Berlin Heidelberg, 2007, pp. 465–468.
- [250] K. Senthil Kumar and M. Ruben, "Emerging trends in spin crossover (SCO) based functional materials and devices," 2017.
- [251] P. Gamez, J. S. Costa, M. Quesada, and G. Aromí, "Iron Spin-Crossover compounds: From fundamental studies to practical applications," *J. Chem. Soc. Dalton Trans.*, no. 38, pp. 7845–7853, Sep. 2009.
- [252] "Spin-Crossover Materials: Properties and Applications | Wiley." [Online]. Available: <https://www.wiley.com/en-us/Spin+Crossover+Materials%3A+Properties+and+Applications-p-9781119998679>. [Accessed: 12-Jun-2021].
- [253] G. Molnár, S. Rat, L. Salmon, W. Nicolazzi, and A. Bousseksou, "Spin Crossover Nanomaterials: From Fundamental Concepts to Devices," *Adv. Mater.*, vol. 30, no. 5, p. 1703862, Feb. 2018.
- [254] W. Kaim, "Vital volumes. Molecular magnetism. By Olivier Kahn, VCH, Weinheim 1993, XVI, 380 pp., hardcover, DM 154.00, ISBN 3-527-89566-3," *Adv. Mater.*, vol. 6, no. 10, pp. 807–808, Oct. 1994.
- [255] S. Foner, "Versatile and sensitive vibrating-sample magnetometer," *Rev. Sci. Instrum.*, vol. 30, no. 7, pp. 548–557, 1959.
- [256] D. Drung *et al.*, "Highly sensitive and easy-to-use SQUID sensors," in *IEEE Transactions on Applied Superconductivity*, 2007, vol. 17, no. 2, pp. 699–704.

- [257] E. Milin *et al.*, "Elastic frustration triggering photoinduced hidden hysteresis and multistability in a two-dimensional photoswitchable hofmann-like spin-crossover metal-organic framework," *Inorg. Chem.*, vol. 55, no. 22, pp. 11652–11661, Nov. 2016.
- [258] P. Guionneau *et al.*, "X-ray diffraction investigation of a spin crossover hysteresis loop," *J. Phys. Condens. Matter*, vol. 19, no. 32, p. 326211, Aug. 2007.
- [259] S. Pillet, J. Hubsch, and C. Lecomte, "Single crystal diffraction analysis of the thermal spin conversion in [Fe(btr)₂(NCS)₂](H₂O): Evidence for spin-like domain formation," *Eur. Phys. J. B*, vol. 38, no. 4, pp. 541–552, 2004.
- [260] A. Rotaru *et al.*, "Calorimetric measurements of diluted spin crossover complexes [FeM_{1-x}(btr)₂(NCS)₂]-H₂O with MII = Zn and Ni," *Polyhedron*, vol. 28, no. 13, pp. 2531–2536, Sep. 2009.
- [261] M. Sorai, Y. Nagano, A. J. Conti, and D. N. Hendrickson, "Calorimetric study of spin-state transformation of ferric spin-crossover complexes in the solid state-2. Heat capacity of [Fe(3-OEt-SalAPA)₂](ClO₄ · C₆H₅Cl)," *J. Phys. Chem. Solids*, vol. 55, no. 4, pp. 317–326, Apr. 1994.
- [262] O. Roubeau, M. Castro, R. Burriel, J. G. Haasnoot, and J. Reedijk, "Calorimetric investigation of triazole-bridged Fe(II) spin-crossover one-dimensional materials: Measuring the cooperativity," *J. Phys. Chem. B*, vol. 115, no. 12, pp. 3003–3012, Mar. 2011.
- [264] J. H. Takemoto and B. Hutchinson, "Effect of magnetic crossover on the low-frequency IR spectrum of [Fe(1,10-phenanthroline)₂(NCS)₂]," *Inorg. Nucl. Chem. Lett.*, vol. 8, no. 9, pp. 769–772, Sep. 1972.
- [265] Y. A. Tobon *et al.*, "Resonance Raman study of spin-crossover [Fe(Htrz)₂(trz)](BF₄)·H₂O particles coated with gold," *Eur. J. Inorg. Chem.*, vol. 2012, no. 35, pp. 5837–5842, Dec. 2012.
- [266] B. Benaïcha *et al.*, "Interplay between spin-crossover and luminescence in a multifunctional single crystal iron(ii) complex: Towards a new generation of molecular sensors," *Chem. Sci.*, vol. 10, no. 28, pp. 6791–6798, Jul. 2019.
- [267] V. M. Hiiuk *et al.*, "Influence of the ultra-slow nucleation and growth dynamics on the room-temperature hysteresis of spin-crossover single crystals," *Chem. Phys. Lett.*, vol. 770, p. 138442, May 2021.
- [268] M. Sy, R. Traiche, H. Fourati, Y. Singh, F. Varret, and K. Boukheddaden, "Spatiotemporal Investigations on Light-Driven High-Spin-Low-Spin Interface Dynamics in the Thermal Hysteresis Region of a Spin-Crossover Single Crystal," *J. Phys. Chem. C*, vol. 122, no. 36, pp. 20952–20962, Sep. 2018.
- [269] H. Fourati and K. Boukheddaden, "Experimental evidence for the elastic long-range character of the spin crossover transition in cooperative single crystals," *Phys. Rev. B*, vol. 101, no. 22, p. 224101, Jun. 2020.
- [270] H. Fourati, G. Bouchez, M. Paez-Espejo, S. Triki, and K. Boukheddaden, "Spatio-temporal investigations of the incomplete spin transition in a single crystal of [Fe(2-pytrz)₂{Pt(CN)₄}]·3H₂O: Experiment and theory," *Crystals*, vol. 9, no. 1, pp. 1–18, Jan. 2019.
- [271] H. Fourati *et al.*, "Interplay between a crystal's shape and spatiotemporal dynamics in a spin transition material," *Phys. Chem. Chem. Phys.*, vol. 20, no. 15, pp. 10142–10154, Apr. 2018.
- [272] M. Sy *et al.*, "Structure-driven orientation of the high-spin-low-spin interface in a spin-crossover single crystal," *Angew. Chemie - Int. Ed.*, vol. 53, no. 29, pp. 7539–7542, Jul. 2014.
- [273] F. Varret *et al.*, "The propagation of the thermal spin transition of [Fe(btr)₂(NCS)₂]-H₂O single crystals, observed by optical microscopy," *New J. Chem.*, vol. 35, no. 10, pp. 2333–2340, Sep. 2011.
- [274] K. Boukheddaden and M. Sy, "Dance of interference patterns during the spin transition of a single crystal," *J. Phys. Chem. C*, vol. 124, no. 51, pp. 28093–28107, Dec. 2020.
- [275] A. Slimani *et al.*, "Visualization and quantitative analysis of spatiotemporal behavior in a first-order thermal spin transition: A stress-driven multiscale process," *Phys. Rev. B - Condens. Matter Mater. Phys.*, vol. 84, no. 9, p. 094442, Sep. 2011.
- [276] C. Chong *et al.*, "Electronic and structural aspects of spin transitions observed by optical microscopy. the case of [Fe(ptz)₆](BF₄)₂," *J. Phys. Chem. B*, vol. 114, no. 5, pp. 1975–1984, Feb. 2010.
- [277] A. Goujon *et al.*, "An optical microscope study of photo-switching and relaxation in single crystals of the spin transition solid [Fe(ptz)₆](BF₄)₂, with image processing," *Inorganica Chim. Acta*, vol. 361, no. 14–15, pp. 4055–4064, Oct. 2008.
- [278] C. Chong *et al.*, "The kinetics features of a thermal spin transition characterized by optical microscopy on the example of [Fe(bbtr)₃](ClO₄)₂ single crystals: Size effect and mechanical instability," *Chem. Phys. Lett.*, vol.

- 504, no. 1–3, pp. 29–33, Feb. 2011.
- [279] F. Varret, C. Chong, A. Goujon, and K. Boukheddaden, “Light-induced phase separation (LIPS) in [Fe(ptz)₆](BF₄)₂ spin-crossover single crystals: Experimental data revisited through optical microscope investigation,” *J. Phys. Conf. Ser.*, vol. 148, no. 1, p. 012036, Feb. 2009.
- [281] G. Félix *et al.*, “Surface plasmons reveal spin crossover in nanometric layers,” *J. Am. Chem. Soc.*, vol. 133, no. 39, pp. 15342–15345, Oct. 2011.
- [282] A. Akou *et al.*, “Soft lithographic patterning of spin crossover complexes. Part 2: Stimuli-responsive diffraction grating properties,” *J. Mater. Chem.*, vol. 22, no. 9, pp. 3752–3757, Mar. 2012.
- [283] D. Aravena and E. Ruiz, “Coherent transport through spin-crossover single molecules,” *J. Am. Chem. Soc.*, vol. 134, no. 2, pp. 777–779, Jan. 2012.
- [284] F. Prins, M. Monrabal-Capilla, E. A. Osorio, E. Coronado, and H. S. J. Van Der Zant, “Room-temperature electrical addressing of a bistable spin-crossover molecular system,” *Adv. Mater.*, vol. 23, no. 13, pp. 1545–1549, Apr. 2011.
- [285] M. S. Alam *et al.*, “Spin-state patterns in surface-grafted beads of iron(II) complexes,” *Angew. Chemie - Int. Ed.*, vol. 49, no. 6, pp. 1159–1163, Feb. 2010.
- [286] A. Bousseksou, G. Molnár, L. Salmon, and W. Nicolazzi, “Molecular spin crossover phenomenon: Recent achievements and prospects,” *Chem. Soc. Rev.*, vol. 40, no. 6, pp. 3313–3335, May 2011.
- [287] A. Rotaru, I. A. Gural'skiy, G. Molnár, L. Salmon, P. Demont, and A. Bousseksou, “Spin state dependence of electrical conductivity of spin crossover materials,” *Chem. Commun.*, vol. 48, no. 35, pp. 4163–4165, Apr. 2012.
- [288] A. Bousseksou, G. Molnár, P. Demont, and J. Menegotto, “Observation of a thermal hysteresis loop in the dielectric constant of spin crossover complexes: Towards molecular memory devices,” *J. Mater. Chem.*, vol. 13, no. 9, pp. 2069–2071, Sep. 2003.
- [289] A. Hauser, “Spin-Crossover Materials. Properties and Applications. Edited by Malcolm A. Halcrow,” *Angew. Chemie Int. Ed.*, vol. 52, no. 40, pp. 10419–10419, Sep. 2013.
- [290] G. Molnár, L. Salmon, W. Nicolazzi, F. Terki, and A. Bousseksou, “Emerging properties and applications of spin crossover nanomaterials,” *J. Mater. Chem. C*, vol. 2, no. 8, pp. 1360–1366, Feb. 2014.
- [291] H. J. Shepherd, G. Molnár, W. Nicolazzi, L. Salmon, and A. Bousseksou, “Spin crossover at the nanometre scale,” *European Journal of Inorganic Chemistry*, vol. 2013, no. 5–6. John Wiley & Sons, Ltd, pp. 653–661, 18-Feb-2013.
- [292] A. Carné, C. Carbonell, I. Imaz, and D. Maspoch, “Nanoscale metal–organic materials,” *Chem. Soc. Rev.*, vol. 40, no. 1, pp. 291–305, Dec. 2011.
- [293] M. Mikolasek, G. Félix, W. Nicolazzi, G. Molnár, L. Salmon, and A. Bousseksou, “Finite size effects in molecular spin crossover materials,” *New J. Chem.*, vol. 38, no. 5, pp. 1834–1839, Apr. 2014.
- [294] E. Freysz, S. Montant, S. Létard, and J. F. Létard, “Single laser pulse induces spin state transition within the hysteresis loop of an Iron compound,” *Chem. Phys. Lett.*, vol. 394, no. 4–6, pp. 318–323, Aug. 2004.
- [295] C. M. Jureschi *et al.*, “Pressure sensor via optical detection based on a 1D spin transition coordination polymer,” *Sensors (Switzerland)*, vol. 15, no. 2, pp. 2388–2398, Jan. 2015.
- [296] S. Shi *et al.*, “Study of molecular spin-crossover complex Fe(phen)₂(NCS)₂ thin films,” *Appl. Phys. Lett.*, vol. 95, no. 4, p. 043303, Jul. 2009.
- [297] T. Miyamachi *et al.*, “Robust spin crossover and memristance across a single molecule,” *Nat. Commun.*, vol. 3, 2012.
- [299] T. G. Gopakumar, F. Matino, H. Naggert, A. Bannwarth, F. Tucek, and R. Berndt, “Electron-induced spin crossover of single molecules in a bilayer on gold,” *Angew. Chemie - Int. Ed.*, vol. 51, no. 25, pp. 6262–6266, Jun. 2012.
- [300] G. Kuang *et al.*, “Mechanically-Controlled Reversible Spin Crossover of Single Fe-Porphyrin Molecules,” *ACS Nano*, vol. 11, no. 6, pp. 6295–6300, Jun. 2017.
- [301] A. Köbke *et al.*, “Reversible coordination-induced spin-state switching in complexes on metal surfaces,” *Nature Nanotechnology*, vol. 15, no. 1. Nature Research, pp. 18–21, 01-Jan-2020.
- [302] J. Liu *et al.*, “Collective Spin Manipulation in Antiferroelastic Spin-Crossover Metallo-Supramolecular Chains,”

- ACS Nano*, vol. 14, no. 9, pp. 11283–11293, Sep. 2020.
- [303] V. B. Jakobsen *et al.*, “Stress-Induced Domain Wall Motion in a Ferroelastic Mn³⁺ Spin Crossover Complex,” *Angew. Chemie - Int. Ed.*, vol. 59, no. 32, pp. 13305–13312, Aug. 2020.
- [304] I. A. Ado, O. A. Tretiakov, and M. Titov, “Microscopic theory of spin-orbit torques in two dimensions,” *Phys. Rev. B*, vol. 95, no. 9, p. 094401, Mar. 2017.
- [305] A. Fert, N. Reyren, and V. Cros, “Magnetic skyrmions: Advances in physics and potential applications,” *Nature Reviews Materials*, vol. 2, no. 7. Nature Publishing Group, pp. 1–15, 13-Jun-2017.
- [306] O. Kahn and C. J. Martinez, “Spin-transition polymers: From molecular materials toward memory devices,” *Science*, vol. 279, no. 5347. American Association for the Advancement of Science, pp. 44–48, 02-Jan-1998.
- [307] S. A. Wolf *et al.*, “Spintronics: A spin-based electronics vision for the future,” *Science*, vol. 294, no. 5546. American Association for the Advancement of Science, pp. 1488–1495, 16-Nov-2001.
- [308] “Organic Electronics: Emerging Concepts and Technologies | Wiley.” [Online]. Available: <https://www.wiley.com/en-us/Organic+Electronics%3A+Emerging+Concepts+and+Technologies-p-9783527411313>. [Accessed: 12-Jun-2021].
- [309] P. N. Martinho, C. Rajnak, and M. Ruben, “Nanoparticles, Thin Films and Surface Patterns from Spin-Crossover Materials and Electrical Spin State Control,” in *Spin-Crossover Materials: Properties and Applications*, John Wiley and Sons, 2013, pp. 375–404.
- [310] M. Cavallini *et al.*, “Thin deposits and patterning of room-temperature-switchable one-dimensional spin-crossover compounds,” *Langmuir*, vol. 27, no. 7, pp. 4076–4081, Apr. 2011.
- [311] M. Cavallini *et al.*, “Micro- and Nanopatterning of Spin-Transition Compounds into Logical Structures,” *Angew. Chemie*, vol. 120, no. 45, pp. 8724–8728, Oct. 2008.
- [312] M. Cavallini, “Status and perspectives in thin films and patterning of spin crossover compounds,” *Physical Chemistry Chemical Physics*, vol. 14, no. 34. The Royal Society of Chemistry, pp. 11867–11876, 14-Sep-2012.
- [313] A. Atitoaie, R. Tanasa, A. Stancu, and C. Enachescu, “Study of spin crossover nanoparticles thermal hysteresis using FORC diagrams on an Ising-like model,” *J. Magn. Magn. Mater.*, vol. 368, pp. 12–18, Nov. 2014.
- [314] I. A. Gural'skiy, G. Molnár, I. O. Fritsky, L. Salmon, and A. Bousseksou, “Synthesis of [Fe(hptrz)₃](OTs)₂ spin crossover nanoparticles in microemulsion,” *Polyhedron*, vol. 38, no. 1, pp. 245–250, May 2012.
- [315] Y. Prado *et al.*, “Tailored coordination nanoparticles: Assessing the magnetic single-domain critical size,” *Chem. Commun.*, vol. 47, no. 3, pp. 1051–1053, Dec. 2011.
- [316] S. Brossard *et al.*, “Investigation of the photoinduced magnetization of copper octacyanomolybdates nanoparticles by X-ray magnetic circular dichroism,” *J. Am. Chem. Soc.*, vol. 134, no. 1, pp. 222–228, Jan. 2012.
- [317] R. Tanasa, J. Laisney, A. Stancu, M. L. Boillot, and C. Enachescu, “Hysteretic behavior of Fe(phen)₂(NCS)₂ spin-transition microparticles vs. the environment: A huge reversible component resolved by first order reversal curves,” *Appl. Phys. Lett.*, vol. 104, no. 3, p. 031909, Jan. 2014.
- [318] L. Catala, F. Volatron, D. Brnzei, and T. Mallah, “Functional coordination nanoparticles,” *Inorg. Chem.*, vol. 48, no. 8, pp. 3360–3370, Apr. 2009.
- [319] Y. Raza *et al.*, “Matrix-dependent cooperativity in spin crossover Fe(pyrazine)Pt(CN)₄ nanoparticles,” *Chem. Commun.*, vol. 47, no. 41, pp. 11501–11503, Nov. 2011.
- [320] F. Volatron, L. Catala, E. Rivière, A. Gloter, O. Stéphan, and T. Mallah, “Spin-crossover coordination nanoparticles,” *Inorg. Chem.*, vol. 47, no. 15, pp. 6584–6586, Aug. 2008.
- [321] G. Félix, W. Nicolazzi, M. Mikolasek, G. Molnár, and A. Bousseksou, “Non-extensivity of thermodynamics at the nanoscale in molecular spin crossover materials: A balance between surface and volume,” *Phys. Chem. Chem. Phys.*, vol. 16, no. 16, pp. 7358–7367, Apr. 2014.
- [322] I. Boldog *et al.*, “Spin-Crossover Nanocrystals with Magnetic, Optical, and Structural Bistability Near Room Temperature,” *Angew. Chemie*, vol. 120, no. 34, pp. 6533–6537, Aug. 2008.
- [323] C. Bartual-Murgui *et al.*, “Guest effect on nanopatterned spin-crossover thin films,” *Small*, vol. 7, no. 23, pp. 3385–3391, Dec. 2011.
- [324] I. Tokarev and S. Minko, “Tunable plasmonic nanostructures from noble metal nanoparticles and stimuli-

- responsive polymers,” *Soft Matter*, vol. 8, no. 22. The Royal Society of Chemistry, pp. 5980–5987, 14-Jun-2012.
- [325] H. Oubouchou, A. Slimani, G. Zribi, N. Haine, M. Zergoug, and K. Boukheddaden, “Thermal hysteresis behavior of spin crossover nanoparticles from a deformable lattice model: Monte Carlo investigations,” *Sens. Lett.*, vol. 11, no. 8, pp. 1432–1439, 2013.
- [326] O. Yalçın, R. Erdem, and S. Özüm, “Origin of the martensitic and austenitic phase transition in core-surface smart nanoparticles with size effects and hysteretic splitting,” *J. Appl. Phys.*, vol. 115, no. 5, p. 054316, Feb. 2014.
- [327] G. Félix *et al.*, “Enhanced cooperative interactions at the nanoscale in spin-crossover materials with a first-order phase transition,” *Phys. Rev. Lett.*, vol. 110, no. 23, p. 235701, Jun. 2013.
- [328] R. M. Van Der Veen, O. H. Kwon, A. Tissot, A. Hauser, and A. H. Zewail, “Single-nanoparticle phase transitions visualized by four-dimensional electron microscopy,” *Nat. Chem.*, vol. 5, no. 5, pp. 395–402, Mar. 2013.
- [329] S. Cobo, G. Molnár, J. A. Real, and A. Bousseksou, “Multilayer sequential assembly of thin films that display room-temperature spin crossover with hysteresis,” *Angew. Chemie - Int. Ed.*, vol. 45, no. 35, pp. 5786–5789, Sep. 2006.
- [330] P. Gütllich, A. Hauser, and H. Spiering, “Thermal and Optical Switching of Iron(II) Complexes,” *Angewandte Chemie International Edition in English*, vol. 33, no. 20. John Wiley & Sons, Ltd, pp. 2024–2054, 02-Nov-1994.
- [331] D. Mader, S. Pillet, C. Carteret, M. J. Stebe, and J. L. Blin, “Confined growth of spin crossover nanoparticles in surfactant-based matrices: Enhancing shape anisotropy,” *J. Dispers. Sci. Technol.*, vol. 32, no. 12, pp. 1771–1779, 2011.
- [332] P. N. Martinho *et al.*, “Template Assembly of Spin Crossover One-Dimensional Nanowires,” *Angew. Chemie*, vol. 124, no. 48, pp. 12161–12165, Nov. 2012.
- [333] A. D. Naik, L. Stappers, J. Snauwaert, J. Fransaer, and Y. Garcia, “A biomembrane stencil for crystal growth and soft lithography of a thermochromic molecular sensor,” *Small*, vol. 6, no. 24, pp. 2842–2846, Dec. 2010.
- [334] G. & G. H. A. Renz, F., Souza, P. A. D., Klingelhöfer, “No Title,” *ind. Appl. Mössbauer Eff*, no. (Springer Netherlands, pp. 699–704, 2002.
- [335] V. Legrand, “Cristallographie et photo-cristallographie haute résolution de composés moléculaires à transition de spin : propriétés structurales, électroniques et mécanismes de conversion,” <http://www.theses.fr>, Jan. 2005.
- [336] I. Šalitroš, N. T. Madhu, R. Boča, J. Pavlik, and M. Ruben, “Room-temperature spin-transition iron compounds,” *Monatshefte für Chemie*, vol. 140, no. 7. pp. 695–733, Jul-2009.
- [337] M. D. Manrique-Juárez *et al.*, “Switchable molecule-based materials for micro- and nanoscale actuating applications: Achievements and prospects,” *Coordination Chemistry Reviews*, vol. 308. Elsevier B.V., pp. 395–408, 01-Feb-2016.
- [338] M. D. Manrique-Juárez, I. Suleimanov, E. M. Hernández, L. Salmon, G. Molnár, and A. Bousseksou, “In situ AFM imaging of microstructural changes associated with the spin transition in [Fe(Htrz)₂(Trz)](Bf₄) nanoparticles,” *Materials (Basel)*, vol. 9, no. 7, Jul. 2016.
- [339] M. D. Manrique-Juarez *et al.*, “Microelectromechanical systems integrating molecular spin crossover actuators,” *Appl. Phys. Lett.*, vol. 109, no. 6, p. 061903, Aug. 2016.
- [340] C. Lefter *et al.*, “Current Switching Coupled to Molecular Spin-States in Large-Area Junctions,” *Adv. Mater.*, vol. 28, no. 34, pp. 7508–7514, Sep. 2016.
- [341] V. Shalabaeva *et al.*, “Vacuum deposition of high-quality thin films displaying spin transition near room temperature,” *J. Mater. Chem. C*, vol. 5, no. 18, pp. 4419–4425, May 2017.
- [342] M. D. Manrique-Juarez *et al.*, “A Bistable Microelectromechanical System Actuated by Spin-Crossover Molecules,” *Angew. Chemie*, vol. 129, no. 28, pp. 8186–8190, Jul. 2017.
- [343] M. D. Manrique-Juarez *et al.*, “Spin crossover materials for MEMS actuation: Film integration and characterization,” in *TRANSDUCERS 2017 - 19th International Conference on Solid-State Sensors, Actuators and Microsystems*, 2017, pp. 1300–1303.
- [344] J. F. Létard, G. Chastanet, P. Guionneau, and C. Desplanches, “Optimizing the Stability of Trapped Metastable Spin States,” in *Spin-Crossover Materials: Properties and Applications*, John Wiley and Sons, 2013, pp. 475–

506.

- [345] G. J. Halder, C. J. Kepert, B. Moubaraki, K. S. Murray, and J. D. Cashion, "Guest-dependent spin crossover in a nanoporous molecular framework material," *Science (80-.)*, vol. 298, no. 5599, pp. 1762–1765, Nov. 2002.

Chapter 2.

Magnetoelastic modelling of core-shell spin-crossover composites

Adapted from article “Magnetoelastic modeling of core-shell spin-crossover nanocomposites”

Hassane Oubouchou, **Yogendra Singh**, and Kamel Boukheddaden *Phys. Rev. B* 98, 014106

2.1 Introduction

Core-shell nanoparticles have garnered a lot of interest in recent years owing to their fascinating properties and extensive choice of applications in a variety of fields ranging from catalysis, photocatalysis, drug delivery, sensors, electronic device applications, surface plasmon resonance[1], and other phenomena[2][3]. In recent years different core-shell gold nanostructures have been studied regarding their catalytic properties[4][5], gas storage and separation, information storage[6-10]. Core-Shell nanostructures falls into a special category of materials which could be wisely modified and designed to tune the cores and the shells material and morphology to serve our purpose. Various core-shell nanostructures can be created with tunable properties that can perform vital roles in several developments and promise sustainable solutions to current problems. The core-shell nanostructured materials present tremendous opportunities as we can couple different or same types of materials of diverse shapes and sizes while varying core/shell widths, which could support different structural morphologies. These nanoparticles could be fabricated into any shapes such as: centric, eccentric, spherical, star-shaped, fibrous or tubular and so on, to name a few[8]. The control which could be exerted over the physicochemical properties of the core-shell nanostructures, simply by modifying or adjusting their size and shape is truly exciting[9][10]. Different core-shell nanostructures correspond to many distinct characteristics which are being exploited in various fields of biomedical and nanomedicine, like drug delivery,[11] bioimaging[12], cancer treatment, so on and so forth[13]. Metal-based magnetic core-shell nanoparticles would provide excellent magnetic sensitivity and biocompatibility.

Interestingly, there are various kinds of core-shell nanostructures possible, ranging from the permutation and combination of various types and classes of metal, semiconductor, non-metal, and polymeric materials. Owing to their benefits, such as scalability, cost-effectiveness, and stress-free device fabrication capabilities [17- 20], core-shell have amassed reputation as a class of innovative nanomaterials with numerous advantages in already advanced and saturated field of electronics containing organic photovoltaic solar cells, sensors, organic light-

emitting diodes, and field-effect transistors.

The well-established synthesis methods afford good reproducibility, narrow size distribution, and good control over the shape and size of the nanoparticles (NPs)[16]. Different chemical and physical properties of the core-shell interface and their components contribute to the system's complexity and attract efforts to understand them. The various fabrication methods employed for designing core-shell nanoparticles such as: sol-gel process, hydrothermal production, emulsion polymerization technique, microemulsion polymerization, solvothermal synthesis, and chemical vapor deposition method etc.[17-26].The core-shell architecture is typically fabricated by a dual-step or many-step synthesis route, firstly core is prepared and then shell is formed on the core particle through various techniques subjected to the variety of core - shell nanostructured materials and their surface morphologies.[19]

It is important because many of the core-shell properties depend on the size, shape and composition. The collective behavior associated with the interparticle, dipolar and/or exchange interactions is critically important to understand the magnetic response of an ensemble of nanoparticles. However, there is scarcity of research related to magnetostatic, magnetoelastic, and magneto-dynamic properties of core-shell structures. In the case of nanoparticles, interfaces play a very crucial role in these systems for example let's say diamagnetic cores and magnetic shells, the exchange-coupling between two different magnetic regions such as a disordered surface layer and a magnetically ordered core drives to exciting effects. The Interface region, which plays a crucial role in the core-shell structure could be used to moderate or amplify the magnetic frustration through various mechanism, as this is the region where we see a breakdown in translation symmetry. This could be either manufactured through lattice mismatch or due to the inherited randomness in the system, which increases the probability of broken bonds at the interface, thus lowering the coordination number, which changes the local exchange interaction and drives to magnetic frustration. As we are already working in the nano regime [20- 22], the effect of surface spins disorder could be controlled through tweaking the surface to volume ratio. Taking into account that high anisotropy nanoparticles have weaker surface effects, with further reduction in size, it is expected that they will demonstrate further reduction in exchange bias effect, thus, in turn, inheriting furthermore complexity to the magnetic response of the system, which is reflected in a shift of the hysteresis loop during field-cooling processes[23][24]

Recently the occurrence of such effects has been revealed in bicomponent systems; for instance, in Au/Fe₃O₄ core-shell nanoparticles, it is related to the presence of a spin-glass-like layer at the particle surface[25]. While for the single-phase magnetic nanoparticles, this effect is ascribed to surface spin disorders[26-28]. Thus, we have various parameters through which we can attune the magnetic response of multicomponent nanostructures such as the atomic structure of the interface (uncompensated spins), finite-size effect, morphology, surface

effects[29][30], shell thickness or differences between effective anisotropies[31] are crucial factors, as they determine the strength of the exchange bias effect in nanoparticles. The dependence of the exchange bias field on temperature can be used to probe whether the magnetic response arises from finite-size effect or the surface layer with canted spins are to be suspected.

One of the promising strategies to achieve such multifunctionality is combining several coordination networks of different chemical compositions into core-shell heterostructures. Such approaches have been used in the last decade, for instance, on micron-scaled MOFs giving heterogeneous core-shell MOFs[31-35] or “MOFs-on-MOFs” crystals[36][37] exhibiting optimized porosity, enhanced storage capacity and multifunctionality. Another approach to designing original multifunctional materials consists in combining coordination networks with inorganic materials of completely different nature. Among the major breakthroughs in the field, most of the studies concern the formation of metal or metal oxide nanoparticles embedded in various MOFs using either, post-synthetic incorporation methods or growth of a MOF shell at the surface of metal, metal oxide (Fe_3O_4), quantum dots or rare-earth nanoparticles.

Among the various types of core-shell structures, system exhibiting molecular magnetism are also attracting huge scientific interest because of the extraordinary variety of their physical properties (electrochromism, ferromagnetism, photomagnetism, piezomagnetism, spin crossover), which opens up prospects for original functional materials [38-50]. An upside of using these materials is that we can use molecular chemistry to our advantage, which allows us to use soft synthetic routes, providing greater flexibility in designing and tuning physical properties of the molecule-based materials.

In addition, the control of their size and morphology at the nanoscale permits not only to investigate the impact of the size-reduction effect on physical and chemical properties, but also opens new perspectives for technological applications. The idea is to utilize various platforms available (MOFs, PBA,...), while designing multifunctional nano-systems so that we can combine various physical aspects or give rise to new exotic features through synergetic effect.

2.2 Core–Shell Spin Crossover

During the last decade, compounds with multistep spin conversion remained quite rare and attracted increasing attention in theoretical and experimental studies[51-55] due to their possibility of building up three-byte electronics. Multistep SCO behavior results from structural ordering or/and the existence of multistability in the molecule itself, like in binuclear SCO systems[56][57] In contrast, some multistep SCO systems consist of an asymmetric unit containing two or more non-equivalent sites [58][59], having different local environments. At the macroscopic scale, the competition or the interplay between the two types of SCO sites manifest

through the existence of an intermediate phase associated with partial conversion from HS to LS states. It is worth noticing that the processing of SCO materials with two inequivalent sites, although possible, is hardly controllable, and most of the time, the behavior of the high-spin fraction is hardly predictable. That is why recently, chemists and physicists started designing well controllable and reproducible SCO core-shell nanocomposites made of two SCO materials, thus combining the SCO properties of both the core and the shell components in the same system[60]. Till now, the interest in the finite-size effects properties[61-64] and the manipulation[65], the design and visualization[66] of small objects at the nanoscale is rapidly growing since the adapted near-field technologies are now available. This was the case, for example, of Prussian Blue Analogs for which core-shell nanoparticles have been synthesized, and their thermal and photo-striction properties have been investigated as a function of the thickness and the nature of the core and the shell[67-70][59]. With the development of nanotechnologies and the availability of experimental results, several types of nanocomposites integrating the SCO properties have been designed by embedding SCO nanoparticles within organic polymers[71-74] in biopolymers [75] or in mesoporous silica matrices[72][76-78].

However, the critical function of the matrix and interface has been the crux of debate for years and is still being investigated. In the first studies devoted to SCO nanoparticles (NPs), puzzling and intriguing trends between SCO behaviors were identified, such as 7 nm NPs of Hoffman clathrate family $[\text{Fe}(\text{pz})\text{M}(\text{CN})_4]$ ($\text{M} = \text{Pt}, \text{Ni}$) showing a partial and gradual SCO transition without any hysteresis[79]. In contrast, 4 nm particles of $[\text{Fe}(\text{pz})\text{Ni}(\text{CN})_4]$ embedded in chitosan beads revealed a large thermal hysteresis loop close to room temperature[80][81]. Having the same environment poses a significant challenge for chemists because tuning size necessitates the use of various methods or surfactant-based approaches. Surfactants, even in trace amounts, can interact with and change the behavior of the SCO [82]. Also, later it was found that even in the absence of any contamination, the role and effect of environment cannot be fully explained, and it is not just the content of the interface (chemical nature) but the interface as a whole (rigidity and thickness) [83] might play a much more crucial role than anticipated. Which has been illustrated effectively using an electro-elastic model by Boukheddaden and co-workers[84][85]; the authors suggest that acoustic impedance mismatch between the core and the shell may be detrimental to the cooperativity.

2.2.1 Experimental observations

A lot of work has been done experimentally on the core-shell architecture in the SCO field; among the numerous synergies that can be targeted, the most studied one is related to SCO[46] / CTIST synergistically combined with ferromagnetism. As it is well-known, PBAs [86] exhibit electron transfers accompanied by a spin shift that are caused by light and/or temperature, a wide range of magnetic

properties, including ferro/ferrimagnetic ordering, are also observed at high Curie temperatures[87]. Since most PBAs have minute variation in cell parameters, growth of the similar or different PBA networks could be achieved. Single-step synthesis of self-standing charged PBA particles and core-shells/heterostructures without the use of a surfactant by homo- and heteroepitaxial growth on PBA charged seeds demonstrated by Catala et al. [46], Fig. 2.1 enables the development of heterostructures with control over PBA thicknesses.

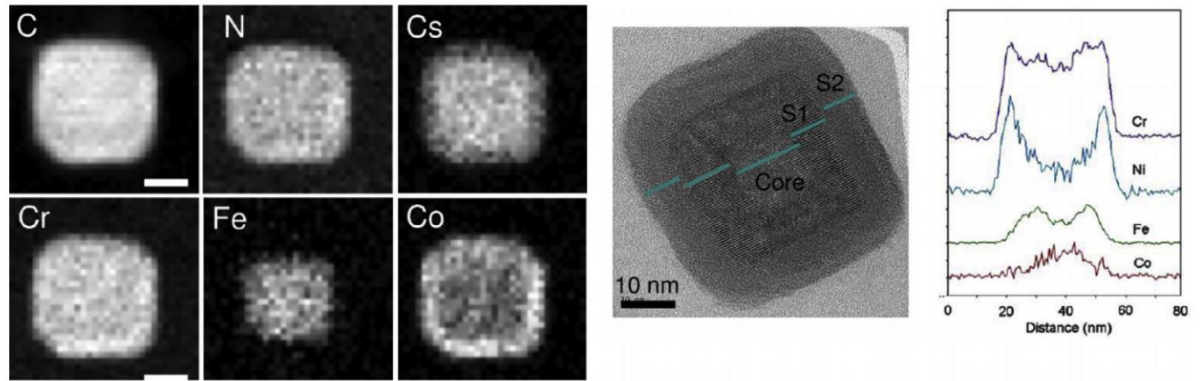


Figure 2. 1 (Left) Example of STEM-EELS mapping of CsFeCr@CoCr showing the core-shell architecture. (Right) Example of a high-resolution TEM micrograph of a CsCoCr@CsFeCr@CsNiCr heterostructure and the elemental profile across the particle. Adapted from Ref. [46].

It is crucial during the growth to avoid the contamination of the interface and various mechanisms are employed to avoid it[88]. Growth mode may also get affected if the lattice misfit between the core and shell entities is well above a specific critical value ($\sim 4 - 5 \%$), formation of islands on the edges may start appearing in order to relax the strain[89]. Various studies [36][90][91] regarding heterostructures with a core that exhibits a CTIST (either photoinduced or thermoinduced) and ferromagnetic shells were conducted, which discussed about the role strain played in shifting the magnetization of core entities[90] (Co II/Fe III pairs), towards higher temperatures which were closer to that of shell (CsNiCr) entities. This synergy between core and shell was explained through magnetic dipolar interactions between the core and the shell entities (CsNiCr@CoIIIFeII@CsNiCr particles, 10 nm photoactive shell sandwiched between a 12 nm ferromagnetic core and 5 nm external ferromagnetic shell).

However, almost no photo-transformation was observed by Presle et al. [91] for larger particles ($\text{Rb}_{0.5}\text{CoIIIFeII}_{0.8}@ \text{Rb}_{0.2}\text{NiCr}_{0.7}$ 45 nm core and 26 nm shell), for a similar misfit range, which was again explained due to strong coupling between the core and shell and the ratio between the core and shell thicknesses (shell layers affecting the expansion of core). Although, studies conducted on larger heterostructures (greater than 200 nm, of $\text{Rb}_{0.2}\text{CoIIIFeIII}@ \text{RbMCr}$, where $M = \text{Ni, Co, and Cr}$), with low misfits ($\sim 0.9 \%$) by Talham and co-workers [36][91-93], shows a 90 K decrease in magnetization, due to CTIST induced switching in

core from HS to LS state during the cooling regime. A strained layer with a thickness of 24 nm for KCoCr and 43 nm for KNiCr was proposed [94] see Fig. 2.2, above which a bulk behavior could be considered. This highlights the importance of the volume ratios between the core and the shell in optimizing these mechanical effects, for both SCO core's impact on the shell and vice-versa. This is a simple demonstration of mechanical coupling caused by the CTIST's volume transition. The most significant argument is that, even though CsNiCr shell exerts strain over the core, SCO transition is sustained at a slightly lower transition temperature (though without hysteresis) while the core remains contracted. These examples show how synergies can be obtained by elastically binding the center to a magnetic shell.

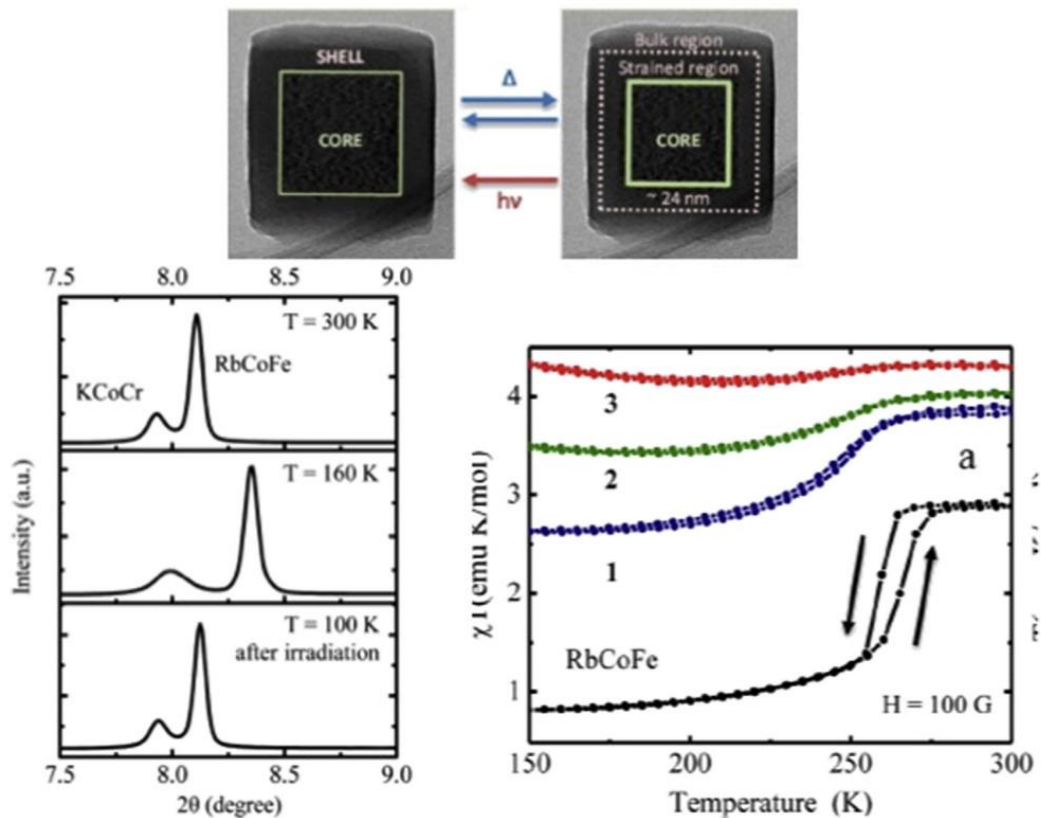


Figure 2. 2 RbCoFe@KCoCr heterostructures and scheme showing the presence of a strained region released by light. (Bottom left) XRD diagrams showing the contraction of the core and strained shell at 160 K and the released strain under light. (Bottom right) $\chi^T = f(T)$ plots for heterostructures comprising a 137 ± 12 nm core and thicknesses of 11 nm (1), 23 nm (2), and 37 nm (3) showing SCO of the core at the same temperature. Adapted from Ref. [94]

Aside from PBA-based core-shells, an interesting illustration was given on iron triazole-based core-shells [52], which combine a $[\text{Fe}(\text{NH}_2\text{trz})_3](\text{BF}_4)_2$ core and a $[\text{Fe}(\text{Htrz})_2(\text{trz})](\text{BF}_4)$ shell with the aim of coupling different SCO behaviors. The rods (crystallites that make up the shell) on the upper/lower sides of the core are shorter than the rods rising on the core sides (see Fig. 2.3).

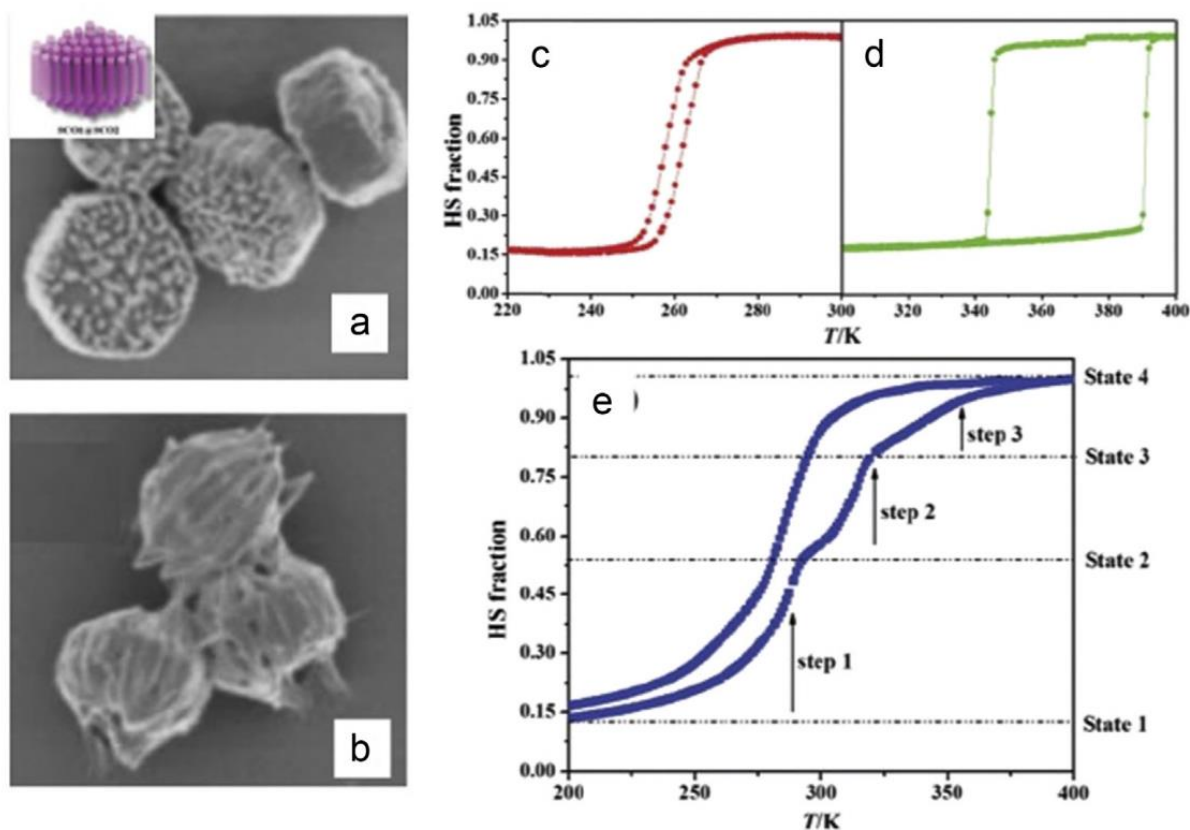


Figure 2. 3 SEM images of the SCO@SCO particles at an early stage (a) and final stage (b). $cT \frac{1}{4} f(T)$ plots for the core alone (c), the shell alone (d), and the resulting core shells (e). Adapted from Ref.[52].

The authors propose a mixed-composition shell with $[\text{Fe}(\text{NH}_2\text{trz})_3\text{z}(\text{Htrz})_3\text{-}3\text{z}](\text{BF}_4)_2$ instead of pure $[\text{Fe}(\text{Htrz})_2(\text{trz})](\text{BF}_4)$. The total SCO behavior indicates the existence of three SCO transitions (core, shell, and interface layer) on the ascending branch, while the $[\text{Fe}(\text{NH}_2\text{trz})_3\text{z}(\text{Htrz})_3\text{-}3\text{z}](\text{BF}_4)_2$ shell has intermediate temperatures, resulting in a very gradual conversion around 285 K.

2.2.2 Theoretical observations

In a pioneering work, Kawamoto and Abe[95] were the first to point out the value of surface relaxations, demonstrating that the hysteresis width decreases with size reduction in a different manner depending on the nanoparticle form. At the same time, the equilibrium temperature remains unchanged (Fig. 2.4). However, experimental observations of phase stability in some coordination nanoparticles have revealed a clear size dependence, resulting in a downshift of the equilibrium temperature and the existence of incomplete transitions[79][81]. Surface chemical reactions, structural disorder, and/or ligand modification by the external

environment may all be blamed for various physical and chemical properties at the surface. Such observations have been taken into account by adding specific boundary conditions (surface molecules fixed in the HS state [96] or a weakening of the ligand field at the surface [97][98]). An investigation of local surface effects using the Ising-like model has shown that the HS surface sheet acts as a "negative pressure" [96], but pressure effects can be grasped through an effective modification of the model (Fig. 5).

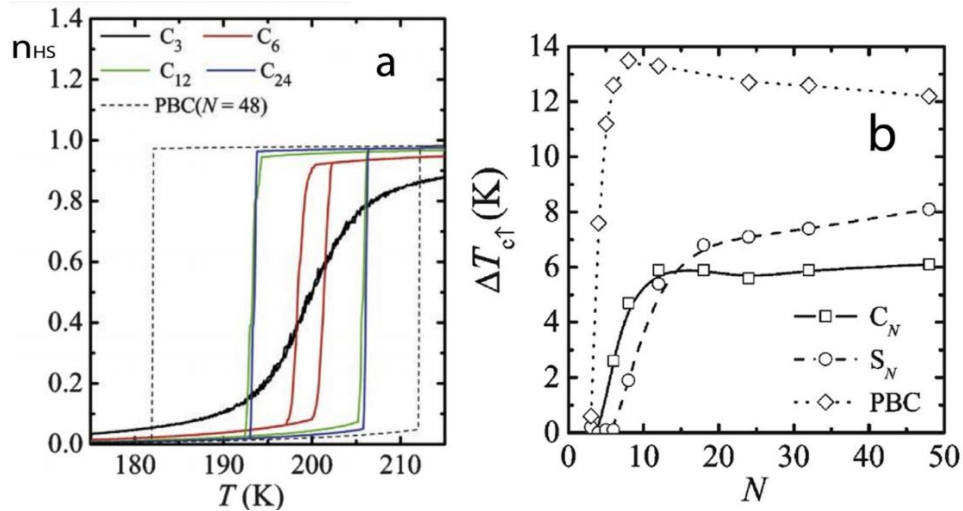


Figure 2. 4 (a) The fraction of the unit in the HS state in an equilibrium state, n_H , for various sizes of cubic particles. For comparison, the result at $N \approx 48$ with the PBC is also shown. (b) Size dependence of the width of the thermal hysteresis ΔT_c for cubic particles (C_N), spherical ones (S_N) and the PBC case.

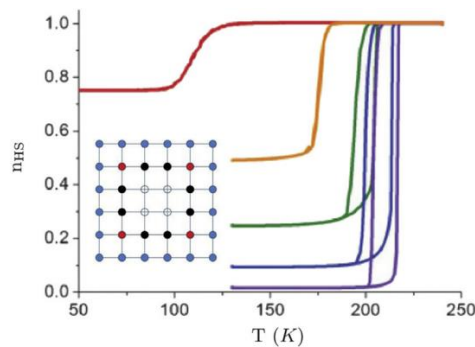


Figure 2. 5 Calculated temperature dependence of the HS fraction for square-shaped nanoparticles of different sizes in the framework of the Ising-like model with fixed boundary conditions (HS state fixed at the surface). From left to right, $L = 4, 7, 10, 40, 200$ (quasi-infinity). Inset: Lattice configuration in the case $L = 6$. Blue filled circles are HS-fixed (edge) atoms. All inside atoms are active: filled red (black) circles stand for atoms having two (one) inactive HS as nearest neighbors, and open circles stand for atoms surrounded by only active sites.

Since the thermodynamic method can allow direct comparisons with experimental observations [99], the existence of surface physical properties different from those

of the nanoparticle core has been integrated in terms of surface energies in a simple nano-thermodynamic model [61]. The so-called core-shell approach is used to create spherical SCO nanoparticles with a bulk (core-like) and a surface (shell-like). As the nanoparticle radius is reduced, the size reduction causes either a downshift or an upshift of the transition temperature (Fig. 2.6b) and follows the same decay as presented in Ref. [96] (Fig. 2.6a). Incomplete transitions and the inactivity of molecules at the surface can also be predicted using thermodynamic models, so the fixed boundary conditions suggested in Ref. [97] are retrieved; however, the possibility of fixing the surface in the LS state is not ruled out. Main conclusions derived thus far from these models are that the surface energy plays a significant role as the driving force of the spin transition at the nanoscale, and downshifting of the transition temperature with the occurrence of a residual HS fraction at low temperature appears to be much more prevalent than upshifting of the transition temperature with the occurrence of a residual LS fraction at low temperature [99].

Continuation is essential to keep enriching the future prospects of any field. Similarly, here spin-phonon models [100-103] and the extension of these models accounting for the volume change during spin transition designed by several groups [104-106] leads to the electro-elastic model [107], which takes into account the coupling between the spin state change of the molecule (from LS to HS) and the change of the local molecular volume in the course of the spin transition and other models including the role of surface relaxations [108][109] and the particle environment [85][110-111]. Oubouchou et al. [107] conducted Monte Carlo simulations using the electro-vibrational model, with a nanoparticle embedded in an external environment whose elastic properties and structure were chosen to be close to the HS phase ("soft" matrix). The strain and local pressure mappings show that raising the thickness of the surrounding medium causes the elastic strain at the nanoparticle/matrix interface to be released and the transition temperature to be lowered (Fig. 2.7). This work results in predicting the thermal hysteresis, which moves according to the atomic surface/volume ratio and is in excellent agreement with the available experimental data of Volatron et al [79]. Since this pioneering work, the electro-elastic model has been extended to incorporate the case of core-shell SCO nanoparticles, made of an active SCO core and an inert shell, where SCO core is investigated in detail as a function of the elastic properties (rigidity, lattice parameter misfit, and size) of the shell [84][112-115]

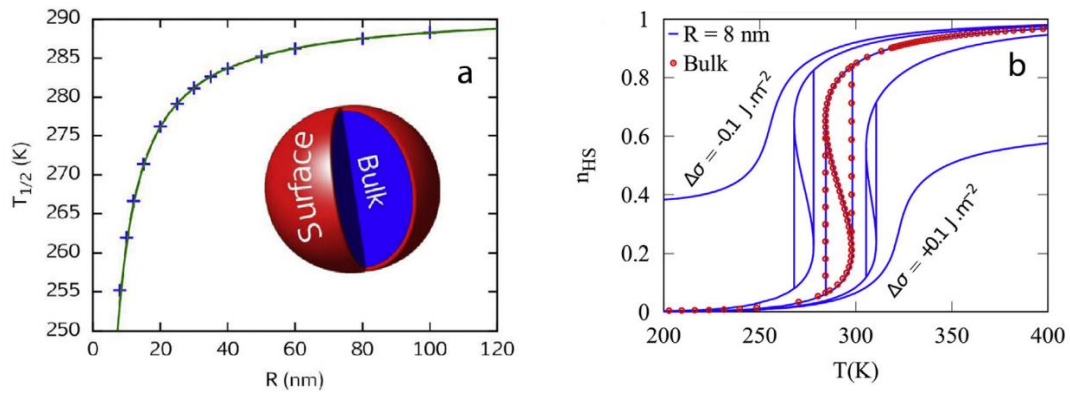


Figure 2. 6 (a) Evolution of the equilibrium temperature with the size reduction. Insert: schematic representations of a spherical core-shell nanoparticle; (b) simulation of spin transition curves with the nano-thermodynamic model. The symbols display the spin transition for the bulk material. The lines show the transition for an 8 nm nanoparticle with different surface energy density differences between the HS and LS phases $\Delta\sigma = \sigma_{HS} - \sigma_{LS}$.

All of these experimental and theoretical findings of the physical properties of hybrid nano-objects and hollow nanoparticles pique enough curiosity and interest to warrant further research for both functional and fundamental reasons, as these structures depict the fundamental role of the external environment and interfacial interactions on phase stability at the nanoscale.

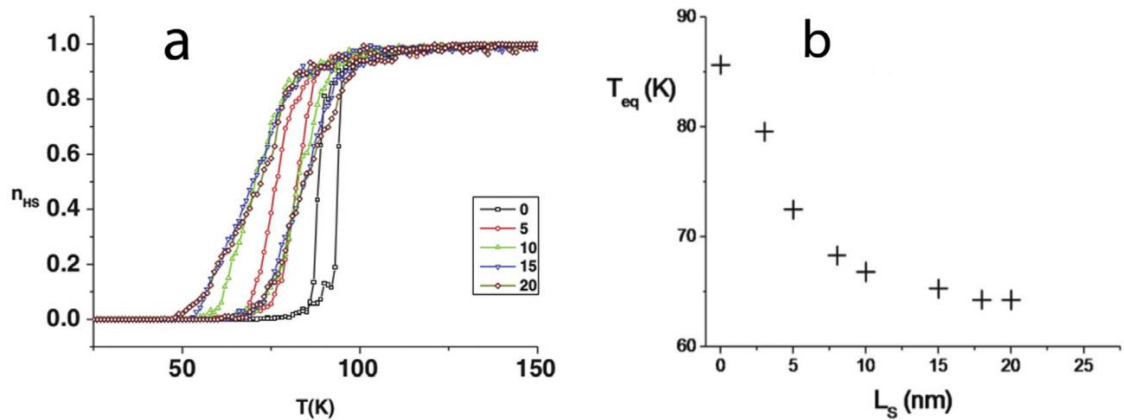


Figure 2. 7 (a) Thermal dependence of the HS fraction for square-shaped nanoparticles at constant core size surrounded by a various number of HS shell layers (0-20). The hysteresis shifts downwards as a result of the negative elastic pressure induced by the shell. (b) Evolution of the equilibrium temperature for different shell thickness (L_S)

Slimani et al. [112] used a similar method to show that if the matrix/nanoparticle couplings are strong enough, the external matrix will retain the bistability property in the SCO nanoparticle. To simulate SCO heterostructures, a further extension of the electro-elastic model was used [85]. Monte Carlo simulation was used to

examine the thickness and rigidity effect of the surrounding shell on the spin transition properties of the core. The SCO core's thermal hysteresis is found to be heavily influenced by the shell rigidity. Furthermore, when the shell rigidity is similar to that of the core, resonance activity is observed (Fig. 2.8).

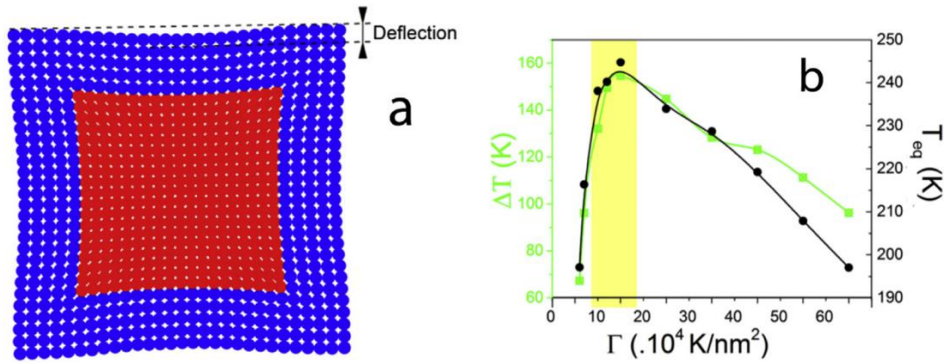


Figure 2. 8 (a) Example of a simulated squared core-shell nanoparticle using the electro-elastic model. The elastic misfit between the core and the shell induces a strain in the heterostructure, which the deflection calculation can quantify. (b) Effect of the shell stiffness on the thermoinduced spin transition of the core-shell nanoparticle: hysteresis width (green line) and equilibrium temperature (black line).

Felix et al.[97] used the spin-phonon model and Monte Carlo simulations to simulate core-shell nanoparticles. The interfacial energy is zero when the core and shell have identical elastic properties, and no change in phase stability shift is observed when compared to the corresponding nanoparticle or hollow nanoparticle. The elastic misfit, on the other hand, causes a compressive (respectively tensile) stress on the SCO core, resulting in an upshift (respectively downshift) in the transition temperature. Despite the fact that elastic models provide an origin for the core-shell coupling process, establishing a relation between Hamiltonian parameters and experimentally accessible quantities remains difficult. As a result, a continuum medium mechanism-based analytical method for modeling a core-shell nanoparticle with a coherent interface has been developed [116]. To optimize the elastic coupling between the core and the shell, a quantitative analysis of the effect of the interfacial elastic energy on phase stability can be carried out, and thus by injecting the interfacial energy density into the model, the spin transformation of the core-shell nanoparticle can be simulated. Since the elastic interaction between molecules is not explicitly taken into account in the model[117] (Slichter and Drickamer), and the elastic interfacial stress cannot be coupled with the distortions occurring during the spin-state transition, the effect of the elastic misfit on collective behavior and bistability cannot be grasped with this model. This is the key disadvantage of this method.

Elastic models are a step forward in understanding the behavior of cooperative

SCO materials and providing a full explanation of the SCO material's interaction with its environment. They are more accurate and functional than mean-field or Ising-like models for simulating phenomenological behaviors of bulk SCO in all of their various yet convergent ways, vastly improving previous models. One of the most challenging tasks is to thoroughly monitor and evaluate the design of the interface in ultrasmall nanosystems (defects, types of bonds, etc.). Computational methods will be crucial in evaluating certain surface/interface energies and guiding chemists in nanostructure optimization.

Experimental investigations in this field have been performed by several groups[52][118-121] among whom, Wang et al. [52] (see Fig. 2.3), in particular, have succeeded to grow high-quality spin-crossover nano-composites, which have different SCO properties since the former has a transition temperature $T_1 = 260$ K and a hysteresis width of 4 K, while the latter shows a transition temperature $T_2 = 368$ K and an associated thermal hysteresis width of 46 K. Thus, these two materials have different ligand fields and most likely different strengths of cooperativity between the molecules. In the experiment, the core is constituted by the material which has the smaller ligand field, which was then covered by the second material (stronger ligand field) in rather hetero-epitaxial conditions. The magnetic studies of the formed nanocomposite, reported by the authors in two References[52][119] showed the occurrence of clearly two transition temperatures on heating, located at 288 K and 314 K. Thus, the transition temperature of the first constituent (the core) increased by 28K while that of the second material (the shell) decreased by 54 K, due to the elastic interplay between the core and the shell nanostructures. Furthermore, a very gradual and third transition involving a small fraction of molecules occurs at 347 K.

In this contribution, we propose to describe an ideal situation of active core-shell SCO nanoparticle, made of two SCO constituents able to convert between LS and HS states, using the electro-elastic model, with electronic and elastic parameters adapted to emulate as far as possible realistic data of SCO nanocomposites. Thus, we have chosen the core to have a smaller transition temperature than that of the shell, as core and shell constitute two different SCO compounds with specific ligand fields and elastic constants. The study of the core-shell nanoparticles is realized by Monte Carlo simulations in 2D lattices with square symmetry, with the aim to reveal the role of the elastic interaction between the two constituents on their transition temperatures on the one hand and the effect of their interplay on the mode of the nucleation and growth of their spin states during their thermal switching on the other hand.

2.3 The Model

As we have discussed in detail about the experimental and theoretical challenges and studies conducted previously. Here, we attempt to simulate a SCO nanocomposite core-shell nanoparticle constructed as a square lattice, where both

the core and the shell atoms can switch between the LS and the HS states. The core geometry is that of a square comprising $N_C \times N_C$ sites, while the shell lattice forms a hollow square formation around the core geometry (see Fig. 2.9a). The number of atomic layers along the width, after the core boundary is considered as shell width and is denoted by N_S . As a result, the number of shell atoms is easily derived as, $(N_C + 2N_S)^2 - N_C^2 = 4 N_S(N_C + N_S)$, and the total number of atoms of the composite is N^2 .

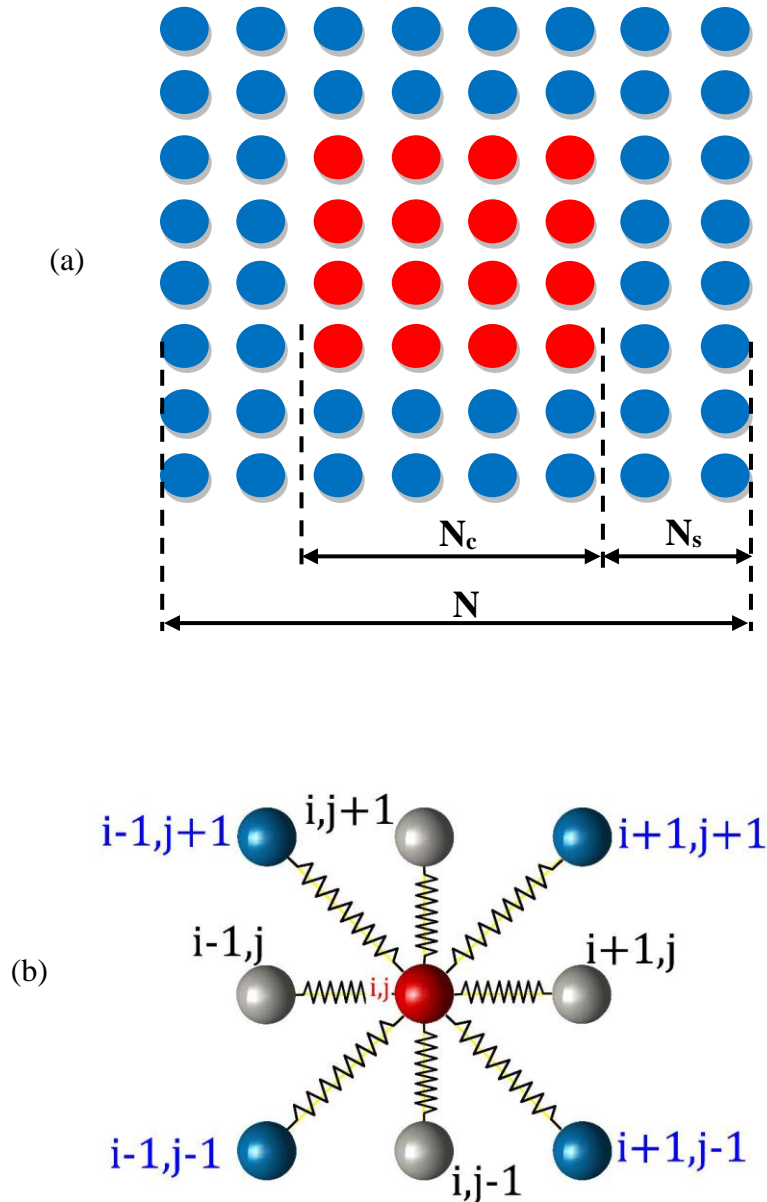


Figure 2. 9 (a) Schematic structure of the SCO nanocomposite. Blue and red dots are two spin-crossover sites belonging to different materials. (b) The configuration of the elastic interaction in the two dimensions square model considered in this study.

As we have already discussed in detail the original electro-elastic model with some

of its thermodynamic properties in recent works. In this model we have introduced coupling between the electronic and elastic state properties which will account for the change in the local volume of the SCO molecules while switching from one state to another. Each atom at site “i, j” is characterized by its spin state $S_i = \pm 1$ and its coordinates (x_i, y_i) . The atoms are constrained to move only in the x-y plane while their spin state and positions are being updated, by taking into account various local and global changes taking place in the lattice, which in turn determine the equilibrium of the system as whole.

In this SCO core-shell nanocomposite (Fig. 2.9a) both core and shell entities have two accessible states, thus the system could be described by two-states fictitious spin S , where $S_i = +1$ or HS and $S_i = -1$ or LS. In order to represent the thermodynamic features of SCO nanocomposites, we extend the general electro-elastic model, which takes into account the coupling of two SCO materials in a particular lattice configuration. The general Hamiltonian^[113] describing SCO lattices is written as follows,

$$H = H_{\text{core}} + H_{\text{shell}} + H_{\text{inter}} \quad (2.1)$$

Where, the core, shell and interface contributions write as follows

$$H_{\text{core}} = \sum_i \frac{1}{2} [\Delta_c - k_B T \ln g] S_i + A_c \sum_{(i,j)}^{\text{nn}} [r_{ij} - R_0(S_i, S_j)]^2 + B_c \sum_{(i,k)}^{\text{nnn}} [r_{ik} - R'_0(S_i, S_k)]^2 \quad (2.2)$$

$$H_{\text{shell}} = \sum_i \frac{1}{2} [\Delta_s - k_B T \ln g] S_i + A_s \sum_{(i,j)}^{\text{nn}} [r_{ij} - R_0(S_i, S_j)]^2 + B_s \sum_{(i,k)}^{\text{nnn}} [r_{ik} - R'_0(S_i, S_k)]^2 \quad (2.3)$$

$$H_{\text{inter}} = A_i \sum_{(i,j)}^{\text{nn}} [r_{ij} - R_0(S_i, S_j)]^2 + B_i \sum_{(i,k)}^{\text{nnn}} [r_{ik} - R'_0(S_i, S_k)]^2 \quad (2.4)$$

In the shell and core Hamiltonians, the first term expresses the effective ligand field energy which contains the contribution of the ligand field Δ (Δ_s for the shell and Δ_c for the core) and that of the entropy $k_B T \ln g$, where, g , is the degeneracy ratio between the HS and the LS states and is assumed to be same for the core and shell constituents. The origin of this degeneracy lies in the change of intra and inter-molecular vibrations spectra during the LS to HS conversion of the spin states.

In the present model, A_c , and B_c (resp. A_s , B_s , and A_i, B_i) represent the elastic constants between the first nearest neighbors (nn) and the next nearest neighbors (nnn) of the core (resp. the shell and the interface). For simplicity's sake, all elastic constants are taken as constant over the whole lattice, to reduce the number of free parameters in the model, we have chosen $A_c = A_s = A_i$ and $B_c = B_s = B_i$.

An added benefit of the present model as we have previously introduced in^[107] is that we can account for the change in the equilibrium distances between two neighboring sites depending on the spin states, or during the spin transition

between LS and HS states. If we take two nodes between nearest- or next-nearest neighbors of the lattice, located at sites (i, j) and (i', j') , which are supposedly connected through springs or spring mimicking entities (polymeric chains) in this case, the instantaneous distance between them is written as $r(i, j | i', j') = |\vec{r}(i', j') - \vec{r}(i, j)|$, whose indexes for the nn are $(i' = i, j' = j \pm 1$ and $i' = i \pm 1, j' = j)$ and for the nnn are $(i' = i \pm 1, j' = j \pm 1)$. This arrangement of molecules (here, the sites) interacts via elastic springs, as depicted in Fig. 2.9b, and the equilibrium bond-lengths of which, denoted $R_0(S_i, S_j)$ (resp. $R'_0(S_i, S_k)$) between two nn (resp. nnn) spin-crossover atoms located at sites i and j (resp. i and k) and having the spin state S_i and S_j (resp. S_i and S_k) are given by

$$R_0(S_i, S_j) = R_0^{\text{HL}} + \frac{\delta_R}{4}(S_i + S_j) \quad (2.5a)$$

$$R'_0(S_i, S_k) = \sqrt{2}R_0^{\text{HL}} + \frac{\delta_R\sqrt{2}}{4}(S_i + S_k) \quad (2.5b)$$

Where the quantities R_0^{HL} and δ_R are, the equilibrium distance of HS-LS configuration and the lattice parameter misfit of two nn sites, between the HS and LS states respectively. They are obtained as a function of the nn equilibrium distances, $R_0^{\text{HH}} = R_0(+1, +1)$, $R_0^{\text{HL}} = R_0(+1, -1)$ and $R_0^{\text{LL}} = R_0(-1, -1)$ as follows,

$$R_0^{\text{HL}} = \frac{R_0^{\text{HH}} + R_0^{\text{LL}}}{2}, \quad (2.6a)$$

$$\delta_R = (R_0^{\text{HH}} - R_0^{\text{LL}}). \quad (2.6b)$$

In view of the complex structure of Hamiltonian of the nanocomposite, in which spin and distortion variables are intricate, which prevents any possible analytical resolution, we employ Monte Carlo to our aid in order to solve this model Hamiltonian and study its thermal properties. We can achieve this through different mechanisms, we can visit these sites sequentially, randomly, or choose the sites randomly but relax both the spin and position for a given site simultaneously, although each procedure has its downside and benefits revolving around metastability and computational time involved. For the current scenario we chose to go with computationally intensive process so as to not compromise on the behalf of metastable states generated. The simulations are performed on the square lattice, by using a sequential procedure in terms of first updating spin and then relaxing lattice position variables, although the sites to update are chosen randomly.

We used stochastic algorithm to conduct these investigations[122] by firstly selecting a site, i , randomly among the N^2 sites of the lattice and calculated its total energy (both electronic and elastic), then its spin state is flipped i.e., if initially spin $S_i = \pm 1$ and position, \vec{r}_i , a new spin value $S'_i = -S_i$ is set without any change in its position, energy is recalculated after each flip. As now we have the energy for both the spin states, next step naturally is to compare the energy of the system in both the states and then employ usual Monte Carlo Metropolis algorithm to decide for

the final outcome. Subsequently, we proceed in the similar fashion to employ second MC process, this time applied on the positions of the sites in order to mechanically relax the lattice. For that, we move over the whole lattice randomly visiting each lattice site, while nudging each site from its instantaneous position by a small displacement δ_R ($\ll R_0^{LL}$) in this case $\delta r = 0.001$ nm, which is much smaller than the average distance between two neighboring sites (~ 1 nm). Afterwards, we compute the difference in total energy due to the change in final and the initial positions and accordingly accept or reject the final outcome employing the same mechanisms used during spin flips. This procedure although computationally intensive can be repeated several times for each spin flip in order to reach the equilibrium from both electronic (spin) and elastic (equilibrium distances) degrees of freedom. For this particular case we repeat the procedure of the lattice relaxation 10 times for each spin flip. Afterwards, a new site will be selected, randomly, and so on. Once all nodes of the lattice are visited for the spin change, we define such step as the unit of the Monte Carlo step and denoted "MCS". In the present simulations, the thermal properties are calculated. At each temperature, we perform 10^5 MCS to reach the equilibrium state and we use 1000 other MCS for the statistics. Within this procedure, each site is displaced $10 \times N_{\text{tot}}^2$ times for 1 MCS. So, at each temperature, each spin state and lattice position are updated $\sim 10^5$ and $10^6 \times N_{\text{tot}}^2$ times, respectively. We have checked that increasing the simulation time does not affect the final results, which ensures that we reached the stationary state for spin and lattice position variables. The system is warmed up from $T = 5$ to 200 K in steps of increment 1 K, and then cooled down to the initial temperature.

2.4 Results and Discussions

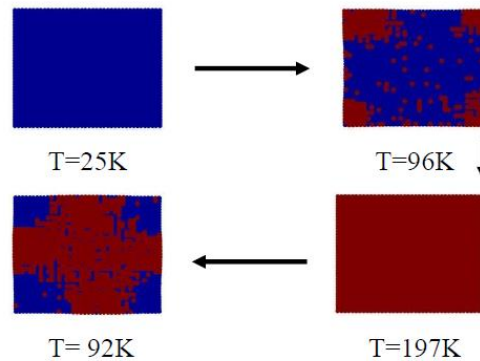
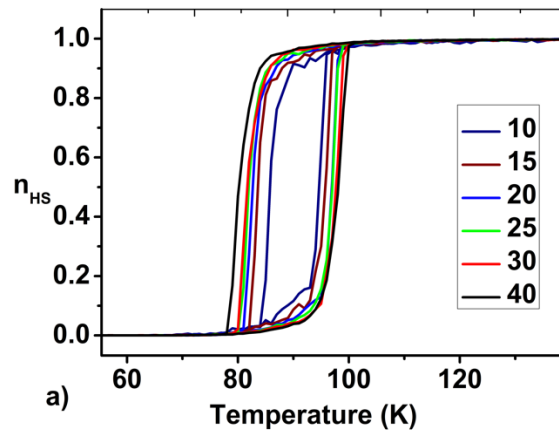
2.4.1 Thermal Properties of the uncoated core

To begin with we will start from investigating the individual core and shell lattice as a function of the temperature for different sizes, we will start from the square shaped core lattice size with cross section ranging from 10×10 to 40×40 , as can be seen in Fig. 2.10a. The parameter values of the model, $\Delta_C = 450$ K, $g = 150$, $A_C = B_C = 10^5$ K.nm⁻² are chosen so as to reach the behavior of a first-order thermal transition with relatively small sizes.

The LS $R_0^{LL} = 1$ nm and HS $R_0^{HH} = 1.05$ nm ($R_{HL} = \frac{R_{HH} + R_{LL}}{2} = 1.025$ nm), lattice parameter distances, are selected after consulting the structural experimental data[123], so that they should reproduce relative lattice expansions ~ 1 -5%, depending on the molecular crystal packing (presence of pi-pi strong $\pi - \pi$ stacking, "weak" hydrogen-hydrogen bonding, etc.). Although these distances should not be confused with the Fe-ligand distances of the molecular coordination sphere.

Eventhough we consider an isotropic deformation of the crystal lattice, anisotropy in unit cell deformations may arise due to elastic constraints imposed by the interactions between ligands of adjacent molecules who have extended spatial occupations[124-126], as observed in several SCO systems and reported in recent theoretical investigations[127][128]. If we survey the experimental data we can find through Brillouin scattering performed on the single crystals of $[\text{Fe}(\text{ptz})_6](\text{ClO}_4)_2$ we have estimates of bulk modulus values ranging from 5–20 GPa [129][130], we have taken this into account while choosing the values for the elastic constants, so that they can lead to an estimated average bulk modulus, $G \approx \frac{\Delta_C}{R_0} \sim 10$ GPa.

It is evident by observing Fig. 2.10a that increase in the size of lattice (core) leads to increase in the width of thermal hysteresis, which could be explained considering the increase in the lifetime of the metastable states, which are stabilized by the long-range elastic interactions between the SCO particles. The transition temperature of MC simulations in Fig 2.10a is more or less near 90 K, which is in excellent agreement with the one given by the relation, $T_{\text{eq}} = \frac{\Delta_C}{k_B \ln g} \sim 90$ K.



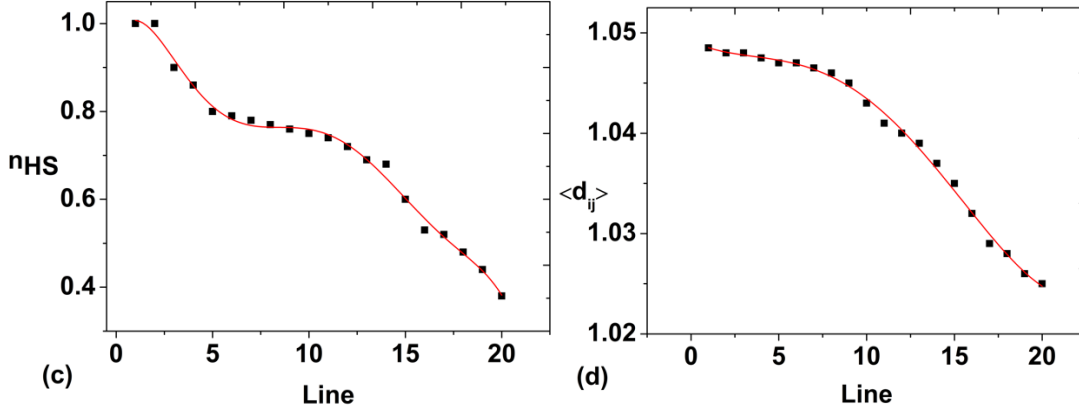


Figure 2.10 (a) Thermal variation of the HS fraction of the bare 2D nanoparticle (with square symmetry) for different sizes, showing the occurrence of a first-order transition and the increase of the thermal hysteresis width with the nanoparticle size. (b) Snapshots showing the spatial distribution of the HS fraction along the thermal hysteresis for the particle 40×40 . (c) and (d) provide the average HS fraction, n_{HS} , and nn distance, $\langle d_{ij} \rangle$, over concentric square perimeters (the center is that of the lattice) as a function of their distance from the center of the nanoparticle for the configuration $T = 92 K$ of panel (b). The parameter values are given in the text.

The spatial distribution of domain nucleation and the HS fraction along the heating and cooling branches of the thermal hysteresis of a bare core lattice of size 40×40 is depicted in Fig 2.10b. As we can see surface effects aids in the propagation of nucleation from the corners toward the center of the lattice, the nucleation cannot start from the center due to the excessive energy barrier it has to face to grow the stable phase inside the metastable one.

To clearly demonstrate and emphasize the role of boundary effects in the present results, we calculate the average nn distance, $\langle d_{ij} \rangle$, and the average magnetization (or HS fraction n_{HS}), over concentric square perimeters, of size $2\ell + 1$ (where ℓ goes from 0 to $(N - 1)/2$), for the temperature $T = 92 K$ during cooling cycle, which are then plotted in Figs. 2.10c and 10d as a function of their distance ($= \ell$) from the center of the nanoparticle. Prima facie, one can clearly remark the effect of boundary conditions over the HS fraction and average nn distances (sigmoidal) which are decreasing in synergy as one move farther from the HS (R_0^{HH}) dominated bulk towards the LS (R_0^{LL}) populated surface of the lattice.

Now that we have studied the core lattice in detail we will see the same for square shaped shell lattice size with layer width ranging from 3 to 10, as can be seen in Fig. 2.11. The parameter values of the model, $\Delta_C = 450 K, g = 150, A_C = B_C = 10^5 K \cdot nm^{-2}$ are chosen same as that of the core. It is again evident by observing Fig. 2.11a that increase in the size of lattice (shell) leads to increase in the width of thermal hysteresis. The transition temperature of MC simulations in Fig 2.11a is more or less near 90 K.

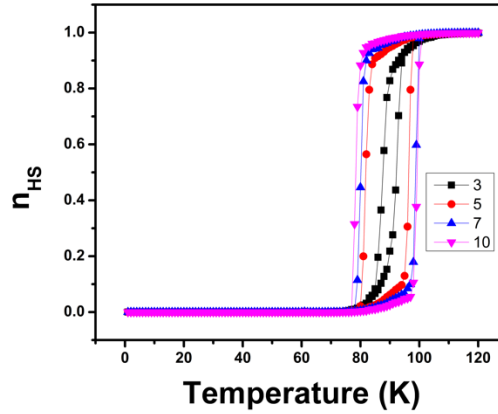


Figure 2. 11 (a) Thermal variation of the HS fraction of the hollow 2D nanoparticle (with square symmetry) for different sizes, showing the occurrence of a first-order transition and the increase of the thermal hysteresis width with the nanoparticle size.

2.4.2 Case of active core and shell spin-crossover nanoparticles

Now that we have studied the core and shell lattices in seclusion, we can move on to spin-crossover nanocomposite, schematically described in Fig. 2.9a. To begin with, we start from 2D lattice with core lattice size, 40×40 , with the same model parameters as those of the uncoated core of Fig. 2.10, although this time it is coupled with a shell lattice, which have a ligand field $\Delta_S = 200 K$ with the same degeneracy ratio as that of the core ($g = 150$), whose width is varied from 0 to 10 layers.

We used the same Monte Carlo procedure to solve the thermodynamic properties of this composite system, which we used for the uncoated core and the hollow shell. The results of the simulations are summarized in the following sections in Figs. 2.12-2.15. To begin with, we study the effect of shell width, by varying the temperature to observe its effects on the total HS fraction of the nanocomposite in Fig. 2.12. Indeed we see that, the difference in ligand fields of the core and the shell of the nanocomposite start playing crucial role as we keep increasing the shell width, a two-step transition behavior is becoming more and more pronounced, with transition temperatures which are constrained between that of the uncoated core ($T_{eq}^{Core} = \frac{\Delta_C}{k_B \ln g} \approx 90 K$) and that of a free shell $T_{eq}^{Shell} = \frac{\Delta_S}{k_B \ln g} \approx 40 K$. Indeed, synergy between the two components of the SCO nanocomposite affects the transition of the whole system leading to the spin transitions appearing in Fig. 2.12 shift to lower temperatures as a function of shell thickness. Evidently, the value of HS fraction in the plateau region of the total nanocomposite increases linearly with the shell-core ratio, this could be understood considering that as we keep increasing the shell width, we affect the HS fraction in two ways: (i) we directly add entities with lower ligand field value i.e., low-temperature transition (around 50 K) in the shell region, (ii) we lower the transition temperature for nano-

composite as whole by the increase in the number of layers will affect the distance of interface region(core surface) from the surface of the composite (shell region), which shift the high-temperature transition (around 100 K) relating to the core to lower temperatures.

Interestingly in Fig. 2.13, we can see these shifts in the equilibrium transition temperatures of both core and shell regions, which behaves almost linearly with the variance in the shell width, as we calculate the average value between the upper and lower transition temperatures, however a difference in slope emerges for both the regions, bigger slope ($\frac{dT_{eq}^{core}}{dN_S} = -1 K$), for the core region which is more affected by the shell thickness, than the shell part ($\frac{dT_{eq}^{shell}}{dN_S} = -0.25 K$).

This difference is attributed to the inherent architectural geometry of the core-shell system, and thus the role played by elastic configurations of the two systems become much more pronounced. By design core which is supposed to be completely bounded by the shell loses its free boundaries and thus any propagation of excess energy (stress, strain) has to be released through shell, and thus the behavior of relaxation will be dependent on the state of the shell (HS and LS relaxation dynamics). Also, depending on the transition dynamics of each region they in turn can affect (favor or disfavor) the transition of the other part, in this case we can see the shell favoring or inciting the LS to HS transition or disfavoring the HS to LS transition in the core.

Since, the shell has a free surface, which helps the relaxation of the elastic energy excess it is only minorly affected from the core behavior. Overall, these aspects, lead to a different behavior for the core and the shell with the change in temperature.

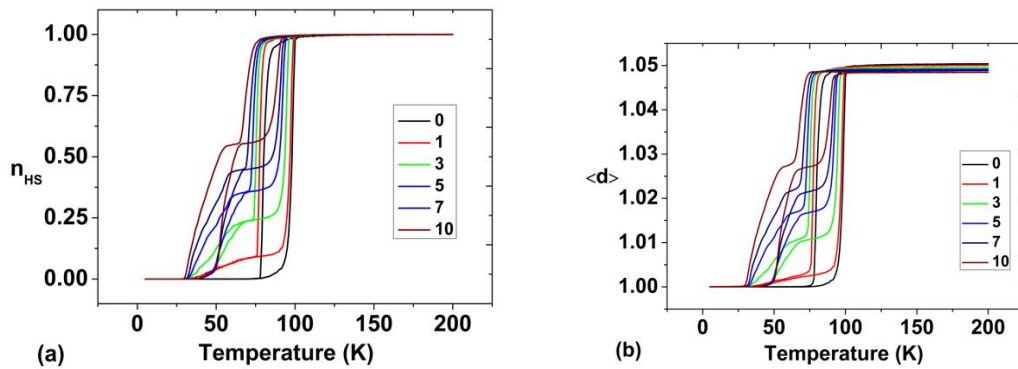


Figure 2. 12 Thermal variation of the total HS fraction (a) and the average lattice parameter (b) of the SCO nanocomposite for different shell thicknesses for a core size 40×40 . The parameter values are: $\Delta_S = 200 K$, $T_{eq}^{shell} \approx 40 K$, $\Delta_C = 450 K$, $T_{eq}^{core} \approx 90 K$. The used values of the elastic constants are: $A_C = A_S = 10^5 K.nm^{-2}$ for nn interactions and $B_C = B_S =$

10^5 K.nm^{-2} for the nnn interactions in the core and the shell. The equilibrium lattice parameter values were $R_0^{HH} = 1.05 \text{ nm}$, $R_0^{LL} = 1 \text{ nm}$ and $R_0^{HL} = 1.025 \text{ nm}$ for both constituents.

However, the transition temperature of a spin-crossover nanocomposite, where SCO core is surrounded by an inert matrix, which have already been studied[71], for core-shell spin crossover and Prussian Blue analogs, behaves differently: it can rise or decrease depending on the sign of the lattice parameter misfit between the core and the shell as a result of the shell's elastic effect, which causes the core to undergo compressive or tensile stress.

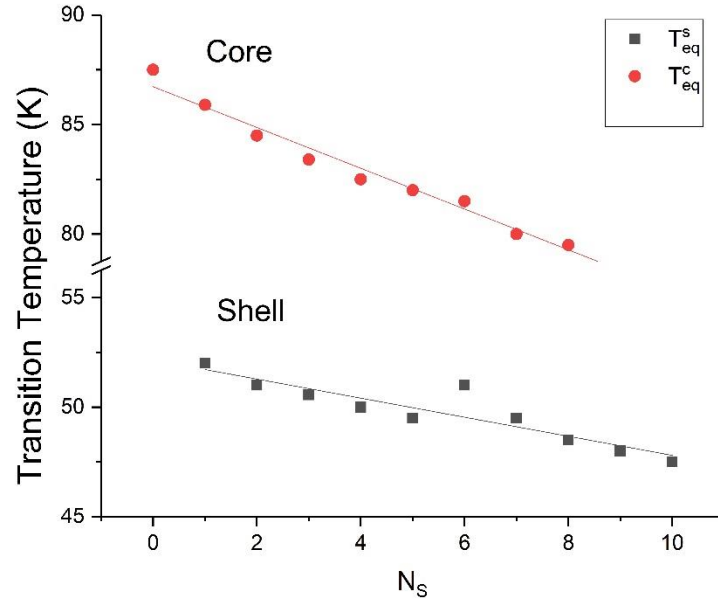


Figure 2.13 Average equilibrium transition temperatures of the shell and the core components of the nanocomposite deduced from MC simulations of Fig. 2.12. Bold lines are the best linear fitting.

2.4.3 Electronic properties of the SCO nanocomposite

To better understand the SCO nanocomposite, we will now dissect the system further into two sub-systems core and shell, and assess the effect of one on the other. In order to get a better perception regarding the synergy between the two SCO subsystems, we plotted the thermal behavior of the average value of the HS fraction of the core (n_{HS}^{Core}) and the shell (n_{HS}^{Shell}), for different shell thicknesses. Figures 2.14a and 2.14b show a summary of the findings.

Let's begin with the core system (Figs. 2.14a). It is evident that upon increasing the shell thickness, the entire hysteresis of the core region is shifted towards lower temperatures. This behavior is in fact bit intuitive if we consider the fact that the transition in shell will induce some elastic effects in both regions, and depending

on the nature of these effects, it may alter the local ligand field by exerting pressure on each connected site at the interface and further connected region during expansion/contraction when heated (resp. cooled), the LS (resp. HS) core benefits from the shell's HS (resp. LS) state, which drives its transition at lower temperature due to the elastic field induced by the shell on the core, which expands (resp. contracts) the core network.

However, Fig. 2.14b differs somewhat. Depending on the results from sec. II, it is easy to deduce that the spin transition made by a free shell (shell without core) is around, $T_{eq}^{shell} = \frac{\Delta_s}{k_B \ln g} \sim 40$ K. In this scenario, we see that as a function of shell width the thermal hysteresis will either have enhancing of its width or will have more of a gradual transition. The latter senses the effect of the core when reducing the size of the shell, as the switch to HS(LS) is hindered by the LS (HS) core state when the shell is heated (cooling), which 'opposes' the expansion (contraction) of the shell. Since the shell is smaller in comparison to core lattice, the benefits of having free surface is easily overpowered by the size effects (ability to accommodate/dissipate excess stress/strain) of the core lattice, and the balance is thus shifted when the shell lattice further grow in size. This point is thus worth noticing that even though a thin shell layer which has much easier access to the surface is found to be more affected by the core elastic strain effect than the thick shell layer thus pointing toward the importance of both surface and size effects, and the roles they play in altering the shell's effective ligand field, which increases/decreases its transition temperature, as shown in Fig. 2.13.

Other than aforementioned processes, other factors are also affecting the transition temperature of the shell lattice, such as core exerting pressure on the shell lattice which prevents single domain nucleation from developing in the thin shells. This could be controlled by enhancing the cooperative character of the shell, resulting in a decrease in its transition temperature towards that of the infinite free shell i.e., $T_{eq}^{shell} = \frac{\Delta_s}{k_B \ln g} \sim 40$ K. One simpler way to do this is simply increasing the shell thickness, which in turn reduces the effect of the core, and improves the cooperativity, thus effectively resulting in the emergence of thermal hysteresis.

Thus, in theory we have another way to control the transition temperature and tailoring the thermal hysteresis. Although it should be taken into account, that in this study, we treated the mechanical properties of the core and the shell as equal, which means that we used the same elastic constants for both elastic networks.

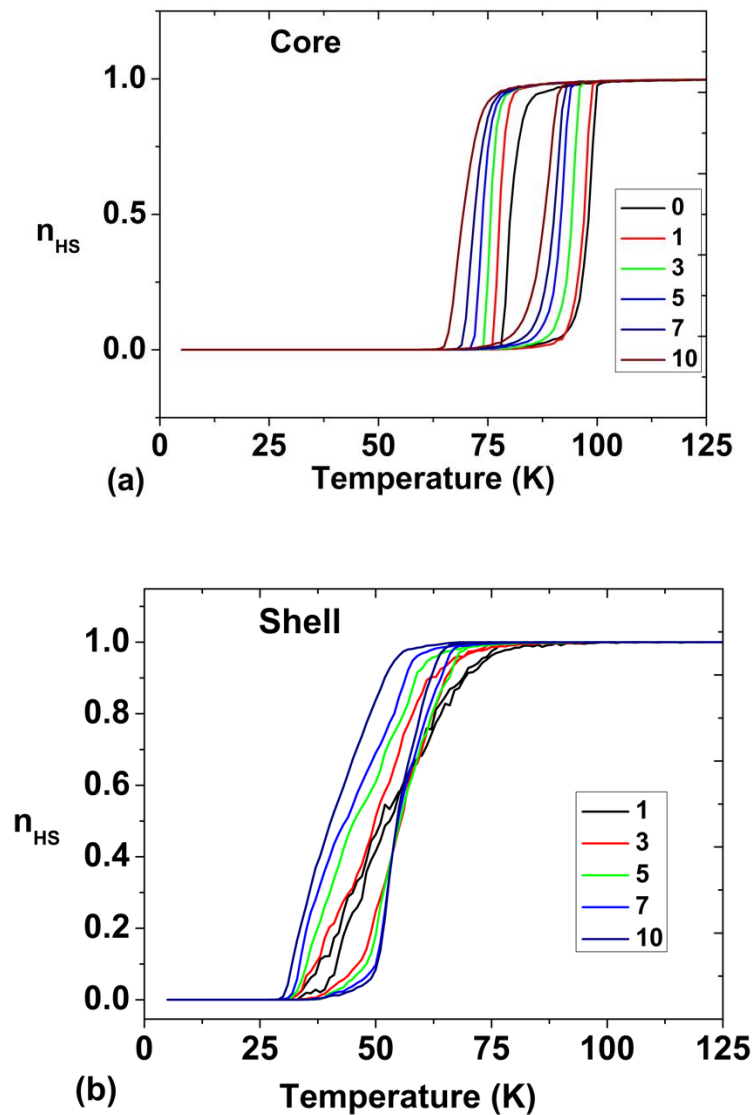


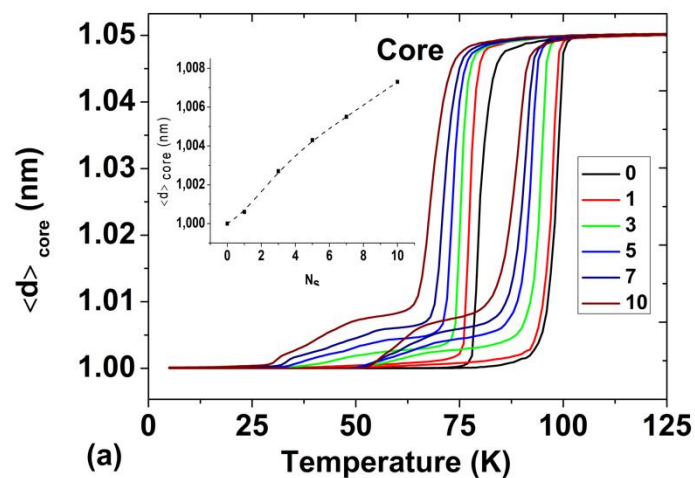
Figure 2. 14: Thermal response of the HS fraction of the core (a) and shell (b) of the SCO nanocomposite, for different shell thicknesses (from $N_s = 0$ to 10), corresponding to the results of Fig. 2.12.

2.4.4 Mechanical properties of the SCO nanocomposite

Now done with the magnetic behavior of the core-shell architecture, we deep dive into the elastic properties of the SCO nanocomposite. To do so, we examine the thermal dependence of its mechanical properties by plotting its average nearest-neighbor (nn) distances for the entire lattice, as shown in Fig. 2.12b. It is interesting to note the similarity between the HS fraction in Fig. 2.12a, and avg. lattice parameter in Fig. 2.12b, with a clear presence of the two-step transitions character in both the hysteresis as a function of shell thickness, depicts a well-coupled magneto-elastic architecture.

To have a better foothold on the SCO nanocomposite behavior, we further dissect the whole architecture into core and shell lattice and examine the thermal dependency of their avg. nn distances as shown in Fig. 2.15a and 2.15b. Moreover, if we look closely, we can see the unfolding of role mechanical coupling plays in this problem, comparing the mechanical responses of the core and the shell in Fig. 2.15a and Fig. 2.15b with the HS fraction of Figs. 2.14a and 2.14b for $N_s = 5$ (for example), shows that on heating (resp. cooling) the avg. nn distances of the core (resp. shell) starts responding to the change of that of the shell (resp. core) before $T=50\text{K}$, while in this temperature range, its corresponding HS fraction is still insensitive to this change. This behavior undoubtedly emphasizes the crucial role of the mechanical coupling between the two subsystems in the resulting thermal behavior of the whole system.

We would now like to focus on the avg. nn parameters values of the core-shell architecture. For different thickness of the shell in Fig. 15, every lattice parameter changes between the LS (1.0) and HS (1.05) nm for the nn values. However, the values of the relaxed shell and core parameters in the plateau area, which stem directly from antagonistic interactions between the core and the shell and within it, are interesting to understand. By using a simple analysis to predict the shell thickness, the next section will better clarify the relevant physical parameters in relation to this aspect.



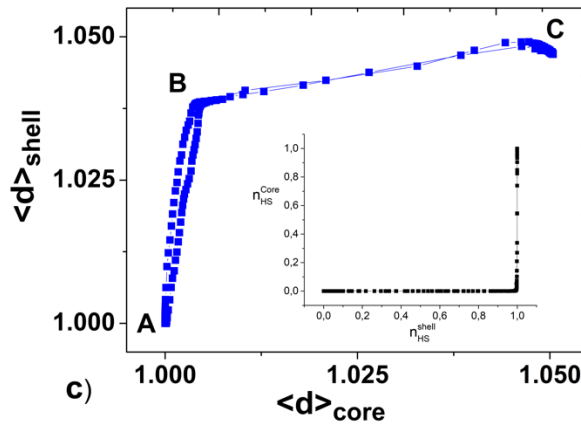
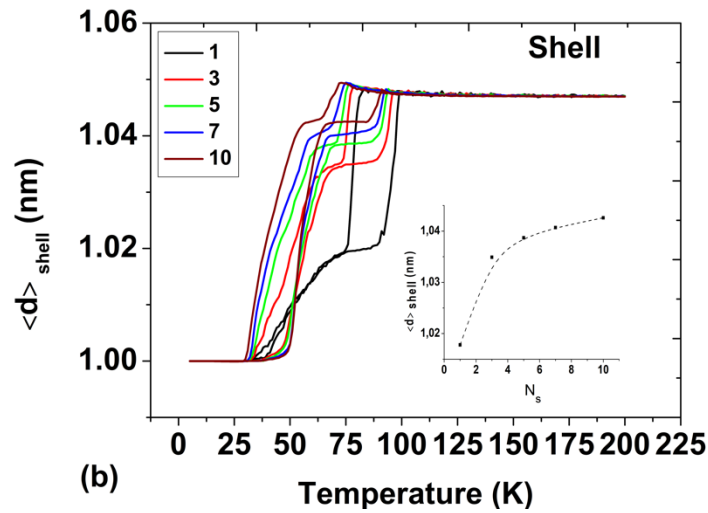


Figure 2. 15 Thermal-dependence of the average nearest-neighbors distance of (a) the core $\langle d \rangle_{\text{core}}$ and (b) the shell $\langle d \rangle_{\text{shell}}$, for different shell thickness values. Insets represent the average nn distance in the plateau region as a function of the shell's thickness. (c) The thermal dependence of the whole core-shell system in the phase space, $(\langle d \rangle_{\text{core}}, \langle d \rangle_{\text{shell}})$ where the temperature is a hidden variable. The associated inset displays the HS fraction of the core vs that of the shell. The parameter values are the same as those of Fig. 2.12.

To emphasize the elastic interaction between the core and the shell, we plot the dependence of the average nn parameter of the core, $\langle d \rangle_{\text{core}}$, as a function of that of the shell, $\langle d \rangle_{\text{shell}}$, in Fig. 2.15c, while in the inset of the figure, we report the dependence of the HS fraction of the core, $n_{\text{HS}}^{\text{Core}}$ vs that of the shell, $n_{\text{HS}}^{\text{Shell}}$ during the thermal transitions for the case of a shell width $N_s = 5$.

Surprisingly, the two HS fractions shown in the inset of Fig. 2.15c seems to be completely separate, as the HS fraction of the core begins to shift only after the entire shell has been converted to the HS state. Figure 2.15c, on the other hand, shows a strong correlation among the structural evolutions of the shell and core

lattice parameters. The changes in the shell's lattice parameter affects the core's lattice parameter. As a result, we can easily see that the shell (resp. the core) experiences a positive (resp. negative) pressure between point A with $n_{\text{HS}}^{\text{Shell}} = 0$ and $n_{\text{HS}}^{\text{Core}} = 0$, and point B with $n_{\text{HS}}^{\text{Shell}} = 1$ and $n_{\text{HS}}^{\text{Core}} = 1$, since $\langle d \rangle_{\text{shell}} < R_0^{\text{HH}}$ (resp. $\langle d \rangle_{\text{core}} > R_0^{\text{LL}}$).

As we can clearly see the transition plays out in two different regime in the core-shell architecture, in the first regime i.e., **A** to **B**, when the shell transforms from LS to HS, the lattice parameter of the shell (resp. core) approaches 1.037 nm (resp. 1.0047 nm) instead of 1.05 nm (resp. 1.0 nm). The retroaction of the core to the spin conversion of the shell creates a non-uniform distribution of compressive and tensile strain within the shell. The core is then transformed in the HS state between points **B** and **C**, from both electronic and elastic degrees of freedom. The latter drives the shell, which completes its elastic conversion, in this regime, where the main elastic changes occur in the core drive.

Thus, in the first regime where the shell converts from LS to HS, the shell's (resp. core's) lattice parameter reaches the value 1.037 nm (resp. 1.0047 nm) instead of 1.05 nm (resp. 1.0 nm). This nonuniform distribution of compressive strain inside the shell and tensile strain is the result of the retroaction of the core to the spin conversion of the shell. Between point **B** and **C**, the core is then converted in the HS state from both electronic and elastic degrees of freedom. In this regime, transformations in the core be the major tour de force in driving the shell transformation and finishing the lagging elastic conversion.

2.4.5 Analytical expressions of the relaxed lattice parameters

To resolve the behavior of the model's elastic properties, which govern the HS fraction, we try analytical model to study the shell-thickness dependency of the mechanically relaxed lattice parameters of the core and shell sections of the nanocomposite.

Although, it's worth noting that the interplay between the elastic properties of the core and the shell SCO parts is quite intriguing, even though bit complicated, and certainly lies in domain where the exact analytical treatment is beyond reach at least for now. By design, the avg. nn distances of the core and shell in the LS and HS states are, R_0^{LL} , and R_0^{HH} respectively. Thus, in these two states, the system is considered in perfectly relaxed state both electronically and elastically.

However, as shown by MC simulations in the previous section, the relaxed lattice parameters of the core and shell in the plateau region, which correspond to a core in the LS state and a shell in the HS state (from an electronic standpoint), are not the same as the pure LS and HS states of free core or shell (from an elastic standpoint).

We present an approximate method for evaluating the relaxed lattice parameters

of the core and shell using analytical expressions. In order to simplify, the strategy is to consider uniform instantaneous nn distances, x_c , x_s and x_i for the core, shell and interface respectively. Then, for each of these three areas of the nanocomposite, we count the number of nn and nnn bonds. Table 1 gives a list of these expressions. This knowledge is then used to calculate the elastic energy, which allows for the determination of equilibrium distances on the one hand, and the expression of transition temperatures on the other hand, using the total energy (elastic + electronic).

Table 2. 1 Number of nn and nnn distances of the core, shell and interface that are used to evaluate the analytical expression of the elastic energy of Eq. (2.7).

Number of bonds	Core	Shell	Interface
nn bonds	$N_c^{nn} = 2 \times N_c(N_c - 1)$	$N_s^{nn} = 2 \times N \times (N - 1) - N_c^{nn} - N_{int}^{nn}$	$N_{int}^{nn} = 4 \times N_c$ (= 0 if $N_s = 0$)
nnn bonds	$N_c^{nnn} = 2 \times (N_c - 1)^2$	$N_s^{nnn} = 2 \times (N - 1)^2 - N_c^{nnn} - N_{int}^{nnn}$	$N_{int}^{nnn} = 8 \times N_c$ (= 0 if $N_s = 0$)

In Table 1, $N = N_c + 2N_s$, represents the total number of atoms along the edge of the core-shell system. On the other hand, the total numbers of atoms in the composite are, $N_t^2 = (N_c + 2N_s)^2$, while inside the core and the shell they are respectively equal to, N_c^2 and $4N_s(N_s + N_c)$.

Since we know that the total elastic energies in the pure LS and HS states are equal to zero, under this assumption, we calculate the expression of the lattice's total elastic energy in the plateau field. As previously stated, we consider a 2D homogeneous lattice with the uniform average nn distances "x" in the core, shell and interface. In the plateau area, however, the equilibrium distances between core nn (resp. nnn) is equal to R_0^{LL} (resp. $R_0^{LL}\sqrt{2}$), that of the shell is R_0^{HH} (resp. $R_0^{HH}\sqrt{2}$) and that of the sites located at the interface is R_0^{HL} (resp. $R_0^{HL}\sqrt{2}$). The instantaneous and equilibrium nn and nnn distances of the core, shell and interface are summarized in Table 2.2.

Table 2. 2 instantaneous and equilibrium nn and nnn distances of the core, shell and interface, considered in the analytical calculations are developed in Eqs. (2.7) and (2.8).

	nn distance	nnn distance	Nn equilibrium distance	nnn equilibrium distance
Core	x	$x\sqrt{2}$	R_0^{LL}	$R_0^{LL}\sqrt{2}$
Shell	x	$x\sqrt{2}$	R_0^{HH}	$R_0^{HH}\sqrt{2}$
Interface	x	$x\sqrt{2}$	$\frac{1}{2}(R_0^{LL} + R_0^{HH})$	$\frac{1}{2}(R_0^{LL} + R_0^{HH})\sqrt{2}$

Using the data of Tables 1 and 2, one can easily calculate the total elastic energy in the plateau region, whose expression is given by

$$E_{\text{elas}} = \left(\frac{A}{2}N_c^{\text{nn}} + BN_c^{\text{nnn}}\right)(x - R_0^{\text{LL}})^2 + \left(\frac{A}{2}N_s^{\text{nn}} + BN_s^{\text{nnn}}\right)(x - R_0^{\text{HH}})^2 + \left(\frac{A}{2}N_i^{\text{nn}} + BN_i^{\text{nnn}}\right)(x - R_0^{\text{HL}})^2 \quad (2.7)$$

Minimizing the elastic energy Eq. (2.7) with respect to the average lattice parameter, x , gives the average relaxed lattice parameter, x_{relax} , as follows:

$$x_{\text{relax}} = \frac{1}{AN_{\text{tot}}^{\text{nn}} + 2BN_{\text{tot}}^{\text{nnn}}} [(AN_c^{\text{nn}} + 2BN_c^{\text{nnn}})R_0^{\text{LL}} + (AN_s^{\text{nn}} + 2BN_s^{\text{nnn}})R_0^{\text{HH}} + (AN_i^{\text{nn}} + 2BN_i^{\text{nnn}})R_0^{\text{HL}}] \quad (2.8)$$

Where, $N_{\text{tot}}^{\text{nn}} = N_c^{\text{nn}} + N_s^{\text{nn}} + N_i^{\text{nn}}$ and $N_{\text{tot}}^{\text{nnn}} = N_c^{\text{nnn}} + N_s^{\text{nnn}} + N_i^{\text{nnn}}$ are the total numbers of nn and nnn bonds inside the whole lattice.

In the plateau area, the relaxed parameter, x_{relax} , is dependent on the shell-thickness, as shown in Fig. 2.16, where the relaxed parameter avg. nn distance is equal to the LS state for a bare core and tends to be similar to the HS lattice parameter for thicker shells.

It's reasonable to wonder why these o K calculations perform so well in comparison to MC data, given that the lattice relaxation in the MC simulations is done at fixed temperatures. In fact, the nanoparticle has a particular spin configuration in the plateau region (all shell atoms are HS and all core atoms are LS), and the aim was to find the lowest elastic energy of this configuration. The analytical approach used here is analogous to lattice relaxation using deterministic Newton equations, given the presence of a high viscosity. This method was first implemented in Miguel et al[128], and its utility was recently evaluated in Traiche et al[127], while analyzing frustrated SCO lattices.

The main reason of its efficiency comes from the fact that, when the right spin configuration is fixed, relaxing the lattice using deterministic mechanics or Molecular Dynamics or Monte Carlo simulations on positions leads to the same average results. However, significant differences will emerge between local and global fluctuations of the average distance (or elastic energy), which are not taken into account in the analytical procedure.

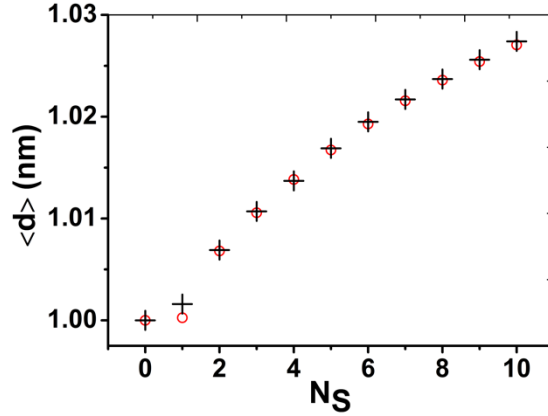


Figure 2.16 Average lattice parameter, $\langle d \rangle$, in the plateau region as a function of the shell's thickness. Black crosses are the results of the MC simulations data and open red circles are the prediction of the analytical treatment, derived from Eq. (2.8).

2.4.6 Spatial distribution of the HS fraction

We monitor the spatial distribution of the HS fraction in the core and shell during the formation of the spin states along the thermal hysteresis of the whole lattice (see Fig. 2.17a), for shell width $N_S = 5$, to gain more insight into the spatiotemporal character of dynamics of the SCO transition. Fig. 2.17b depicts selected snapshots of the system's electronic state along the heating and cooling branches of the related thermal hysteresis. The red (respectively blue) dots represent HS (respectively LS) atoms. During heating, the HS phase domain nucleation appears in the shell portion of the nanocomposite from the corners and spreads around the edges, while the core lattice stays in the LS state, despite the lattice's global volume increasing, causing the core to experience tensile strain from the shell. On the spatial dependence of the lattice parameter along the x-direction for the atomic line located at the coordinate $j = \frac{N}{2}$, in the plateau region, the latter is easily readable (see Fig. 2.17c).

We can see that the nn distances in the shell part are higher than that of the equilibrium distances for the HS state in the shell region, decreases slightly as we get closer to the core-shell interface region (due to the core's mechanical retroaction), and then decreases abruptly in the core region. However, the relaxed lattice parameter remains bigger than its equilibrium values, $R_0^{HH} = 1.05$ nm in the shell, while for the core, it is a bit tricky because in the centre of the core, the distances are higher than that of $R_0^{LL} = 1$ nm while as we move toward the core-shell interface, the nn distances plunge lower than the in the $R_0^{LL} = 1$ nm core. These findings, of course, are dependent on the thickness of the shell, but the conclusions drawn here are qualitatively valid for other sizes.

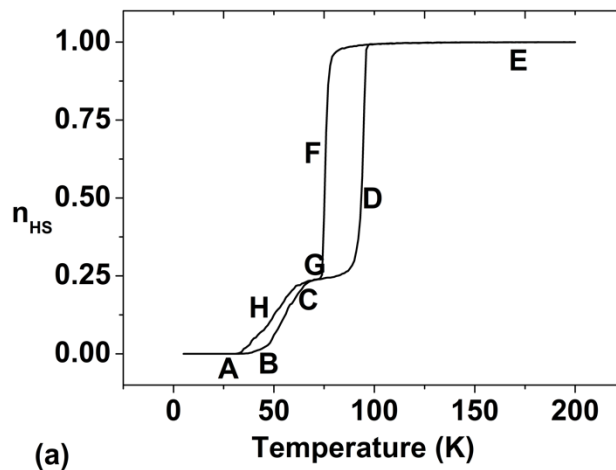
The tensile stress exerted by the shell on the core is presented Fig. 2.17e through

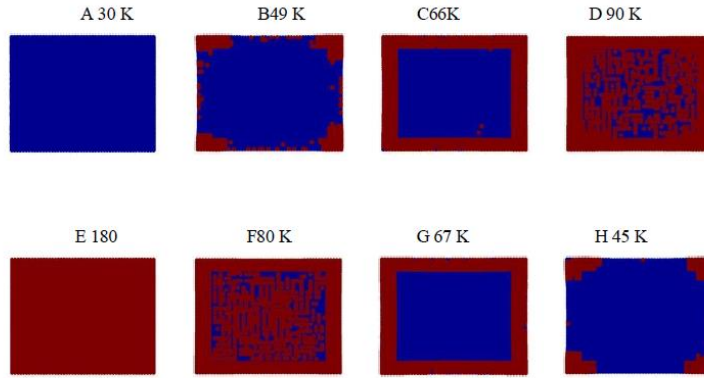
the plot of the spatial map of the local pressure, calculated on each site of the lattice. In Fig. 2.17b, where we report the spatial distribution of the HS and LS states, we can observe a significant change in the growth mode of the HS fraction of the core. Indeed, the transition of the core does not lead to the usual single domain nucleation, in spite of being of first-order (due to the existence of a thermal hysteresis). In fact, the shell facilitates the formation of core nucleation sites, which leads the nucleation to start from everywhere, to form a ramified HS structure, as seen in snapshots (D 90).

On the other hand, following the same procedure as in Fig. 2.10c and 2.10d, to compare the behavior of the bulk and surface sites, we plot in Fig. 2.17d, the average lattice parameter (calculated over concentric square perimeters) as a function of their distance from the center of the core-shell nanoparticle. The obtained results show a continuous increase of the lattice parameter following two regimes: (i) a slow regime in the bulk and (ii) an “explosive” growth starting from the core-shell interface and reaching its maximum at the surface, where the spin state combined with the open boundary effects allow the interatomic distance to reach its maximum value.

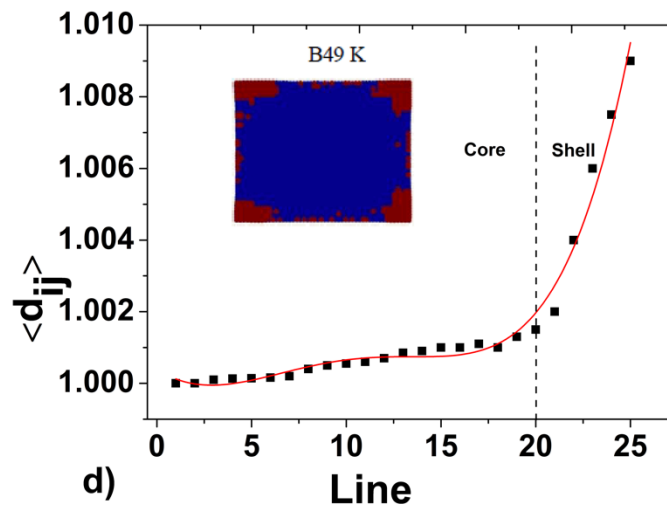
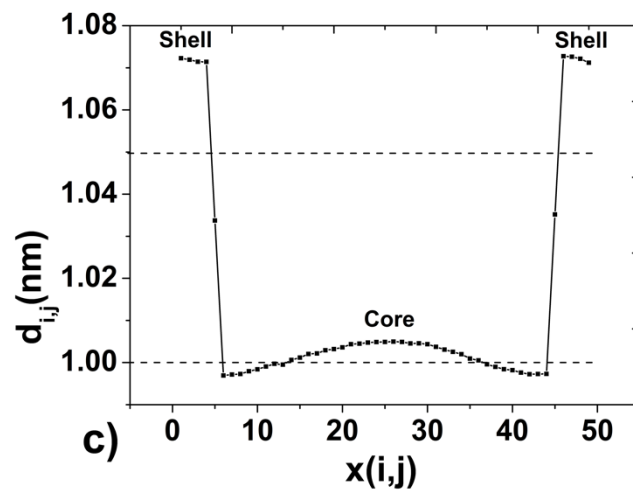
On cooling from the snapshot (E180), the core surrounded by a HS shell switches first to the LS state (G 67). Here, the shell prevents mechanically the HS to LS switching of the core. However, the nucleation of the LS state is initiated preferentially in the vicinity of the interface region (F 80), where the LS state experiences less tensile strain due to the retroaction of the core (see Fig. 2.17c). As a result, the LS domains grow rapidly along the interface region and then propagate towards the center of the lattice.

After the complete transformation of the core, the shell starts to convert from HS to LS from the edge atoms which are favored compared to those of the shell’s corners. Indeed, each shell atom situated in the edge connects to three (one nn and two nnn) HS core atoms, while those of the corner connect only to one HS core atom.





(b)



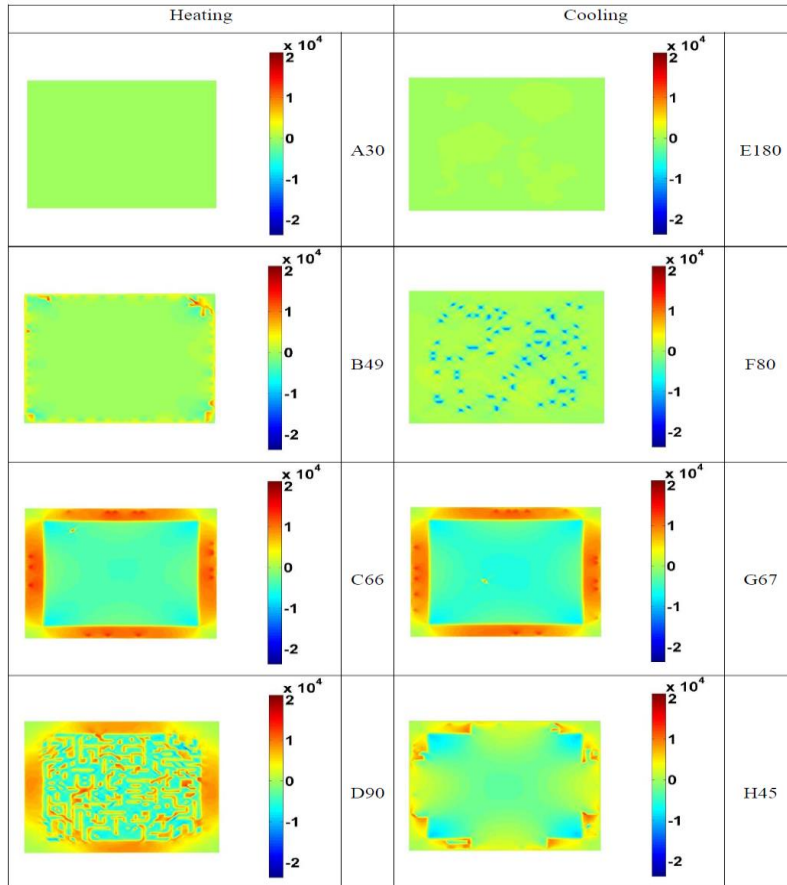
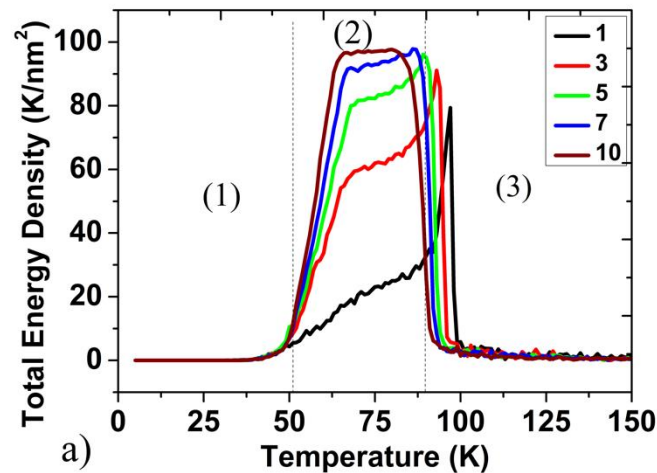


Figure 2. 17 (a) Temperature dependence of the SCO nanocomposite showing a plateau behavior, obtained for $N_C = 40$ and $N_S = 5$. (b) HS fraction snapshots showing the spatial distribution of the HS and LS states corresponding to the thermal hysteresis given in (a). (c) Spatial dependence of the nn distance along the x-direction in the plateau region of the thermal hysteresis of (a). (d) Average nn distance, $\langle d_{ij} \rangle$, calculated over concentric square perimeters (the center is that of the lattice) as a function of their distance from the center of the core-shell for $T = 49$ K on heating. Remark the abrupt increase of the nn distance near the surface. (e) Spatial map of the distribution of the local pressure over the lattice along the thermal hysteresis (a) corresponding to the snapshots of (b).

2.4.7 Elastic energy and spatiotemporal behavior of the nanocomposite at the transition

To continue in the detailed investigations on the physical mechanisms underlying the previous behaviors, we have first calculated the thermal dependence of the total elastic energy density for different shell thicknesses, the results of which are presented in Fig. 2.18a. The contributions from the core and the shell are summarized in Fig. 2.18b and 2.18c. First of all, we observe that the thermal behavior of the total elastic energy exhibits a similar behavior as that of the HS

fraction since it shows the existence of three regions. On heating, the elastic energy density suddenly increases at the transition temperature of the shell (~50 K) then its slope smooths significantly in the region 50-90 K, to increase again before 100 K and to fall down at a higher temperature. These regions ((1), (2) and (3)) fit well with the spatiotemporal behavior of the nanocomposite during the heating process, presented in Fig. 2.18a. We then find that the first abrupt increase of the elastic energy at 50 K corresponds to the nucleation of the HS fraction in the shell part, causing an increase of the misfit elastic energy. While in the plateau region of Fig. 2.18a, we observe deceleration in the increase of elastic energy, which we attribute to the saturation of the HS state in the shell. However due to the connection of the shell with the core, which is still LS, the former experiences a complex tensile/compressive strain spatially distributed over both parts of the nanocomposite. The presence of these strains creates the plateau-like (2nd region) in the thermal behavior of the elastic energy. In this region, the thermal fluctuations increase, leading to the transformation of the core.



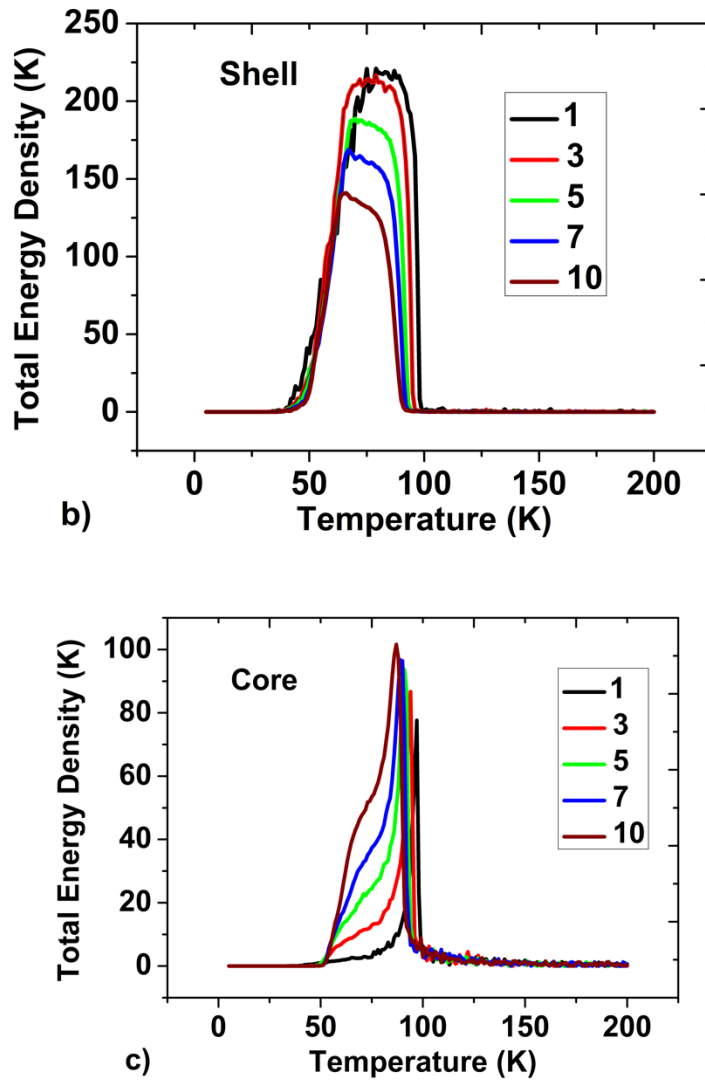


Figure 2. 18 Thermal variation of the total elastic energy density in the whole nanocomposite (a), (b) shell and (c) core, for different shell thicknesses, for the same core size, 40×40 , along with the heating branch of the thermal hysteresis.

2.5 Conclusion

In conclusion, we have analyzed the thermodynamic properties of a spin-crossover nanocomposite made of two different spin-crossover units in the core-shell configuration. We have seen that this configuration allows an efficient mechanical coupling between the two spin-crossover materials since they influence the thermodynamic of each other. Due to this mechanical coupling, the thermal dependence of the total nanocomposite is far from the sum of each of its constituents. To describe this phenomenon, we have adapted our electro-elastic model to the case of a nanocomposite made of two elastically coupled SCO materials having different transitions temperatures and thermal hysteresis widths.

The results showed that according to the difference of transition temperatures and elastic interactions, the nanocomposite may lead to all possibilities of spin transitions: two-step, gradual, one step with thermal hysteresis, etc. In the case of a two-step spin transition, with $T_{eq}^{Shell} < T_{eq}^{Core}$, we found that the transition of the shell part at low temperature does affect significantly the elastic properties of the core (and vice-versa), whose lattice parameter starts to change long before any variation of its spin state. We found that the interplay between the electro-elastic properties of both constituents leads to a complex distribution of a pressure (or elastic energy) inside the lattice. In practice, we have demonstrated that although the thermal spin-transition of the core (in the nanocomposite) is of first-order, the growth of HS macroscopic domains is prevented by the presence of the shell, which changes this mechanism to that of homogenous ramified structures, in a similar way as those observed in the Ising models[131].

Finally, the model results are qualitatively comparable with the available experimental results of Wang et al[52]. Moreover, the quantitative approach to go towards the experimental results should include the size distribution of the nanocomposites (shell/core), the effect of shape [112][132][133] as well as their 3D character[134]. Here, we have considered a square-shaped SCO core nanoparticle surrounded by a regular shell width. However, several parameters may affect the switching properties of the nanoparticles. Among them, one may quote: (i) the existence of voids which occurs in nanoparticles as reported by Lacroix et al[120][135], in magnetic nanoparticles and the presence of microstructural defects. Moreover, as we have emphasized in H.Oubouchou et al[107], the stability of the bulk structure for small particles is questionable, as reported in nanoparticles of Co-Pt bimetallic clusters[136] that have shown different structures, depending on their size. In addition, real nanoparticle materials, involve surface relaxation and surface reconstructions, which may play on the geometric features and act as boundary effects, leading to irregular shapes or widths of the shell. On another level, we mention that to our best knowledge, there were no experimental proofs leading to discriminate between these possible causes. Indeed, most of the experimental studies on SCO nanoparticles, if not all, have been performed have been realized on a large number of nanoparticles. As long as experimental studies on one single nanoparticle, as it was done in magnetic nanoparticles, are not realized in switchable SCO solids, this issue will be still a matter for debate.

Furthermore, an interesting extension of the current model related to the consideration of 2D core-shell triangular lattices[110], which do not require the use of nnn interactions to keep their stability is very appealing, especially if we consider antiferromagnetic interactions between the spin states. Their competition with the magneto-elastic interactions which stabilize long-range ferromagnetic order may lead to nontrivial behaviors; a very interesting problem from both elastic and magnetic point of views, deserving to be investigated in the future.

Finally, we would like to emphasize, that when the rigidities of the core and the shell are significantly different and require the use of different elastic constants

and lattice parameters for the two media, we expect a less efficient core-shell mechanical coupling, due to the existence of an acoustic impedance. The use of SCO materials having different transition temperatures and similar elastic properties is then of interest to generate new multistabilities (two-three or even more steps), which can be used as q-bit systems for memories. SCO nanocomposites made of several multilayers with different transition temperatures constitute an excellent way to design multi-stable SCO materials with high tailored performances.

References: -

- [1] X. M. Li, H. L. Liu, X. Liu, N. Fang, X. H. Wang, and J. H. Wu, "Synthesis of bi-phase dispersible core-shell FeAu@ZnO magneto-opto-fluorescent nanoparticles," *Sci. Rep.*, vol. 5, pp. 1–10, 2015, doi: 10.1038/srep16384.
- [2] K. C. F. Leung *et al.*, "Gold and iron oxide hybrid nanocomposite materials," *Chem. Soc. Rev.*, vol. 41, no. 5, pp. 1911–1928, 2012, doi: 10.1039/c1cs15213k.
- [3] T. Wen and K. M. Krishnan, "Magnetic properties of Au-core-Coshell nanoparticles," *J. Appl. Phys.*, vol. 109, no. 7, pp. 5–8, 2011, doi: 10.1063/1.3544493.
- [4] Y. Tuo *et al.*, "Microbial synthesis of Pd/Fe₃O₄, Au/Fe₃O₄ and PdAu/Fe₃O₄ nanocomposites for catalytic reduction of nitroaromatic compounds," *Sci. Rep.*, vol. 5, no. July, pp. 1–12, 2015, doi: 10.1038/srep13515.
- [5] D. Chen, C. Li, H. Liu, F. Ye, and J. Yang, "Core-shell Au@Pd nanoparticles with enhanced catalytic activity for oxygen reduction reaction via core-shell Au@Ag/Pd constructions," *Sci. Rep.*, vol. 5, no. 19, pp. 1–9, 2015, doi: 10.1038/srep11949.
- [6] S. M. Holmes and G. S. Girolami, "Sol-gel synthesis of KV(II)[Cr(III)(CN)₆]-2H₂O: A crystalline molecule-based magnet with a magnetic ordering temperature above 100°C," *J. Am. Chem. Soc.*, vol. 121, no. 23, pp. 5593–5594, 1999, doi: 10.1021/ja990946c.
- [7] A. J. Epstein, "Organic-Based Magnets : Photoinduced Fractal Magnetism , and Beyond," *Chart*, no. July, pp. 492–499, 2003.
- [8] K. S. Kumar, V. B. Kumar, and P. Paik, "Recent Advancement in Functional Core-Shell Nanoparticles of Polymers: Synthesis, Physical Properties, and Applications in Medical Biotechnology," *J. Nanoparticles*, vol. 2013, pp. 1–24, 2013, doi: 10.1155/2013/672059.
- [9] R. Hayes, A. Ahmed, T. Edge, and H. Zhang, "Core-shell particles: Preparation, fundamentals and applications in high performance liquid chromatography," *J. Chromatogr. A*, vol. 1357, pp. 36–52, 2014, doi: 10.1016/j.chroma.2014.05.010.
- [10] S. Pyne *et al.*, "Synthesis and photo physical properties of Au @ Ag (core @ shell) nanoparticles disperse in poly vinyl alcohol matrix," *J. Nanoparticle Res.*, vol. 13, no. 4, pp. 1759–1767, 2011, doi: 10.1007/s11051-010-9955-9.
- [11] B. Mandal *et al.*, "Core-shell-type lipid-polymer hybrid nanoparticles as a drug delivery platform," *Nanomedicine Nanotechnology, Biol. Med.*, vol. 9, no. 4, pp. 474–491, 2013, doi: 10.1016/j.nano.2012.11.010.
- [12] X. Xie, N. Gao, R. Deng, Q. Sun, Q. H. Xu, and X. Liu, "Mechanistic investigation of photon upconversion in Nd³⁺-sensitized core-shell nanoparticles," *J. Am. Chem. Soc.*, vol. 135, no. 34, pp. 12608–12611, 2013, doi: 10.1021/ja4075002.
- [13] W. Zhu, S. J. Lee, N. J. Castro, D. Yan, M. Keidar, and L. G. Zhang, "Synergistic Effect of Cold Atmospheric Plasma and Drug Loaded Core-shell Nanoparticles on Inhibiting Breast Cancer Cell Growth," *Sci. Rep.*, vol. 6, no. February, pp. 1–11, 2016, doi: 10.1038/srep21974.
- [14] R. Ghosh Chaudhuri and S. Paria, "Core/shell nanoparticles: Classes, properties, synthesis mechanisms, characterization, and applications," *Chem. Rev.*, vol. 112, no. 4, pp. 2373–2433, 2012, doi: 10.1021/cr100449n.
- [15] L. Zhang, R. Tu, and H. Dai, "Parallel core - Shell metal-dielectric-semiconductor germanium nanowires for high-current surround-gate field-effect transistors," *Nano Lett.*, vol. 6, no. 12, pp. 2785–2789, 2006, doi: 10.1021/nl061833b.
- [16] J. Zhang, Y. Tang, K. Lee, and M. Ouyang, "Tailoring light-matter-spin interactions in colloidal hetero-nanostructures," *Nature*, vol. 466, no. 7302, pp. 91–95, 2010, doi: 10.1038/nature09150.
- [17] O. M. Sadek, S. M. Reda, and R. K. Al-Bilali, "Preparation and Characterization of Silica and Clay-Silica Core-Shell Nanoparticles Using Sol-Gel Method," *Adv. Nanoparticles*, vol. 02, no. 02, pp. 165–175, 2013, doi: 10.4236/anp.2013.22025.
- [18] J. Zheng, Z. Q. Liu, X. S. Zhao, M. Liu, X. Liu, and W. Chu, "One-step solvothermal synthesis of Fe₃O₄@C core-shell nanoparticles with tunable sizes," *Nanotechnology*, vol. 23, no. 16, 2012, doi: 10.1088/0957-4484/23/16/165601.
- [19] V. A. Bershtein *et al.*, "Well-defined oxide core-polymer shell nanoparticles: Interfacial interactions, peculiar dynamics,

- and transitions in polymer nanolayers," *Langmuir*, vol. 26, no. 13, pp. 10968–10979, 2010, doi: 10.1021/la101038z.
- [20] H. Khurshid, M. H. Phan, P. Mukherjee, and H. Srikanth, "Tuning exchange bias in Fe/ γ -Fe₂O₃ core-shell nanoparticles: Impacts of interface and surface spins," *Appl. Phys. Lett.*, vol. 104, no. 7, 2014, doi: 10.1063/1.4865904.
- [21] R. H. Kodama, A. E. Berkowitz, E. J. McNiff, and S. Foner, "Surface spin disorder in ferrite nanoparticles (invited)," *J. Appl. Phys.*, vol. 81, no. 8 PART 2B, pp. 5552–5557, 1997, doi: 10.1063/1.364659.
- [22] B. Martínez, X. Obradors, L. Balcells, A. Rouanet, and C. Monty, "Low Temperature Surface Spin-Glass Transition in γ -Fe₂O₃ Nanoparticles," *Phys. Rev. Lett.*, vol. 80, no. 1, pp. 181–184, 1998, doi: 10.1103/PhysRevLett.80.181.
- [23] V. Skumryev, S. Stoyanov, Y. Zhang, G. Hadjipanayis, D. Givord, and J. Nogués, "Beating the superparamagnetic limit with exchange bias," *Nature*, vol. 423, no. 6942, pp. 850–853, 2003, doi: 10.1038/nature01687.
- [24] T. Yamauchi *et al.*, "Magnetic Cu-Ni (core-shell) nanoparticles in a one-pot reaction under microwave irradiation," *Nanoscale*, vol. 2, no. 4, pp. 515–523, 2010, doi: 10.1039/b9nr00302a.
- [25] E. V. Shevchenko *et al.*, "Gold/iron oxide core/hollow-shell nanoparticles," *Adv. Mater.*, vol. 20, no. 22, pp. 4323–4329, 2008, doi: 10.1002/adma.200702994.
- [26] R. H. Kodama, A. E. Berkowitz, E. J. McNiff, and S. Foner, "Surface spin disorder in ferrite nanoparticles," *Mater. Sci. Forum*, vol. 235–238, no. PART 2, pp. 643–650, 1997, doi: 10.4028/www.scientific.net/msf.235-238.643.
- [27] D. Peddis, C. Cannas, G. Piccaluga, E. Agostinelli, and D. Fiorani, "Spin-glass-like freezing and enhanced magnetization in ultra-small CoFe₂O₄ nanoparticles," *Nanotechnology*, vol. 21, no. 12, 2010, doi: 10.1088/0957-4484/21/12/125705.
- [28] K. Maaz, M. Usman, S. Karim, A. Mumtaz, S. K. Hasanain, and M. F. Bertino, "Magnetic response of core-shell cobalt ferrite nanoparticles at low temperature," *J. Appl. Phys.*, vol. 105, no. 11, 2009, doi: 10.1063/1.3139293.
- [29] V. Dimitriadis, D. Kechrakos, O. Chubykalo-Fesenko, and V. Tsiantos, "Shape-dependent exchange bias effect in magnetic nanoparticles with core-shell morphology," *Phys. Rev. B - Condens. Matter Mater. Phys.*, vol. 92, no. 6, pp. 1–6, 2015, doi: 10.1103/PhysRevB.92.064420.
- [30] Z. Nemati, H. Khurshid, J. Alonso, M. H. Phan, P. Mukherjee, and H. Srikanth, "From core/shell to hollow Fe/ γ -Fe₂O₃ nanoparticles: Evolution of the magnetic behavior," *Nanotechnology*, vol. 26, no. 40, 2015, doi: 10.1088/0957-4484/26/40/405705.
- [31] W. Baaziz *et al.*, "High exchange bias in Fe₃- δ O₄@CoO core shell nanoparticles synthesized by a one-pot seed-mediated growth method," *J. Phys. Chem. C*, vol. 117, no. 21, pp. 11436–11443, 2013, doi: 10.1021/jp402823h.
- [32] D. A. Pejaković, A. J. Epstein, C. Kitamura, J. S. Miller, and A. J. Epstein, "Photoinduced Magnetization in the Organic-Based Magnet [Formula presented]," *Phys. Rev. Lett.*, vol. 88, no. 5, p. 4, 2002, doi: 10.1103/PhysRevLett.88.057202.
- [33] R. D. Ser, J. Sci, C. I. Sci, F. Soc, J. Phys, and C. Faculty, "1 25 0]," *Interface*, vol. 141, no. 2, pp. 1990–1992, 1991.
- [34] G. Srinivasan, "Magnetoelectric composites," *Annu. Rev. Mater. Res.*, vol. 40, pp. 153–178, 2010, doi: 10.1146/annurev-matsci-070909-104459.
- [35] K. Miyano, T. Tanaka, Y. Tomioka, and Y. Tokura, "Photoinduced insulator-to-metal transition in a perovskite Manganite," *Phys. Rev. Lett.*, vol. 78, no. 22, pp. 4257–4260, 1997, doi: 10.1103/PhysRevLett.78.4257.
- [36] M. F. Dumont *et al.*, "Photoinduced magnetism in core/shell prussian blue analogue heterostructures of K₃Ni[Cr(CN)₆] · n H₂O with Rb₂Cob[Fe(CN)₆] · n H₂O," *Inorg. Chem.*, vol. 50, no. 10, pp. 4295–4300, 2011, doi: 10.1021/ic1022054.
- [37] D. M. Pajerowski *et al.*, "Photoinduced magnetism in a series of Prussian blue analogue heterostructures," *Chem. Mater.*, vol. 23, no. 12, pp. 3045–3053, 2011, doi: 10.1021/cm2003337.
- [38] T. Mallah, S. Thiébaud, M. Verdaguer, and P. Veillet, "High-TC molecular-based magnets: Ferrimagnetic mixed-valence chromium(III)-chromium(II) cyanides with TC at 240 and 190 kelvin," *Science (80-.)*, vol. 262, no. 5139, pp. 1554–1557, 1993, doi: 10.1126/science.262.5139.1554.
- [39] S. Ferlay, T. Mallah, R. Ouahès, P. Veillet, and M. Verdaguer, "A room-temperature organometallic magnet based on prussian blue," *Nature*, vol. 378, no. 6558, pp. 701–703, 1995, doi: 10.1038/378701a0.
- [40] W. R. Entley and G. S. Girolami, "High-temperature molecular magnets based on cyanovanadate building blocks: Spontaneous magnetization at 230 K," *Science (80-.)*, vol. 268, no. 5209, pp. 397–400, 1995, doi: 10.1126/science.268.5209.397.

- [41] Y. Sato, S. I. Ohkoshi, K. I. Arai, M. Tozawa, and K. Hashimoto, "Solvatomagnetism-Induced Faraday Effect in a Cobalt Hexacyanochromate-Based Magnet," *J. Am. Chem. Soc.*, vol. 125, no. 47, pp. 14590–14595, 2003, doi: 10.1021/ja030375v.
- [42] O. Sato, T. Iyoda, A. Fujishima, and K. Hashimoto, "Photoinduced magnetization of a cobalt-iron cyanide," *Science (80-.)*, vol. 272, no. 5262, pp. 704–705, 1996, doi: 10.1126/science.272.5262.704.
- [43] J. S. Miller and J. L. Manson, "Designer magnets containing cyanides and nitriles," *Acc. Chem. Res.*, vol. 34, no. 7, pp. 563–570, 2001, doi: 10.1021/ar0000354.
- [44] S. I. Ohkoshi *et al.*, "Photoinduced magnetization in copper octacyanomolybdate," *J. Am. Chem. Soc.*, vol. 128, no. 1, pp. 270–277, 2006, doi: 10.1021/ja0559092.
- [45] O. Sato, "Electrochromism and electrochemical magnetism in Ni-Fe Prussian blue," *J. Solid State Electrochem.*, vol. 11, no. 6, pp. 773–779, 2007, doi: 10.1007/s10008-006-0203-2.
- [46] W. Kosaka, K. Nomura, K. Hashimoto, and S. I. Ohkoshi, "Observation of an Fe(II) spin-crossover in a cesium iron hexacyanochromate," *J. Am. Chem. Soc.*, vol. 127, no. 24, pp. 8590–8591, 2005, doi: 10.1021/ja050118l.
- [47] E. Coronado *et al.*, "Pressure-tuning of magnetism and linkage isomerism in iron(II) hexacyanochromate," *J. Am. Chem. Soc.*, vol. 127, no. 13, pp. 4580–4581, 2005, doi: 10.1021/ja043166z.
- [48] V. Niel, J. M. Martínez-Agudo, M. C. Muñoz, A. B. Gaspar, and J. A. Real, "Cooperative spin crossover behavior in cyanide-bridged Fe(II)-M(II) bimetallic 3D Hofmann-like networks (M = Ni, Pd, and Pt)," *Inorg. Chem.*, vol. 40, no. 16, pp. 3838–3839, 2001, doi: 10.1021/ic010259y.
- [49] S. Bonhommeau *et al.*, "One Shot Laser Pulse Induced Reversible Spin Transition in the Spin-Crossover Complex [Fe(C4H4N2){Pt(CN)4}] at Room Temperature," *Angew. Chemie*, vol. 117, no. 26, pp. 4137–4141, 2005, doi: 10.1002/ange.200500717.
- [50] N. R. De Tacconi, K. Rajeshwar, and R. O. Lezna, "Metal Hexacyanoferrates: Electrosynthesis, in Situ Characterization, and Applications," pp. 3046–3062, 2003.
- [51] R. J. Wei, Q. Huo, J. Tao, R. Bin Huang, and L. S. Zheng, "Spin-crossover FeII4 squares: Two-step complete spin transition and reversible single-crystal-to-single-crystal transformation," *Angew. Chemie - Int. Ed.*, vol. 50, no. 38, pp. 8940–8943, 2011, doi: 10.1002/anie.201103648.
- [52] Y. X. Wang *et al.*, "Iron(II)-triazole core-shell nanocomposites: Toward multistep spin crossover materials," *Chem. Commun.*, vol. 52, no. 51, pp. 8034–8037, 2016, doi: 10.1039/c6cc02334g.
- [53] C. Jureschi, J. Linares, A. Rotaru, and Y. Garcia, "Multi-Step in 3D Spin Crossover Nanoparticles Simulated by an Ising Model Using Entropic Sampling Monte Carlo Technique," *Magnetochemistry*, vol. 2, no. 1, p. 13, Mar. 2016, doi: 10.3390/magnetochemistry2010013.
- [54] D. Chiruta, C.-M. Jureschi, J. Linares, P. R. Dahoo, Y. Garcia, and A. Rotaru, "On the origin of multi-step spin transition behaviour in 1D nanoparticles," *Eur. Phys. J. B*, vol. 88, no. 9, p. 233, Sep. 2015, doi: 10.1140/epjb/e2015-60340-x.
- [55] E. Milin, S. Belaïd, V. Patinec, S. Triki, G. Chastanet, and M. Marchivie, "Dinuclear Spin-Crossover Complexes Based on Tetradentate and Bridging Cyanocarbanion Ligands," *Inorg. Chem.*, vol. 55, no. 17, pp. 9038–9046, 2016, doi: 10.1021/acs.inorgchem.6b01542.
- [56] T. Kosone, I. Tomori, C. Kanadani, T. Saito, T. Mochida, and T. Kitazawa, "Unprecedented three-step spin-crossover transition in new 2-dimensional coordination polymer {FeII(4-methylpyridine)2[Au I(CN)2]2}," *Dalt. Trans.*, vol. 39, no. 7, pp. 1719–1721, 2010, doi: 10.1039/b914330k.
- [57] M. Nihei *et al.*, "Multiple bistability and tristability with dual spin-state conversions in [Fe(dpp)2][Ni(mnt)2]2·MeNO2," *J. Am. Chem. Soc.*, vol. 132, no. 10, pp. 3553–3560, 2010, doi: 10.1021/ja910122r.
- [58] A. Kaiba *et al.*, "Crystallographic elucidation of purely structural, thermal and light-induced spin transitions in an iron(ii) binuclear complex," *Dalt. Trans.*, vol. 39, no. 11, p. 2910, Mar. 2010, doi: 10.1039/b914841h.
- [59] M. Seredyuk, K. O. Znovnyak, J. Kusz, M. Nowak, M. C. Muñoz, and J. A. Real, "Control of the spin state by charge and ligand substitution: two-step spin crossover behaviour in a novel neutral iron(ii) complex," *Dalt. Trans.*, vol. 43, no. 43, pp. 16387–16394, Aug. 2014, doi: 10.1039/C4DT01885K.

- [60] H. P. Zhang *et al.*, "Core-shell structured electrode materials for lithium ion batteries," *J. Solid State Electrochem.*, vol. 13, no. 10, pp. 1521–1527, Oct. 2009, doi: 10.1007/s10008-009-0804-7.
- [61] G. Félix *et al.*, "Enhanced Cooperative Interactions at the Nanoscale in Spin-Crossover Materials with a First-Order Phase Transition," *Phys. Rev. Lett.*, vol. 110, no. 23, p. 235701, Jun. 2013, doi: 10.1103/PhysRevLett.110.235701.
- [62] H. J. Shepherd, G. Molnar, W. Nicolazzi, L. Salmon, and A. Bousseksou, "Spin Crossover at the Nanometre Scale," *Eur. J. Inorg. Chem.*, no. 5–6, pp. 653–661, 2013, doi: 10.1002/ejic.201201205.
- [63] A. Bousseksou, G. Molnár, L. Salmon, and W. Nicolazzi, "Molecular spin crossover phenomenon: Recent achievements and prospects," *Chem. Soc. Rev.*, vol. 40, no. 6, pp. 3313–3335, 2011, doi: 10.1039/c1cs15042a.
- [64] A. Rotaru *et al.*, "Size effect in spin-crossover systems investigated by FORC measurements, for surfacted [Fe(NH₂-trz)(3)](Br)(2)center dot 3H(2)O nanoparticles: reversible contributions and critical size," *Eur. Phys. J. B*, vol. 84, no. 3, pp. 439–449, Dec. 2011, doi: 10.1140/epjb/e2011-10903-x.
- [65] A. Carné, C. Carbonell, I. Imaz, and D. Maspoch, "Nanoscale metal–organic materials," *Chem. Soc. Rev.*, vol. 40, no. 1, pp. 291–305, 2011, doi: 10.1039/c0cs00042f.
- [66] R. M. Van Der Veen, O. H. Kwon, A. Tissot, A. Hauser, and A. H. Zewail, "Single-nanoparticle phase transitions visualized by four-dimensional electron microscopy," *Nat. Chem.*, vol. 5, no. 5, pp. 395–402, 2013, doi: 10.1038/nchem.1622.
- [67] L. Catala *et al.*, "Core-Multishell Magnetic Coordination Nanoparticles: Toward Multifunctionality on the Nanoscale," *Angew. Chemie Int. Ed.*, vol. 48, no. 1, pp. 183–187, Jan. 2009, doi: 10.1002/anie.200804238.
- [68] A. C. Felts *et al.*, "Evidence for Interface-Induced Strain and Its Influence on Photomagnetism in Prussian Blue Analogue Core-Shell Heterostructures, Rb₃Co[Fe(CN)₆]₂·xH₂O@K₃Ni[Cr(CN)₆]₂·nH₂O," *J. Phys. Chem. C*, vol. 120, no. 10, pp. 5420–5429, 2016, doi: 10.1021/acs.jpcc.5b10761.
- [69] D. M. Pajerowski, M. J. Andrus, J. E. Gardner, E. S. Knowles, M. W. Melsel, and D. R. Talham, "Persistent photoinduced magnetism in heterostructures of Prussian blue analogues," *J. Am. Chem. Soc.*, vol. 132, no. 12, pp. 4058–4059, 2010, doi: 10.1021/ja100246n.
- [70] D. M. Pajerowski, B. Ravel, C. H. Li, M. F. Dumont, and D. R. Talham, "X-ray Absorption Study of Structural Coupling in Photomagnetic Prussian Blue Analogue Core@Shell Particles," *Chem. Mater.*, vol. 26, no. 8, pp. 2586–2594, Apr. 2014, doi: 10.1021/cm4042007.
- [71] A. Tissot, C. Enachescu, and M. L. Boillot, "Control of the thermal hysteresis of the prototypal spin-transition Fe II(phen)₂(NCS)₂ compound via the microcrystallites environment: Experiments and mechanoelastic model," *J. Mater. Chem.*, vol. 22, no. 38, pp. 20451–20457, 2012, doi: 10.1039/c2jm33865c.
- [72] Y. Chen *et al.*, "Spin crossover-macromolecule composite nano film material," *Chem. Commun.*, vol. 46, no. 28, p. 5073, Jul. 2010, doi: 10.1039/b927191k.
- [73] V. Martínez *et al.*, "Spin crossover phenomenon in nanocrystals and nanoparticles of [Fe(3-Fpy)₂M(CN)₄] (MII = Ni, Pd, Pt) two-dimensional coordination polymers," *Chem. Mater.*, vol. 22, no. 14, pp. 4271–4281, 2010, doi: 10.1021/cm101022u.
- [74] M. Rubio, R. Hernández, A. Nogales, A. Roig, and D. López, "Structure of a spin-crossover Fe(II)@1,2,4-triazole polymer complex dispersed in an isotactic polystyrene matrix," *Eur. Polym. J.*, vol. 47, pp. 52–60, 2011, doi: 10.1016/j.eurpolymj.2010.10.029.
- [75] J. Larionova *et al.*, "Towards the Ultimate Size Limit of the Memory Effect in Spin-Crossover Solids," *Angew. Chemie-international Ed.*, vol. 47, no. 43, pp. 8236–8240, 2008, doi: 10.1002/anie.200802906.
- [76] P. Durand *et al.*, "Room temperature bistability with wide thermal hysteresis in a spin crossover silica nanocomposite," *J. Mater. Chem. C*, vol. 1, no. 10, pp. 1933–1942, 2013, doi: 10.1039/c3tc00546a.
- [77] S. Titos-Padilla, J. M. Herrera, X.-W. Chen, J. J. Delgado, and E. Colacio, "Bifunctional hybrid SiO₂ nanoparticles showing synergy between core spin crossover and shell luminescence properties," *Angew. Chem. Int. Ed. Engl.*, vol. 50, no. 14, pp. 3290–3, Mar. 2011, doi: 10.1002/anie.201007847.
- [78] C. Faulmann, J. Chahine, I. Malfant, D. De Caro, B. Cormary, and L. Valade, "A facile route for the preparation of nanoparticles of the spin-crossover complex [Fe(Htrz)₂(trz)](BF₄) in xerogel transparent composite films," *Dalt. Trans.*,

- vol. 40, no. 11, pp. 2480–2485, 2011, doi: 10.1039/c0dt01586e.
- [79] F. Volatron, L. Catala, E. Rivière, A. Gloter, O. Stéphan, and T. Mallah, “Spin-crossover coordination nanoparticles,” *Inorg. Chem.*, vol. 47, no. 15, pp. 6584–6586, 2008, doi: 10.1021/ic800803w.
- [80] J. Larionova *et al.*, “Towards the ultimate size limit of the memory effect in spin-crossover solids,” *Angew. Chemie - Int. Ed.*, vol. 47, no. 43, pp. 8236–8240, 2008, doi: 10.1002/anie.200802906.
- [81] H. Peng *et al.*, “Re-appearance of cooperativity in ultra-small spin-crossover [Fe(pz){Ni(CN)₄}] nanoparticles,” *Angew. Chemie - Int. Ed.*, vol. 53, no. 41, pp. 10894–10898, 2014, doi: 10.1002/anie.201406710.
- [82] Y. Raza *et al.*, “Matrix-dependent cooperativity in spin crossover Fe(pyrazine)Pt(CN)₄ nanoparticles,” *Chem. Commun.*, vol. 47, no. 41, pp. 11501–11503, 2011, doi: 10.1039/c1cc14463d.
- [83] G. Molnár, S. Rat, L. Salmon, W. Nicolazzi, and A. Bousseksou, “Spin Crossover Nanomaterials: From Fundamental Concepts to Devices,” *Adv. Mater.*, vol. 30, no. 5, pp. 1–23, 2018, doi: 10.1002/adma.201703862.
- [84] A. Slimani, K. Boukheddaden, F. Varret, H. Oubouchou, M. Nishino, and S. Miyashita, “Microscopic spin-distortion model for switchable molecular solids: Spatiotemporal study of the deformation field and local stress at the thermal spin transition,” *Phys. Rev. B*, vol. 87, no. 1, p. 14111, Jan. 2013, doi: 10.1103/PhysRevB.87.014111.
- [85] A. Slimani, H. Khemakhem, and K. Boukheddaden, “Structural synergy in a core-shell spin crossover nanoparticle investigated by an electroelastic model,” *Phys. Rev. B*, vol. 95, no. 17, p. 174104, May 2017, doi: 10.1103/PhysRevB.95.174104.
- [86] S. I. Ohkoshi, H. Tokoro, and K. Hashimoto, “Temperature- and photo-induced phase transition in rubidium manganese hexacyanoferrate,” *Coord. Chem. Rev.*, vol. 249, no. 17-18 SPEC. ISS., pp. 1830–1840, 2005, doi: 10.1016/j.ccr.2004.11.015.
- [87] M. Verdaguer *et al.*, “Molecules to build solids: High T_c molecule-based magnets by design and recent revival of cyano complexes chemistry,” *Coord. Chem. Rev.*, vol. 190–192, pp. 1023–1047, 1999, doi: 10.1016/S0010-8545(99)00156-3.
- [88] M. Presle *et al.*, “Controlled growth of core@shell heterostructures based on Prussian blue analogues,” *New J. Chem.*, vol. 35, no. 6, pp. 1296–1301, 2011, doi: 10.1039/c0nj00857e.
- [89] O. N. Risset and D. R. Talham, “Effects of Lattice Misfit on the Growth of Coordination Polymer Heterostructures,” *Chem. Mater.*, vol. 27, no. 11, pp. 3838–3843, 2015, doi: 10.1021/acs.chemmater.5b00205.
- [90] H. Hafez, Z. Saad, C. Mathonie, L. Catala, and T. Mallah, “Synergy in Photomagnetic/Ferromagnetic Sub -50 nm Core-Multishell Nanoparticles,” 2013.
- [91] M. Presle *et al.*, “Photostrictive / Piezomagnetic Core - Shell Particles Based on Prussian Blue Analogues : Evidence for Confinement Effects ?,” 2014.
- [92] C. R. Gros *et al.*, “Synergistic photomagnetic effects in coordination polymer heterostructure particles of Hofmann-like Fe(4-phenylpyridine)₂[Ni(CN)₄]-0.5H₂O and K_{0.4}Ni[Cr(CN)₆]-0.8 n H₂O,” *Dalt. Trans.*, vol. 45, no. 42, pp. 16624–16634, 2016, doi: 10.1039/c6dt02353c.
- [93] O. N. Risset, T. V. Brinzari, M. W. Meisel, and D. R. Talham, “Light Switchable Magnetism in a Coordination Polymer Heterostructure Combining the Magnetic Potassium Chromiumhexacyanochromate with the Light-Responsive Rubidium Cobalthexacyanoferrate,” *Chem. Mater.*, vol. 27, no. 18, pp. 6185–6188, 2015, doi: 10.1021/acs.chemmater.5b02785.
- [94] O. N. Risset *et al.*, “Olivia N. Risset, † Pedro A. Quintero, ‡ Tatiana V. Brinzari, † Matthew J. Andrus, † Michael W. Lufaso, § Mark W. Meisel, *, ‡ and Daniel R. Talham *, † ‡,” 2014.
- [95] T. Kawamoto and S. Abe, “Thermal hysteresis loop of the spin-state in nanoparticles of transition metal complexes: Monte Carlo simulations on an Ising-like model,” *Chem. Commun.*, vol. 1, no. 31, pp. 3933–3935, 2005, doi: 10.1039/b506643c.
- [96] A. Muraoka, K. Boukheddaden, J. Linarès, and F. Varret, “Two-dimensional Ising-like model with specific edge effects for spin-crossover nanoparticles: A Monte Carlo study,” *Phys. Rev. B - Condens. Matter Mater. Phys.*, vol. 84, no. 5, pp. 1–7, 2011, doi: 10.1103/PhysRevB.84.054119.
- [97] G. Félix, M. Mikolasek, G. Molnár, W. Nicolazzi, and A. Bousseksou, “Tuning the spin crossover in nano-objects: From hollow to core-shell particles,” *Chem. Phys. Lett.*, vol. 607, pp. 10–14, 2014, doi: 10.1016/j.cplett.2014.05.049.

- [98] A. Atitoaie, R. Tanasa, and C. Enachescu, "Size dependent thermal hysteresis in spin crossover nanoparticles reflected within a Monte Carlo based Ising-like model," *J. Magn. Magn. Mater.*, vol. 324, no. 8, pp. 1596–1600, 2012, doi: 10.1016/j.jmmm.2011.12.011.
- [99] V. Shalabaeva *et al.*, "Unprecedented Size Effect on the Phase Stability of Molecular Thin Films Displaying a Spin Transition," *J. Phys. Chem. C*, vol. 121, no. 45, pp. 25617–25621, 2017, doi: 10.1021/acs.jpcc.7b10124.
- [100] J. A. Nasser, "First order high-spin/low-spin phase transition induced by acoustic-phonons," *Eur. Phys. J. B*, vol. 21, no. 1, pp. 3–10, 2001, doi: 10.1007/s100510170206.
- [101] J. A. Nasser, K. Boukheddaden, and J. Linares, "Two-step spin conversion and other effects in the atom-phonon coupling model," *Eur. Phys. J. B*, vol. 39, no. 2, pp. 219–227, 2004, doi: 10.1140/epjb/e2004-00184-y.
- [102] K. Boukheddaden, S. Miyashita, and M. Nishino, "Elastic interaction among transition metals in one-dimensional spin-crossover solids," *Phys. Rev. B*, vol. 75, no. 9, p. 094112, Mar. 2007, doi: 10.1103/PhysRevB.75.094112.
- [103] K. Boukheddaden, M. Nishino, and S. Miyashita, "Molecular dynamics and transfer integral investigations of an elastic anharmonic model for phonon-induced spin crossover," *Phys. Rev. Lett.*, vol. 100, no. 17, p. 177206, May 2008, doi: 10.1103/PhysRevLett.100.177206.
- [104] M. Nishino, K. Boukheddaden, Y. Konishi, and S. Miyashita, "Simple two-dimensional model for the elastic origin of cooperativity among spin states of spin-crossover complexes," *Phys. Rev. Lett.*, vol. 98, no. 24, p. 247203, Jun. 2007, doi: 10.1103/PhysRevLett.98.247203.
- [105] C. Enachescu, L. Stoleriu, A. Stancu, and A. Hauser, "Model for Elastic Relaxation Phenomena in Finite 2D Hexagonal Molecular Lattices," *Phys. Rev. Lett.*, vol. 102, no. 25, p. 257204, Jun. 2009, doi: 10.1103/PhysRevLett.102.257204.
- [106] W. Nicolazzi, S. Pillot, and C. Lecomte, "Two-variable anharmonic model for spin-crossover solids: A like-spin domains interpretation," *Phys. Rev. B*, vol. 78, no. 17, p. 174401, Nov. 2008, doi: 10.1103/PhysRevB.78.174401.
- [107] H. Oubouchou, A. Slimani, and K. Boukheddaden, "Interplay between elastic interactions in a core-shell model for spin-crossover nanoparticles," *Phys. Rev. B*, vol. 87, no. 10, p. 104104, Mar. 2013, doi: 10.1103/PhysRevB.87.104104.
- [108] M. Mikolasek, W. Nicolazzi, F. Terki, G. Molnár, and A. Bousseksou, "Surface transition in spin crossover nanoparticles," *Chem. Phys. Lett.*, vol. 678, pp. 107–111, 2017, doi: 10.1016/j.cplett.2017.04.031.
- [109] M. Mikolasek, W. Nicolazzi, F. Terki, G. Molnár, and A. Bousseksou, "Investigation of surface energies in spin crossover nanomaterials: The role of surface relaxations," *Phys. Chem. Chem. Phys.*, vol. 19, no. 19, pp. 12276–12281, 2017, doi: 10.1039/c7cp01364g.
- [110] C. Enachescu, R. Tanasa, A. Stancu, A. Tissot, J. Laisney, and M. L. Boillot, "Matrix-assisted relaxation in Fe(phen)₂(NCS)₂ spin-crossover microparticles, experimental and theoretical investigations," *Appl. Phys. Lett.*, vol. 109, no. 3, 2016, doi: 10.1063/1.4959262.
- [111] L. Stoleriu, A. Stancu, P. Chakraborty, A. Hauser, and C. Enachescu, "Analysis of first order reversal curves in the thermal hysteresis of spin-crossover nanoparticles within the mechanoelastic model," *J. Appl. Phys.*, vol. 117, no. 17, 2015, doi: 10.1063/1.4914953.
- [112] A. Slimani, K. Boukheddaden, and K. Yamashita, "Thermal spin transition of circularly shaped nanoparticles in a core-shell structure investigated with an electroelastic model," *Phys. Rev. B*, vol. 89, no. 21, p. 214109, Jun. 2014, doi: 10.1103/PhysRevB.89.214109.
- [113] A. Slimani, K. Boukheddaden, F. Varret, M. Nishino, and S. Miyashita, "Properties of the low-spin high-spin interface during the relaxation of spin-crossover materials, investigated through an electro-elastic model," *J. Chem. Phys.*, vol. 139, no. 19, 2013, doi: 10.1063/1.4829462.
- [114] A. Slimani, K. Boukheddaden, and K. Yamashita, "Effect of intermolecular interactions on the nucleation, growth, and propagation of like-spin domains in spin-crossover materials," *Phys. Rev. B*, vol. 92, no. 1, p. 014111, Jul. 2015, doi: 10.1103/PhysRevB.92.014111.
- [115] V. A. Online, "Non-extensivity of thermodynamics at the nanoscale in molecular spin crossover materials : a balance between surface and volume \dagger ," pp. 7358–7367, 2014, doi: 10.1039/c3cp55031a.
- [116] G. Félix, M. Mikolasek, G. Molnár, W. Nicolazzi, and A. Bousseksou, "Control of the Phase Stability in Spin-Crossover

- Core-Shell Nanoparticles through the Elastic Interface Energy," *Eur. J. Inorg. Chem.*, vol. 2018, no. 3, pp. 435–442, 2018, doi: 10.1002/ejic.201700121.
- [117] C. P. Slichter and H. G. Drickamer, "Pressure-induced electronic changes in compounds of iron," *J. Chem. Phys.*, vol. 56, no. 5, pp. 2142–2160, 1972, doi: 10.1063/1.1677511.
- [118] A. Tokarev *et al.*, "Spin crossover polysaccharide nanocomposites," *New J. Chem.*, vol. 37, no. 11, pp. 3420–3432, 2013, doi: 10.1039/c3nj00534h.
- [119] D. Qiu *et al.*, "Spin crossover-graphene nanocomposites: Facile syntheses, characterization, and magnetic properties," *RSC Adv.*, vol. 4, no. 59, pp. 31323–31327, 2014, doi: 10.1039/c4ra04257c.
- [120] C. Gatel *et al.*, "Size-Specific Spin Configurations in Single Iron Nanomagnet: From Flower to Exotic Vortices," *Nano Lett.*, vol. 15, no. 10, pp. 6952–6957, 2015, doi: 10.1021/acs.nanolett.5b02892.
- [121] L.-M. Lacroix, N. Frey Huls, D. Ho, X. Sun, K. Cheng, and S. Sun, "Stable Single-Crystalline Body Centered Cubic Fe Nanoparticles," *Nano Lett.*, vol. 11, no. 4, pp. 1641–1645, Apr. 2011, doi: 10.1021/nl200110t.
- [122] M. Sy *et al.*, "Structure-driven orientation of the high-spin-low-spin interface in a spin-crossover single crystal," *Angew. Chemie - Int. Ed.*, vol. 53, no. 29, pp. 7539–7542, 2014, doi: 10.1002/anie.201403971.
- [123] H. Fourati *et al.*, "Interplay between a crystal's shape and spatiotemporal dynamics in a spin transition material," *Phys. Chem. Chem. Phys.*, vol. 20, no. 15, pp. 10142–10154, 2018, doi: 10.1039/c8cp00868j.
- [124] E. Milin *et al.*, "Elastic Frustration Triggering Photoinduced Hidden Hysteresis and Multistability in a Two-Dimensional Photoswitchable Hofmann-Like Spin-Crossover Metal–Organic Framework," *Inorg. Chem.*, vol. 55, no. 22, pp. 11652–11661, Nov. 2016, doi: 10.1021/acs.inorgchem.6b01081.
- [125] N. Ortega-Villar, M. Muñoz, and J. Real, "Symmetry Breaking in Iron(II) Spin-Crossover Molecular Crystals," *Magnetochemistry*, vol. 2, no. 1, p. 16, Mar. 2016, doi: 10.3390/magnetochemistry2010016.
- [126] A. J. Fitzpatrick *et al.*, "Electronic vs. structural ordering in a manganese(III) spin crossover complex," *Chem. Commun.*, vol. 51, no. 99, pp. 17540–17543, 2015, doi: 10.1039/c5cc05129k.
- [127] R. Traiche, M. Sy, and K. Boukheddaden, "Elastic Frustration in 1D Spin-Crossover Chains: Evidence of Multi-Step Transitions and Self-Organizations of the Spin States," *J. Phys. Chem. C*, vol. 122, no. 7, pp. 4083–4096, Feb. 2018, doi: 10.1021/acs.jpcc.7b12304.
- [128] M. Paez-Espejo, M. Sy, and K. Boukheddaden, "Elastic Frustration Causing Two-Step and Multistep Transitions in Spin-Crossover Solids: Emergence of Complex Antiferroelastic Structures," *J. Am. Chem. Soc.*, vol. 138, no. 9, pp. 3202–3210, Mar. 2016, doi: 10.1021/jacs.6b00049.
- [129] J. Jung, F. Bruchhäuser, R. Feile, H. Spiering, and P. Gülich, "The cooperative spin transition in $[\text{Fe}_x\text{Zn}_{1-x}(\text{ptz})_6](\text{BF}_4)_2$: I. Elastic properties — an oriented sample rotation study by Brillouin spectroscopy," *Zeitschrift für Phys. B Condens. Matter*, vol. 100, no. 4, pp. 517–522, Dec. 1996, doi: 10.1007/s002570050156.
- [130] H. Spiering, K. Boukheddaden, J. Linares, and F. Varret, "Total free energy of a spin-crossover molecular system," *Phys. Rev. B - Condens. Matter Mater. Phys.*, vol. 70, no. 18, pp. 1–15, 2004, doi: 10.1103/PhysRevB.70.184106.
- [131] M. Nishino, C. Enachescu, S. Miyashita, P. A. Rikvold, K. Boukheddaden, and F. Varret, "Macroscopic nucleation phenomena in continuum media with long-range interactions," *Sci. Rep.*, vol. 1, p. 162, 2011, doi: 10.1038/srep00162.
- [132] C. Enachescu, M. Nishino, S. Miyashita, K. Boukheddaden, F. Varret, and P. A. Rikvold, "Shape effects on the cluster spreading process of spin-crossover compounds analyzed within an elastic model with Eden and Kawasaki dynamics," *Phys. Rev. B*, vol. 91, no. 10, p. 104102, Mar. 2015, doi: 10.1103/PhysRevB.91.104102.
- [133] C. Enachescu, M. Nishino, S. Miyashita, L. Stoleriu, and A. Stancu, "Monte Carlo Metropolis study of cluster evolution in spin-crossover solids within the framework of a mechanoelastic model," *Phys. Rev. B*, vol. 86, no. 5, p. 54114, Aug. 2012, doi: 10.1103/PhysRevB.86.054114.
- [134] L. Stoleriu, M. Nishino, S. Miyashita, A. Stancu, A. Hauser, and C. Enachescu, "Cluster evolution in molecular three-dimensional spin-crossover systems," *Phys. Rev. B*, vol. 96, no. 6, p. 064115, Aug. 2017, doi: 10.1103/PhysRevB.96.064115.
- [135] L. M. Lacroix, N. Frey Huls, D. Ho, X. Sun, K. Cheng, and S. Sun, "Stable single-crystalline body centered cubic Fe

- nanoparticles," *Nano Lett.*, vol. 11, no. 4, pp. 1641–1645, 2011, doi: 10.1021/nl200110t.
- [136] G. Rossi, R. Ferrando, and C. Mottet, "Structure and chemical ordering in CoPt nanoalloys," *Faraday Discuss.*, vol. 138, no. 0, pp. 193–210, Feb. 2008, doi: 10.1039/B705415G.

Chapter 3.

Elastic Frustration Driven Unusual Magnetoelastic Properties in a Switchable Core-Shell Spin-Crossover Nanostructure

Adapted from article “Elastic-frustration-driven unusual magnetoelastic properties in a switchable core-shell spin-crossover nanostructure” **Yogendra Singh**, Hassane Oubouchou, Masamichi Nishino, Seiji Miyashita, and Kamel Boukheddaden *Phys. Rev. B* 101, 054105

3.1 Introduction

Heteroepitaxial modification of nanomaterials has become a powerful means to create novel functionalities for various applications. One of the most elementary factors in heteroepitaxial nanostructures is the misfit strain arising from mismatched lattices of the constituent parts. Misfit strain is often used to alter material properties in applications ranging from bandgap tuning for semiconductor electronics to performing work through mechanical actuation and thus provides rational control over materials properties. Spin transitions are accompanied by volume changes in the solid state and are being explored in actuation as a source of mechanical strain inducible by the many controllable stimuli known to trigger spin state changes. The elastic response of dynamic heterostructures depends on a number of factors beyond the simple choice of materials, including the structural dimensions/geometry of the system and the specific nature of the interface.

The lattice mismatch between core and shell regions induces strain, affecting the electronic properties of the shell and core material. The resulting strain modifies the d-band orbital overlap and, thus, the electronic structure of the surface metal [1]. Thus by precise tuning of the misfit parameters as well as by taking advantage of the interaction and/or synergy of the constituent parts, electronic band structure, chemical bonding, and magnetic exchange coupling of heterostructures, a diversity of novel core-shell nanostructures have been prepared with unprecedented optical, and magnetic properties [2-13].

Core-shell structural engineering is one of the most successful strategies for controlling the property of functional nanomaterials. In recent years, advances in chemical synthesis along with the rapid development in experimental (electron microscopy, and X-ray diffraction) and modeling methods have provided an accurate quantification of misfit strain with picometer sensitivity, thereby enabling an extensive understanding of strain build-up and relaxation processes in core-

shell nanocrystals. However, still a detailed understanding of these factors is lacking at small length scales. Another feature frequently observed in such systems is that in general these systems are driven out of equilibrium, and thus the pattern formation is a consequence of instabilities governed by competing forces [14]. The variation in pattern types and length scales is striking, yet one also finds that seemingly unrelated processes may produce patterns with similar characteristics [15-16]. As in most other pattern-forming systems, the instability develops as a compromise between competing forces. Previous work using core-shell heterostructures explored how interfacial strain can be used to modify electronic and phase transition behavior [17-23] in either the core or the shell, often with dramatic results. For the significant stresses encountered in many spin-transition heterostructures, the strain induced in one component is determined in large part by the stiffness of the other, but the stiffnesses of both are determined not only by their chemical nature but also by the heterostructure geometry [24].

As strain is closely related to the property and stability of heteroepitaxial nanostructures, the knowledge of strain evolution can provide additional insights into the behavior of core-shell nanostructures [25-28]. Accordingly, strain engineering is gaining popularity for deliberate control of core-shell nanocrystals [29-35]. Multicomponent hierarchical core/shell configurations may provide enhanced control over misfit strain for maximizing the overall performance of nanomaterials and generate new topics for future research in the meantime. The approach of strain engineering is developing and will continue to expand the controllability of core-shell nanocrystals. However, these studies have largely focused on the strain induced in one of the components, rather than taking a holistic view of the strained heterostructure, and therefore neglected the factors controlling the partitioning of elastic strain between the components [36].

Further progress in utilizing strain effect will hinge on a deepened understanding of strain dynamics and strain distribution. Theoretical efforts modeling spin-transition particles in a matrix provide significant insights, but this remains an area where systematic experimental studies are limited. Intensive studies by both experimental and theoretical means are required to offer theoretical foundation and practical guidance for researchers to refine heteroepitaxial nanostructures and their properties.

Herein, recent investigations on heterogeneous core-shell nanocrystals containing lattice misfit in either of their spin states (High/ Low spin) are summarized. We analyze this strain in core-shell nanocomposite as a function of lattice mismatch with a focus on the mechanistic understanding of strain and strain-induced effects such as shift in its transition temperature, behavior of the transition itself (i.e., gradual/multistep/re-entrant transition), coupling/decoupling of its electronic and elastic synergies. So, the present study of the active core-shell nanoparticles is realized by Monte Carlo simulations, conducted on spin and lattice positions in 2D lattices with square symmetry for simplicity. Core and shell are allowed to switch thermally between Low Spin (LS) and High Spin (HS) states and have different

ligand-fields. We have chosen the core and shell to have equal lattice parameters in the LS (HS) state, while they are different in the HS (LS) state. Moreover, an elastic frustration is considered at the interface, by imposing for the interface bonds antagonist values depending on whether the considered atom belongs to the core or shell parts. Elastic parameters are kept the same for both core and shell in both LS and HS state. We investigate the effect of this lattice misfit in order to study their mechanical (average lattice parameters) and electronical (HS fractions) responses around the transition region with respect to temperature. In this exploratory work, we aim to investigate original situations that have not yet been studied in the experiments; by considering a core with a higher ligand field than that of the shell. The objective here is to draw new predictions on the influence of the magnetoelastic coupling in switchable SCO nanostructures, looking for unprecedented thermal behaviors of HS fraction lattice parameter, emerging from the interplay between the SCO transitions of the core and the shell constituting the nanoparticle.

The manuscript is organized as follows: in Sec. II, we present the model, describe the simulation technique, justify the choice of T_{eq} for core and shell. Sec. III is devoted to the presentation and discussion of the obtained results for the case where we have lattice misfit in HS state and in Sec. IV we discuss the results for the misfit in LS state, finally in Sec. V we conclude and outline some possible developments in the present work.

3.2 The Model

An example of a core-shell structure is schematized in Fig. 3.1a. The core has a square shape containing $N_C \times N_C$ sites and the shell has the shape of a thick frame of width N_S surrounding all the core. As a result, the number of shell atoms is $(N_C + 2N_S)^2 - N_C^2 = 4N_S(N_C + N_S)$, and the total number of atoms of the nanocomposite is N_{tot}^2 , where $N_{tot} = N_C + 2N_S$.

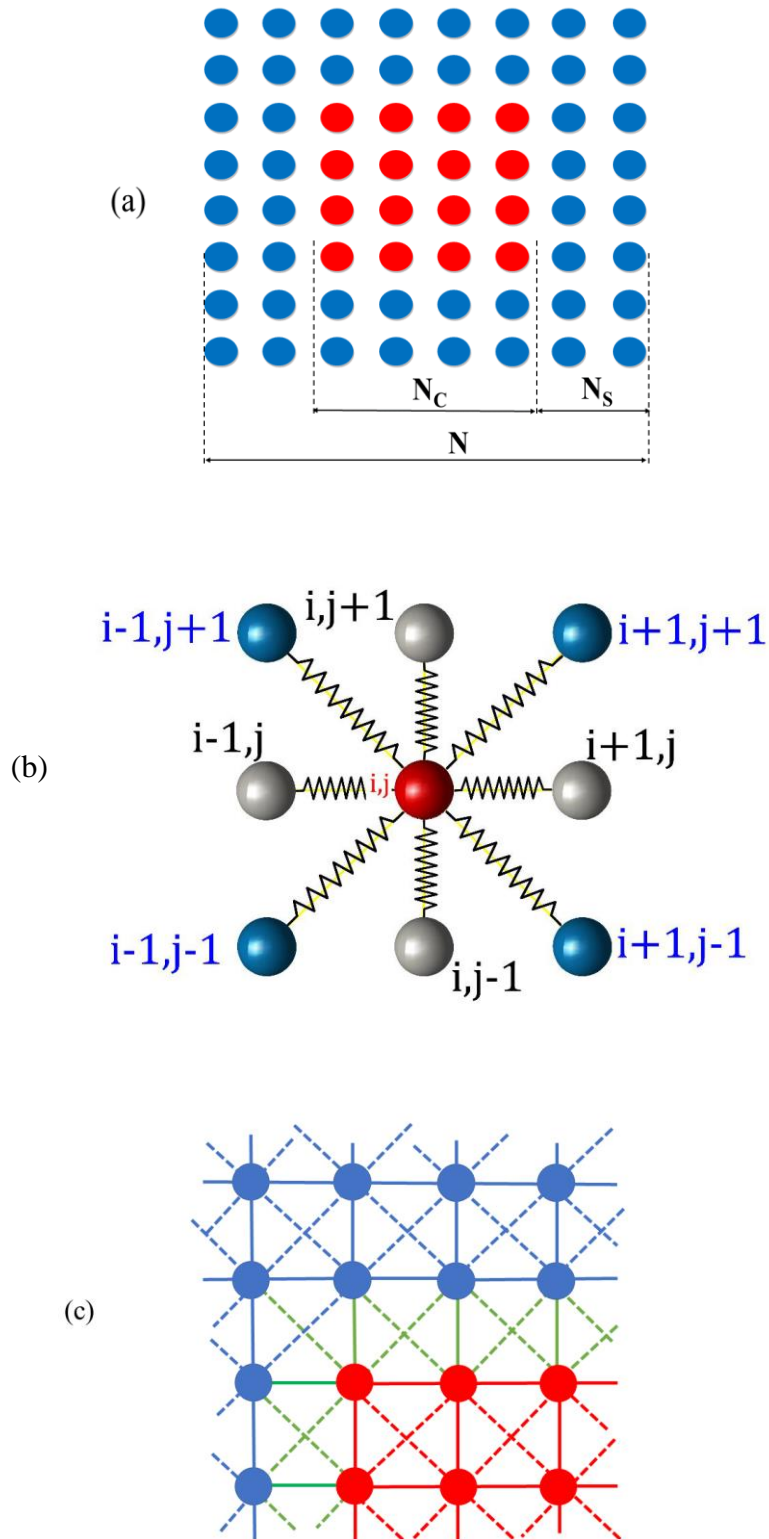


Figure 3. 1 (a) Schematic structure of the SCO nanocomposite. Blue and red dots are two spin-crossover sites belonging to different materials. (b) The configuration of the elastic interactions in the two dimensions' square model considered in this study showing a central red ball connected by springs to grey and blue sites, representing the nearest and next-nearest neighbors respectively. (c) The blue, green and red solid lines denote $R_0^S(S_i, S_j)$,

$R_0^{int}(S_i, S_j)$, and $R_0^C(S_i, S_j)$, respectively. The blue, green and red dashed lines denote $d_0^S(S_i, S_j)$, $d_0^{int}(S_i, S_j)$, and $d_0^C(S_i, S_j)$, respectively. As a reference lattice, we take $R_0^S(-1, -1) = R_0^{int}(-1, -1) = R_0^C(-1, -1) = 1$ ($R_{0,S}^{LL} = R_{0,C}^{LL} = R_{0,int}^{LL} = 1$).

Each core or shell sites, i , may have two states, HS or LS-with respective fictitious spin values $S_i = +1$ (HS) and $S_i = -1$ (LS). The present model includes the change of the local volume of the SCO molecules during their switching from one state to the other. Each atom located at site " i " is described by its spin state S_i and its coordinates (x_i, y_i) . The atoms are constrained to be in the plane. The position and spin state change in the MC simulation depends on the energetic situation. The reader can find a review of the original electro-elastic model, for which we have already discussed in detail some of its thermodynamic properties in recent works [37-39].

The Hamiltonian [40]describing the core-shell system is written as,

$$H = H_{core} + H_{shell} + H_{inter}, \quad (3.1)$$

where the core and shell contain electronic (H_{core}^{elec} and H_{shell}^{elec}) and elastic (H_{core}^{elast} and H_{shell}^{elast}) contributions, while the interface has only elastic interactions, written as follows:

$$H_{core}^{elec} = \sum_i \frac{1}{2} [\Delta_c - k_B T \ln g] S_i, \quad (3.2a)$$

$$H_{core}^{elast} = A_c \sum_{(i,j)}^{nn} [r_{ij} - R_0^C(S_i, S_j)]^2 + B_c \sum_{(i,k)}^{nnn} [r_{ik} - d_0^C(S_i, S_k)]^2 \quad (3.2b)$$

$$H_{shell}^{elec} = \sum_i \frac{1}{2} [\Delta_s - k_B T \ln g] S_i, \quad (3.3a)$$

$$H_{shell}^{elast} = A_s \sum_{(i,j)}^{nn} [r_{ij} - R_0^S(S_i, S_j)]^2 + B_s \sum_{(i,k)}^{nnn} [r_{ik} - d_0^S(S_i, S_k)]^2 \quad (3.3b)$$

$$H_{inter}^{elast} = \frac{1}{2} (H_{inter}^{C,elast} + H_{inter}^{S,elast}) \quad (3.4a)$$

where,

$$H_{inter}^{C,elast} = A_{int} \sum_{(i,j)}^{nn} [r_{ij} - R_{0C-S}^{int}(S_i, S_j)]^2 + B_{int} \sum_{(i,k)}^{nnn} [r_{ik} - d_{0C-S}^{int}(S_i, S_k)]^2, \quad (3.4b)$$

$$H_{inter}^{S,elast} = A_{int} \sum_{(i,j)}^{nn} [r_{ij} - R_{0S-C}^{int}(S_i, S_j)]^2 + B_{int} \sum_{(i,k)}^{nnn} [r_{ik} - d_{0S-C}^{int}(S_i, S_k)]^2. \quad (3.4c)$$

Hamiltonians are given in Eqs. (3.2a, 3.2b) (resp. Eqs. (3.3a, 3.3b)) account exclusively for the energetic contribution of core (resp. shell) atoms only. The elastic interface energy (Eq. (3.4a)) is split in two contributions related to the core (Eq. (3.4b)) and the shell (Eq. (3.4c)) parts. Here, we consider that a core imposes

its equilibrium distances at the interface to its neighboring shell atoms, and vice-versa for the shell. The situation is similar to that of two adversaries sharing the same extended border and where everyone considers it belongs to him.

In the Hamiltonians of core (3.2a) and shell (3.3a), the first term expresses the effective ligand field energy (Δ_c for the core and Δ_s for the shell) and that of the entropy effects, $k_B T \ln g$, where g is the degeneracy ratio between the HS and the LS states, which is assumed here as same for both constituents and temperature-independent. A_C and B_C (resp. A_S and B_S) are the elastic constants of the core (resp. the shell) of the first nearest neighbors (nn) and the next nearest neighbors (nnn), respectively. Similarly, the elastic constants in the interface region are noted by A_{int} and B_{int} and are considered the same whatever the nature (core or shell) of the considered atom. In addition, to reduce the number of free parameters in the model, we have chosen $A_C = A_S = A_{int}$ and $B_C = B_S = B_{int}$.

To account for the volume change at the transition obtained in experimental structural studies⁶¹, which reported relative lattice expansions of $\sim 1-5\%$, the equilibrium bond lengths (the equilibrium distance) between two neighboring sites depend on their spin states, as already introduced in previous work [40]. Here, the molecules interact via elastic springs (see Fig. 1b). The equilibrium bond-lengths are denoted $R_0^x(S_i, S_j)$ (resp. $d_0^x(S_i, S_k)$) for two nn (resp. nnn) atoms S_i, S_j (resp. S_i, S_k). For the core and the shell bonds, they are given by

$$R_0^x(S_i, S_j) = R_{0,x}^{HL} + \frac{\delta_R^x}{4}(S_i + S_j), \quad (3.5a)$$

$$d_0^x(S_i, S_k) = \sqrt{2}(R_{0,x}^{HL} + \frac{\delta_R^x}{4}(S_i + S_k)), \quad (3.5b)$$

where $x = C, S$ stands for the core and shell, respectively. The quantities $R_{0,x}^{HL}$ and δ_R^x are respectively the nn equilibrium distance in the HS-LS configuration and the misfit between the lattice parameters of the HS and LS phases ($\delta_R^x = R_0^x(+1, +1) - R_0^x(-1, -1)$, where, $x=S, C$).

These quantities are obtained as a function of the different lattice parameters, $R_{0,x}^{HH} = R_0^x(+1, +1)$, $R_{0,x}^{HL} = R_0^x(+1, -1)$ and $R_{0,x}^{LL} = R_0^x(-1, -1)$ as follows,

$$R_{0,x}^{HL} = \frac{R_{0,x}^{HH} + R_{0,x}^{LL}}{2}, \quad (3.6a)$$

$$\delta_R^x = (R_{0,x}^{HH} - R_{0,x}^{LL}). \quad (3.6b)$$

For interface bonds, made of core and shell atoms, the equilibrium bond lengths, $R_{0\ C-S}^{int}(S_i, S_j)$ (resp. $R_{0\ S-C}^{int}(S_i, S_j)$) where S_i is the spin state of the core (resp. shell) site and S_j is that of the shell (resp. core), is given by

$$R_{0\ x-y}^{int}(S_i, S_j) = R_{0,x}^{HL} + \frac{\delta_R^x}{4}(S_i + S_j) \quad (3.7a)$$

$$d_{0\ x-y}^{int}(S_i, S_k) = \sqrt{2}(R_{0,x}^{HL} + \frac{\delta_R^x}{4}(S_i + S_k)), \quad (3.7b)$$

Where $(x, y) = (C, S)$ or (S, C) provides information about the location (core or shell) from which the bond is considered. The quantities $R_{0,x}^{HL}$ and δ_R^x are the same as those defined in Eqs. (3.6a) and (3.6b).

In the Montecarlo simulations, the system is warmed up from $T = 5$ to 200 K (390 K for $R_{0,S}^{HH} = 1.0$) in steps of increment 1 K, and then cooled down to the initial temperature for the situation when we have misfit in the HS state. While, for the case when we have a misfit in the LS state the system is first cooled down from $T = 100$ to 1 K in steps of decrement 1 K, and then heated again to the initial temperature. At each temperature step, we evaluate the HS fraction, n_{HS} , that is the fraction of molecules occupying the HS state, given by,

$$n_{HS} = \frac{1 + \langle S \rangle}{2}, \quad (3.8)$$

where $\langle S \rangle$ is the average value of the spin state, and the average nn distance, $\langle r \rangle$, defined as:

$$\langle r \rangle = \frac{\sum_{i \neq j} \sqrt{(x_i - x_j)^2 + (y_i - y_j)^2}}{N_b^x}, \quad (3.9)$$

where $N_b^{tot} = 2N_{tot}(N_{tot} - 1)$ is the total number of bonds. These two quantities, which can be viewed as order parameters characterizing the electronic and the elastic state of the system, are calculated for the core $N_b^c = 2N_c(N_c - 1)$, the shell $N_b^s = 2N_s(N_s + 2N_c - 1)$ and the whole lattice. The next section gives a description and explanation of the numerical procedures leading to solving Hamiltonian (1).

3.2.1 Technical details of Monte Carlo simulations.

The stochastic procedure was alternatively performed on spin and lattice positions of the square lattice, with free boundary conditions. The stochastic algorithm is performed in the following way: for a site, i randomly selected (among the N^2 lattice sites), with spin $S_i = \pm 1$ and position, \vec{r}_i , a new spin value $S_i' = -S_i$ is set without position change. This spin change is accepted or rejected by the usual Metropolis criterion. Whatever the result of this first step (spin state accepted or rejected), a new MC procedure is performed on the lattice positions. The lattice sites are selected randomly and slightly moved from their previous position with a random quantity whose maximum value is $\delta r = 0.001 \text{ nm}$ ($\ll R_0^{LL}$), which is much smaller than the distance between two nn ($\sim 1 \text{ nm}$). This procedure of the lattice relaxation is repeated 10 times for each spin flip. Afterwards, a new site will be selected randomly, and so on. Once all sites are updated on average, we define such step as the unit of the Monte Carlo step and denote "MCS." At each temperature, we perform 10^5 MCS to reach the equilibrium state, and we use 1000 other MCS for the statistics. Within this procedure, each site is displaced $10 \times N_{tot}^2$ times for

1 MCS. So, at each temperature, each spin state and lattice position is updated $\sim 10^5$ and $10^6 \times N_{tot}^2$, times, respectively. We have checked that increasing the simulation time does not affect the final results, ensuring that we reached the stationary state for spin and lattice position variables.

In a previous chapter [41], we have considered the study of a core-shell SCO nanoparticle, schematically represented in Fig. 3.1a, where both constituents are active from the point of view of spin transitions. There, we studied the effect of the shell thickness on the thermal properties of the core and the shell as well. In this previous work, we assumed equal core and shell lattice parameters in their respective HS and LS states.

3.3 Results and discussion

3.3.1 Thermal behavior of uncoated core and hollow shell

The analysis of the thermodynamic properties of this spin-crossover nanostructure showed the existence of an efficient mechanical coupling between the core and the shell moieties, which influences the thermodynamic behavior of each other. Due to this mechanical coupling, the temperature dependences of the total nanocomposite is far from the sum of each of its constituents. Indeed, according to the difference of transition temperatures and elastic interactions between core and shell, the whole nanocomposite may lead to several possibilities of spin transitions (two-step, gradual, one step with thermal hysteresis, etc.) as a result of an interplay between the electro-elastic properties of both constituents, resulting in a complex distribution of pressure (or elastic energy) inside the lattice. In the first part of this study, we started with the thermal investigations of the uncoated SCO core of size $N_c \times N_c = 40 \times 40$ and hollow shell of the same size and five layers thickness. The parameter values used throughout this study are for the core part, $\Delta_C = 450 K$, g (degeneracy ratio) = 150, $A_C = B_C = 10^5 K.nm^{-2}$ and for the shell: $\Delta_S = 200 K$ and $A_S = B_S = 10^5 K.nm^{-2}$. For simplicity, the equilibrium bond-lengths between nearest-neighboring atoms of spin configurations HS-HS, HS-LS and LS-LS were considered as respectively equal to 1.05 nm, 1.025 nm and 1.0 nm for the core. For the present simulations on the uncoated shell, the equilibrium distances between LS-LS, HS-LS and HS-HS nearest neighbors are taken equal to 1.03 nm, 1.015 nm and 1.0 nm, respectively.

The transition temperatures of the isolated core (resp. shell) are given by the relation, $T_{eq}^C = \frac{\Delta_C}{k_B \ln g} \sim 90 K$ (resp. $T_{eq}^S = \frac{\Delta_S}{k_B \ln g} \sim 40 K$).

As a reference, Fig. 3.2 summarizes the temperature dependences of the HS fraction of shell (Fig. 3.2a) and core (Fig. 3.2b), which undergo first-order phase transitions, accompanied by thermal hysteresis. Moreover, one can easily see that the transition temperatures arising from the MC simulations are confirmed to be the ones predicted by

the simple relation $T_{eq} = \frac{\Delta}{k_B \ln g}$.

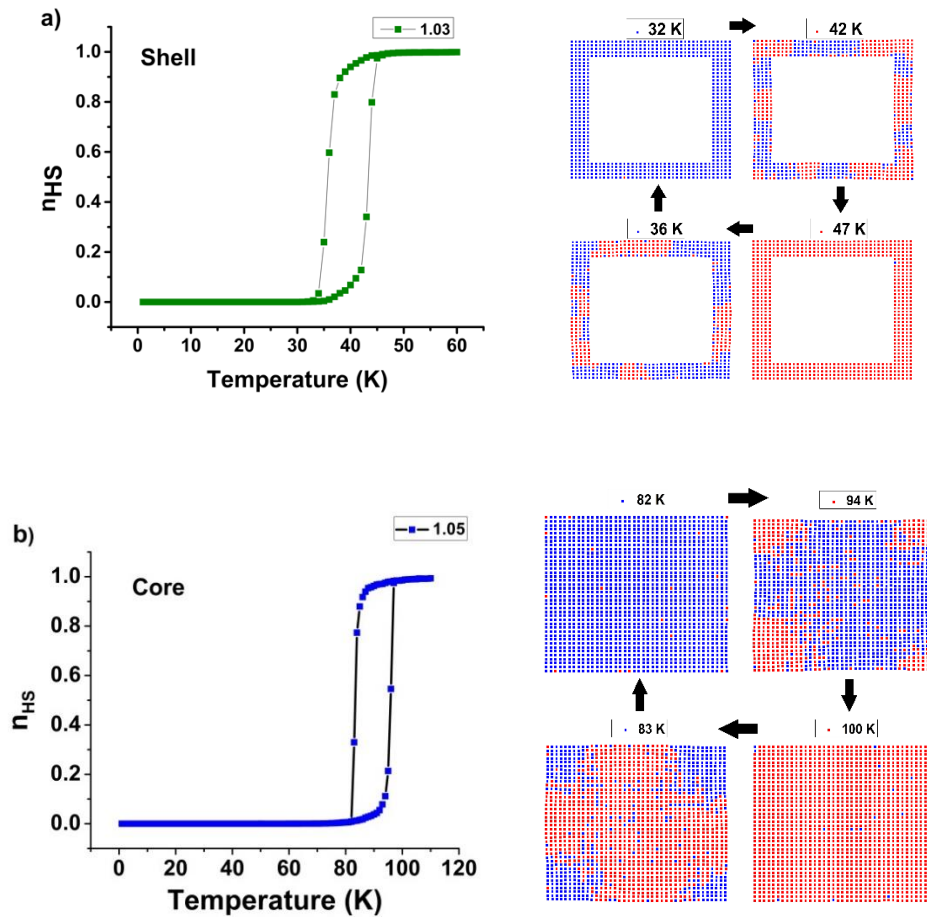


Figure 3. 2Thermal variation of the HS fractions and lattice parameters of the uncoated 2D hollow (a) and core (b) nanoparticle (with square symmetry). The core size is 40×40 , and the hollow shell has five layers of thickness. The equilibrium nn distances in HS-HS, HS-LS, and LS-LS configurations are respectively equal to 1.05 nm, 1.025 nm and 1.0 nm for the core, and 1.03 nm, 1.015 nm and 1.0 nm, for the shell. For both cases, the spatial distributions of the HS (red dots) and LS (blue dots) sites along the spin transition phenomenon are shown in the right panels.

3.3.2 Case of spin-crossover nanostructure with active core and shell

Now we turn to the case of the spin-crossover nanocomposite, schematically represented in Fig. 3.1a, in which core and shell consist of active spin-transition materials. For that, we decorate the uncoated core of Fig. 3.2b by the hollow spin-crossover shell (Fig. 3.2a), of 5 layer's thickness ($N_S=5$). The used Monte Carlo

procedure to solve the thermodynamic properties of this hybrid system is the same as that used for the uncoated core.

In the MC simulations, a lattice site is randomly selected. This site is inside the core (i.e., surrounded by core atoms only) or inside the shell (i.e., surrounded by shell atoms only) or at the interface, belonging to the core or shell parts. If the atom is inside the core or the shell, we calculate its elastic energy using Hamiltonians (3.2b) and (3.3b), combined with the spin-dependence of equilibrium distances, given in expressions (3.5a) and (3.5b). In contrast, in the interface region, if we select in the MC process a site belonging to the core (resp. shell) part, its elastic energy is calculated using Eq. (3.4b) [resp. (3.4c)] with the corresponding equilibrium distances are given by Eq. (3.7a) [resp. (3.7b)]. This constraint causes an elastic frustration that deploys over the lattice, whose consequences are discussed below.

3.3.2.1 Effect of the core-shell lattice parameter misfit in HS state on the whole system

In the previous chapter [41], we admitted that the core and the shell have the same equilibrium bond-lengths in HS and LS states. In the present work, we take, $R_{0,S}^{HH}$, as a variable, which causes the change: $R_{0,S}^{HL} = \frac{R_{0,S}^{HH} + R_{0,S}^{LL}}{2}$.

Now let us summarize the situation: $R_{0,S}^{LL} = R_{0,C}^{LL} = 1$, $R_{0,C}^{HH} = 1.05$ are kept invariant while $R_{0,S}^{HH}$ changes from the value of $R_{0,C}^{LL}$ to that of $R_{0,C}^{HH}$. The values of all nn lattice distances are summarized in Table I. Owing to the 2D character and square symmetry of the lattice, the nnn equilibrium distances corresponding to the electronic configurations given in Table I are obtained from the nn equilibrium distances multiplied by $\sqrt{2}$.

Now, we focus on the imposed equilibrium distances at the core-shell interface. It can be easily checked that the core-shell interface contains $4N_C$ nn bonds and $4(2N_C - 1)$ nnn bonds.

It is important to stress here on the individual definition of the equilibrium distances, $R_0^{int}(S_i, S_j)$, at the core-shell interface. In a previous work [41], where the equilibrium nn distances of HH, HL and LL configurations were the same for the core and the shell, those of the interface was simply calculated as the average values of those of core and shell atoms, taking into account for their spin states. Here, we consider a different scenario, for which the equilibrium bond lengths at the interface are summarized in Table I. Thus, a chosen atom belonging to the core-shell interface and located in the core side wants to impose to its nn (or nnn) shell atom the equilibrium core bond length and similarly for shell atoms. Within this condition, bonds at the interface viewed from the core (resp. shell) have the equilibrium bond lengths $R_0^C(S_i, S_j)$ [resp. $R_0^S(S_i, S_j)$], given in Table I. As a result, the same bond at the core-shell interface is asked to have the equilibrium distance

of the core (resp. shell) when calculating the energy of the core (resp. shell) atom. For example, an HS-LS interface bond constituted of a HS core site and a shell LS site has the apparent equilibrium distance $R_{0C-S}^{int}(+1, -1) = \frac{R_{0,C}^{LL} + R_{0,C}^{HH}}{2}$ ($= 1.025$ nm) from the point of view of the core side and $R_{0S-C}^{int}(-1, +1) = \frac{R_{0,S}^{LL} + R_{0,S}^{HH}}{2}$ when viewed from the shell side. When the value of $R_{0,S}^{HH}$ is different from that of $R_{0,C}^{HH}$ an elastic frustration immediately takes place at the core-shell interface in bonds unless its connecting sites are not in the LS state, as it appears in Table I, where we summarize the expressions of the different equilibrium distances corresponding to the various bond configurations in the core, shell and interface regions.

Table 3. 1 Equilibrium nn distances used for the core, shell, and core-shell bonds. The HS shell nn bond-length ($R_{0,S}^{HH}$) is used here as a variable.

nn configurations	HH	HL	LL
core nn distance (nm)	$R_{0,C}^{HH} = 1.05$	$R_{0,C}^{HL} = \frac{1 + R_{0,C}^{HH}}{2} = 1.025$	$R_{0,C}^{LL} = 1.0$
shell nn distance (nm)	$R_{0,S}^{HH}$	$R_{0,S}^{HL} = \frac{1 + R_{0,S}^{HH}}{2}$	$R_{0,S}^{LL} = 1.0$
nn distance (nm) at interface viewed from the shell	$R_{0,S}^{HH}$	$R_{0,S}^{HL} = \frac{R_{0,S}^{LL} + R_{0,S}^{HH}}{2}$	$R_{0,S}^{LL} = 1.0$
nn distance (nm) at interface viewed from the core	$R_{0,C}^{HH} = 1.05$	$R_{0,C}^{HL} = \frac{R_{0,S}^{LL} + R_{0,C}^{HH}}{2} = 1.025$	$R_{0,C}^{LL} = 1.0$

The simulations are performed for different values of the equilibrium lattice parameter of the shell in the HS phase, going from $R_{0,S}^{HH} = 1.05$ nm (nn bond length value of the core in HS) to $R_{0,S}^{HH} = 1.0$ nm (nn bond length value of the core in LS). The change in $R_{0,S}^{HH}$ values cause the change of HL configurations of the shell as well as those of HH and HL configurations of core-shell bond lengths located in the interface region. The other lattice parameters are kept invariant, as shown in Table I.

Thus, we now examine the general situation where the nanocomposite comprises two SCO materials with different HS lattice parameters. Due to the elastic nature of the spin transition phenomenon, it is expected that this difference of the lattice parameter between the core and the shell will play an important role in the thermal behavior of the HS fraction of the whole system.

The results of the simulations are summarized in Fig. 3.3 which reports the thermal variation of the total HS fraction and average lattice parameter of the whole nanocomposite for various values of $R_{0,S}^{HH}$. It is observed that the change in $R_{0,S}^{HH}$ affects the thermal behavior of the entire system. This is due to the fact that

the elastic interaction energy, ΔE , responsible for the SCO transition of the shell, depends on the lattice parameter misfit inside the shell between the LS and HS states: $\Delta E = \frac{1}{2}(A_S + 2B_S)(\delta_R^S)^2 = \frac{1}{2}(A_S + 2B_S)(R_{0,S}^{HH} - R_{0,S}^{LL})^2$. These changes are then mechanically communicated to the core through the core-shell interface. Thus, the decrease in $R_{0,S}^{HH}$ shifts the whole thermal response of the system to higher temperature and causes interesting behaviors on the thermal dependence of the average bond lengths, which transforms through several steps. The origin of this behavior will be discussed in the next section, where we examine the thermal behavior of the core and the shell individually.

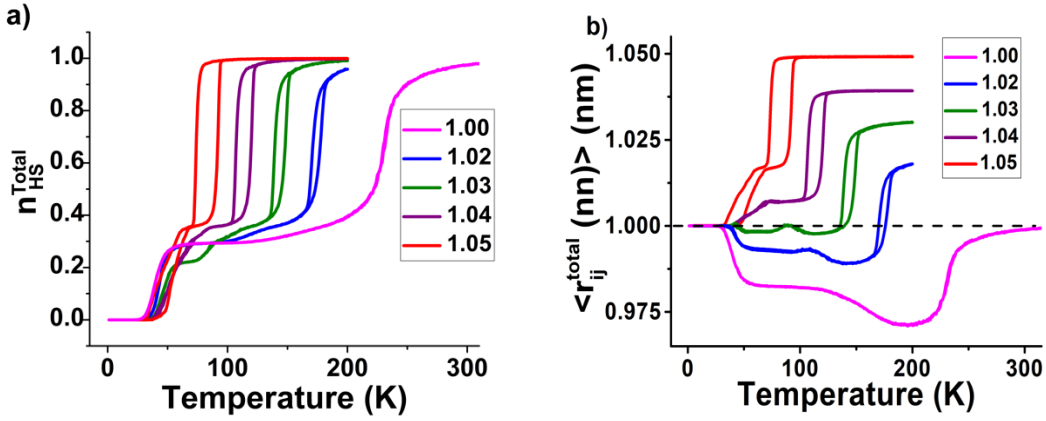


Figure 3: Thermal variation of (a) the total HS fraction and (b) average lattice parameter of the whole SCO nanocomposite for different equilibrium lattice parameter of the shell, which was varied from $R_{0,S}^{HH} = 1.00$ to 1.05 nm. The other lattice parameter values are given in Table I. The used values of the elastic constants are: $A_c = A_s = A_{int} = 10^5 \text{ K.nm}^{-2}$ for nn interactions and $B_c = B_s = B_{int} = 10^5 \text{ K.nm}^{-2}$ for the nnn interactions in the core (C), the shell (S) and interface (int).

3.3.2.2 Thermal properties of shell and core components

Now, we examine the thermal behavior of the electronic and mechanical responses of the core and the shell separately as a function of $R_{0,S}^{HH}$. Figure 3.4 shows the thermal dependences of the average HS fraction and the average lattice distance, $\langle r \rangle_s$, of the shell (Figs. 3.4a and 3.4b) for different $R_{0,S}^{HH}$ values going from 1.05 to 1.00 nm (i.e. from $R_{0,C}^{HH}$ to $R_{0,C}^{LL}$), while $R_{0,S}^{LL}$, $R_{0,C}^{LL}$, $R_{0,C}^{HH}$ and $R_{0,C}^{HL}$ are kept invariant as given in Table I. The associated HS fraction and lattice spacing, $\langle r \rangle_c$, of the core are depicted in Figs. 3.4c and 3.4d, respectively.

It is interesting to mention that, for used $R_{0,S}^{HH}$ values, the HS fraction of the shell (Fig. 3.4a) has a large plateau for $R_{0,S}^{HH} = 1.00, 1.02$ and 1.03 nm, which drastically reduces for $R_{0,S}^{HH} = 1.04$ and almost disappears for $R_{0,S}^{HH} = 1.05$. The existence of this plateau is caused by the misfit between the equilibrium nn distance of the core,

$R_{0,C}^{HH} = 1.05$ and that of the shell $R_{0,S}^{HH}$, thus originates from the mechanical compressive strain exerted by the LS core on the shell. This prevents its complete transformation during the thermal transition process. As a consequence, the average shell nn distance in the HS state decreases (Fig. 3.4b) as $R_{0,S}^{HH}$ decreases, leading to a delay in the transition temperature of the core, whose volume expansion between LS and HS states is hindered by the shell. On the other hand, for $R_{0,S}^{HH} < 1.05$, the expansion or the contraction of the shell during its first-step transition is accompanied by the systematic contraction of the core (Fig. 3.4d), while its expansion starts only when its corresponding HS fraction increases (Fig. 3.4c). This behavior indicates that the first contractions of the core are the result of its mechanical response to the shell's behavior.

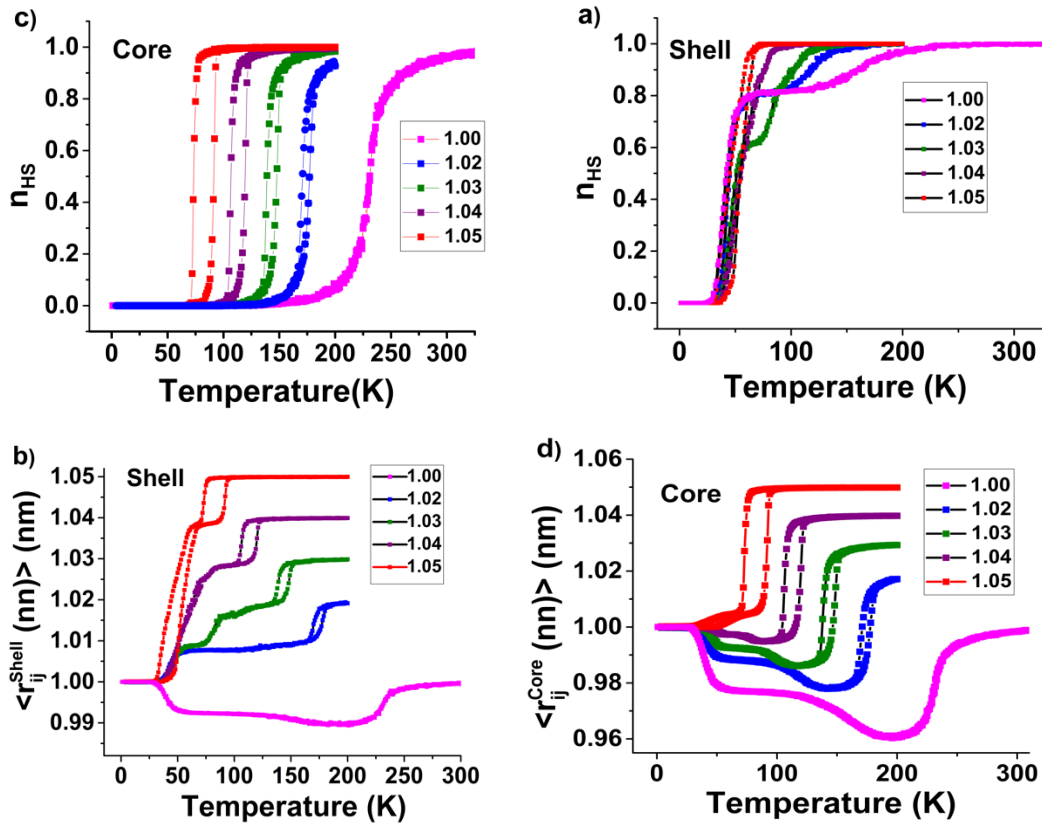


Figure 3. 4 Thermal variations of (a) the shell HS fraction and (b) average nn distance for different $R_{0,S}^{HH}$ values, varied from $R_{0,S}^{HH} = 1.0$ to 1.05 nm. (c) and (d) are the temperature dependences of the core HS fraction and average nn distance for the same $R_{0,S}^{HH}$ values. The other lattice parameter values are given in Table I. The other model parameters are given in the text.

Interestingly, while the first transition temperature of the shell-shows only a slight shift towards 50 K as a function of $R_{0,S}^{HH}$ (see Fig. 3.4a), that of the core, displayed in Fig. 3.4c, is significantly affected. That is, the center of the thermal hysteresis moves from 75 K to ~ 230 K, by decreasing $R_{0,S}^{HH}$ from 1.05 to 1.00 nm. Due to this critical change, the thermal hysteresis width of the core diminishes from 17 K to 0 K.

Furthermore, it is clear from Fig. 3.4a that the HS fraction of the shell makes the transition in one step for $R_{0,S}^{HH} = 1.05$ nm, which converts to two-steps with a plateau for $R_{0,S}^{HH} = 1.04, 1.03, 1.02$ and 1.0 nm, while the temperature dependences of the average bond length, $\langle r \rangle$, depict a double step transition for all $R_{0,S}^{HH}$. The first step is related to an incomplete electronic transformation of the shell due to compressive strain induced by the core, which is still in the LS state, while the second step which takes place around 70 K for $R_{0,S}^{HH} = 1.03$, for example, relates to the change in the bond lengths of the shell, which hardly reach their equilibrium values in the HS state as $R_{0,S}^{HH}$ decreases.

An interesting situation arises from the comparison between the thermal dependence of the HS fraction (Fig. 3.4a) and the bond lengths of the shell, shown in Fig. 3.4b. The temperature-dependence of the bond lengths of the shell exhibit thermal hysteresis for $R_{0,S}^{HH} = 1.02, 1.03$ and 1.04 , which are absent in the thermal behavior of the HS fraction. In addition, as previously indicated, more marked plateaus appear in Fig. 3.4b, compared to those of Fig. 3.4a. This situation is even more pronounced for the core part where the temperature-dependence of the HS fraction (Fig. 3.4c) giving the temperature dependence of the HS fraction, n_{HS} , shows a single-step first-order transition for $R_{0,S}^{HH} = 1.05, 1.04, 1.03, 1.02$ while the corresponding average core nn distance leads to multi-step transitions (Fig. 3.4d).

This point is important and demonstrates that the magnetic response can be silent to the interplay between the core and shell structural changes. Indeed, the behavior of the HS fraction of the core (Fig. 3.4c) is blind regarding the multi-step transitions occurring in the core bond lengths (Fig. 3.4d), which are mostly sensitive to the changes of elastic parameters of the shell (Fig. 3.4a). This point contrasts with the usual elastic models of SCO where the HS fraction and the average bond lengths are linked linearly [42].

It is worth noticing that the temperature dependence of the average core bond length shows very unusual and non-monotonous trends around the temperature region of the transition of the shell. These behaviors are unique and of merit to be discussed in a detailed way.

To thoroughly understand the unconventional thermal behavior of $\langle r \rangle$ in Fig. 3.4d, for $R_{0,S}^{HH} \geq 1.04$, one has to consider that the expansion of the shell part during its phase transition, induces tensile stresses on the core. For equal equilibrium HS lattice parameters of core and shell (i.e. $R_{0,S}^{HH} = R_{0,C}^{HH} = 1.05$ nm), the two subsystems form a unique and uniform elastic lattice (same bond lengths and elastic constants in LS and HS states). As a result, a ferroelastic interaction takes place between the shell and the core. Indeed, the first expansion of the shell (Fig. 3.4b) below 70 K, is accompanied by an expansion of the core (Fig. 3.4d). That is, the average nn distance of the core increases monotonously with temperature from the value of the LS state ($R_{0,C}^{LL} = 1.0$ nm) until that of HS ($R_{0,C}^{HH} = 1.05$ nm), with the presence of a small plateau around $T=75$ K (on heating) at which $\langle r \rangle_c$

reaches the value 1.005. This effect is attributed to the transition of the shell, thus causing a negative pressure on the LS core's lattice. It is worth mentioning that this plateau is hardly visible in the temperature dependence of the core HS fraction of Fig. 3.4c.

In contrast, for $1.00 \leq R_{0,S}^{HH} \leq 1.04$, the first expansion of the shell, on heating, induces a compressive stress on the core, which then contracts (see Fig. 3.4d). This contraction continues as long as the core HS fraction keeps the value $n_{HS} = 0$ (Fig. 3.4c). When the HS fraction of the core starts to increase (due to thermal effects), $\langle r \rangle_c$ goes through a minimum and finally increases towards the value $R_{0,S}^{HH}$ instead of $R_{0,C}^{HH}$ ($> R_{0,S}^{HH}$). In that sense, the core remains under high compressive pressure even in the HS state.

The observed contractions of the core are also due to the strong lattice misfit existing between the core and the shell lattice spacing. It is essential to mention that the amplitude of this core contraction also depends on the ratio of core/shell elastic constants, which are taken in the present case as equal to 1. Thus, a more compressible core may show significant mechanical responses, while a rigid one will prevent the transition of the shell. This exciting aspect will be investigated in further work.

On the other hand, the thermal behavior of the average shell and core bond length (Fig. 3.4b and 3.4d) clearly demonstrates that for small lattice spacing of the HS shell, the transition temperature is shifted upwards, recalling the effect of pressure on SCO materials. Indeed, it is crucial to keep in mind that, on heating, the shell makes the LS to HS transition before the core. As a result, when the shell reaches the HS state, two different processes emerge: (i) the core experiences compressive or tensile stress depending on the misfit lattice parameter and (ii) the expansion of core lattice under the inhibited boundary conditions set by shell part which in turn prevents the conversion of the core which needs space to expand all the bond lengths. Thus, it delays the emergence of the thermally-induced spin-state switching, which appears at higher temperatures.

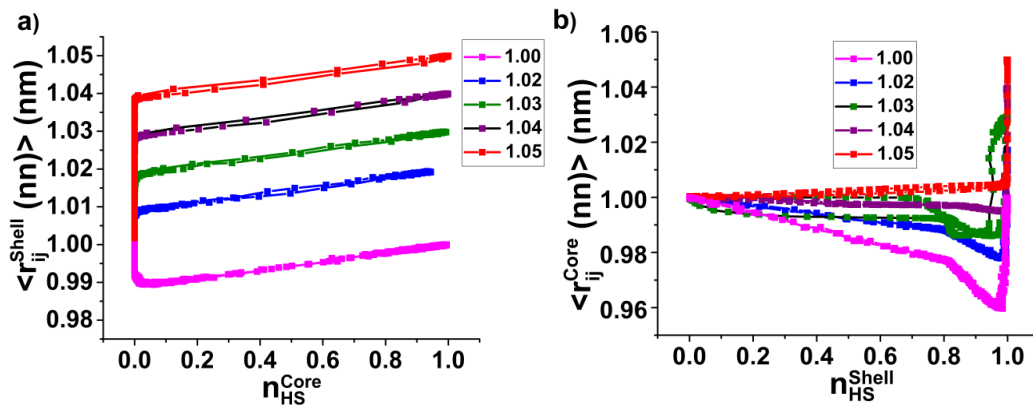


Figure 3.5 Variation of different HS equilibrium lattice parameters, (a) shell and (b) core, along the total HS fraction (a) core and (b) shell, for different HS shell equilibrium lattice parameters, which is varied from $R_{0,S}^{HH} = 1.00$ to 1.05 nm.

So, to summarize, the weak effect of the core on the shell lattice parameter (Fig. 3.4b) is attributed to the existence of a free surface of the shell, which allows relaxing of elastic strain. For example, for the case $R_{0,S}^{HH} = 1.02$ nm, the shell switches from LS to HS (whose corresponding average nn distances are 1.0 nm and ~1.02 nm) around $T_S^{eq} \approx 41$ K, which is very close to the transition temperature of the isolated shell, given by $T_S^{eq} = \frac{\Delta_S}{k_B \ln g} = 40$ K. In contrast, the behavior of the core part with $R_{0,C}^{HH} = 1.05$ nm and $R_{0,C}^{LL} = 1.0$ nm, is significantly affected by the change of $R_{0,S}^{HH}$, particularly when the misfit ($R_{0,C}^{HH} - R_{0,S}^{HH}$) increases. Several observations can be drawn: (i) the transition temperature of the core is clearly shifted to higher temperatures; (ii) depending on the value of $R_{0,S}^{HH}$, the temperature dependence of the average core lattice parameter may follow a non-monotonous trend, (iii) the thermal hysteresis width progressively vanishes with decreasing the $R_{0,S}^{HH}$ values. In Fig. 3.5 we can clearly see the correlation between the HS state of core and shell with respect to the average lattice parameter of shell and core.

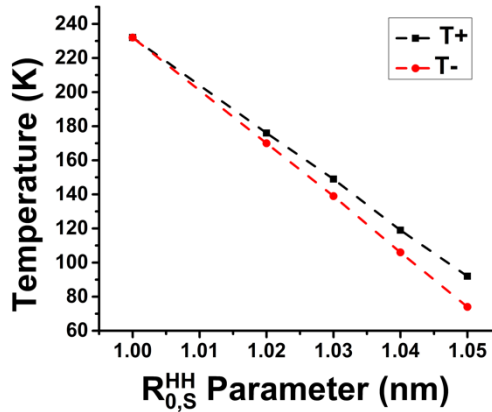


Figure 3.6 High-spin shell lattice parameter dependence of the upper (T^+) and lower (T^-) transition temperatures of the core components, showing a clear vanishing of the thermal hysteresis for below the value, $R_{0,S}^{HH} = 1.01$ nm, as a result of pressure effects exerted by the shell on the core due to the lattice parameter misfit.

To confirm the pressure effect of the shell on the transition of the core, we analyze the dependence of the upper and lower core transition temperatures on $R_{0,S}^{HH}$ in Fig. 3.4c and 3.4d. It shows (see Fig. 3.6) a clear linear trend, reminiscent of the behavior of SCO systems under an applied isotropic pressure [43], P , following the law $T_{eq}^0(p) = \frac{2\Delta}{k_B \ln g} + \frac{p|\Delta V|}{k_B \ln g}$, and $|\Delta V|$ is the volume change between LS and HS states. In Fig. 3.7 we can observe that when the whole system is in the HS state, the differences between the average instantaneous bond length and the corresponding equilibrium distances for the shell and core in the HS state ($\langle r \rangle_{shell}$) and ($\langle r \rangle_{core}$), clearly show that the core is under a large stress compared to the shell,

thus confirming the fact that the relaxation of the core lattice is obstructed by the HS shell lattice, which in turn shifts the transition temperature of the core to higher temperature.

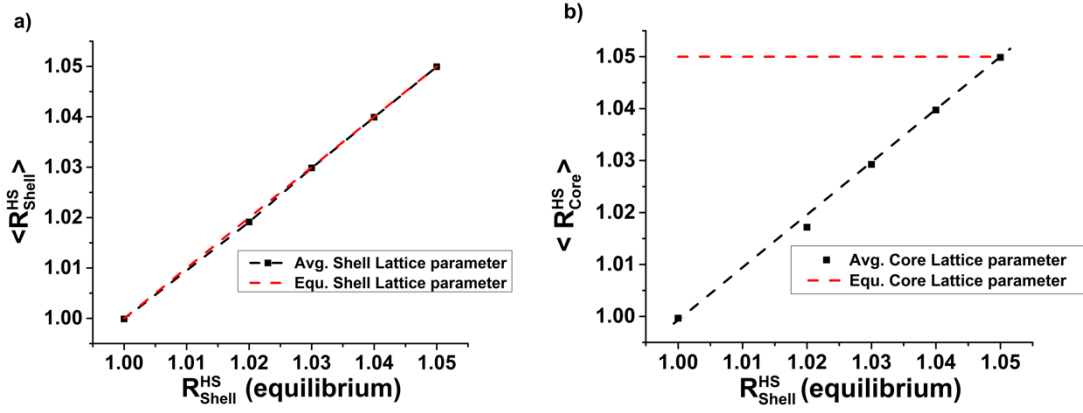


Figure 3. 7 Difference, $\langle r \rangle_{HS} - R_{eq}^{HS}$, between the instantaneous average bond length, $\langle r \rangle_{HS}$, in the HS state of the shell (a) and core (b) and their equilibrium nearest-neighbors distances in HS ($R_{eq}^{HS} = R_{0C}^{HH}$ and $R_{eq}^{HS} = R_{0S}^{HH}$) as a function of the shell lattice parameter in HS. According to the scale of the y-axis, it appears that the core of the nanoparticle is under enormous stress compared to the shell part. Red dashed curves are the shell (a) and core (b) equilibrium lattice parameters.

3.3.2.3 Spatial distribution of the HS fraction and evidence of labyrinth formation inside the core

Here we analyze the spatial dependence of the HS fraction in the core and the shell along with the thermal hysteresis of Fig. 4 and discuss the effect of lattice misfit, $R_{0,S}^{HH} - R_{0,C}^{HH}$, on the nucleation mode of the HS fraction. Selected snapshots depicting the spatial distribution of the HS fraction are presented in Fig. 8 for the values $R_{0,S}^{HH} = 1.00, 1.02, 1.03, 1.04, 1.05$ nm and temperature $T = 229, 174, 144, 115$ and 87 K, respectively. According to Fig. 3.4, this corresponds to the situation where the interplay between the elastic properties of the core and the shell is maximum. At these temperatures, the shell exerts highly anisotropic constraints on the system, which results in special spatial self-organization of the spin states through labyrinths structures (see Fig. 3.8) during the growth of the HS fraction. Such behavior is fascinating and could be correlated to the lattice shape and the spatial distribution of the elastic strain in the lattice. The formation of HS and LS stripes is attributed here to the coexistence of directional ferroelastic and antiferroelastic interactions, which can also be evidenced by the spatial behavior of the average lattice parameter inside the lattice. In addition, the fact that these 1D structures can be formed along both x - and y -directions indicates the absence of any anisotropic effects in the growth modes of these strings. Theoretically, it has been demonstrated that the herringbone mode has the lowest strain energy for a planar film under equibiaxial compression [44], which justifies its existence in various natural circumstances [45]. The feature of the labyrinth-like pattern is also

dependent on the anisotropy of the film stress [46–48], implying that the patterns can be controlled by constraining the film-substrate system, thus creating non-equibiaxial stresses [49–51].

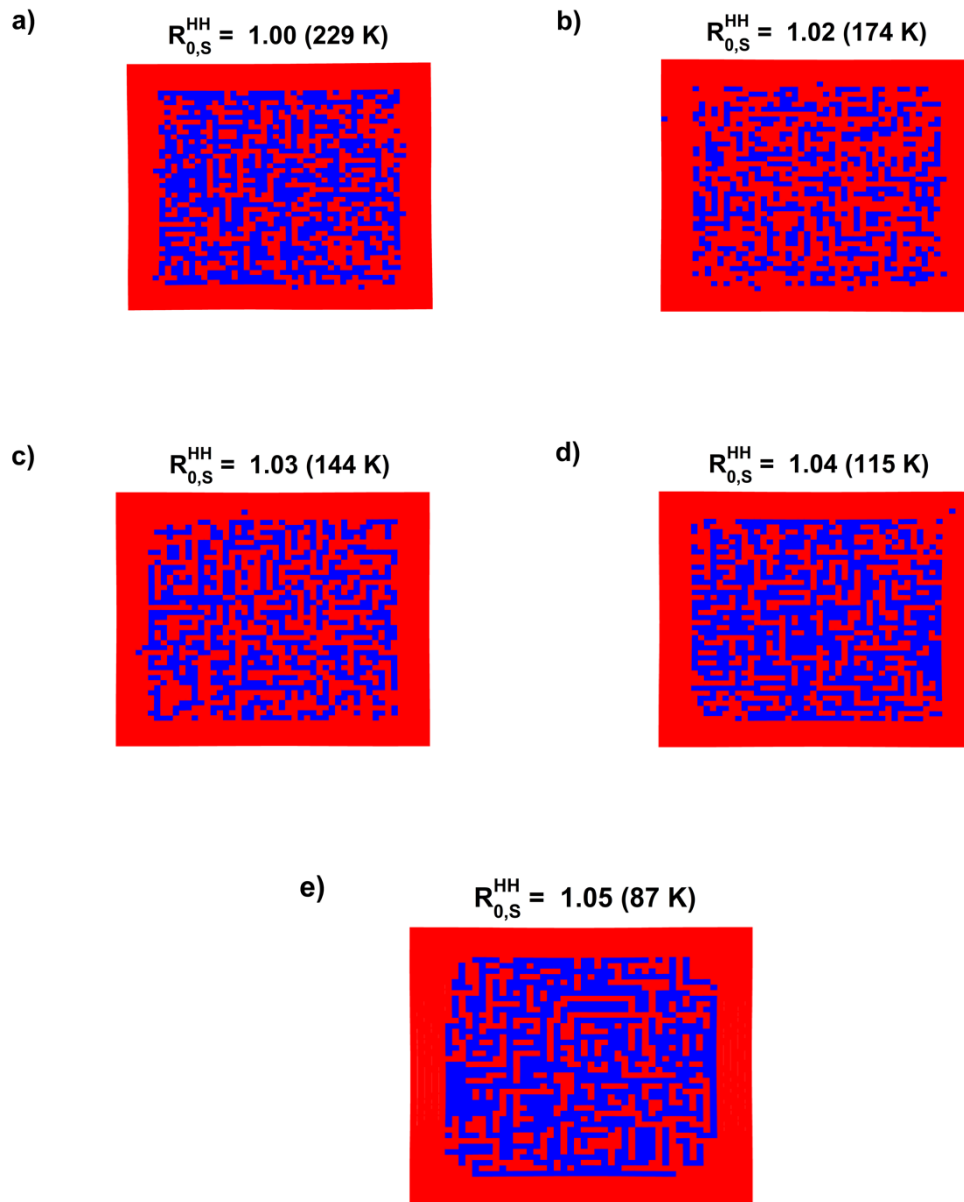


Figure 3. 8 Selected snapshots depicting the spatial distribution of the HS fraction presented in Figs. 4 and 5 for the case $R_{0,S}^{HH} = 1.00, 1.02, 1.03, 1.04, 1.05$ nm and temperature $T = 229, 174, 144, 115$ and 87 K, respectively. The corresponding HS fraction (0.60, 0.52, 0.47, 0.43, 0.40) and lattice parameter (0.98, 0.99, 1.00, 1.01, 1.01) values can be easily read on Fig. 4c and Fig. 4d for the core lattice and Fig. 3a and Fig. 3b for the shell lattice. Remark the emergence of labyrinth HS structures inside the core as a result of the spatial distribution of the strain. Here HS (in red) and LS (in blue) depicts total HS occupation in the shell, and spatial distribution of HS fraction in the core.

3.3.2.4 Spatial profiles of the lattice bond lengths

To get more insights into the magneto-elastic interplay between the electro-elastic properties of the core and the shell, we monitor the spatial distribution of the atomic bond lengths along a horizontal line located at the middle of the lattice (at coordinate $j = \frac{N}{2}$) in the case of a HS shell and LS core, for several values of $R_{0,S}^{HH}$. The results are summarized in Fig. 3.9, which indicates that with $R_{0,S}^{HH}$ values between 1.0 and 1.04, the core experiences a strong non-uniform compressive stress along the x -direction (Figs 3.9a-d), which increases as $R_{0,S}^{HH}$ decreases, enhancing the elastic misfit at the core-shell interface. In contrast, for $R_{0,S}^{HH} = 1.05$ nm (Fig. 3.7e), we observe that the central part of the core experiences tensile stress while a residual weak compressive stress remains at the lattice borders. On the other hand, the shell part shows that the outer layers (close to the surface) are constantly under tensile stress, while the inner layer (close to the interface) is always under compressive stress, whatever the $R_{0,S}^{HH}$ value. More precisely, one may notice that for all cases shown in Fig. 3.9, that or shell layers close to the surface, the distance between successive sites, d_{ij} , is bigger than the equilibrium value, $R_{0,S}^{HH}$ which makes then the shell under tensile stress. For $R_{0,S}^{HH} = 1.0$, only the shell layer at the interface with the core experiences the compressive stress ($d_{ij} \approx 0.98 < R_{0,S}^{HH}$). However, as $R_{0,S}^{HH}$ value increases, other inner shell layers start to feel the compressive strain exerted by the elastic core-shell misfit, as clearly depicted in Figs. 3.9b-e through the number of red points situated below the dashed line indicating the $R_{0,S}^{HH}$ value. Similarly, the behavior of LS core crucially depends on $R_{0,S}^{HH}$. For $1.00 \leq R_{0,S}^{HH} \leq 1.04$ nm, the nn distances, d_{ij} , along the considered horizontal line in the core are always smaller than $R_{0,S}^{HH}$, denoting that the core is under compressive stress. However, it is interesting to notice the non-uniform character of the spatial dependence of the distance, $|d_{ij} - R_{0,C}^{LL}|$, along the core's center. This quantity indeed decreases in a symmetric way when coming from both sides, meaning that the center of the core experiences weaker compressive stress, compared to the outer core layers located at the core-shell interface. As a result, the formation of HS core species from the outer core layers is prevented, at the benefit of the core center part. In addition, it is clearly seen in Figs. 3.9 that the amplitude of this compressive stress decreases as the value of $R_{0,S}^{HH}$ increases. This effect is important and helps in the formation of long HS strings at the origin of the emergence of the labyrinth structures, obtained for all $R_{0,S}^{HH}$ values, as depicted in Fig. 3.8. However, it is worth noticing that the lengths of the HS string forming the labyrinth, as well as the topology of the latter, depend on $R_{0,S}^{HH}$ values. Indeed, for the case, $R_{0,S}^{HH} = 1.05$ nm, the central part of the core experiences now tensile stress ($d_{ij} > R_{0,C}^{LL}$), which enhances the HS string's length inside the core.

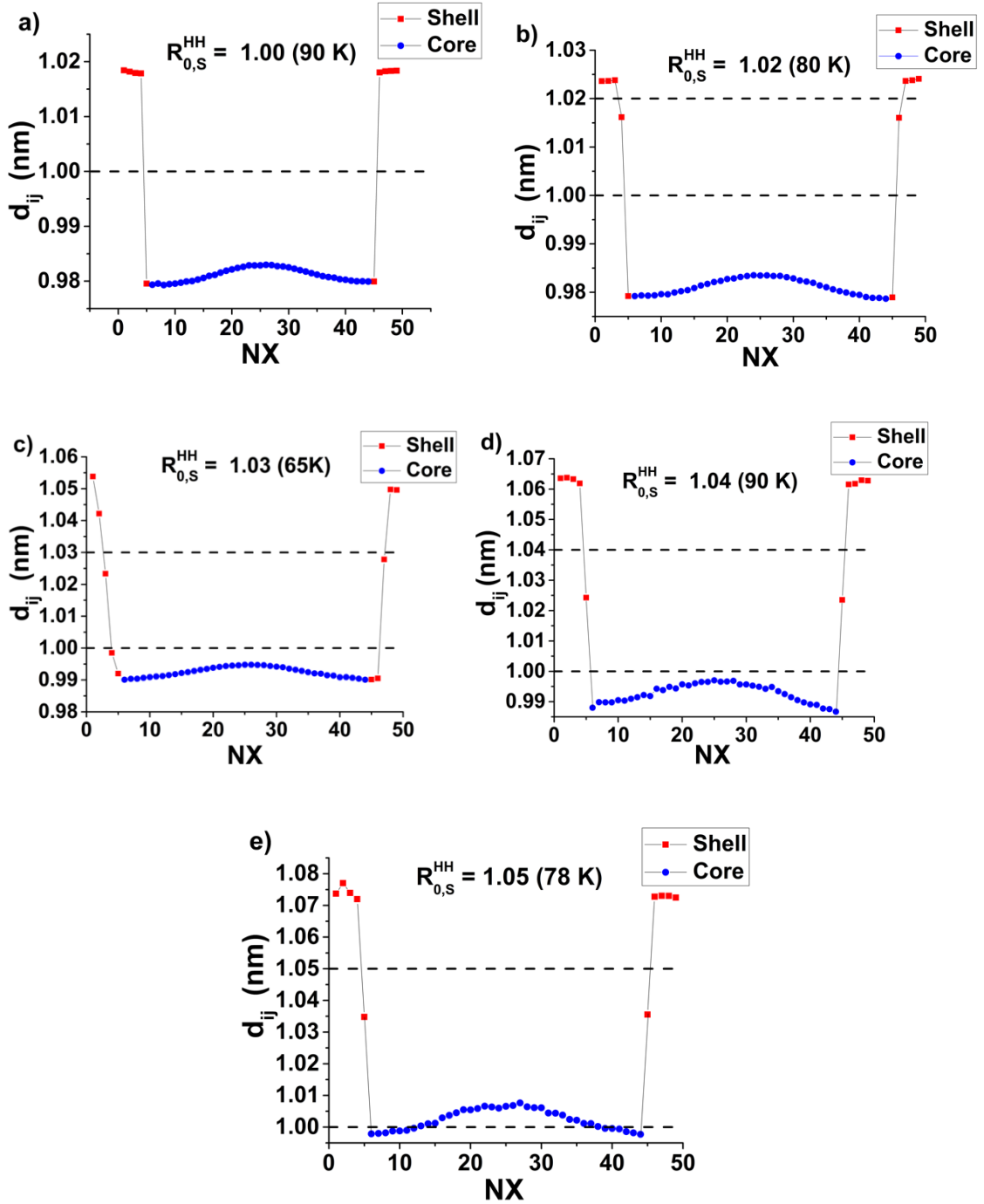


Figure 3. 9 lattice parameter profile along a horizontal line located at coordinate $j = \frac{N}{2}$, in the middle of the lattice, for several HS shell lattice parameters and temperatures corresponding to the plateau regions of Figs. 3.4b and 3.4d. The data of the HS shell part are represented with red squares, and those of the LS core part are represented with blue filled circles. All curves correspond to a LS core surrounded by a HS shell. The horizontal dashed lines corresponding to $d_{ij} = R_{0,S}^{HH}$ and $d_{ij} = 1.0$ nm, are respectively associated with the equilibrium bond lengths of the HS shell and LS core.

3.3.2.5 Lattice distortion and spatial distribution of elastic stresses

Now we focus on the stresses generated by the nucleation and growth process, which is vital for the self-organization of the HS and LS states. For that, we determine the displacement field, $\vec{u}(i,j)$, associated with the lattice site, (i,j) , given by

$$\vec{u}_{ij} = \vec{r}_{ij} - \vec{r}_{ij}^0, \quad (3.10)$$

where, \vec{r}_{ij}^0 and \vec{r}_{ij} are the initial and final atomic positions of the site (i,j) . In the present analysis, we used the positions in the perfect LS state of the whole nanostructure as a reference state because it is common to all the simulations. We have calculated the displacement field and its spatial distribution, of the core and shell atoms, for several values of $R_{0,S}^{HH}$ for the cases of Fig. 3.9. The obtained results are summarized in Fig. 10, and correspond to selected electro-elastic snapshots in the plateaus regions. Overall, they are in agreement with the conclusions drawn from Fig. 3.9. First, Fig. 3.10a corresponds to the situation where $R_{0,S}^{HH} = 1.0$. Compared to Figs. 3.10b-3.10e, it shows a loss of center symmetry, which is attributed to the randomly selected electronic configuration, which is affected by the fluctuations of the spin states induced by the stochastic aspect of the MC procedure. On the other hand, Figs. 3.10b and 3.10c, corresponding respectively to $R_{0,S}^{HH} = 1.02$ and 1.03 nm, show strong compressive stress acting in the core, since all core displacement vectors are directed towards the center of the lattice. Furthermore, the coexistence of tensile and compressive stresses takes place in shell regions. Indeed, it is remarked that the compressive stresses in the shell are located around the shell-core interface, while the tensile stresses occur near the shell surface, where the orientation of the displacement vectors changes along the shell lattice, which then slightly deforms. As a result, the system exhibits compressive but non-uniform stress along the x - and y -directions. When the HS shell lattice parameter is increased, as for $R_{0,S}^{HH} = 1.04$ nm (Fig. 3.10d), a different stress distribution feature is obtained. The nanostructure displays coexisting regions of dilatational strain in the shell region and around the core-shell interface and weak compressive strain in the core. Indeed, the displacement field for the shell is outwards, i.e. shell is expanding, while, at the same time, for the core, the displacement is inwards, i.e. core is experiencing contraction. As a consequence, one can quickly identify a “circular” boundary wall of displacement fields formed between the core and shell lattice structure, varying in width along the corners and edges. This boundary wall formation clearly portrays the two different mechanisms going in the whole lattice structure simultaneously. The first is the expansion of shell lattice parameters at the stake of contraction in core lattice parameters. The second is the stabilization of the LS state in the core due to the contraction. Consequently, the transition temperature of core lattice shifts to higher temperatures, which in turn also withhold the complete transition of shell from LS to HS as can be seen in Fig. 3.5. Finally, for $R_{0,S}^{HH} = 1.05$ (Fig. 3.10e), a pure dilatational strain, acting everywhere in the lattice, stabilizes the HS state and

decreases the spin transition temperatures of both moieties.

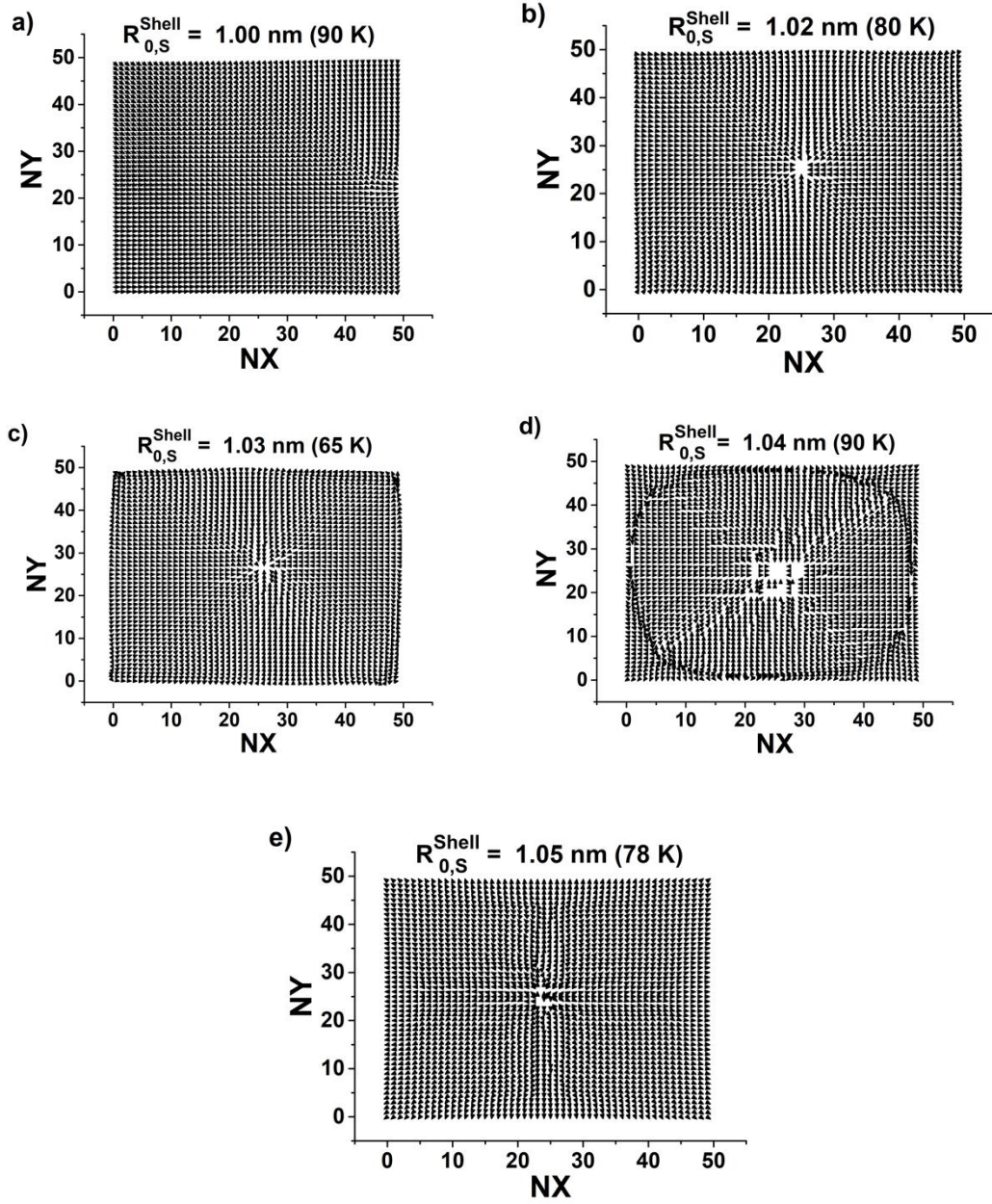
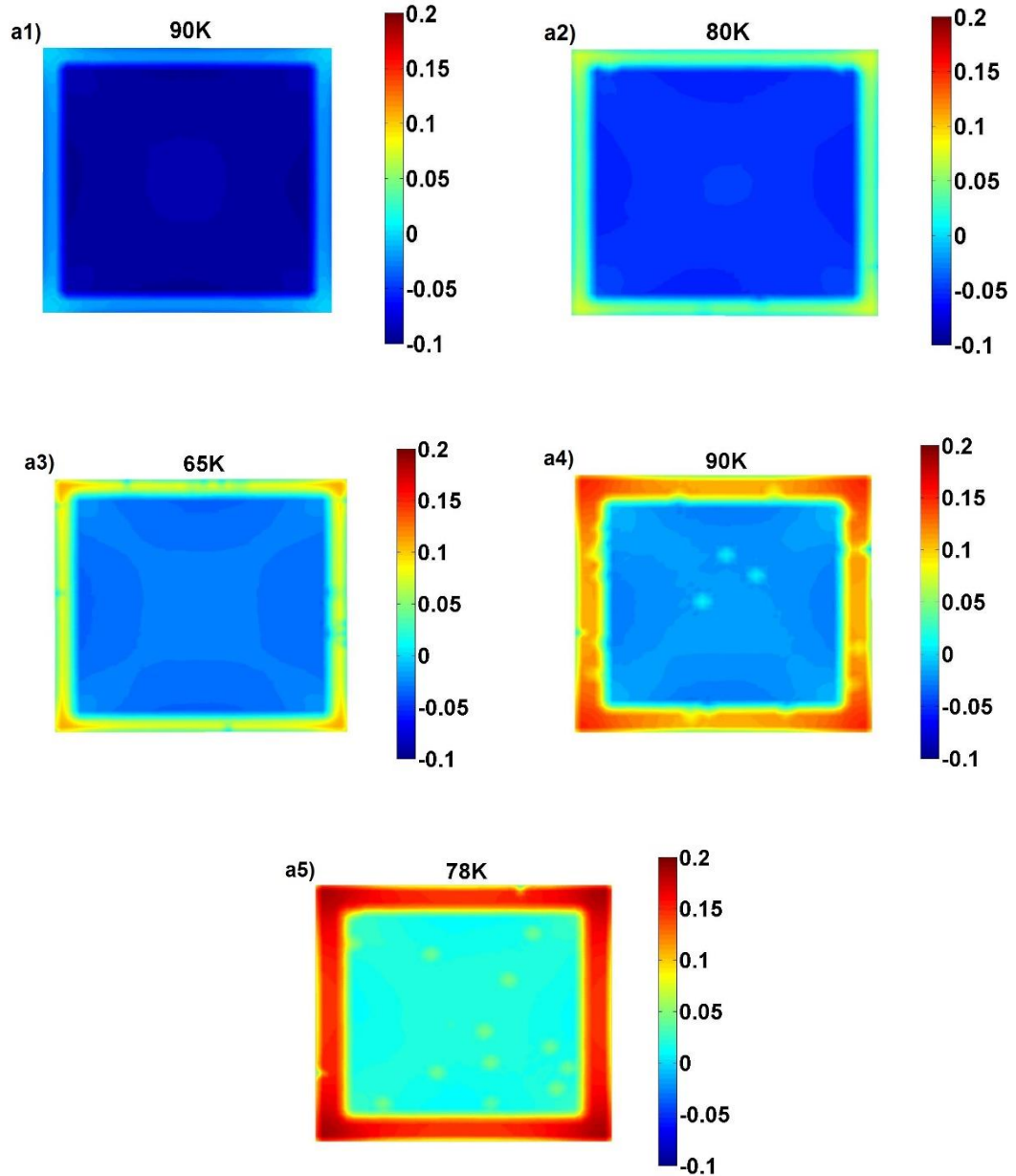


Figure 3. 10: Displacement fields for the different HS shell lattice parameter values a) $R_{0,S}^{HH} = 1.00$ nm b) $R_{0,S}^{HH} = 1.02$ nm c) $R_{0,S}^{HH} = 1.03$ nm d) $R_{0,S}^{HH} = 1.04$ nm and e) $R_{0,S}^{HH} = 1.05$ nm, corresponding to the situations depicted in Figs. 3.9a-e. The LS state, common to all figures, was used as a reference state for the calculations of the displacement field (see Eq. (3.10)).

To confirm the previous conclusions drawn from the discussion of Fig. 3.10, we calculate the divergence and rotational of the displacement field, which corresponds to the trace of the strain tensor, describing the pure relative volume expansion, while the rotational part evidences the enhancement of the shear stresses. The spatial distribution of the divergence of the displacement field

depicted in Fig. 3.11, clearly shows a more or less homogenous distribution of the compressive stress inside the core for $R_{0S}^{HH} \leq 1.04$ nm, which enhances for smaller R_{0S}^{HH} values. In contrast, for the case, $R_{0S}^{HH} = 1.05$ nm, the core experiences tensile stress in the plateau region due to no lattice misfit between the HS core and the HS shell which plays in favor of the HS state, which shifts the transition temperature downward, as we saw in Fig. 3.4.



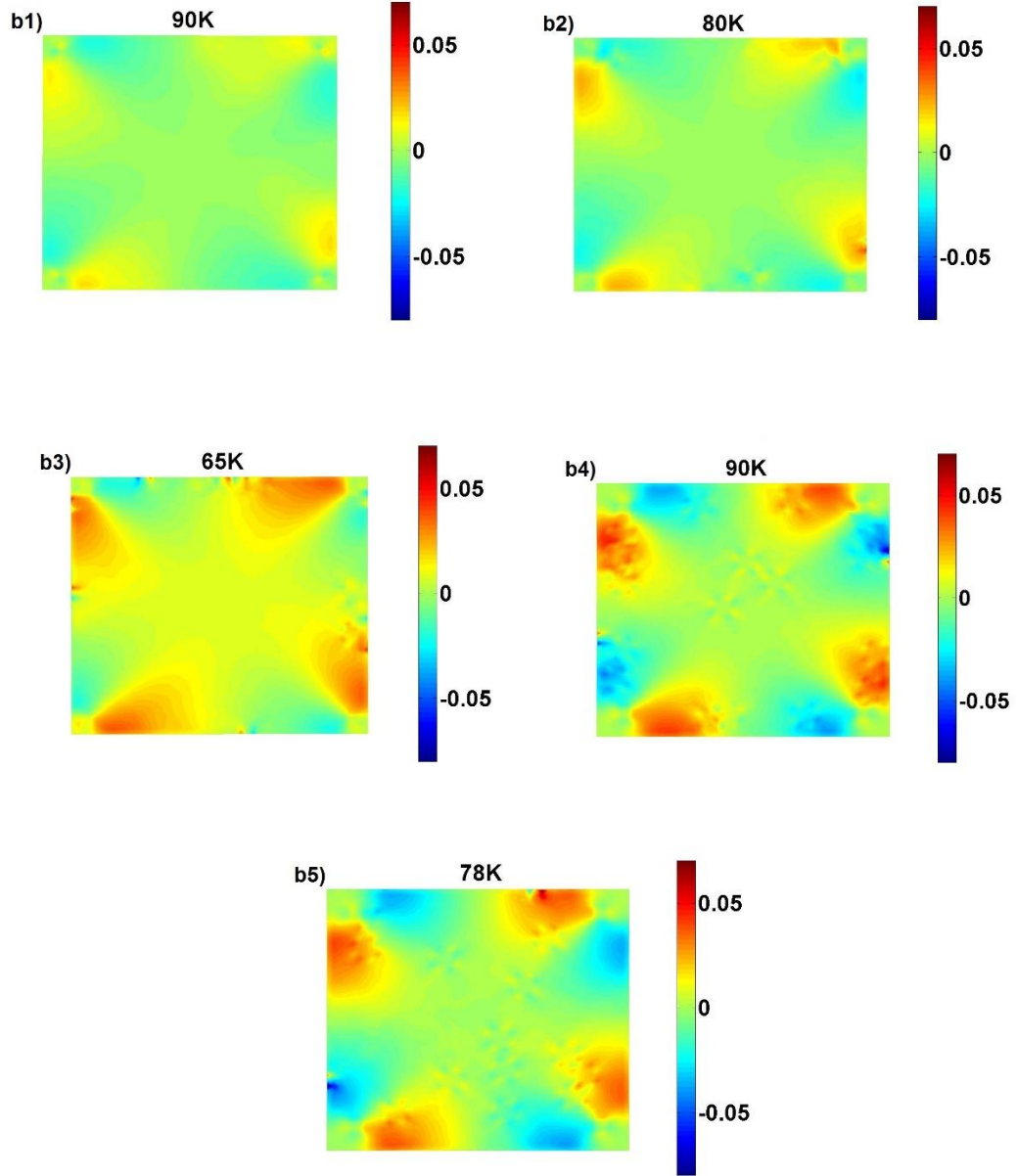


Figure 3.11 The four figures a1 to a5 (resp. b1 to b5) are the spatial distribution of the divergence (resp. rotational) of the displacement fields corresponding to panels of Fig. 10, i.e., obtained for $R_{0S}^{HH} = 1.0, 1.02, 1.03, 1.04$ and 1.05 nm, respectively. The quantity, $\vec{\nabla} \cdot \vec{u}(\vec{r})$ (panels a1-a5) relates to the dilatation field. Red areas are under tensile stress, and blue areas are under compressive stress. Remark the decrease (resp. increase) of the compressive (resp. tensile) in the core (resp. shell) part with increasing the shell's lattice parameter in the HS state, R_{0S}^{HH} . The quantity, $\vec{\nabla} \times [\vec{u}(\vec{r})]$ (panels b1-b5), expresses the spatial distribution of the shear stress, whose maximums are located at the same special positions for all figures, and enhances as R_{0S}^{HH} increases.

Having information about the spatial distribution of the displacement field from Fig. 3.10, $\vec{u}_x(x, y)$ and $\vec{u}_y(x, y)$ on each lattice node, we obtain the components of the strain tensor, given by the formula

$$\epsilon_{\alpha\beta} = \frac{1}{2} \left(\frac{\partial u_\alpha}{\partial x_\beta} + \frac{\partial u_\beta}{\partial x_\alpha} \right). \quad (3.11)$$

Here α and β may be x or y and $x_x = x$, $x_y = y$, which leads to $\epsilon_{xx} = \frac{\partial u_x}{\partial x}$, $\epsilon_{yy} = \frac{\partial u_y}{\partial y}$, and $\epsilon_{xy} = \epsilon_{yx} = \frac{1}{2} \left(\frac{\partial u_x}{\partial y} + \frac{\partial u_y}{\partial x} \right)$. It is well known [52] that ϵ_{xx} and ϵ_{yy} provide information about the local relative volume change, while ϵ_{xy} and ϵ_{yx} connect to the pure shear strains, through the following ‘‘dilatation’’ and ‘‘distortion’’ fields, respectively:

$$\text{div}[\vec{u}(\vec{r})] = \epsilon_{xx}(\vec{r}) + \epsilon_{yy}(\vec{r}) \quad \text{and} \quad \overline{\text{Rot}}[\vec{u}(\vec{r})] = \epsilon_{xy}(\vec{r}) - \epsilon_{yx}(\vec{r}) \quad (3.12)$$

The rotation of the displacement field, shown in the bottom panel of Fig. 3.11, expresses another aspect of the strain acting inside the core-shell nanoparticle. The maximum rotational field takes place in the interface regions between HS and LS phases inside the core and the shell and propagates until the nanostructure’s surface. These peculiar points constitute brittle regions in the nanostructure.

3.3.2.6 Effect of the core-shell lattice parameter misfit in HS state on the whole system

As we have discussed in detail the general situation where the nanocomposite is made of two SCO materials having different HS lattice parameters. Now, moving onto the general situation where the nanocomposite is made of two SCO materials having different LS lattice parameters, but as we move towards the section for avg. High spin fraction (NHs) and avg. bond length, it might be fruitful to recall our previous results regarding core-shell interface dynamic [41], [43], in which we discussed at length the effect of width and interface misfit in HS state of the shell, respectively. From these two study we could expect that introducing the misfit in LS state would also lead to expected multistep and further prolonging the HS state or delay in achieving the LS state, which is shifting it to far lower temperatures. In fact, that was the motive to carry out this study to see the symmetric effect of the applied misfit at the HS and LS state interface. However, instead of unearthing our expected presumption, we end up uncovering more intriguing features of core-shell architecture.

Coming back to our results for core-shell nanocomposite, as we can see in the Fig. 3.12a and Fig. 3.12b, we see counter-intuitive behaviour in both these order parameter (avg. bond length and HS fraction) from what expected. We have plotted the total avg. Nhs (N_{HS}^{tot}) and avg. lattice parameter ($\langle R^{tot}(nn) \rangle$), which we have divided in two categories on the basis of N_{HS}^{tot} , category ‘‘I’’ where we have a mix of multistep and re-entrant transition which can reach the total LS state (except for $R_{0,s}^{LL} = 1.03$), and category ‘‘II’’ where we can see strong re-entrant phenomena for all the cases having $R_{0,s}^{LL} \geq 1.03$, i.e. for these cases, we don’t have stabilised LS state in core, in low-temperature regime; thus we see that either

whole ($R_{0,s}^{LL} \geq 1.04$) or partial ($R_{0,s}^{LL} = 1.03$) core is transformed into HS state as we arrive at low temperature with the average bond length, higher than that of equilibrium bond lengths in HS states (R^{HH}) for some cases.

Table 3. 2 Equilibrium nn distances used for the core, shell, and core-shell bonds. The LS shell nn bond-length ($R_{0,s}^{LL}$) is used here as a variable.

nn configurations	HH	HL	LL
core nn distance (nm)	$R_{0,C}^{HH} = 1.05$	$R_{0,C}^{HL} = \frac{1 + R_{0,C}^{HH}}{2} = 1.025$	$R_{0,C}^{LL} = 1.0$
shell nn distance (nm)	$R_{0,S}^{HH} = 1.05$	$R_{0,S}^{HL} = \frac{1.05 + R_{0,S}^{LL}}{2}$	$R_{0,S}^{LL}$
nn distance (nm) at interface viewed from the shell	$R_{0,S}^{HH} = 1.05$	$R_{0,S}^{HL} = \frac{R_{0,S}^{LL} + R_{0,S}^{HH}}{2}$	$R_{0,S}^{LL}$
nn distance (nm) at interface viewed from the core	$R_{0,C}^{HH} = 1.05$	$R_{0,C}^{HL} = \frac{R_{0,S}^{LL} + R_{0,C}^{HH}}{2} = 1.025$	$R_{0,C}^{LL} = 1.0$

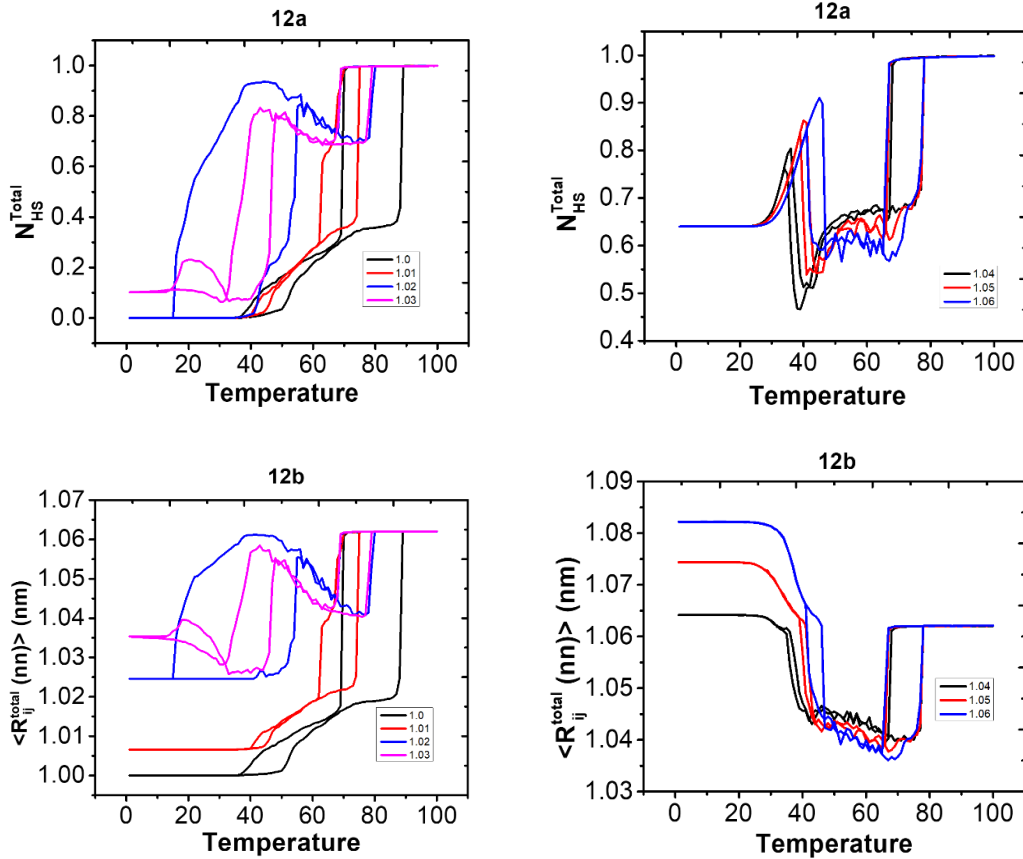


Figure 3. 12 Thermal variations of (a) the total HS fraction and (b) average lattice parameter of the whole SCO nanocomposite for different equilibrium lattice parameters of the shell, which was varied from $R_{0,s}^{LL} = 1.00$ to 1.06 nm. The other lattice parameter values are given in Table II. The used values of the elastic constants are: $A_C = A_S = A_{int} = 10^5 K.nm^{-2}$ for nn interactions and $B_C = B_S = B_{int} = 10^5 K.nm^{-2}$ for the nnn interactions in the core (C), the shell (S) and interface (int).

3.2.2.7 Thermal properties of shell and core components

In order to understand these responses, we dissect further and move on to the individual responses of the core and shell lattices. We examine the thermal behavior of the electronic and mechanical responses of the core and the shell separately as a function of $R_{0,S}^{LL}$. Figure 3.13 shows the thermal dependences of the average HS fraction and the average lattice distance, $\langle r \rangle_S$, of the shell (Figs. 4a and 4b) for different $R_{0,S}^{LL}$ values going from 1.00 to 1.06 nm (i.e. from $R_{0,C}^{LL}$ to $R_{0,C}^{HH}$), while $R_{0,S}^{LL}$, $R_{0,C}^{LL}$, $R_{0,C}^{HH}$ and $R_{0,C}^{HL}$ are kept invariant as given in Table II. The associated HS fraction and lattice spacing, $\langle r \rangle_C$, of the core are depicted in Figs. 3.13, and 3.13, respectively.

An interesting situation arises when we compare between the thermal dependence of HS fraction and bond lengths of the shell and core, in Fig. 3.13 and Fig. 3.13. As we can see the results this time have more variation than the results, previously discussed for the High spin misfit ($R_{0,S}^{HH}$), thus we will first divide the results into two sections “Category I” for the results depicting multistep transition and “Category II” for the results demonstrating re-entrant behavior. We will further discuss each case individually for the varying misfit range i.e., (from $R_{0,S}^{LL} = 1.0 - 1.06$) and will term them as Case 0 - Case 6 respectively.

It is worth noticing that the temperature dependence of the average core bond length shows very unusual and non-monotonous trends around the temperature region of the transition of the shell. These behaviors are unique and of merit to be discussed in a detailed way. The temperature dependence of the avg. bond lengths of shell $\langle r \rangle_S$ (Fig. 3.13 exhibits), plateau region, multistep and re-entrance behavior while the HS fraction (Fig. 3.13 behavior to thermal change is majorly silent (except for case 0, $R_{0,S}^{LL} = 1.0$) to all these phenomena and only depicts normal hysteresis behavior with some changes in its width and a slight indication of plateaus as we keep changing the $R_{0,S}^{LL}$. However, if we check the core part, we find perfect synergy between the magneto-elastic coupling, where we can see the comparison between HS fraction and bond lengths is showing strongly coupled behavior. It is worth noticing that although this behavior of shell HS fraction turning blind eye to its elastic counterparts is in contrast with the usual elastic models of SCO where, in general, both of these parameters are strongly linked, the even more intriguing part is that this situation is just inverse of our previous studied situation [53] with lattice misfit in the HS part of the bond lengths, where we observed the delinking in the core part of the system.

Thus, it will be very beneficial to understand what exactly is happening in the system as a whole (core-shell) and regionally (core & shell), which disrupts this magneto-elastic synergy in either of the core or shell lattice, as it will help us in understanding under what circumstances, we can expect the coupling to be synergic or silent.

It is interesting to mention that, for used $R_{0,S}^{LL}$ values, the HS fraction (N_{HS}^{Shell}) of the shell (Fig. 3.13) experiences an increase in hysteresis width for $R_{0,S}^{LL} = 1.00, 1.02$ and 1.03 nm, which is drastically reduced for $R_{0,S}^{HH} \geq 1.04$ and almost disappears for $R_{0,S}^{LL} = 1.06$.

The switching on/off of the synergy (between N_{HS}^{Shell} , & $\langle r \rangle_s$), widening/disappearance of the thermal hysteresis, caused by the misfit between the equilibrium nn distance of the core, $R_{0,C}^{LL} = 1.00$ and that of the shell, $R_{0,S}^{LL}$, originates from the mechanical stress/strain exerted by the transition of core (shell) on the shell (core). This interference generated by either of lattices on the transformation of other prevent its complete transformation during the thermal transition process.

So, beginning from that of “Case 0” as indicated in Fig. 3.13, we see a similar trend as that found in previous studies, where the expansion of the shell part during its phase transition induces tensile stresses on the core. For equal equilibrium HS lattice parameters of core and shell (i.e., $R_{0,S}^{LL} = R_{0,C}^{LL} = 1.00$ nm), the two subsystems form a unique and uniform elastic lattice (same bond lengths and elastic constants in LS and HS states). As a result, a ferroelastic interaction occurs between the shell and the core, which makes the core expand a little bit before its transition temperature and facilitates its transition to the HS state as the core lattice is feeling negative pressure. It is worth mentioning that this plateau is hardly visible in the temperature dependence of the core HS fraction of Fig. 3.13, which is in agreement with our previous studies [41], [43] where we found the core HS fraction and avg. bond lengths to be in disagreement with each other, while the behavior of shell lattice HS fraction and avg. bond length is weakly synergic for this situation. However, it should be noted this is the case where there is no misfit in the LS or HS state, and as we introduce this misfit in the LS regime of the shell lattice, we find this situation to be reversed entirely that is we will see that slowly core lattice will become synergetic while the shell lattice turns silent to the coupling between HS fraction and the bond lengths. But before we move on to that, we will like to discuss Case 1, which is also quite a special case, as it is kind of turning point for this behavior.

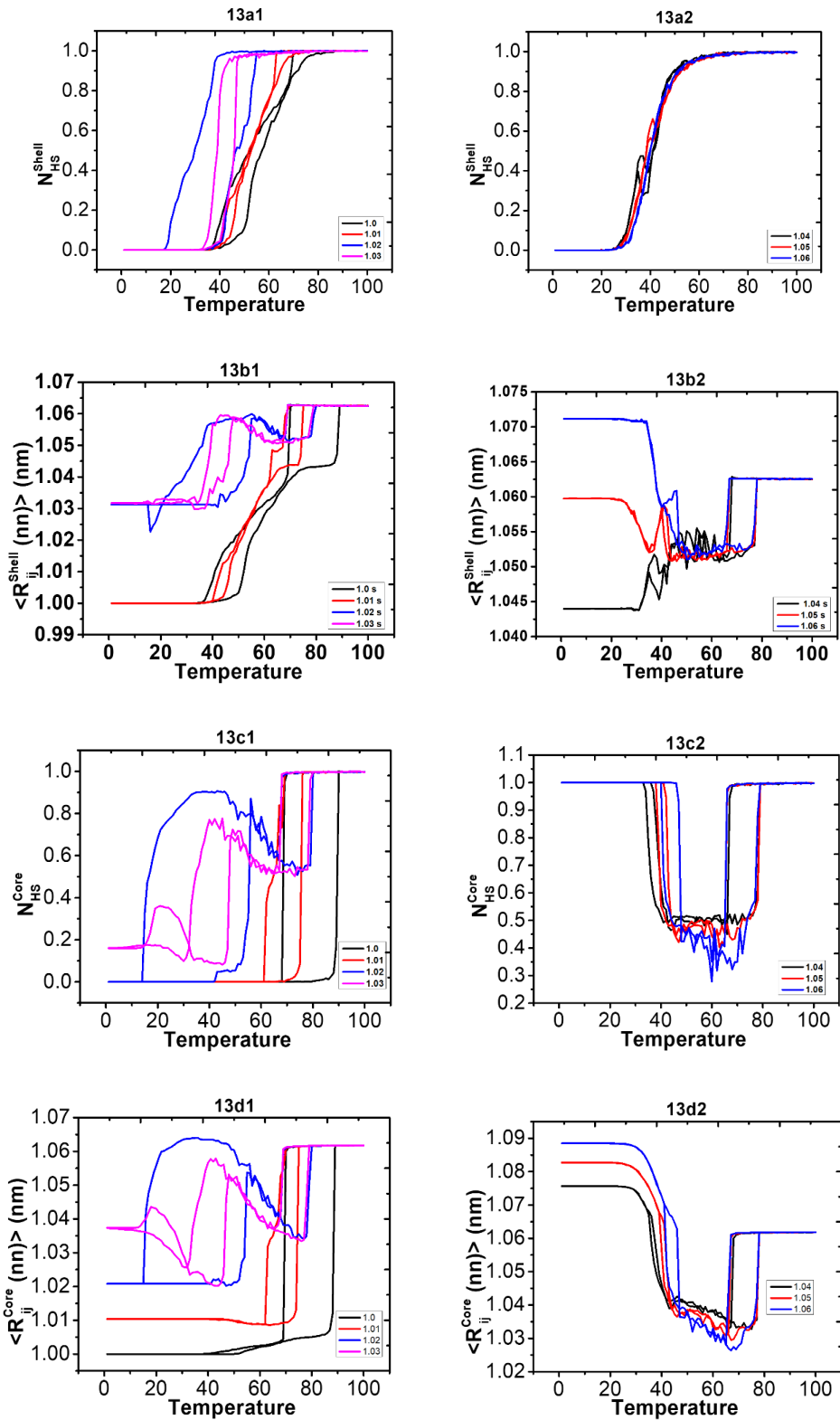


Figure 3. 13 Thermal variations of (a) the shell HS fraction and (b) average nn distance for different R_{0S}^{LL} values, varied from $R_{0S}^{LL} = 1.0$ to 1.06 nm. (c) and (d) are the temperature dependences of the core HS fraction and average nn distance for the same R_{0S}^{HH} values. The

other lattice parameter values are given in Table II. The other model parameters are given in the text.

In this case we can see in Fig. 3.13 that both shell and core lattice HS fraction responds to the changes in the avg. bond length. However, the core lattice shows high degree of correlations between its order parameters (HS fraction & avg. bond length), whereas the order parameters corresponding to shell lattice, which is weakly co-related, shows the departure from this trend. Intriguingly enough, as we have seen in the Case 0 and previous studies [41], [43] that the mechanism through which the core's transition temperature is shifted downwards is through the shell exerting negative pressure on the core lattice, which in turn, affects the avg. bond lengths of the core lattice, and we can see a monotonous increase and emergence of the plateau, however in this case, we don't arrive at any such situation in the core lattice, but we can see that the HS fraction and avg. bond length for core are good resemblance of each other. For Cases 2 and 3 ($R_{0,S}^{LL} = 1.02$ & 1.03) Fig. 3.13, we have an interesting scenario where core and shell lattice are competing for their dominance, as we can see that in these situations, the shell lattice have a very wide hysteresis for both the cases, compared to all other. From these situations, we see clear departure of synergy between shell lattice order parameters, while core lattice's order parameters complement with each other very well. If we see core parameters for Case 2 ($R_{0,S}^{LL} = 1.02$) we can see that core is continuously trying to reach the LS state, as we can see in the HS fraction that during cooling, it starts to fall around 64 K till a value close to 0.6 and then again in a 20 K interval it rises till 0.9, portraying the re-entrant behavior. After which it plateaus around 0.9 HS fraction, then gradually get lowered till 0.7 approx. and finally reaching its LS state, this consecutive rise and falls of HS fraction of core lattice, very effectively portrays the hardships core lattice is going through to reach the LS state. Although in this case we could also see shell lattice also have to wait a more extended period of time to reach its LS state, that is the reason why we see such a wide hysteresis for this case, this is the perfect case where we can see both core and shell inhibiting each other's relaxation after which we see that for shell lattice transition begin around 30K, as both the lattice are coupled we can see a steeper decrease in core lattice in both of its parameters, but very interestingly if we see the shell lattice parameters closely, we can see that the shell's avg. bond lengths try to approach its LS state but then again rise back to the core's HL state value (i.e. 1.03) rather than the shell's LS state value. This behavior is peculiar because although this explains the reason for wide hysteresis, the reason for its cause is not very apparent. As we can see, the total HS fraction was able to approach zero, but as we consult their respective avg. bond lengths, we see that the respective bond length parameters are in frustrated state for both core and shell, as for the core value of avg. bond length is found to be 1.02, while for the shell it is 1.03 nm. These numbers are particularly interesting because we can see that for the shell lattice the avg. bond lengths first drop to 1.02 and then again rise to 1.03, it is somewhat similar to Case 1 ($R_{0,S}^{LL} = 1.01$) where shell relaxed avg. bond length is 1.0 while core's is 1.01. It is like frustration is shared within the whole lattice and is not just dumped into core or shell lattice. Whereas, this was not the case when we misfit in the HS state, where only core lattice has to

compromise with its avg. bond length. Another fact that is magnified in this case is how well the core and shell lattice are coupled elastically for this case. Now, as we move on to Case 3, in the shell part, we can see the hysteresis for HS fraction is wider than the rest of the graphs except for the Case 2. When we view the parameters of the core lattice, we can see a nice correlation between both the parameters, also in this case we can see that core lattice go through re-entrant phase transition almost twice in both heating and cooling cycle. Though more predominantly in the cooling cycle from HS fraction point of view, whereas as far as avg. bond lengths are concerned, we can see the re-entrant effect in both heating and cooling branches for the core lattice.

Now, as we move on to other part where we have the cases having $R_{0,S}^{LL} \geq 1.04$ Fig. 3.13, we will see a similar kind of behavior for all of them. As we increase the misfit in the LS state, we see a predictive behavior for the core and shell lattices individually and core-shell structure as a whole, which we were not able to see in the cases for $R_{0,S}^{LL} \leq 1.04$. So, for temp. greater than 60 K, we can see that we find similar behavior and transition temperature for HS and LS transition during heating and cooling cycles for all three cases. Although what is surprising in these cases is that in core lattice, at lower temperatures, we have no LS state and their respective avg. bond lengths are even higher than that of its HS states at higher temperatures. Whereas for the shell lattice, the situation is the same with respect to avg. bond length, i.e., they can reach values higher than their equilibrium LS state or even than their HS state for these cases, but still, for shell lattice, we can reach its electronic LS state, which is a bit counterintuitive.

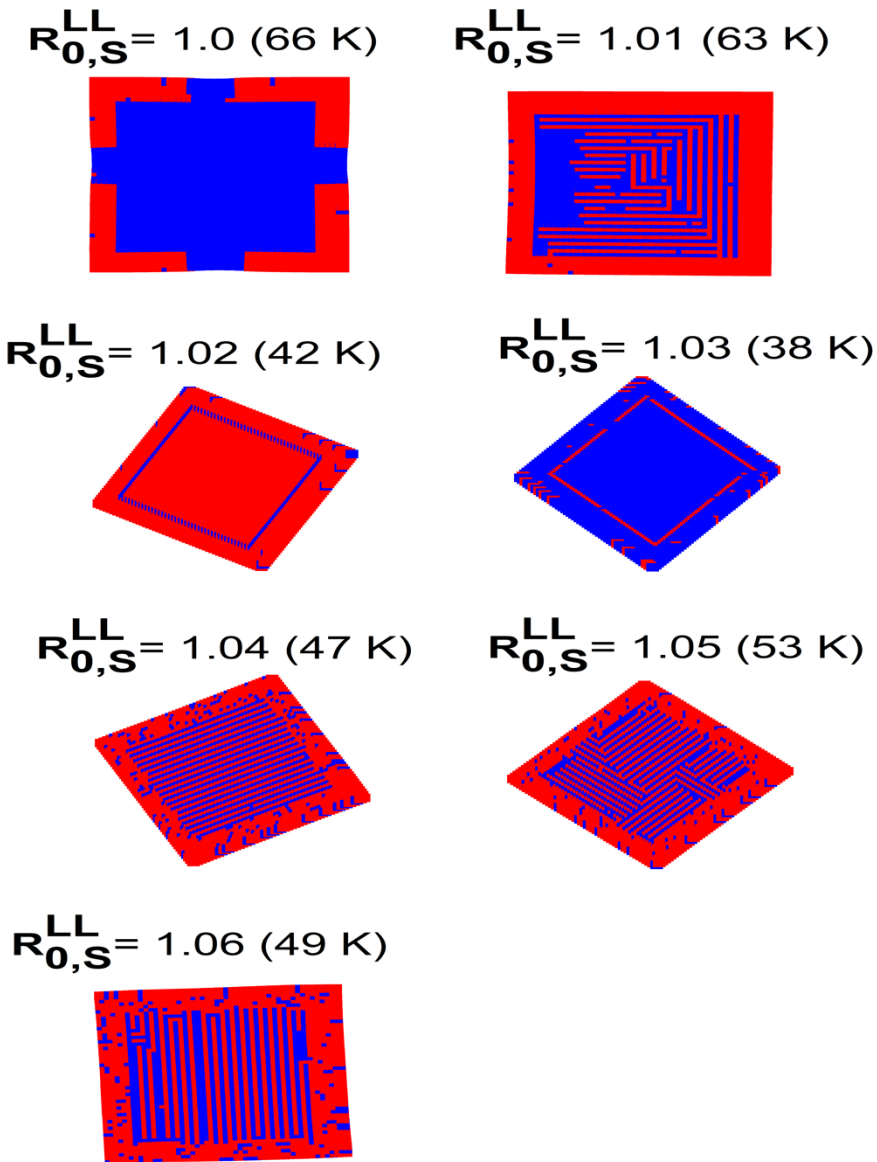


Figure 3. 14 Selected snapshots are depicting the spatial distribution of the HS fraction presented in Figs. 12 and 13 for the case $R_{0,S}^{LL} = 1.00, 1.01, 1.02, 1.03, 1.04, 1.05, \text{ and } 1.06 \text{ nm}$, and temperature $T = 66, 63, 42, 38, 47, 53, \text{ and } 49 \text{ K}$, respectively. The corresponding total HS fraction (0.28, 0.61, 0.93, 0.07, 0.63, 0.64, and 0.59) and lattice parameter (1.01, 1.03, 1.06, 1.02, 1.04, 1.04, and 1.03) values can be easily read on Fig. 3.12 and Fig. 3.13 can be consulted for the core and the shell lattice. Remark the emergence of labyrinth HS structures inside the core as a result of the spatial distribution of the strain. Here HS (in red) and LS (in blue) depicts total HS occupation in the shell and spatial distribution of HS fraction in the core.

3.3.2.8 Spatial distribution of the HS fraction and evidence of labyrinth formation inside the core

We examine the spatial dependence of the HS fraction in the core and shell, along

with the thermal hysteresis of Fig. 3.12, and address the effect of lattice misfit, $R_{0,S}^{LL} - R_{0,C}^{LL}$, on the HS fraction nucleation mode. Selected snapshots of the spatial distribution of the HS fraction are shown in Fig. 3.13 for $R_{0,S}^{LL} = 1.00, 1.01, 1.02, 1.03, 1.04, 1.05, \text{ and } 1.06$ nm and temperature $T = 66, 63, 42, 38, 47, 53, \text{ and } 49$ K, respectively. These correspond to the situation in which the interplay between the elastic properties of the core and the shell is maximum, as shown in Fig. 3.13. The shell exerts highly anisotropic constraints on the system at these temperatures, resulting in special spatial self-organization of the spin states via labyrinth structures (see Fig. 3.14) during the growth/decay of the HS fraction. Such behavior is intriguing and may be related to the lattice shape and the spatial distribution of elastic strain in the lattice. The formation of HS and LS stripes is attributed to the coexistence of directional ferroelastic and antiferroelastic interactions, as evidenced by the spatial behavior of the average lattice parameter within the lattice. Furthermore, the fact that these 1D structures can be formed along both the x and y axes indicates that there are no anisotropic effects in the growth modes of these strings.

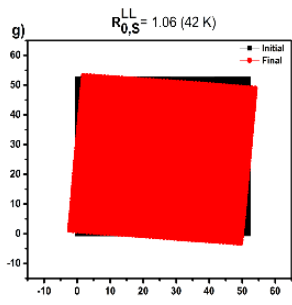
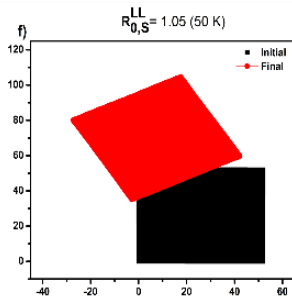
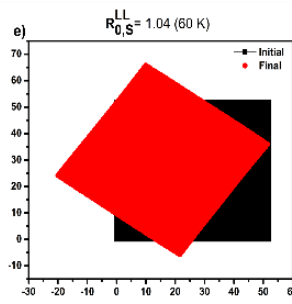
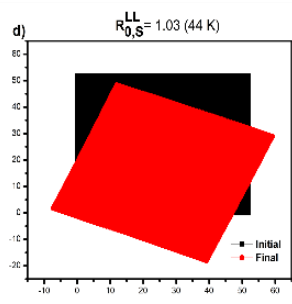
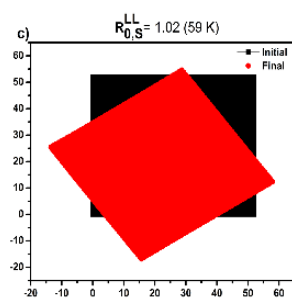
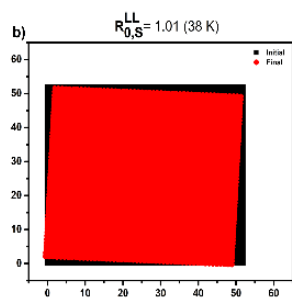
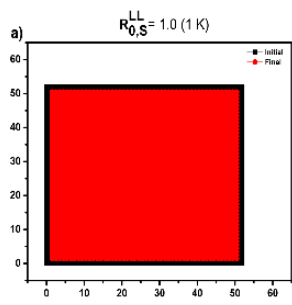
Because of the mechanical anisotropy of the structure, the deformation is smaller towards the corners than the edges [53]. As a result, the core-shell interface bends inwards, creating extra transversal tension. The curvature of the interface is directly related to the sinusoidal variation of the transversal deformation. To preserve the orthogonal relationship between the interface and the column of atoms spanning through, the curvature imposes a distortion locally. This condition opens the lattice towards the core, resulting in the core's expansive deviation of the transversal lattice parameter.

3.3.2.9 Lattice distortion and spatial distribution of elastic stresses

Now we focus on the stresses generated by the nucleation and growth process, which is important in the self-organization of the HS and LS states. For that, we determine the \vec{r}_{ij}^0 and \vec{r}_{ij} , the initial and final atomic positions of the site (i, j) . In the present analysis, we take these two positions and then plot the distances between these two points for the whole lattice.

$$d = \sqrt{(x_i - x_j)^2 + (y_i - y_j)^2}, \quad (3.13)$$

In this case, the usual displacement field, $\vec{u}(i, j)$, as discussed in equation (3.10) is plotted with other plots because the lattice seems to drift/rotate (or both) across the plane, and thus for some situations, it becomes complicated to see how displacement is really taking place in the system. We have calculated the distances and its spatial distribution, of the core and shell atoms, for several values of $R_{0,S}^{LL}$. The obtained results are summarized in Fig. 3.15. As we can see they reveal a possible presence of strong vortices like formations in the core-shell architecture.



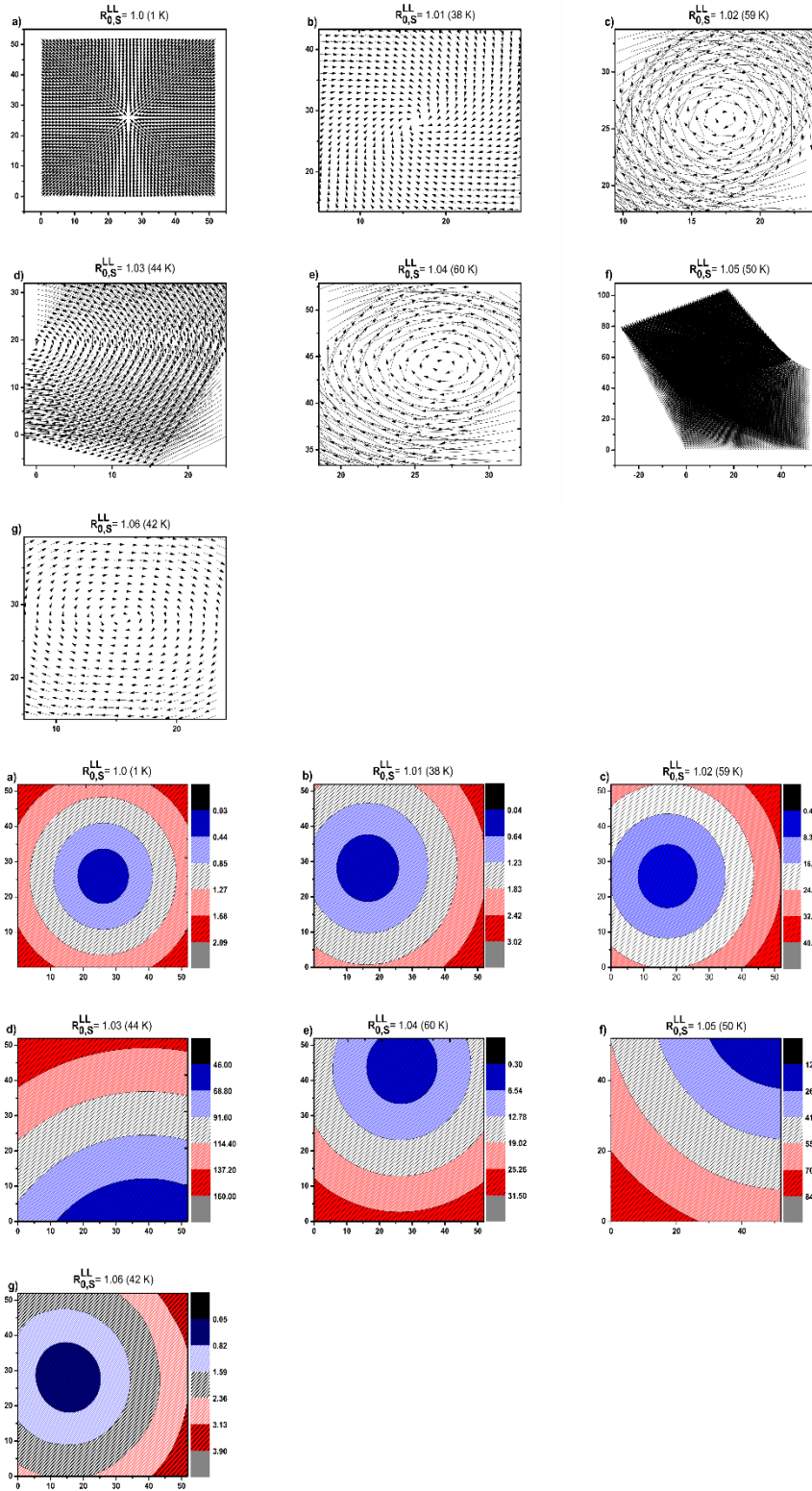


Figure 3. 15 Displacement fields for the different LS shell lattice parameter values $R_{0,S}^{LL} = 1.00$ (a) – 1.06 (g) nm. The HS state, common to all figures, was used as a reference state for the calculations of the displacement field and difference in distance between Initial and Final position (see Eq. (3.10 & 3.13)). Figures are divided into three sections the first section refers to

the initial and final position of the two lattices, the second section is for the displacement field, while the third is for differences in the distances between their atomic positions.

3.3.2.10 Centre of mass

In order to confirm whether the core-shell lattice is just drifting across the plan or have a certain movement, we plot the trajectory for the center of mass for core-shell lattice and indeed for Case 3 ($R_{0,S}^{LL} = 1.03$) we can see the vortex gyration for this particular case. This particular behavior is very intriguing, and more study into it is needed to understand the origin of such behavior. In Fig. 16a, we see the centre of mass for Case 3 making a semicircular motion around the end of the cooling branch of the hysteresis starting around 40 K and finishing around 10 K. In Fig. 3.16b, we plotted the summation of the distances between subsequent position for the centre of mass, with respect to the number of positions we have for the centre of mass, and is then compared with the thermal hysteresis for this case and we can see an uncanny resemblance between the two. In Fig. 16c we plotted the vortex gyration with respect to temperature and can clearly see the effect of temperature on the movement of the core-shell lattice. These Fig. clearly indicates that we need to study this system in detail in order to understand how the misfit and strain offset a particular motion in the core-shell lattice.

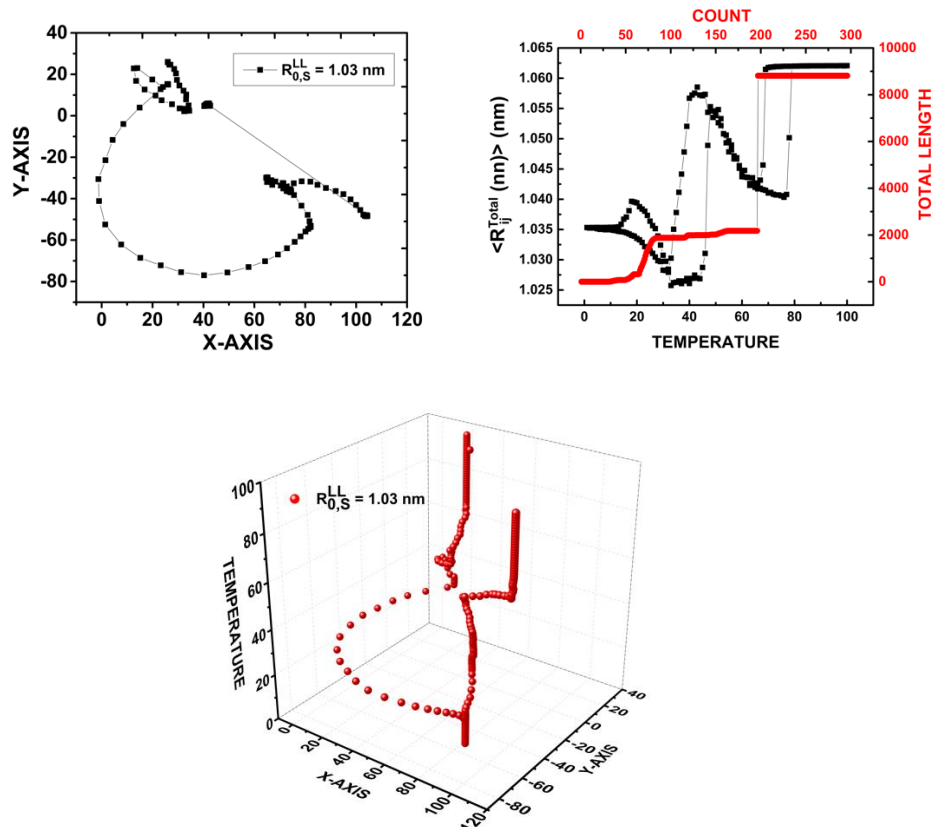


Figure 3. 16 (a) Showing the path traced by the center of mass for Case 3. (b) Showing the correlation between the thermal hysteresis and the total length for the center of mass with

respect to the number of positions we have for the centre of mass. (c) Showing the path traced by the center of mass during thermal hysteresis for Case 3.

3.4 Conclusion

This work was devoted to the study of SCO nanostructures made of a core-shell nanoparticle, where both constituents are spin active and have different transition temperatures. To investigate the interplay between the magneto-elastic properties of these two subsystems, which interact elastically through their common elastic interface, we adopted the case where the lattice parameters of the two constituents are the same in the LS (HS) state and let them be different in the HS (LS) state. To realize this situation, we fixed the LS (HS) lattice parameter to 1.0 (1.06) nm for the core and the shell, the HS (LS) lattice parameter of the core is set equal to 1.05 (1.0) nm, and we change the HS (LS) shell parameter of the shell in the interval 1.00 and 1.05 (1.0-1.06) nm. When HS (LS) core and shell lattice parameters are different, an elastic frustration occurs, which causes a significant alteration in the thermal hysteresis for both core and shell.

One of the most intriguing results emerging from the magneto-elastic interactions within the nanostructure concerns the core's reaction. Indeed, for a strong lattice parameter misfit between the shell and core in HS, the shell shows thermally-induced multistep transitions on both the HS fraction and lattice parameter. In contrast, the core exhibits a multistep transition on its lattice parameters but a simple transition on its HS fraction behavior. Similarly, when there is a strong lattice parameter misfit between the shell and core in LS, the core shows thermally-induced multistep transitions on both the HS fraction and lattice parameter. In contrast, the shell exhibits a multistep transition on its lattice parameters but a simple transition on its HS fraction behavior. The coupling and decoupling of electronic and elastic behavior depend on both values, and the misfit state is very novel and impossible to obtain on a simple lattice.

Consequently, for the present specific case, for misfit in HS (LS) state, the HS fraction of the core (shell) cannot be directly extracted from the behavior of the lattice parameter, and the fact that the lattice parameter converts in two steps does not mean that the spin transition does the same behavior. In addition, although the thermal dependence of the HS fraction of the core (shell) shows a single step transition, the corresponding average bond length exhibits multistep (multi-step and re-entrant) transitions with plateau regions. Spatial self-organization of the spin states with labyrinths formation stabilizing longitudinal or transversal HS and LS strings, anti-ferromagnetically coupled to surrounding strings, is evidenced. This type of organization of the spin states is new and deserves further investigations. Moreover, the case of a spin-crossover core-shell nanostructure, with core and shell having the same lattice parameter in the HS state and a lattice parameter misfit in the LS state, shows very intriguing features such as vortex formation and drifting and rotation of the core-shell lattice is also very interesting.

This particular case is being studied, and the results will be submitted in a separate work.

Finally, it should be noted that the core-shell structure is defined in a finite size, and thus the system does not have phase transitions that are defined in the thermodynamic limit. The transitions studied here give characteristic changes of physical quantities depending on the frustrated situation, which may benefit from finite-size scaling investigations. It is worth mentioning that recent developments on the elastic studies of 3D nanoparticles open the way to interesting studies on 3D core-shell nanoparticles with the aim to investigate the role of the shape's effect and the magnetoelastic coupling at the interface on the thermodynamic properties of the switchable SCO nanostructures.

References: -

- [1] Z. Chen, X. Zhang, and G. Lu, "Multiscale computational design of core/shell nanoparticles for oxygen reduction reaction," *J. Phys. Chem. C*, vol. 121, no. 3, pp. 1964–1973, Jan. 2017, doi: 10.1021/acs.jpcc.6b11337.
- [2] L. Xu, H. W. Liang, Y. Yang, and S. H. Yu, "Stability and Reactivity: Positive and Negative Aspects for Nanoparticle Processing," *Chemical Reviews*, vol. 118, no. 7. American Chemical Society, pp. 3209–3250, Apr. 11, 2018, doi: 10.1021/acs.chemrev.7b00208.
- [3] D. Hudry, I. A. Howard, R. Popescu, D. Gerthsen, and B. S. Richards, "Structure–Property Relationships in Lanthanide-Doped Upconverting Nanocrystals: Recent Advances in Understanding Core–Shell Structures," *Adv. Mater.*, vol. 31, no. 26, p. 1900623, 2019, doi: <https://doi.org/10.1002/adma.201900623>.
- [4] C. Tan, J. Chen, X.-J. Wu, and H. Zhang, "Epitaxial growth of hybrid nanostructures," *Nat. Rev. Mater.*, vol. 3, no. 2, p. 17089, 2018, doi: 10.1038/natrevmats.2017.89.
- [5] J. Gao *et al.*, "Ultrastretchable Multilayered Fiber with a Hollow-Monolith Structure for High-Performance Strain Sensor," *ACS Appl. Mater. Interfaces*, vol. 10, no. 40, pp. 34592–34603, Oct. 2018, doi: 10.1021/acsami.8b11527.
- [6] J. Liu and J. Zhang, "Nanointerface Chemistry: Lattice-Mismatch-Directed Synthesis and Application of Hybrid Nanocrystals," *Chem. Rev.*, vol. 120, no. 4, pp. 2123–2170, Feb. 2020, doi: 10.1021/acs.chemrev.9b00443.
- [7] Z. Xia and S. Guo, "Strain engineering of metal-based nanomaterials for energy electrocatalysis," *Chem. Soc. Rev.*, vol. 48, no. 12, pp. 3265–3278, 2019, doi: 10.1039/C8CS00846A.
- [8] J. Liang *et al.*, "Atomic Arrangement Engineering of Metallic Nanocrystals for Energy-Conversion Electrocatalysis," *Joule*, vol. 3, no. 4, pp. 956–991, 2019, doi: <https://doi.org/10.1016/j.joule.2019.03.014>.
- [9] K. D. Gilroy, X. Yang, S. Xie, M. Zhao, D. Qin, and Y. Xia, "Shape-Controlled Synthesis of Colloidal Metal Nanocrystals by Replicating the Surface Atomic Structure on the Seed.," *Adv. Mater.*, vol. 30, no. 25, p. e1706312, Jun. 2018, doi: 10.1002/adma.201706312.
- [10] B. You, M. T. Tang, C. Tsai, F. Abild-Pedersen, X. Zheng, and H. Li, "Enhancing Electrocatalytic Water Splitting by Strain Engineering," *Adv. Mater.*, vol. 31, no. 17, p. e1807001, Apr. 2019, doi: 10.1002/adma.201807001.
- [11] Y. Yan, J. S. Du, K. D. Gilroy, D. Yang, Y. Xia, and H. Zhang, "Intermetallic Nanocrystals: Syntheses and Catalytic Applications," *Adv. Mater.*, vol. 29, no. 14, p. 1605997, 2017, doi: <https://doi.org/10.1002/adma.201605997>.
- [12] L. Wu, A. Mendoza-Garcia, Q. Li, and S. Sun, "Organic Phase Syntheses of Magnetic Nanoparticles and Their Applications," *Chem. Rev.*, vol. 116, no. 18, pp. 10473–10512, Sep. 2016, doi: 10.1021/acs.chemrev.5b00687.
- [13] M. Luo and S. Guo, "Strain-controlled electrocatalysis on multimetallic nanomaterials," *Nat. Rev. Mater.*, vol. 2, no. 11, p. 17059, 2017, doi: 10.1038/natrevmats.2017.59.
- [14] M. C. Cross and P. C. Hohenberg, "Pattern formation outside of equilibrium," *Rev. Mod. Phys.*, vol. 65, no. 3, pp. 851–1112, Jul. 1993, doi: 10.1103/RevModPhys.65.851.
- [15] T. A. A. Broadbent, "On growth and form. By Sir D'Arcy Thompson; abridged edition edited by J. T. Bonner. Pp. xiv, 346. 32s. 6d. 1961. (Cambridge University Press)," *Math. Gaz.*, vol. 47, no. 360, pp. 163–164, 1963, doi: 10.2307/3612646.
- [16] R. Rudman, "The Self-Made Tapestry: Pattern Formation in Nature (Ball, Philip)," *J. Chem. Educ.*, vol. 77, no. 4, p. 450, Apr. 2000, doi: 10.1021/ed077p450.2.
- [17] M. Presle *et al.*, "Photostrictive/Piezomagnetic Core–Shell Particles Based on Prussian Blue Analogues: Evidence for Confinement Effects?," *J. Phys. Chem. C*, vol. 118, no. 24, pp. 13186–13195, Jun. 2014, doi: 10.1021/jp501758b.
- [18] D. Asakura, C. H. Li, Y. Mizuno, M. Okubo, H. Zhou, and D. R. Talham, "Bimetallic Cyanide-Bridged Coordination Polymers as Lithium Ion Cathode Materials: Core@Shell Nanoparticles with Enhanced Cyclability," *J. Am. Chem. Soc.*, vol. 135, no. 7, pp. 2793–2799, Feb. 2013, doi: 10.1021/ja312160v.
- [19] A. C. Felts *et al.*, "Control of the Speed of a Light-Induced Spin Transition through Mesoscale Core–Shell Architecture," *J. Am. Chem. Soc.*, p. jacs.8b02148, Apr. 2018, doi: 10.1021/jacs.8b02148.
- [20] F. Wu, W. Fitzhugh, L. Ye, J. Ning, and X. Li, "Advanced sulfide solid electrolyte by core-shell structural design," *Nat. Commun.*, vol. 9, no. 1, p. 4037, 2018, doi: 10.1038/s41467-018-06123-2.

- [21] G. Félix, M. Mikolasek, G. Molnár, W. Nicolazzi, and A. Bousseksou, "Control of the Phase Stability in Spin-Crossover Core-Shell Nanoparticles through the Elastic Interface Energy," *Eur. J. Inorg. Chem.*, vol. 2018, no. 3–4, pp. 435–442, Jan. 2018, doi: 10.1002/ejic.201700121.
- [22] A. Adam *et al.*, "Strain engineering of photo-induced phase transformations in Prussian blue analogue heterostructures," *Nanoscale*, vol. 10, no. 34, pp. 16030–16039, 2018, doi: 10.1039/C8NR03597K.
- [23] Y. Ijiri *et al.*, "Correlated spin canting in ordered core-shell $\text{Fe}_3\text{O}_4/\text{Mn}_x\text{Fe}_{3-x}\text{O}_4$ nanoparticle assemblies," *Phys. Rev. B*, vol. 99, no. 9, p. 94421, Mar. 2019, doi: 10.1103/PhysRevB.99.094421.
- [24] K. Affes, A. Slimani, Y. Singh, A. Maalej, and K. Boukheddaden, "Magneto-elastic properties of a spin crossover membrane deposited on a deformable substrate," *J. Phys. Condens. Matter*, vol. 32, no. 25, p. 255402, Mar. 2020, doi: 10.1088/1361-648x/ab7a4a.
- [25] S. W. Chee, Z. M. Wong, Z. Baraissov, S. F. Tan, T. L. Tan, and U. Mirsaidov, "Interface-mediated Kirkendall effect and nanoscale void migration in bimetallic nanoparticles during interdiffusion," *Nat. Commun.*, vol. 10, no. 1, p. 2831, Jun. 2019, doi: 10.1038/s41467-019-10623-0.
- [26] J. C. Ondry, J. P. Philbin, M. Lostica, E. Rabani, and A. P. Alivisatos, "Resilient Pathways to Atomic Attachment of Quantum Dot Dimers and Artificial Solids from Faceted CdSe Quantum Dot Building Blocks," *ACS Nano*, vol. 13, no. 11, pp. 12322–12344, Nov. 2019, doi: 10.1021/acsnano.9b03052.
- [27] Z. Niu *et al.*, "Anisotropic phase segregation and migration of Pt in nanocrystals en route to nanoframe catalysts," *Nat. Mater.*, vol. 15, no. 11, pp. 1188–1194, Nov. 2016, doi: 10.1038/nmat4724.
- [28] F. Shi *et al.*, "Strain-Induced Corrosion Kinetics at Nanoscale Are Revealed in Liquid: Enabling Control of Corrosion Dynamics of Electrocatalysis," *Chem*, vol. 6, no. 9, pp. 2257–2271, 2020, doi: <https://doi.org/10.1016/j.chempr.2020.06.004>.
- [29] R. W. Day, M. N. Mankin, and C. M. Lieber, "Plateau–Rayleigh Crystal Growth of Nanowire Heterostructures: Strain-Modified Surface Chemistry and Morphological Control in One, Two, and Three Dimensions," *Nano Lett.*, vol. 16, no. 4, pp. 2830–2836, Apr. 2016, doi: 10.1021/acs.nanolett.6b00629.
- [30] Y. Xia, K. D. Gilroy, H.-C. Peng, and X. Xia, "Seed-Mediated Growth of Colloidal Metal Nanocrystals," *Angew. Chem. Int. Ed. Engl.*, vol. 56, no. 1, pp. 60–95, Jan. 2017, doi: 10.1002/anie.201604731.
- [31] S. Choi *et al.*, "Highly conductive, stretchable and biocompatible Ag–Au core–sheath nanowire composite for wearable and implantable bioelectronics," *Nat. Nanotechnol.*, vol. 13, no. 11, pp. 1048–1056, 2018, doi: 10.1038/s41565-018-0226-8.
- [32] M. Shim and H. McDaniel, "Anisotropic nanocrystal heterostructures: Synthesis and lattice strain," *Curr. Opin. Solid State Mater. Sci.*, vol. 14, no. 5, pp. 83–94, 2010, doi: <https://doi.org/10.1016/j.cossms.2010.04.001>.
- [33] S. E. Lohse, N. D. Burrows, L. Scarabelli, L. M. Liz-Marzán, and C. J. Murphy, "Anisotropic Noble Metal Nanocrystal Growth: The Role of Halides," *Chem. Mater.*, vol. 26, no. 1, pp. 34–43, Jan. 2014, doi: 10.1021/cm402384j.
- [34] M. J. Enright and B. M. Cossairt, "Synthesis of tailor-made colloidal semiconductor heterostructures," *Chem. Commun.*, vol. 54, no. 52, pp. 7109–7122, 2018, doi: 10.1039/C8CC03498B.
- [35] R. Costi, A. E. Saunders, and U. Banin, "Colloidal Hybrid Nanostructures: A New Type of Functional Materials," *Angew. Chemie Int. Ed.*, vol. 49, no. 29, pp. 4878–4897, 2010, doi: <https://doi.org/10.1002/anie.200906010>.
- [36] E. M. LIFSHITZ, A. M. KOSEVICH, and L. P. PITAEVSKII, Eds., "NOTATION," in *Theory of Elasticity (Third Edition)*, Third Edit., Oxford: Butterworth-Heinemann, 1986, p. viii.
- [37] A. Slimani, K. Boukheddaden, and K. Yamashita, "Thermal spin transition of circularly shaped nanoparticles in a core-shell structure investigated with an electroelastic model," *Phys. Rev. B*, vol. 89, no. 21, p. 214109, Jun. 2014, doi: 10.1103/PhysRevB.89.214109.
- [38] A. Slimani *et al.*, "Visualization and quantitative analysis of spatiotemporal behavior in a first-order thermal spin transition: A stress-driven multiscale process," *Phys. Rev. B*, vol. 84, no. 9, p. 094442, Sep. 2011, doi: 10.1103/PhysRevB.84.094442.
- [39] A. Slimani, F. Varret, K. Boukheddaden, D. Garrot, H. Oubouchou, and S. Kaizaki, "Velocity of the High-Spin Low-Spin Interface Inside the Thermal Hysteresis Loop of a Spin-Crossover Crystal, via Photothermal Control of the Interface Motion," *Phys. Rev. Lett.*, vol. 110, no. 8, p. 87208, Feb. 2013, doi: 10.1103/PhysRevLett.110.087208.

- [40] H. Oubouchou, A. Slimani, and K. Boukheddaden, "Interplay between elastic interactions in a core-shell model for spin-crossover nanoparticles," *Phys. Rev. B*, vol. 87, no. 10, p. 104104, Mar. 2013, doi: 10.1103/PhysRevB.87.104104.
- [41] Y. Singh, H. Oubouchou, M. Nishino, S. Miyashita, and K. Boukheddaden, "Elastic-frustration-driven unusual magnetoelastic properties in a switchable core-shell spin-crossover nanostructure," *Phys. Rev. B*, vol. 101, no. 5, p. 54105, Feb. 2020, doi: 10.1103/PhysRevB.101.054105.
- [42] A. Slimani, K. Boukheddaden, F. Varret, H. Oubouchou, M. Nishino, and S. Miyashita, "Microscopic spin-distortion model for switchable molecular solids: Spatiotemporal study of the deformation field and local stress at the thermal spin transition," *Phys. Rev. B*, vol. 87, no. 1, p. 14111, Jan. 2013, doi: 10.1103/PhysRevB.87.014111.
- [43] H. Oubouchou, Y. Singh, and K. Boukheddaden, "Magnetoelastic modeling of core-shell spin-crossover nanocomposites," *Phys. Rev. B*, vol. 98, no. 1, p. 014106, Jul. 2018, doi: 10.1103/PhysRevB.98.014106.
- [44] X. Chen and J. W. Hutchinson, "Herringbone Buckling Patterns of Compressed Thin Films on Compliant Substrates," *J. Appl. Mech.*, vol. 71, no. 5, pp. 597–603, Nov. 2004, doi: 10.1115/1.1756141.
- [45] N. Bowden, S. Brittain, A. G. Evans, J. W. Hutchinson, and G. M. Whitesides, "Spontaneous formation of ordered structures in thin films of metals supported on an elastomeric polymer," *Nature*, vol. 393, no. 6681, pp. 146–149, 1998, doi: 10.1038/30193.
- [46] Z. Huang, W. Hong, and Z. Suo, "Evolution of wrinkles in hard films on soft substrates," *Phys. Rev. E*, vol. 70, no. 3, p. 30601, Sep. 2004, doi: 10.1103/PhysRevE.70.030601.
- [47] R. Huang, "Kinetic wrinkling of an elastic film on a viscoelastic substrate," *J. Mech. Phys. Solids*, vol. 53, no. 1, pp. 63–89, 2005, doi: <https://doi.org/10.1016/j.jmps.2004.06.007>.
- [48] Z. Y. Huang, W. Hong, and Z. Suo, "Nonlinear analyses of wrinkles in a film bonded to a compliant substrate," *J. Mech. Phys. Solids*, vol. 53, no. 9, pp. 2101–2118, 2005, doi: <https://doi.org/10.1016/j.jmps.2005.03.007>.
- [49] X. Chen and J. W. Hutchinson, "A family of herringbone patterns in thin films," *Scr. Mater.*, vol. 50, no. 6, pp. 797–801, 2004, doi: <https://doi.org/10.1016/j.scriptamat.2003.11.035>.
- [50] E. Cerda and L. Mahadevan, "Geometry and Physics of Wrinkling," *Phys. Rev. Lett.*, vol. 90, no. 7, p. 74302, Feb. 2003, doi: 10.1103/PhysRevLett.90.074302.
- [51] J. Genzer and J. Groenewold, "Soft matter with hard skin: From skin wrinkles to templating and material characterization," *Soft Matter*, vol. 2, no. 4, pp. 310–323, 2006, doi: 10.1039/B516741H.
- [52] A. Slimani, K. Boukheddaden, and K. Yamashita, "Effect of intermolecular interactions on the nucleation, growth, and propagation of like-spin domains in spin-crossover materials," *Phys. Rev. B*, vol. 92, no. 1, p. 14111, Jul. 2015, doi: 10.1103/PhysRevB.92.014111.
- [53] N. C. Popa, "The $\{hkl\}$ Dependence of Diffraction-Line Broadening Caused by Strain and Size for all Laue Groups in Rietveld Refinement," *J. Appl. Crystallogr.*, vol. 31, no. 2, pp. 176–180, Apr. 1998, doi: 10.1107/S0021889897009795.

Chapter 4.

Thermal and mechanical properties of a spin crossover crystal in elastically bounded media.

4.1 Introduction

The advent of nano-era will not be genuinely feasible until we can formulate methods to assert power over nanomaterials and devices and harness useful work from them (motors, actuators, muscles). Because of the significance and perspective, various strategies and materials with a high level of sophistication were created. These 'molecular actuators' have distinct molecular geometries that can be interconverted reversibly in response to chemical or physical stimuli with a wide variety of ranges [1]. Because of their broad amplitude of motion, they are sometimes considered analogous to biological or mechanical machines depending on their flexibility and are thus aptly referred as "molecular machines" or "molecular muscles"[2-4]. Since there is a diverse range to choose from (chemo-mechanical, biomimetic, and other complex systems)[5], we can exercise the liberty to transcend from purely mechanical application at molecular scale and include mesoscopic and truly macroscopic structures. The interest in these stimuli-responsive materials[6-8], such as electroactive polymers, shape memory alloys, and piezoelectric ceramics, have been primarily driven by the unique requirements of emerging robotics[9-11], biomedical[12-13] and micro-nanomechanical[14] technologies.

Historically, materials used for the fabrication of MEMS were typically restricted to silicon, ceramics, metals and polymers. Since the 1970's MEMS based on silicon technology showed a significant development, mainly for sensor and actuator technologies and were a commercial success. However, that was just the start, and evidently, "there's plenty of room at the bottom", the possibility of further miniaturization, wide field of application and more sensitive nanoelectromechanical systems and devices (NEMS), sounds even more lucrative to the scientific community. As demand for systems with stringent size requirements and increasing complex functionality grows, it is necessary to develop and identify new materials with different properties that are able to operate on these minuscule scales.

Understanding and predicting the behavior of these materials is critical for optimizing operation and necessitates a thorough understanding of structure-property relationships. During the last 35 years, various studies have been conducted in order to establish the stress profile of these devices. Yet, the effect of

surface stresses over the device rigidity lacks proper understanding, and a controlled, quantitative measurement regarding the surface effects and stress on cantilever stiffness with commensurate theoretical interpretation is still out of bounds. The theoretical axial-force model proposed by Lagowski et al. [30] works well for explaining the stress generated in the doubly clamped beams and give similar results derived using Euler-Bernoulli beam theory[31]. However, the axial force model, when applied to cantilever beams, has been shown to the fundamental physical principle of force equilibrium[32]–[34]. Although demonstrated to be unphysical, there have been many experimental studies, which comply with the axial force model in cantilever beams [24], [26]–[30]. However, it is important to note that it is not entirely clear whether these measurements were solely due to stress changes on the beam surface of the cantilever beam or other unknown effects originating from unspecified changes in the resonator's mechanical properties[30], [35] are at play. Anyhow, the situation is in contrast to doubly-clamped beams, where the change in stress-induced stiffness can be systematically observed and theoretically predicted [31], [36].

The study conducted by R. B. Karabalin et al. discusses all these points in detail and strongly suggest that previous reports of stress-induced changes in cantilever beams originate from other uncontrolled surface phenomena. Specifically, an emphasis is laid on the cantilever thickness, as devices made of ultrathin materials allow for gigantic tunability in their resonance properties. It suggests a change in the transduction mechanism that is different from the one observed in the present devices. However, there is no significant detail on what this transducing mechanism looks like or its behavior.

Clearly, there are several challenges and bottlenecks to overcome[37]; the primary is enhancing synergy between molecules and their surroundings to produce useful output while maintaining or devising possibilities for external control. Due to these challenges and others highlighted in recent reviews[38–41], despite being the scientific frontier, the nascent field of 'molecular actuators' is still shrouded by concerns since most of the breakthroughs are concerning simple devices and technologies and have yet to reckon in terms of strain, efficiency, durability, scaling, and control for their effective deployment in these disruptive applications[42–48].

Nevertheless, the development of NEMS calls for major issues, including the inclusion of smart actuating materials in nanoscale systems[14]. The challenges of processes for the production of MEMS/NEMS are well known; few high-performance materials for NEMS operations are available.

In this regard, Spin crossover (SCO) material can be of substantial help to the field of molecular actuators as it can add a variety of smart features (e.g. shape memory), a high degree of synthetic versatility, and multifunctionality, such as the coupling of optical, electrical, magnetic, and mechanical properties, since the SCO molecules have the ability to be operated via different stimuli routes [49], such as

pressure[50], [51], temperature [52], electric field [53], magnetic field [54], and light [55]. Furthermore, it has been demonstrated that as far as SCO phenomenon i.e., switching between low-spin (LS) and high-spin (HS) electronic configurations, accompanied by a dramatic change of molecular volume, is concerned is size-independent i.e. SCO complexes or molecules can exhibit useful mechanical response, which ranges from microscopic crystal to the single-molecule level [56], implying that there are no fundamental limitations to their functionality at the nano-scale (eric collet).

The spin transition between LS and HS is usually accompanied by an increase of the Fe-ligand bond length by 10%, a weakening of the metal-ligand bonds, causing local volume changes [57-58], as well as ligand-metal-ligand bond angles by $0.5^\circ - 80^\circ$ which affects magnetic, vibrational and optical [59] properties. In the solid state, the thermal properties of SCO materials, gives rise to a rich variety of behaviors, ranging from (i) first-order thermally-induced spin transition (cooperative behavior), accompanied with thermal hysteresis [60], (ii) gradual spin transition [61] described by a simple Boltzmann distribution between the two states, also obtained in highly diluted crystals, or in weak cooperative systems, as well as many other exotic behaviors such as (iii) like multistep [62] or incomplete spin transition [61].

SCO materials, in particular, have a high potential for strain and work density and can offer a high level of versatility and multifunctionalism through molecular and supramolecular design [63-64]. A lot of work has been done in this field where SCO complexes are studied by various groups [65]. From the theoretical point of view, different models were introduced as the Ising-like model with forced high spin (HS) molecules at the surface [66], atom-phonon (APC) model [67-68] and elastic models [69-82].

This article aims to theoretically understand the electronic and mechanic properties of SCO molecular switches, thereby contributing to the design of better microelectromechanical systems (MEMS). Thus, we extend our previous theoretical work and use microscopic electro-elastic model [78-81] to explain non-negligible changes in the doubly clamped SCO beams due to stress generated through thermal expansion or contraction. The additional insight gained through this study will be a fundamental step toward explaining the effect of fixed edges on the structural and thermal properties of the crystal. This study is based on Monte Carlo (MC) simulations in two dimensions lattice.

The manuscript is organized as follows: In section II, we present the electro-elastic model and describe the simulation procedure. In section III, the effect of edge obstruction on a deformable spin-crossover crystal is reported, as well as the thermo-induced spin transition of crystal, structural properties are studied, and the spatio-temporal aspects were discussed. In section IV, we conclude the paper, and outline the possible developments of the present work.

4.2 Hamiltonian

We investigated a distortable 2 D rectangular lattice with a fixed topology and fixed boundary conditions. Each SCO site is represented by a fictitious spin state; $S_i = \pm 1$, where $S_i = +1$ refers to the HS state and $S_i = -1$ to the LS state.

The SCO molecules interact via elastic springs, including nearest-neighbors (nn) and next nearest-neighbors to maintain lattice stability, as illustrated in Fig.1. The electro-elastic Hamiltonian is written as follows:

$$H = \sum_i (\Delta - k_B T \ln g) S_i + A \sum_{(i,j)} (r_{ij} - R_0(S_i, S_j))^2 + B \sum_{(i,k)} (r_{ik} - R'_0(S_i, S_k))^2 \quad (4.1)$$

The first term in (1) represents the electronic contributions and contains the energetic contributions of the ligand fields in the HS and LS states, such as $\Delta = E_{HS} - E_{LS}$ corresponding 0 K and the entropic contribution originating from the electronic and vibrational degeneracy ration, $g = \frac{g_{HS}}{g_{LS}}$, between the HS and LS states. The second and the third terms describe the elastic contributions between the nn and nnn of spins-crossover units, respectively.

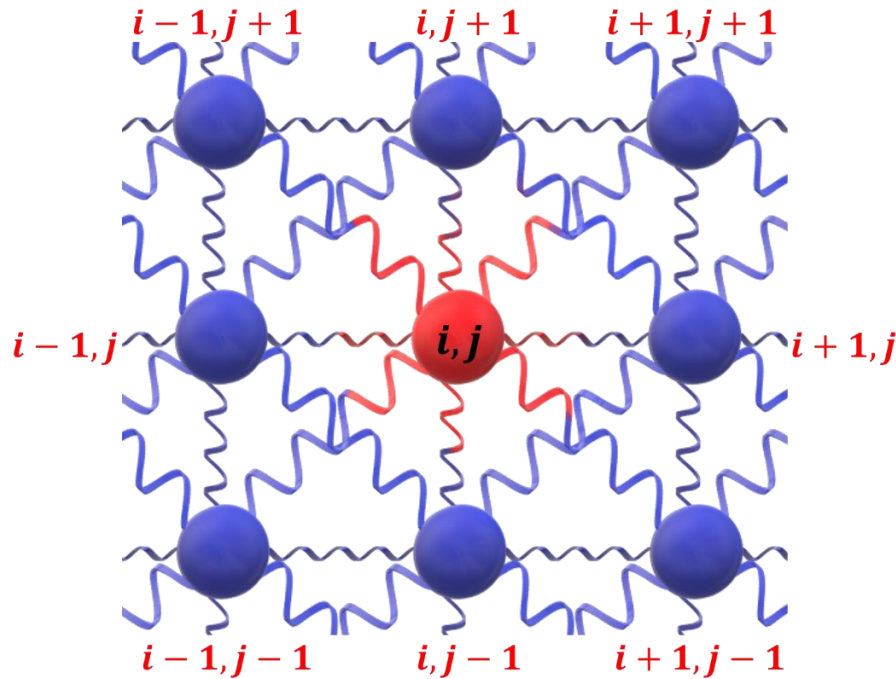


Figure 4. 1 Configuration of the elastic interactions in the two-dimensional square model considered in this site.

The quantity r_{ij} (resp. r_{ik}) is the instantaneous distance between the nn (resp. nnn) nodes i and j (resp. i and k), $R_0(S_i, S_j)$ and $R'_0(S_i, S_k)$ are the equilibrium bond lengths for the nn and nnn which depend on the spins involved in the interaction.

We set the average value of the lattice parameter between nnn neighboring HS

(LS) atoms as equal to $\sqrt{2}R_0(S_i, S_j)$. The equilibrium bond lengths are defined as follow: $R_0(-1, -1) = R_0^{LL}$, $R_0(+1, +1) = R_0^{HH}$ and $R_0(+1, -1) = R_0(-1, +1) = R_0^{HL}$ for the LS-LS, HS-HS and HS-LS sites configurations, respectively. For simplicity, we consider, $R_0^{HL} = \frac{1}{2} (R_0^{HH} + R_0^{LL})$. The general expression of the nn distance writes:

$$R_0(S_i, S_j) = R_0^{HL} + \frac{\delta R}{4}(S_i + S_j) \quad (4.2)$$

Where $\delta R = R_0^{HH} - R_0^{LL}$ is the lattice misfit between the LS and HS phases. A and B are the nn and nnn elastic constants, assumed independent on the spin states.

The simulations performed in the present work have been done using the following parameters values: $g = 150$, $\Delta = 450$ K, [81-83] leading to an enthalpy change $\Delta H = 3.5$ kJ. mol⁻¹ and entropy change $\Delta S = 41.63$ J. K⁻¹mol⁻¹. Within these values, the transition temperature is $T_{eq} = \frac{\Delta H}{\Delta S} = \frac{\Delta}{k_B \ln g} \approx 88.87$ K.

The lattice parameter values of the LS and HS states are respectively equal to $R_0^{LL} = 1$ nm and $R_0^{HH} = 1.05$ nm. For a HS atom with a LS neighbor, the equilibrium bond length is taken as $\frac{R_0^{HH} + R_0^{LL}}{2} = 1.025$ nm. In addition, the equilibrium lattice parameters between nnn in the LS and HS configurations are taken equal to $\sqrt{2}R_0(-1, -1) = 1.414$ nm and $\sqrt{2}R_0(+1, +1) = 1.484$ nm, respectively. On the other hand, the bulk modulus values have been evaluated by the Brillouin spectroscopy in the range 5 – 30 GPa. Considering the uniaxial elongation of a cubic unit cell, with a lattice parameter, a , and omitting the transverse effects, the simple relationship $A + 2B = E.a$ holds, where E is the bulk modulus. So, choosing $A = 150\,000$ K. nm⁻² = 150 meVÅ⁻² and $B \cong 0.3 A$ leads to a bulk modulus value, $E \cong 15$ GPa.

The Hamiltonian (1) is investigated here by MC simulations [84]. For each site randomly selected, with spin ($S_i = \pm 1$) and at position \vec{r}_i , a new spin value ($S'_i = -S_i$) will be set without position change. This new spin value would be accepted or rejected by the usual Metropolis criterion. Once the random spin change is accepted or rejected, the lattice is relaxed mechanically by a slight motion of each node, selected randomly, with a quantity $\|\delta\vec{r}_i\| \ll \|\vec{r}_{ij}\|$ where $\|\vec{r}_{ij}\|$ is the distance between nn. In the present study, we take the amplitude of the random displacements as $\delta r = 0.005$ nm, which is small enough compared to the bond lengths. In the next step, we choose again randomly a new site and the procedure is repeated for each of the $N_x \times N_y = (200 \times 5)$ spins where N_x and N_y are the number of atoms along the length and the width of the lattice. Once all the lattice sites are inspected for the spin change, we define such a step as the Monte Carlo step (MCS).

We used 500 MCS in order to average the physical quantities, like the high spin fraction n_{HS} , the average lattice parameter, $\langle r \rangle$, etc.

4.3 Results and discussion

In the present study, we consider a rectangular lattice of size ($N_x \times N_y = 200 \text{ nm} \times 5 \text{ nm}$) is initially built with the equilibrium lattice parameter. The simulation strategy is as follow: at 1 K (resp. 300 K), the system is built with the lattice parameter, respective to that of its initial state, i.e., the LS (resp. HS) state, and then either of its vertical or horizontal borders are fixed, and then we vary the temperature by 1K at each step, as we approach the transition temperature system is expected to transition from its initial state to the expected state. As it is well known that spin transition in SCO is accompanied by volume expansion or contraction depending on the material's spin states, fixing the edges will then realize in the generation of excess stress in the lattice as we approach transition. In the present study, we studied how lattice accomplish spin transition, how the initial state affects this realisation, the effect of lattice size, and the ratio between length and width affect its transition temperature.

It is worth mentioning that the present 2D lattice is an oversimplified description that has the merit of being numerically tractable. However, it masks several 3D effects, but even being simple serves the object of building intuition by revealing some crucial factors that might play a role in confined transition for 3D lattice. From the point of view of simulations, the study of elastic 3D systems was conducted out in prior work in order to study the crumpling effects created by the volume change during the spin transition [85] and, more recently, intensive simulations on cubic and spherical shaped lattices have been conducted by Enachescu et al. [86]

4.3.1 Boundaries effects

4.3.1.1 Thermo-induced spin transition

In this section, we analyze the effect of the edge obstruction on the thermal transition of the SCO lattice. Starting from stable state, the temperature is varied from 1 to 300 K on heating and cooling process with a thermal step of 1 K. The thermo-induced spin transition for different case, are illustrated in Figs 2(a) and (b) in terms of n_{HS} and average lattice bond lengths $\langle r \rangle$, respectively.

It is worth mentioning that the confinement applied at the edges and the initial conditions considerably influence the thermal hysteresis's global shape. Fig. 2(c & e) shows that without boundaries condition, we have an abrupt transition with hysteresis width ($\Delta T \approx 22 \text{ K}$). The presence of breadth (resp. length) obstruction, starting from the HS or LS states, reduces the cooperativity leading to gradual or incomplete transition. These behaviors are attributed to the role of the stress applied in the edge. We can also denote, starting from the LS state, a shift of the equilibrium temperature $T_{eq} = \frac{T_{HS \rightarrow LS} + T_{LS \rightarrow HS}}{2}$, towards higher values which reaches

184 K. (Here, $T_{HS \rightarrow LS}$ and $T_{LS \rightarrow HS}$ are the transition temperatures from HS to LS and LS to HS, respectively.) Whereas, starting from the HS state, the transition temperature is considerably reduced.

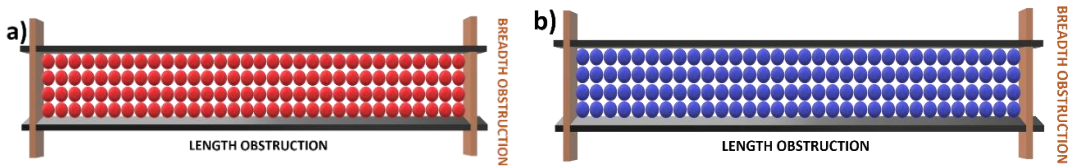
Furthermore, to understand the mechanical effects of the stress, we followed the average nn distance, depicted in Fig. 2(d&f). We can easily notice a difference in the shape of the hysteresis loop and lattice parameter, especially for obstruction along the length. We see that average nn distances are kept the same as that of its initial state, while the spin-state transition is still achievable either partially or fully depending on the initial conditions.

To express the equilibrium temperature as a function of the different parameters studied above, we introduce a simple solution based on the working assumption that the equilibrium temperature of the system results from the average value of the ligand fields. To express analytically the equilibrium temperature T_{eq} , we consider only the nearest and next-nearest neighbors in our development. In our system, the interactions depend on their positions.

Such analysis leads to the following expression of the equilibrium temperature derived from $h_i = 0$:

$$T_{eq} = \frac{\Delta}{k_B \ln g} - \frac{(A+2B)}{k_B \ln g} \Delta R (\langle r \rangle_{Teq} - R_{HL}); R_{HL} = \frac{R_{HH} + R_{LL}}{2} \quad (4.3)$$

One can notice when we have a breadth (resp. length) obstruction and starting from the HS state, $T_{eq} = 34.27 K$ (resp. $T_{eq} = 60.69 K$) values that agree pretty well with that of the simulation. However, starting from the LS state, with a breadth (resp. length) obstruction, T_{eq} could be evaluated as $T_{eq} = 96.55 K$ (resp. $T_{eq} = 162.5 K$) values that agree with that of the simulation.



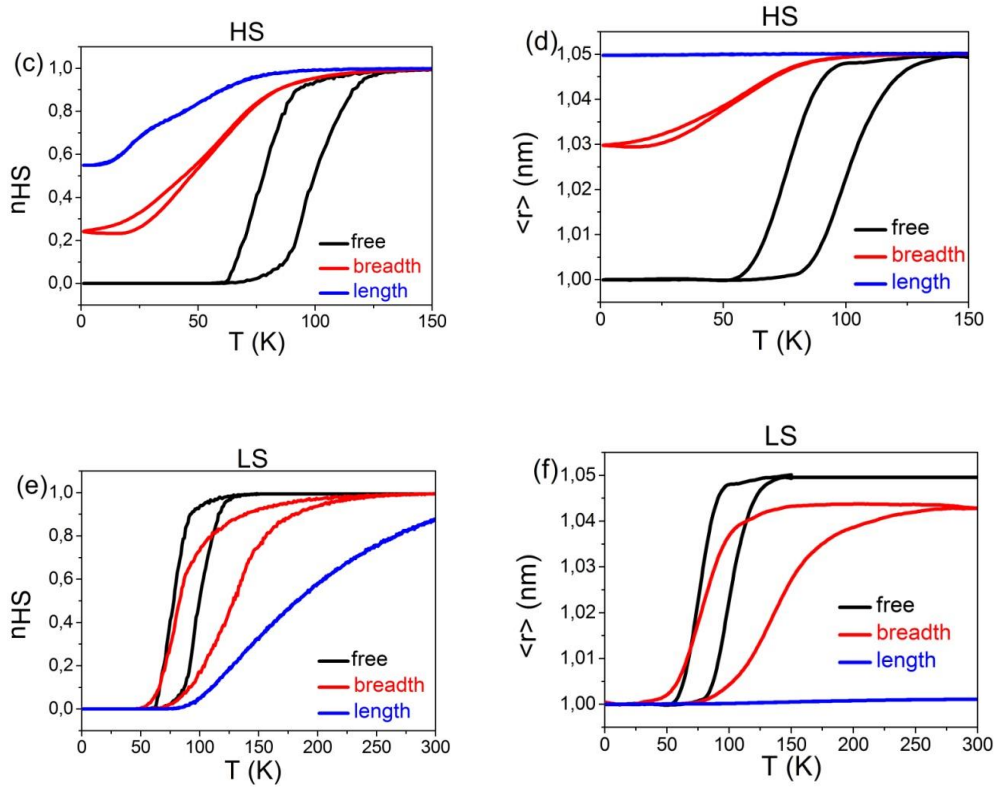


Figure 4. 2 Schematic views of the SCO crystal showing a breadth and length obstruction, starting from the HS(a) (resp. LS(b)) state. (c&d) Thermal dependence of the HS fraction, n_{HS} and average bond lengths $\langle r \rangle$ starting from the HS state for different obstructions. (e&f) Thermal dependence of the HS fraction, n_{HS} and average bond lengths $\langle r \rangle$ starting from the LS state for different obstructions.

4.3.1.2 Spatiotemporal aspects

We have also analyzed the effect of edge obstruction on the spatio-temporal aspects of the thermo-induced spin transition. The results are summarized in Figs. 4.3, where we display the snapshots of the spin state configuration and the lattice deformation along the thermal hysteresis loop of Fig. 2 for free system (a), and width and length obstruction, starting from the HS (b&c), and LS (d&e) respectively.

Fig.3 (a) reveals that upon cooling process ($n_{HS} = 0.25$) for the free system, the LS phase grows exclusively and quite easily (due to surface effects) from the free corners, extending over the entire crystal by an isotropic way along the edges and avoiding the middle, which converts only at the end of the process. We can explain why nucleation in the model starts from the corners by simple energetic considerations. The Spatio-temporal aspects of the LS \rightarrow HS transition (on-heating branch) are similar to those observed on cooling.

On the other hand, starting from the HS states with breadth (resp. length) obstruction, the nucleation and growth processes are almost opposite to those

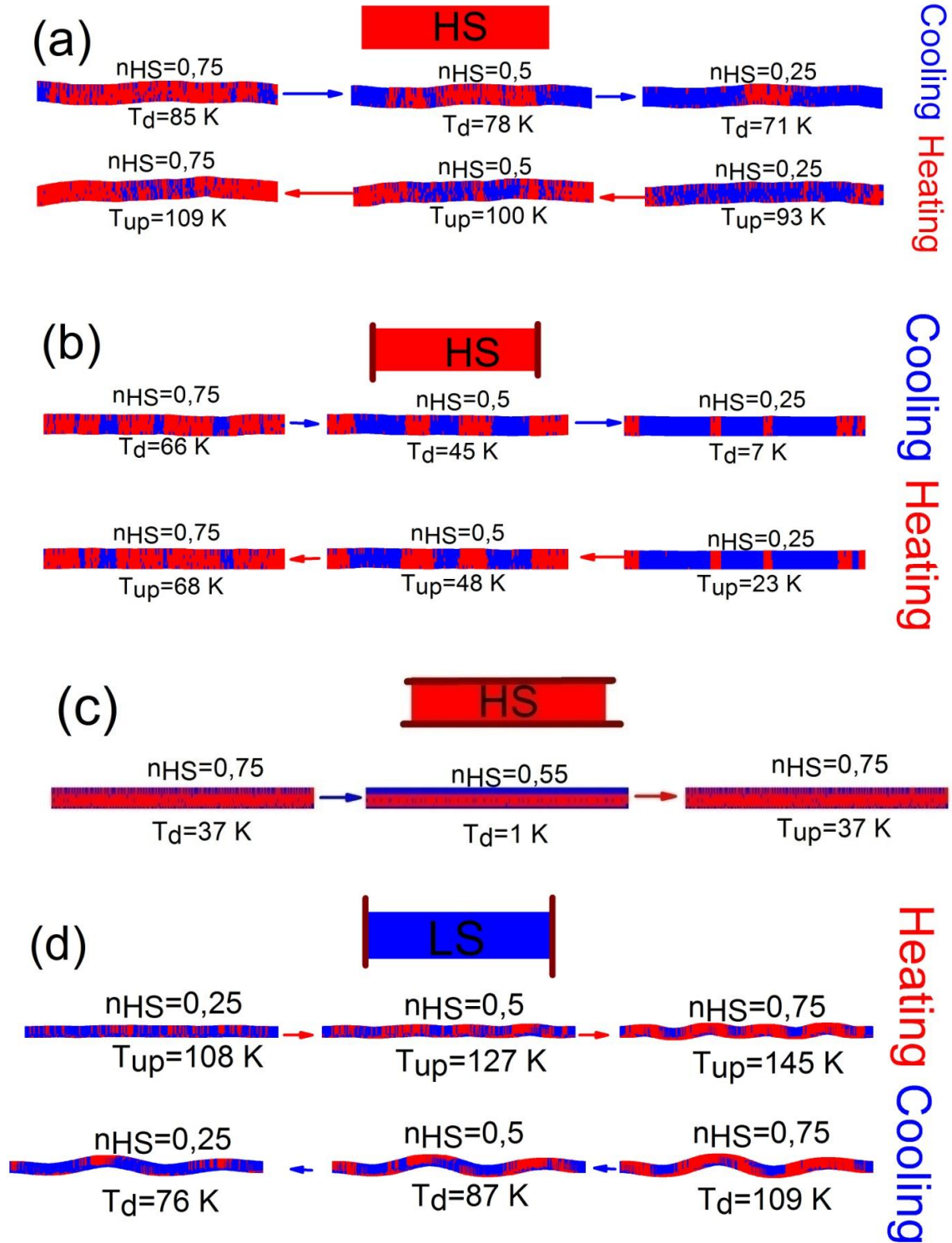
observed in the first case. Indeed, the nucleation of the LS phase, with breadth obstruction, starts (Fig. 3(b)) near the centre, and then propagates longitudinally towards the blocked edges. However, the stress generated through a confined transition in the crystal delays their thermal switching; they have longer relaxation times because they are stabilized by the tensile stress (check) induced by the confinement. While, during heating processes, the HS phase appear to nucleate near the bounded edges and then propagating towards the centre of the lattice (add figure). In fact, it should be expected, as the lattice was initially prepared in HS state and thus at the edges, the lattice parameter due to the obstruction are very similar to that of R_0^{HH} which facilitates the nucleation to the HS states.

In case (c), when we have confinement along the length of the crystal, we could clearly see a completely different mechanism to approach transition, first of all, as we can observe, concavity at the edges along the width (higher resolution, with zoom at concavity), which suggests that the contraction is maximizing as we approach toward the center line, and decreases as we move away from it. Similarly, for the spin states, we can see a large string of LS states forming along the edge (length); but it is not expected as this edge is not free to move and is confined. Thus, it is not intuitive that the spin relaxation initiates along the length of the lattice, as these were the edges which were fixed as per their initial states which in this case is HS, thus the average lattice parameter are expected to be close to that of the HS equilibrium lengths, *i.e.* R_0^{HH} , thus it could be expected that atoms located at the edges along the length should always remain in HS or will be the last one to reach LS, but as we can see, that is not the case.

Similarly, for Fig. 3(d), if we start from the LS states with obstruction along the breadth, the process of nucleation and growth are almost opposite to those observed for the system with free corners. In fact, the nucleation of the HS phase, with breadth obstruction, begins from the middle of the crystal, the HS state starts accumulating in the bulk and start forming some perturbations, which takes shapes of crest and trough of the waveform and thus a new arrangement of HS and LS domain appears, which then propagates longitudinally by an anisotropic way.

While for case (e), where we start from LS state and have set obstruction for the edges along the length, we can see that as the lattice wants to expand itself in this case, we can see convexity at the edges along the width, we have maximum expansion as we approach the centre and it reduces as we move away. Similar to case (c) at the edges along the length, we start to see the formation of chain of HS states, which, then are propagated inwards the lattice during heating cycle, similarly for the cooling cycle, as we would have expected (in the free lattice case) the nucleation would have started from edges along the width as they are free and thus should be the first one susceptible to change but as we can see that the LS propagation starts from the edges along the length and then move towards the centre. In fact we can say that as we move towards the center line along the width there must be many atoms which have lattice parameters much closer to that of the HS, while as we move towards the edges, majority of atoms could still remain

more closer to LS state lattice parameters; thus we can understand this asymmetry along the central line for the cases (c and e), although what could not be understood is that the edges along the length which were specifically fixed to the LS lattice parameters are the first to transition to HS state.



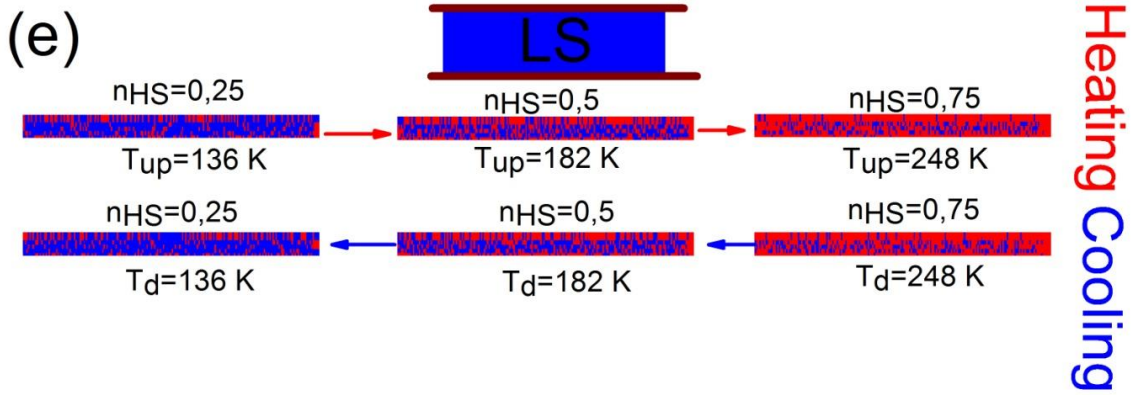


Figure 4. 3 Snapshots of the crystal during the heating and the cooling process for (a) free system. Snapshots of the crystal during the cooling and the heating process starting from HS state with width (b) and length (c) obstruction. Snapshots of the crystal during the heating and the cooling process starting from the LS state with width (d) and length (e) obstruction. The red (blue) dots are associated with HS (LS). N_x and N_y were chosen as follows: $N_x = 200 \text{ nm}$ and $N_y = 5 \text{ nm}$.

Now, we focus on the stress generated by the thermal hysteresis. The elastic stress was evaluated at 0 K. To do so, we estimated the displacement field $\vec{u}(i,j)$ associated with the lattice site (i,j) defined as: $\vec{u}(i,j) = \vec{r}(i,j) - \vec{r}_0(i,j)$, where $\vec{r}_0(i,j)$ is the initial atomic position of the sites (i,j) and $\vec{r}(i,j)$ is the final position at HS state. In the present data analysis, we used the positions of the perfect LS lattice as a reference state: $\vec{r}_0(i,j) = (i \times R_0^{LL}, j \times R_0^{LL})$.

4.3.2 Size effects

4.3.2.1 Length effects of crystal

In this part, we will study the size effect on the thermo-induced spin transition. For this, the crystal, with breadth obstruction and starting from the LS state, was built with different surface ratios, $S = N_x \cdot N_y$, where N_x is changed from 40 to 200 nm and N_y is fixed to 5 nm. The thermal evolution of n_{HS} for different sizes is shown in Fig. 4.4.

One can notice from Fig. 4.4(a) that the presence of breadth obstruction induces an increase of hysteresis width for the case of avg. lattice parameter $\langle r \rangle$ with respect to the increase in N_x/N_y ratio. However, starting from the LS state: upon increasing the length of the crystal, the transition temperature for the n_{HS} fraction during the heating cycle is relatively unchanged, while for the cooling cycle, we can see the difference between transition temperatures for decrease in N_x/N_y ratios, and thus could see the difference between the hysteresis width. Indeed, the equilibrium temperature and the hysteresis are presented in Fig. 4.4(c). It shows a linear behavior as a function of $1/N_x$.

One can quickly notice a distinct difference in the shape of the hysteresis loop of n_{HS} Fig. 4.4(a), and average nn distance Fig. 4.4(b). Indeed, Fig. 4.4(b) reveals that due to the confinement, the LS to HS transition is realized in a frustrated lattice since the lattice parameters are different from its equilibrium parameter and is approaching its equilibrium parameter as we increases the length of the lattice. Interestingly for cases of length ≥ 120 we notice that while decreasing the temperature that is in the cooling cycle, we still have increase in avg. nn distances. Even though there is decrease in total HS fraction, which make this behavior even more puzzling, as it would have been expected that during the cooling regime especially during the reintroduction of LS states in the lattice the lattice will try to relax a bit from its agitated state, but as we can see in Fig. 4.4(b) instead of going down we see a rise in avg. nn distances. (for explanations, we have to plot the differences between max. avg nn during heating cycles and during cooling cycles with respect to NX)

In figure 5, we have analyzed the effect of length on the nucleation and growth of the HS fraction associated with the hysteresis of Fig. 4.4(a). One can notice from Fig.5, the nucleation of the HS phase is very interesting in this case, as we can see the crystal lattice acts as a wave and is deformed in a similar fashion, where the crest and trough of the wave have HS population, while the remaining is predominantly LS in the beginning. As we kept increasing the temperature, these HS domains formed at crests and troughs kept growing and then covered the whole lattice.

One can notice that deformation starts to appear during the cooling process for $S = 40 \times 5$ as we can see in Fig. 4.5(a), and the deformation naturally keeps getting dominant for big crystals, $S = 120 \times 5$ Fig. 4.5 (b), and for $S = 200 \times 5$ (Fig. 4.3(d)). In Fig. 4.5(c), we plotted the total length, given by

$$\langle L \rangle = \sum_{i,j} \sqrt{(x_{i+1} - x_i)^2 + (y_{j+1} - y_j)^2} \quad (4.4)$$

along X-axis for a crystal in the HS phase, with a width obstruction, with the initial state being that of the LS state, as a function of N_x , for different values of N_y . Since we have fixed length along the X-direction through placing obstruction along its breadth, therefore, stunting its possibility to grow along X-direction, thus in such scenario, total length $\langle L \rangle$ gives us an intuition to contemplate how is increment along Y-direction through bending helping the crystal to achieve its HS state length. This characterization helps us to depict the presence of two regimes: a linear behavior where the length increases with an increase in N_x , and then its convergence to a specific value which will depend on its ratio of N_x/N_y .

While for bending, we choose to define it through the following expression:

$$\bar{u}_{ij} = \sum_i \sqrt{\frac{(y_{i+1} - y_i)^2}{R_{HH}}} \quad (4.5)$$

In Fig. 4.5(d), one can notice that bending, calculated for a crystal in the HS phase, with a width obstruction and starting from the LS state, increases with, for different values of N_y and then it reaches a saturation value. The Fig. 4.5(d) behaves almost in a similar fashion to Fig. 4.5(c) the only difference being that the value of avg. length saturation $\langle L \rangle$ is different with each value of N_y . While in the case of bending for all N_y , for the large N_x , converges to the same avg. bending parameter \bar{u}_{ij} . It is to be noted that both the $\langle L \rangle$ and \bar{u}_{ij} are calculated for the same ratios of N_x/N_y with different random seeds and then averaged.

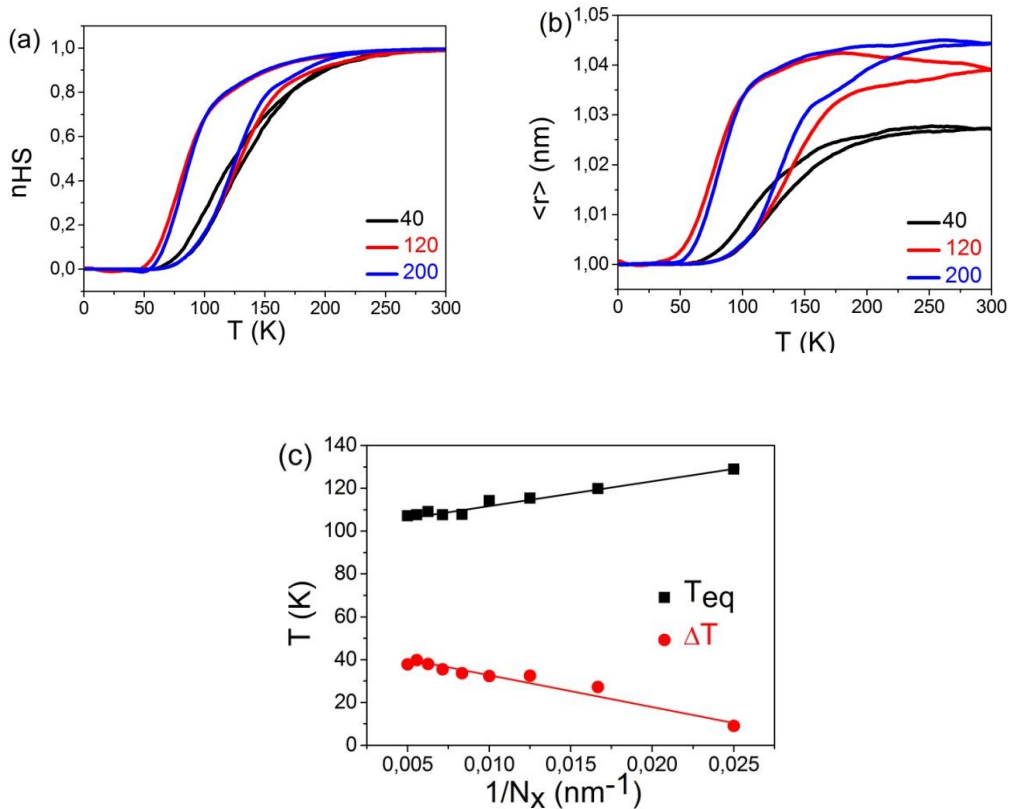


Figure 4. 4 Thermal dependence of the (a) HS fraction, n_{HS} and (b) average bond lengths

$\langle r \rangle$ starting from the LS state for different sizes with a width obstruction. (c) Equilibrium temperature T_{eq} and hysteresis width ΔT as a function of $1/N_x$. We changed N_x from 40 to 200 nm.

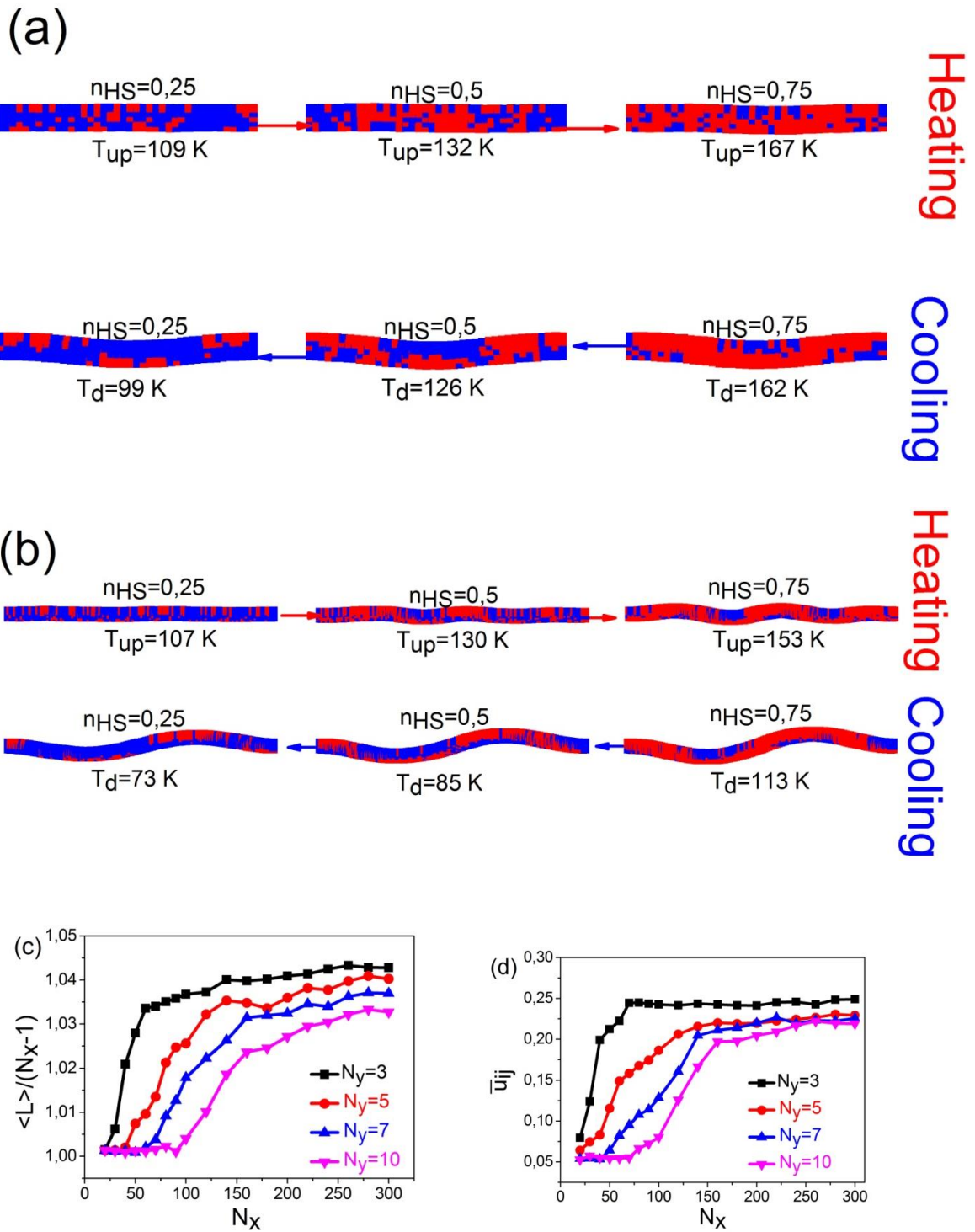


Figure 4. 5 Snapshots of the crystal during the heating and the cooling process starting from the LS state with width obstruction for (a) $N_x \times N_y = 40 \times 5$ (b) $N_x \times N_y = 120 \times 5$. The red (blue) dots are associated with HS (LS). (c) The average length of crystal $\frac{\langle L \rangle}{N_x - 1}$ as a function of N_x for different value of $N_y = 3, 5, 7$ and 10 . (d) Bending as a function of N_x for different value for $N_y = 3, 5, 7$ and 10 . Average length and bending are calculated for a crystal in the HS state at $T = 300$ K.

4.3.2.2 Thickness effects of crystal

In this part, we will study the size effect on the thermo-induced spin transition. For this, the crystal was built in different surface $S = N_x \cdot N_y$, where N_y is changed from 1 to 30 nm and N_x is fixed to 200 nm. The thermal evolution of n_{HS} for different size is shown in Fig. 4.6.

Starting from the LS state: upon increasing the thickness of the crystal, the transition is shifted towards high temperatures, and the width of the hysteresis becomes significant for $N_y = 6$ then decreases. Indeed, the equilibrium temperature and the hysteresis are presented in Fig. 4.6(c). It shows a linear behavior for equilibrium temperature as a function of N_y and a maximum for the width ΔT then it decreases linearly. What is attractive with this figure is that when we plotted the same in Fig. 4.4(c), we found a linear behavior for both the equilibrium temperature and the hysteresis width ΔT ; however, this time we can clearly see in Fig. 4.6(c) that the behaviour is no more linear and at first reaches some maximum and then decreases. Thus, help us in understanding the effect of thickness on the thermal hysteresis. Such behavior can be explained by the thermal dependence of $\langle r_x \rangle$ and $\langle r_y \rangle$. In fact, $\langle r_x \rangle$ and $\langle r_y \rangle$ are given by the following expressions:

$$\langle r_x \rangle = \frac{\langle L \rangle}{N_y(N_x - 1)} \quad (6)$$

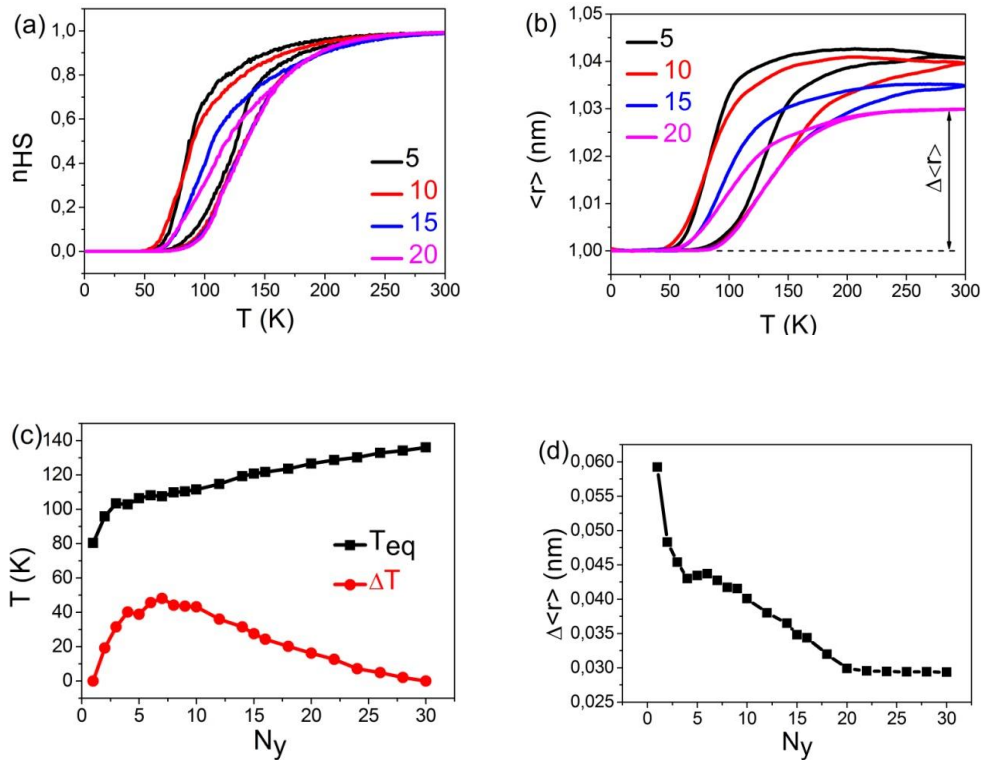
$$\langle r_y \rangle = \{ [N_y(N_x - 1) + (N_y - 1)N_x] \langle r \rangle - N_y(N_x - 1) \langle r_x \rangle \} * 1/N_x(N_y - 1) \quad (7)$$

Where $\langle L \rangle$ is the total length of the system. From Fig. 4.6 (e) and (f), increasing the thickness of the crystal leads to a decrease in the value of $\langle r_y \rangle_{HS}$, while that of $\langle r_x \rangle_{HS}$ almost remain constant, this is particularly important since now we can identify whether the major challenge in increase or decrease of average length is anisotropic or isotropic in nature. Fig. 4.6 (e) and 6 (f) shade an essential light on this nature, and we can see that as the thickness increases, it is essentially the value of $\langle r_y \rangle_{HS}$, which takes the major blow while that of the $\langle r_x \rangle_{HS}$ stays the same. Also, if we look back at the Fig. 4.4 (b) where we had already noted the peculiar behavior for the average distance for $N_x = 120$, in which while decreasing the temperature (i.e. in the cooling cycle), we could see the increase in avg. nn distances even if there is a decrease in avg. HS fraction. Now we could see in Fig. 4.6 (e) and 4.6 (f) and pin-point this increase in avg. distances during cooling is specifically associated to the distances along the Y-direction and its value could vary depending on the ratio of N_x/N_y .

One can easily notice a distinct difference in the shape of hysteresis loop of n_{HS} Fig. 4.6 (a), and lattice parameter Fig. 4.6 (b). Indeed, Fig. 4.6 (b) reveals that the LS to HS transition is realized in a frustrated lattice due to the confinement, since the lattice parameters are different from its equilibrium parameter and are

approaching its equilibrium parameter as we decrease the thickness of the lattice. In Fig. 4.7, we have analyzed the effect of thickness on the nucleation and growth of the HS fraction associated with the hysteresis of Fig. 4.6(a). One can notice that substantial deformation appears process for $S = 200 \times 5$ and decreases for an increase in the thickness $S = 200 \times 20$. In Fig. 4.7 (c), we plotted the average length along X-axis for a crystal in the HS phase, with a width obstruction and starting from the LS state, as a function of N_y , for different values of N_x , it shows the presence of two regimes: a linear (resp. exponential) behavior for $N_x = 200$, (resp. $N_x = 50$) then it converges to ≈ 1 when $N_y \geq 20$.

In Fig. 4.7 (d), one can notice that bending, calculated for a crystal in the HS phase, with a width obstruction and starting from the LS state, is almost the same for the lower values of N_y for different N_x , but starts to separate for certain values of N_y , and then again meet each other as they converges to zero as we keep on increasing N_y . This give an interesting insight into the occurrence of bending in the lattice, as it indicates toward a region where there is a difference in the rate of changing in bending vs the rate of change of avg. length (Fig. 4.7 (c)) with an addition of extra layer in thickness for the case of $N_x = 200$, till there is no more bending observed due to the additional layer, and as we can see the amount of layers required to reduce the bending to zero depends on the ratio of N_x and N_y .



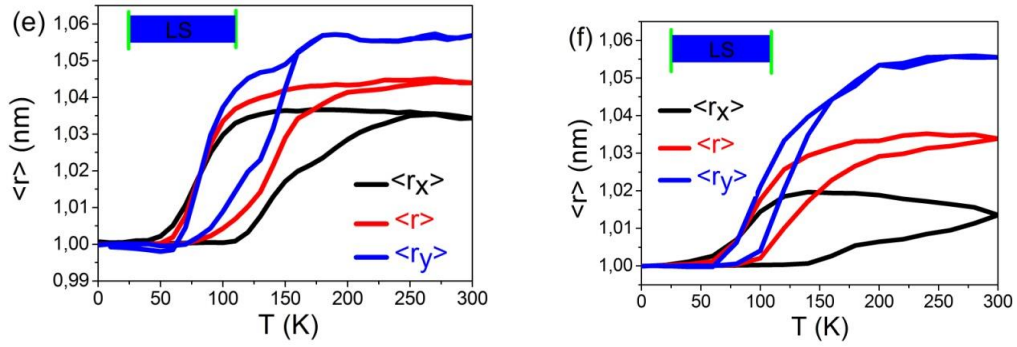
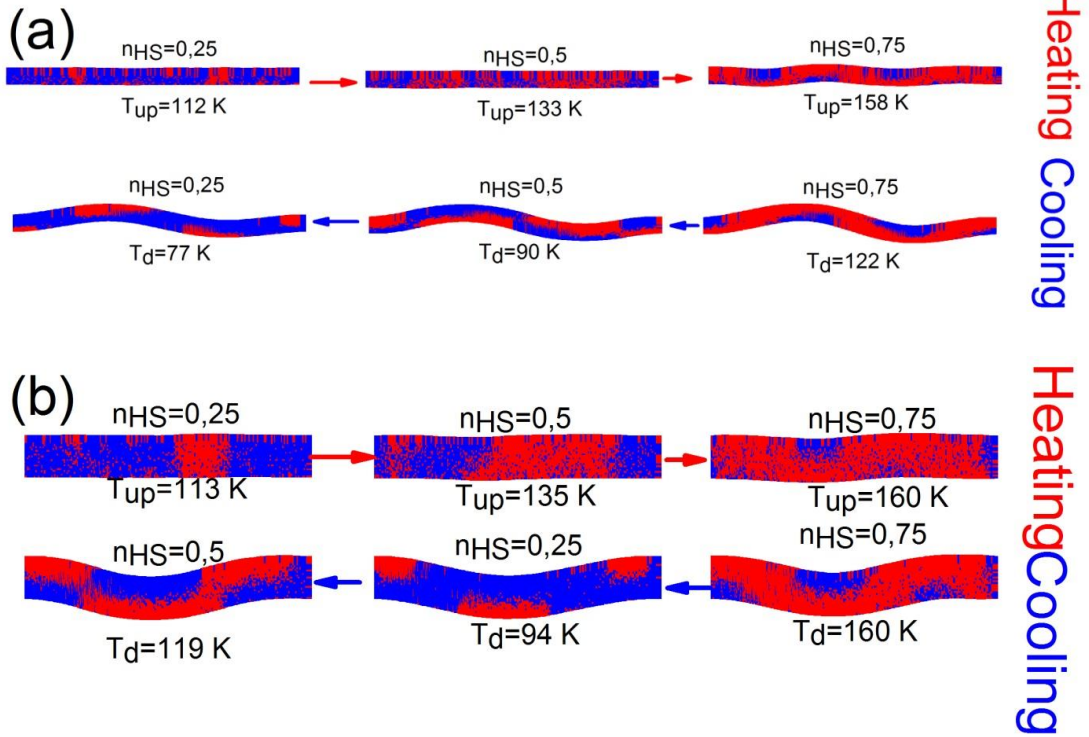


Figure 4. 6 Thermal dependence of the HS fraction, n_{HS} (a) and average bond lengths $\langle r \rangle$ (b) starting from the LS state for different sizes with a width obstruction. (c) Equilibrium temperature T_{eq} and hysteresis width ΔT as a function of N_y . (d) $\Delta \langle r \rangle$ as a function of N_y . We changed N_y from 1 to 30 nm. Thermal dependence of the average bond lengths $\langle r_x \rangle$ and $\langle r_y \rangle$ starting from the LS state with width obstruction for (e) $N_y = 5$ nm and (f) $N_y = 15$ nm. N_x was fixed to $N_x = 200$ nm.



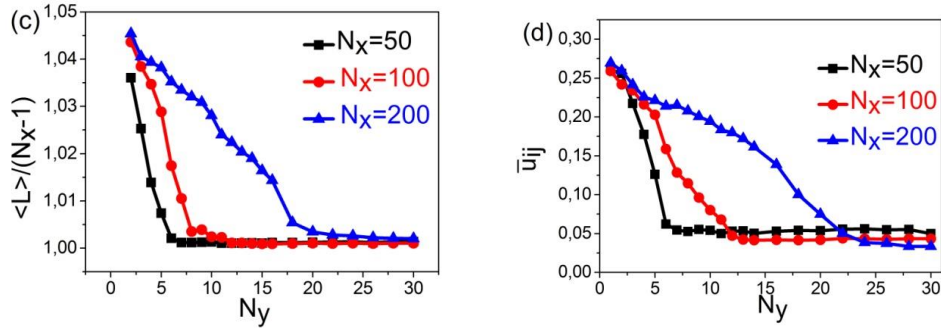


Figure 4. 7 Snapshots of the crystal during the heating and the cooling process starting from the LS state with width obstruction for (a) $N_x \times N_y = 200 \times 10$ and (b) $N_x \times N_y = 200 \times 20$. The red (blue) symbols are associated with HS (LS). (c) Average length of crystal $\frac{\langle L \rangle}{N_x - 1}$ as a function of N_y for different value of $N_x = 50, 100$ and 200 . (d) Bending as a function of N_y for different value for $N_x = 50, 100$ and 200 . Average length and bending are calculated for a crystal in the HS state at $T = 300$ K.

4.3.3 Relaxation Dynamics

In this part, we studied the relaxation dynamics of the SCO crystal with width obstruction in different ways. Here, we prepare our SCO crystal initially in an electronically HS state, while the avg. nn distances are kept those of LS state, with width obstruction in place. Naturally, the system is in a frustrated state, and we don't interfere with the electronic part and keep it as such, but will start to relax the crystal mechanically. It is to be noted that this time we did not work on a simple straight rectangular crystal, but instead, we made it have an initial curvature so that we can have crystal bending with different normal modes. Thus the symbols $2L$, L , $0.5L$, and $0.25L$ corresponds to normal mode (N.M) 1, 2, 4, 8, respectively.

The objective behind this study is to see whether the system would prefer to have multiple stable configurations for a given $N_x \times N_y$ or will have a preference for a particular standing wave configuration. As we can see in the Fig. 4.7 (a), with different initial normal modes the SCO crystal (of $N_x \times N_y = 200 \times 5$) seems to side with a particular wavelength (i.e. with normal mode = 2 or symbol L) for the bending period, it could be clearly seen that for this particular wavelength, the relaxation time for the crystal is smallest (\sim approx. 0.5 million Montecarlo Steps (MCS)) and without any plateaus, while for all other normal modes the relaxation curves goes through some plateaus and where the rate of relaxation is affected adversely or slowed down. Similar inferences could be drawn from the Fig. 4.7 (b), where we could see the time (MCS) taken for the SCO crystal to reach its HS state avg. nn distances, which is again shortest for the $N.M = 2$ while longest for the $N.M = 1$.

Now, it is important to understand what does these particular plateaus with different $N.M$ corresponds to; they correspond to change in the $N.M$ of the system.

At each plateau, the peaks of the plateau are collapsing in order to reduce the number of $N.M$ in the system until it reaches $N.M = 2$. Thus, we can see that after some MCS, the relaxation curve of the higher $N.M$ follows or overlap with the relaxation curve of lower $N.M$. Thus, if we see the relaxation curve for $0.5 L$ ($N.M = 4$) in Fig. 8 (a), we see this plateau, which takes almost an extra 1.5 million MCS to converge with the curve of $N.M = 2$ (L), this corresponds to the time the four peaks in the SCO crystal takes to converge to two and then increase in amplitude. Similarly, for the curve for $0.25 L$ ($N.M = 8$), take the same number of MCS as that of $0.5 L$, to converge with the curve of $N.M = 2$ (L), but this time we go through two plateaus first one corresponds to the time taken for the eight peaks in the SCO crystal to converge to four and then the second plateau to take it further down to two and then increase in amplitude.

At this point, a curious reader might be wondering, if that is so, then why does $N.M = 1$ (or $2L$) is following or overlapping with the relaxation curves of $0.25 L$ in both the Fig. 4.8 (a) and (b). To answer this, first, we have to understand what is going in the SCO crystal for the orange dashed line termed N.C (No Curvature) in Fig. 4.8 (a) and (b), which correspond to the simple straight rectangular crystal without any initial curvature or N.M associated with it and is allowed to relaxed mechanically, while all else is similar to previously discussed curves. As we can see, the relaxation curve for this system is somewhat between that of $0.25 L$ and $0.5 L$ ($N.M = 4$ & 8) for the first million steps, while for the next two million steps, it has different relaxation dynamics compared to the rest of the curves. This is because when we do not initiate the relaxation from a chosen N.M, the system itself starts bending from different places in order to increase the avg. nn distances and thus in this process different N.M starts appearing in the system for few initial steps (which, of course, will depend on $N_x \times N_y$) for this case, it happens to be six. This is why we see some resemblance for the first million steps (six N.M to four) and then see the divergence from the rest, while ultimately converging to the same values as that for the L ($N.M = 2$).

This result is significant as it sheds light and helps us understand the relaxation dynamics of the bounded SCO crystal. Even though we started from different initial states, we reached the same relaxed state and almost went through the same path. Now coming back to our dilemma regarding the $N.M = 1$ (L), what we are seeing is because of the low amplitude of the single arch or $N.M$, the system behaves almost like a rectangular system with little bit of curvature. Therefore, in order to relax, we see the appearance of different N.M in the system initially, thus at first we can see the increase in N.M from one to five and then its convergence to three over the course of MCS and is the only relaxation curve that has not reached the lowest Elastic energy.

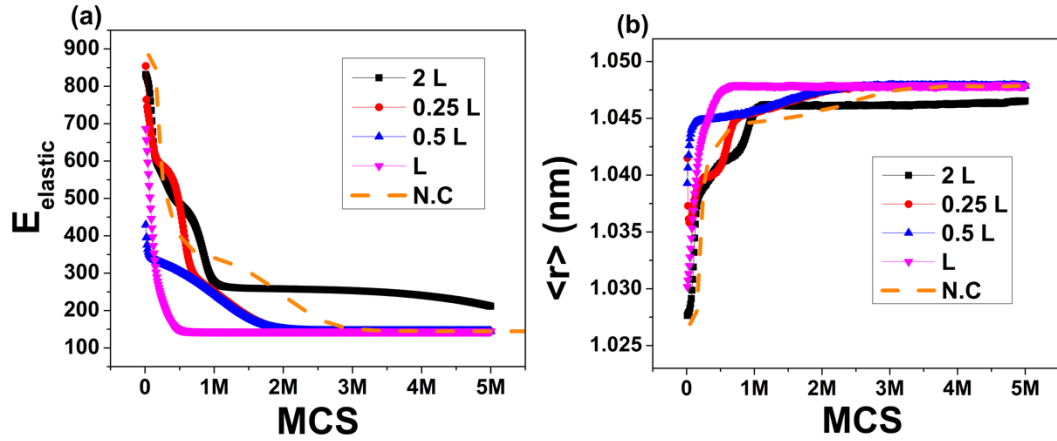


Figure 4. 8 Showing the mechanical relaxation curves for a High Spin SCO crystal with the Low Spin average nn distances for a system size $N_x \times N_y = 200 \times 5$ with width obstructions. The symbols 2 L, L, 0.5 L, and 0.25 L corresponds to normal modes 1, 2, 4, 8, respectively. (a) Showing the elastic relaxation curve for the crystal with different initial bending periods. (b) Showing the avg. nn distances relaxation for different initial bending periods.

Now that we understood the relaxation dynamics of the bounded SCO crystal and demonstrated the presence of standing wave depending on the size and other factors, it will be crucial to establish an added layer of bistability to the system, i.e., regarding the shape of the system. Since each size will be corresponding to a certain N.M, for each value of N.M, there will be two ways to rearrange or reorder the crystal, and thus may lead to another order of control over SCO crystal and devices.

4.4 Conclusion

We investigated in the thermo-induced spin transition of spin-crossover crystal through the electro-elastic model. The study was focused on the properties of the macroscopic nucleation, growth and propagation mechanisms. The Spatio-temporal aspects of the transformation were studied as a function of the position of obstruction (length or width) and the initial state of the lattice. We found that fixed edges prevent the nucleation from the corner of the crystal at the beginning of processes; however, starting from the HS states with breadth (resp. length) obstruction, the nucleation of the LS phase, with breadth (resp. length) obstruction near the centre, and then propagates longitudinally towards the edges.

We have also analyzed the effect of obstruction on the thermal and structural properties of the spin crossover crystal, starting from the HS and LS states. Indeed, for length obstruction, we reduce the cooperativity and leads to gradual or incomplete transition, while in the case of breadth obstruction, it seems we increase the cooperativity when we start from LS state while reducing it when we start from HS state and thus leading to broader and narrower hysteresis respectively. We noticed a distinct difference in the shape of the hysteresis loop of

n_{HS} and avg. nn distances. Indeed, starting from the HS (resp. LS) states, a residual lattice parameter appears at low (resp. high) temperature. We studied the size effects on the thermal and mechanical properties of the spin crossover crystal. We found that the increase of the length of crystal leads to a change in the thermo-induced spin transition and shift towards lower temperatures, and we see that increase or decrease in the ratio of $N_x \times N_y$ affects the bending and total length of the lattice in different ways and is key in understanding the lattice behavior.

The spatiotemporal arrangement of spin states is also quite important as we can see that in the cases where we have the obstruction along the breadth, and we start from the LS state, during the heating cycle for very low bending, we can see the occurrence of stripes (Turing like pattern), which might be helpful in explaining the origin of such patterns in many experimental works if we follow the curvature of the crystal. Similarly, for the case where we start from the HS state during the length obstruction, we see that a core-shell like structure for a spin state is formed where we have high spin states at the center of lattice while the edges are all low spin, which is interesting considering that the edges along the length are fixed to the distance that of HS and thus should be the last to make this transition. Thus we can safely assume that the frustration in this system is propagated inwards, and thus we see at the center a big domain of HS with some LS states trapped alternatively.

Such behaviors underline the crucial role of the obstruction in the magnetic and mechanical properties of the crystal. It is interesting to mention that the reasoning developed here could be extended to the effect of misfit between the LS and HS phases on the nucleation, growth and propagation mechanisms.

References:-

- [1] W. R. Browne and B. L. Feringa, "Making molecular machines work," *Nat. Nanotechnol.*, vol. 1, no. 1, pp. 25–35, 2006.
- [2] "Molecular Devices and Machines: Concepts and Perspectives for the Nanoworld, 2nd Edition | Wiley." [Online]. Available: <https://www.wiley.com/en-us/Molecular+Devices+and+Machines%3A+Concepts+and+Perspectives+for+the+Nanoworld%2C+2nd+Edition-p-9783527318001>. [Accessed: 03-Jun-2021].
- [3] J.-P. Sauvage *et al.*, Eds., *Molecular Machines and Motors*, vol. 99. Berlin, Heidelberg: Springer Berlin Heidelberg, 2001.
- [4] V. Amendola, L. Fabbrizzi, C. Mangano, and P. Pallavicini, "Molecular Movements and Translocations Controlled by Transition Metals and Signaled by Light Emission," 2001, pp. 79–115.
- [5] J. M. Abendroth, O. S. Bushuyev, P. S. Weiss, and C. J. Barrett, "Controlling Motion at the Nanoscale: Rise of the Molecular Machines," *ACS Nano*, vol. 9, no. 8. American Chemical Society, pp. 7746–7768, 25-Aug-2015.
- [6] "Emerging Actuator Technologies: A Micromechatronic Approach | Wiley." [Online]. Available: <https://www.wiley.com/en-us/Emerging+Actuator+Technologies%3A+A+Micromechatronic+Approach-p-9780470091975>. [Accessed: 03-Jun-2021].
- [7] M. Zupan, M. F. Ashby, and N. A. Fleck, "Actuator classification and selection - The development of a database," *Adv. Eng. Mater.*, vol. 4, no. 12, pp. 933–940, Dec. 2002.
- [8] J. D. W. Madden *et al.*, "Artificial muscle technology: Physical principles and naval prospects," *IEEE J. Ocean. Eng.*, vol. 29, no. 3, pp. 706–728, Jul. 2004.
- [9] "Electroactive Polymers for Robotic Applications."
- [10] J. D. Madden, "Mobile robots: Motor challenges and materials solutions," *Science*, vol. 318, no. 5853. Science, pp. 1094–1097, 16-Nov-2007.
- [11] S. Kim, C. Laschi, and B. Trimmer, "Soft robotics: A bioinspired evolution in robotics," *Trends in Biotechnology*, vol. 31, no. 5. Trends Biotechnol, pp. 287–294, May-2013.
- [12] F. Carpi, R. Kornbluh, P. Sommer-Larsen, and G. Alici, "Electroactive polymer actuators as artificial muscles: Are they ready for bioinspired applications?," *Bioinspiration and Biomimetics*, vol. 6, no. 4, p. 045006, Dec. 2011.
- [13] "Biomedical Applications of Electroactive Polymer Actuators | Wiley." [Online]. Available: <https://www.wiley.com/en-us/Biomedical+Applications+of+Electroactive+Polymer+Actuators-p-9780470744680>. [Accessed: 03-Jun-2021].
- [14] "Mems/Nems: (1) Handbook Techniques and Applications Design Methods, (2 ... - Google Books." [Online]. Available: [https://books.google.fr/books?hl=en&lr=&id=7gXSMEMhuKgC&oi=fnd&pg=PP8&dq=MEMS/NEMS+Handbook,+Techniques+and+Applications\(Ed:+C.T.Leondes\),+Springer,+Berlin+2006&ots=WRlVbSyYr&sig=PZcuLKBj1tvz9pzbDFn3SEb5DI#v=onepage&q&f=false](https://books.google.fr/books?hl=en&lr=&id=7gXSMEMhuKgC&oi=fnd&pg=PP8&dq=MEMS/NEMS+Handbook,+Techniques+and+Applications(Ed:+C.T.Leondes),+Springer,+Berlin+2006&ots=WRlVbSyYr&sig=PZcuLKBj1tvz9pzbDFn3SEb5DI#v=onepage&q&f=false). [Accessed: 03-Jun-2021].
- [15] D. Ramos, J. Tamayo, J. Mertens, M. Calleja, L. G. Villanueva, and A. Zaballos, "Detection of bacteria based on the thermomechanical noise of a nanomechanical resonator: Origin of the response and detection limits," *Nanotechnology*, vol. 19, no. 3, p. 035503, Jan. 2008.
- [16] K. Babaei Gavan, H. J. R. Westra, E. W. J. M. Van Der Drift, W. J. Venstra, and H. S. J. Van Der Zant, "Size-dependent effective Young's modulus of silicon nitride cantilevers," *Appl. Phys. Lett.*, vol. 94, no. 23, p. 233108, Jun. 2009.
- [17] A. K. Naik, M. S. Hanay, W. K. Hiebert, X. L. Feng, and M. L. Roukes, "Towards single-molecule nanomechanical mass spectrometry," *Nat. Nanotechnol.*, vol. 4, no. 7, pp. 445–450, 2009.
- [18] Y. T. Yang, C. Callegari, X. L. Feng, K. L. Ekinici, and M. L. Roukes, "Zeptogram-scale nanomechanical mass sensing," *Nano Lett.*, vol. 6, no. 4, pp. 583–586, Apr. 2006.
- [19] N. V. Lavrik, M. J. Sepaniak, and P. G. Datskos, "Cantilever transducers as a platform for chemical and biological sensors," *Review of Scientific Instruments*, vol. 75, no. 7. American Institute of PhysicsAIP, pp. 2229–2253, 21-Jul-2004.
- [20] A. Boisen, S. Dohn, S. S. Keller, S. Schmid, and M. Tenje, "Cantilever-like micromechanical sensors," *Reports Prog. Phys.*, vol. 74, no. 3, p. 036101, Mar. 2011.
- [21] J. L. Arlett, E. B. Myers, and M. L. Roukes, "Comparative advantages of mechanical biosensors," *Nature Nanotechnology*, vol. 6, no. 4. Nature Publishing Group, pp. 203–215, 27-Mar-2011.
- [22] D. Ramos, J. Tamayo, J. Mertens, M. Calleja, and A. Zaballos, "Origin of the response of nanomechanical resonators to

- bacteria adsorption," *J. Appl. Phys.*, vol. 100, no. 10, p. 106105, Nov. 2006.
- [23] J. Tamayo, D. Ramos, J. Mertens, and M. Calleja, "Effect of the adsorbate stiffness on the resonance response of microcantilever sensors," *Appl. Phys. Lett.*, vol. 89, no. 22, p. 224104, Dec. 2006.
- [24] K. S. Hwang *et al.*, "Dominant surface stress driven by biomolecular interactions in the dynamical response of nanomechanical microcantilevers," *Appl. Phys. Lett.*, vol. 89, no. 17, p. 173905, Oct. 2006.
- [25] J. Dorignac, A. Kalinowski, S. Erramilli, and P. Mohanty, "Dynamical response of nanomechanical oscillators in immiscible viscous fluid for in Vitro biomolecular Recognition," *Phys. Rev. Lett.*, vol. 96, no. 18, p. 186105, May 2006.
- [26] A. W. McFarland, M. A. Poggi, M. J. Doyle, L. A. Bottomley, and J. S. Colton, "Influence of surface stress on the resonance behavior of microcantilevers," *Appl. Phys. Lett.*, vol. 87, no. 5, p. 53505, Jul. 2005.
- [27] J. H. Lee, T. S. Kim, and K. H. Yoon, "Effect of mass and stress on resonant frequency shift of functionalized Pb(Zr_{0.52}Ti_{0.48})O₃ thin film microcantilever for the detection of C-reactive protein," *Appl. Phys. Lett.*, vol. 84, no. 16, pp. 3187–3189, Apr. 2004.
- [28] S. Cherian and T. Thundat, "Determination of adsorption-induced variation in the spring constant of a microcantilever," *Appl. Phys. Lett.*, vol. 80, no. 12, pp. 2219–2221, Mar. 2002.
- [29] G. Y. Chen, T. Thundat, E. A. Wachter, and R. J. Warmack, "Adsorption-induced surface stress and its effects on resonance frequency of microcantilevers," *J. Appl. Phys.*, vol. 77, no. 8, pp. 3618–3622, Aug. 1995.
- [30] J. Lagowski, H. C. Gatos, and E. S. Sproles, "Surface stress and the normal mode of vibration of thin crystals: GaAs," *Appl. Phys. Lett.*, vol. 26, no. 9, pp. 493–495, Sep. 1975.
- [31] "(No Title)." [Online]. Available: [https://engineering.purdue.edu/~ce597m/Handouts/Theory of elasticity by Timoshenko and Goodier.pdf](https://engineering.purdue.edu/~ce597m/Handouts/Theory%20of%20elasticity%20by%20Timoshenko%20and%20Goodier.pdf). [Accessed: 04-Jun-2021].
- [32] M. J. Lachut and J. E. Sader, "Effect of surface stress on the stiffness of cantilever plates," *Phys. Rev. Lett.*, vol. 99, no. 20, p. 206102, Nov. 2007.
- [33] P. Lu, H. P. Lee, C. Lu, and S. J. O'Shea, "Surface stress effects on the resonance properties of cantilever sensors," *Phys. Rev. B - Condens. Matter Mater. Phys.*, vol. 72, no. 8, p. 085405, Aug. 2005.
- [34] M. E. Gurtin, X. Markenscoff, and R. N. Thurston, "Effect of surface stress on the natural frequency of thin crystals," *Appl. Phys. Lett.*, vol. 29, no. 9, pp. 529–530, Aug. 1976.
- [35] V. Pini *et al.*, "Shedding light on axial stress effect on resonance frequencies of nanocantilevers," *ACS Nano*, vol. 5, no. 6, pp. 4269–4275, Jun. 2011.
- [36] L. G. Villanueva, R. B. Karabalin, M. H. Matheny, E. Kenig, M. C. Cross, and M. L. Roukes, "A nanoscale parametric feedback oscillator," *Nano Lett.*, vol. 11, no. 11, pp. 5054–5059, Nov. 2011.
- [37] A. Coskun, M. Banaszak, R. D. Astumian, J. F. Stoddart, and B. A. Grzybowski, "Great expectations: Can artificial molecular machines deliver on their promise?," *Chem. Soc. Rev.*, vol. 41, no. 1, pp. 19–30, Dec. 2012.
- [38] S. M. Mirvakili and I. W. Hunter, "Artificial Muscles: Mechanisms, Applications, and Challenges," *Advanced Materials*, vol. 30, no. 6. Wiley-VCH Verlag, p. 1704407, 08-Feb-2018.
- [39] L. Hines, K. Petersen, G. Z. Lum, and M. Sitti, "Soft Actuators for Small-Scale Robotics," *Advanced Materials*, vol. 29, no. 13. Wiley-VCH Verlag, p. 1603483, 04-Apr-2017.
- [40] H. Okuzaki, "Progress and current status of materials and properties of soft actuators," in *Soft Actuators: Materials, Modeling, Applications, and Future Perspectives*, vol. 9784431547679, Springer Japan, 2014, pp. 3–18.
- [41] L. Ionov, "Polymeric actuators," *Langmuir*, vol. 31, no. 18, pp. 5015–5024, May 2015.
- [42] B. K. Juluri *et al.*, "A mechanical actuator driven electrochemically by artificial molecular muscles," *ACS Nano*, vol. 3, no. 2, pp. 291–300, Feb. 2009.
- [43] P. Naumov, S. C. Sahoo, B. A. Zakharov, and E. V. Boldyreva, "Dynamic single crystals: Kinematic analysis of photoinduced crystal jumping (the photosalient effect)," *Angew. Chemie - Int. Ed.*, vol. 52, no. 38, pp. 9990–9995, Sep. 2013.
- [44] W. R. Browne and B. L. Feringa, "Making molecular machines work," *Nat. Nanotechnol.*, vol. 1, no. 1, pp. 25–35, 2006.
- [45] Y. Yu, M. Nakano, and T. Ikeda, "Directed bending of a polymer film by light," *Nature*, vol. 425, no. 6954, p. 145, Sep. 2003.

- [46] M. Morimoto and M. Irie, "A diarylethene cocrystal that converts light into mechanical work," *J. Am. Chem. Soc.*, vol. 132, no. 40, pp. 14172–14178, Oct. 2010.
- [47] W. Shu *et al.*, "DNA molecular motor driven micromechanical cantilever arrays," *J. Am. Chem. Soc.*, vol. 127, no. 48, pp. 17054–17060, Dec. 2005.
- [48] G. Du, E. Moulin, N. Jouault, E. Buhler, and N. Giuseppone, "Muscle-like supramolecular polymers: Integrated motion from thousands of molecular machines," *Angew. Chemie - Int. Ed.*, vol. 51, no. 50, pp. 12504–12508, Dec. 2012.
- [49] H. J. Shepherd *et al.*, "Molecular actuators driven by cooperative spin-state switching," *Nat. Commun.*, vol. 4, no. 1, pp. 1–9, Oct. 2013.
- [50] J. Linares, E. Codjovi, and Y. Garcia, "Pressure and temperature spin crossover sensors with optical detection," *Sensors*, vol. 12, no. 4, pp. 4479–4492, Apr. 2012.
- [51] G. Molnár, V. Niel, J. A. Real, L. Dubrovinsky, A. Bousseksou, and J. J. McGarvey, "Raman spectroscopic study of pressure effects on the spin-crossover coordination polymers Fe(pyrazine)[M(CN)4]·2H₂O (M = Ni, Pd, Pt). First observation of a piezo-hysteresis loop at room temperature," *J. Phys. Chem. B*, vol. 107, no. 14, pp. 3149–3155, Apr. 2003.
- [52] P. Gütllich, "Spin crossover in iron(II)-complexes," in *Metal Complexes*, Springer Berlin Heidelberg, 2007, pp. 83–195.
- [53] A. Bousseksou *et al.*, "Dynamic response of the spin-crossover solid Co(H₂fsa)₂en(py)₂ to a pulsed magnetic field," *Phys. Rev. B - Condens. Matter Mater. Phys.*, vol. 65, no. 17, pp. 1724121–1724124, May 2002.
- [54] F. Prins, M. Monrabal-Capilla, E. A. Osorio, E. Coronado, and H. S. J. Van Der Zant, "Room-temperature electrical addressing of a bistable spin-crossover molecular system," *Adv. Mater.*, vol. 23, no. 13, pp. 1545–1549, Apr. 2011.
- [55] A. Hauser, "Light-Induced Spin Crossover and the High-Spin→Low-Spin Relaxation," Springer, 2012, pp. 155–198.
- [56] G. D. Harzmann, R. Frisenda, H. S. J. Van Der Zant, and M. Mayor, "Single-Molecule Spin Switch Based on Voltage-Triggered Distortion of the Coordination Sphere," *Angew. Chemie - Int. Ed.*, vol. 54, no. 45, pp. 13425–13430, Nov. 2015.
- [57] B. Gallois, C. Hauw, J. A. Real, and J. Zarembowitch, "Structural Changes Associated with the Spin Transition in Fe(phen)₂(NCS)₂: A Single-Crystal X-ray Investigation," *Inorg. Chem.*, vol. 29, no. 6, pp. 1152–1158, 1990.
- [58] P. Gütllich, A. Hauser, and H. Spiering, "Thermal and Optical Switching of Iron(II) Complexes," *Angewandte Chemie International Edition in English*, vol. 33, no. 20, pp. 2024–2054, 02-Nov-1994.
- [59] D. Tanaka *et al.*, "Thin films of spin-crossover coordination polymers with large thermal hysteresis loops prepared by nanoparticle spin coating," *Chem. Commun.*, vol. 50, no. 70, pp. 10074–10077, Aug. 2014.
- [60] "Molecular magnetism (Book, 1993) [WorldCat.org]." [Online]. Available: <https://www.worldcat.org/title/molecular-magnetism/oclc/490069637>. [Accessed: 04-Jun-2021].
- [61] Y. Raza *et al.*, "Matrix-dependent cooperativity in spin crossover Fe(pyrazine)Pt(CN)₄ nanoparticles," *Chem. Commun.*, vol. 47, no. 41, pp. 11501–11503, Nov. 2011.
- [62] K. Boukheddaden, J. Linares, E. Codjovi, F. Varret, V. Niel, and J. A. Real, "Dynamical Ising-like model for the two-step spin-crossover systems," in *Journal of Applied Physics*, 2003, vol. 93, no. 10 2, pp. 7103–7105.
- [63] G. Molnár, S. Rat, L. Salmon, W. Nicolazzi, and A. Bousseksou, "Spin Crossover Nanomaterials: From Fundamental Concepts to Devices," *Adv. Mater.*, vol. 30, no. 5, p. 1703862, Feb. 2018.
- [64] M. D. Manrique-Juárez *et al.*, "Switchable molecule-based materials for micro- and nanoscale actuating applications: Achievements and prospects," *Coordination Chemistry Reviews*, vol. 308, Elsevier B.V., pp. 395–408, 01-Feb-2016.
- [65] H. J. Shepherd *et al.*, "High-pressure spin-crossover in a dinuclear Fe(II) complex," *Phys. Chem. Chem. Phys.*, vol. 14, no. 15, pp. 5265–5271, Apr. 2012.
- [66] A. Muraoka, K. Boukheddaden, J. Linares, and F. Varret, "Two-dimensional Ising-like model with specific edge effects for spin-crossover nanoparticles: A Monte Carlo study," *Phys. Rev. B - Condens. Matter Mater. Phys.*, vol. 84, no. 5, Aug. 2011.
- [67] J. A. Nasser, "First order high-spin/low-spin phase transition induced by acoustic-phonons," *Eur. Phys. J. B*, vol. 21, no. 1, pp. 3–10, May 2001.
- [68] J. A. Nasser, K. Boukheddaden, and J. Linares, "Two-step spin conversion and other effects in the atom-phonon coupling model," *Eur. Phys. J. B*, vol. 39, no. 2, pp. 219–227, 2004.
- [69] H. J. Shepherd, G. Molnár, W. Nicolazzi, L. Salmon, and A. Bousseksou, "Spin crossover at the nanometre scale,"

European Journal of Inorganic Chemistry, vol. 2013, no. 5–6. John Wiley & Sons, Ltd, pp. 653–661, 18-Feb-2013.

- [70] G. Félix *et al.*, “Enhanced cooperative interactions at the nanoscale in spin-crossover materials with a first-order phase transition,” *Phys. Rev. Lett.*, vol. 110, no. 23, p. 235701, Jun. 2013.
- [71] C. Enachescu, L. Stoleriu, A. Stancu, and A. Hauser, “Model for elastic relaxation phenomena in finite 2D hexagonal molecular lattices,” *Phys. Rev. Lett.*, vol. 102, no. 25, p. 257204, Jun. 2009.
- [72] M. Nishino, K. Boukheddaden, Y. Konishi, and S. Miyashita, “Simple two-dimensional model for the elastic origin of cooperativity among spin states of spin-crossover complexes,” *Phys. Rev. Lett.*, vol. 98, no. 24, p. 247203, Jun. 2007.
- [73] S. Miyashita, Y. Konishi, M. Nishino, H. Tokoro, and P. A. Rikvold, “Realization of the mean-field universality class in spin-crossover materials,” *Phys. Rev. B - Condens. Matter Mater. Phys.*, vol. 77, no. 1, Oct. 2007.
- [74] L. Stoleriu, P. Chakraborty, A. Hauser, A. Stancu, and C. Enachescu, “Thermal hysteresis in spin-crossover compounds studied within the mechanoelastic model and its potential application to nanoparticles,” *Phys. Rev. B - Condens. Matter Mater. Phys.*, vol. 84, no. 13, p. 134102, Oct. 2011.
- [75] L. Stoleriu, A. Stancu, P. Chakraborty, A. Hauser, and C. Enachescu, “Analysis of first order reversal curves in the thermal hysteresis of spin-crossover nanoparticles within the mechanoelastic model,” *J. Appl. Phys.*, vol. 117, no. 17, p. 17B307, May 2015.
- [76] C. Enachescu and W. Nicolazzi, “Elastic models, lattice dynamics and finite size effects in molecular spin crossover systems,” *Comptes Rendus Chimie*, vol. 21, no. 12. Elsevier Masson SAS, pp. 1179–1195, 01-Dec-2018.
- [77] A. Slimani and K. Boukheddaden, “An electro-elastic theory for the mechanically-assisted photo-induced spin transition in core-shell spin-crossover nanoparticles,” *Phys. Chem. Chem. Phys.*, vol. 20, no. 45, pp. 28583–28591, Nov. 2018.
- [78] H. Oubouchou, Y. Singh, and K. Boukheddaden, “Magnetoelastic modeling of core-shell spin-crossover nanocomposites,” *Phys. Rev. B*, vol. 98, no. 1, p. 014106, Jul. 2018.
- [79] A. Slimani, K. Boukheddaden, and K. Yamashita, “Effect of intermolecular interactions on the nucleation, growth, and propagation of like-spin domains in spin-crossover materials,” *Phys. Rev. B - Condens. Matter Mater. Phys.*, vol. 92, no. 1, p. 014111, Jul. 2015.
- [80] A. Slimani, K. Boukheddaden, F. Varret, H. Oubouchou, M. Nishino, and S. Miyashita, “Microscopic spin-distortion model for switchable molecular solids: Spatiotemporal study of the deformation field and local stress at the thermal spin transition,” *Phys. Rev. B - Condens. Matter Mater. Phys.*, vol. 87, no. 1, p. 014111, Jan. 2013.
- [81] A. Slimani, H. Khemakhem, and K. Boukheddaden, “Structural synergy in a core-shell spin crossover nanoparticle investigated by an electroelastic model,” *Phys. Rev. B*, vol. 95, no. 17, p. 174104, May 2017.
- [82] W. Nicolazzi and S. Pilet, “Structural aspects of the relaxation process in spin crossover solids: Phase separation, mapping of lattice strain, and domain wall structure,” *Phys. Rev. B - Condens. Matter Mater. Phys.*, vol. 85, no. 9, p. 094101, Mar. 2012.

Chapter 5.

Conclusion and Perspectives

5.1 General Conclusion

With the trend for ever faster and smaller devices, there are considerable critical pressures (environmental, energy consumption, etc.), technological challenges like the end of Moore's law, bottlenecks (data storage, energy storage, etc.). Furthermore, economic benefits to meet these new demands and develop new switchable macro/micro/nano-materials, to be used in different applications as spintronic, nano-electronic, nano-photonic or even nano-mechanical actuators devices. Nowadays, one of the most promising and stimulating research areas, pertaining to molecular electronics is represented by Spin Crossover (SCO) materials in which different stimuli drive the memory effect. This thesis deals with the SCO phenomenon and provides specific and flexible models and methods to describe SCO compounds, with a primary focus on specific questions related to the use of SCO materials and nanomaterials in technological applications. Looking at the increasing progress made in the past years, in all experimental, theoretical and computational fields, also from the chemical and physical aspects, regarding the understating of SCO processes in solids, liquids, nanoparticles, and thin-films, will not be just crucial for this field but also would be functionally essential and enriching for physics in general and future of the broad class of domains (i.e., nanomaterials, molecular-, magnetism, Elec-/spin-tronics, etc.). Thus, we can forecast that the SCO materials embedded in devices is going to be mainstream very soon. While the hysteretic thermal spin transition has been well documented, the recently novel behaviors (i.e., incomplete transition multi-step transition) displayed by these materials are much less common, which prompted us to work on them to better understand the related observed phenomena. Our present work is devoted to the fundamental aspect of *Fe(II)* compound and aims to offer some high-tech "characterizations" tools that help understand the spin transition phenomena. In order to introduce SCO materials in technological devices with various architectures, the geometrical characteristics of the material are very important. Moreover, controlling the cooperative nature of SCO represents a significant challenge in materials-device technologies, nowadays. Based on the results reported recently in the literature we have analyzed, and shown that the cooperativity of a SCO system depends not only on short- and long-range interactions but also strongly on the lattice architecture.

During this work we tried to bring theoretical elements both in the description by macroscopic and microscopic models of the spatio-temporal aspects, statistics, and thermodynamics making it possible to understand and reproduce recent

experimental observations, and to predict new behaviors in the theme of spin transition. We have proven the validity of the elastic models to describe the macroscopic behavior of spin transition crystals in the thermal hysteresis cycle during the first-order phase transition. The model presented here is developed from the Hamiltonian of Ising's model. The elastic model still has a lot of secrets to reveal to us, which will surely help to better understand the essential role of elasticity and magneto-elastic coupling in the leading phenomena of the spin transition.

Here, we have exposed the various behaviors obtained via the competition or effects arising at the boundary (or interfaces) due to the change of variables (i.e., ligand field (transition temperature), elastic parameters (equilibrium distances, & elastic rigidity, etc.), either due to different lattice geometries (square, rectangle, etc.), architecture (core-shell, membrane-substrate), or simply due to the externally introduced barriers (such as clamping, along length, or breadth). Elastic frustration emerges as the parameter responsible for the appearance of an antiferro-elastic phase in a plateau, causing a transition in two or multi-steps, re-entrant, or incomplete. These organized patterns of the spin state, with a periodicity, emerge from a spatial variation of the network parameter, periodic or aperiodic, which could be the key to understanding the incommensurable phases recently found experimentally by various authors. The general perspective of this work lies in using the elastic Hamiltonian to study and enrich the understanding of various phenomena that arise, when frustrations in one form or another are introduced in the system, while simultaneously taking thermal effects into account. So, although limited, the atomistic description by Monte Carlo has merit when it comes to taking into account the microscopic structure. Chapter Two and Chapter Three of this thesis are dedicated to the study of rich features of magneto-elastic coupling in SCO active core-shell nanocomposite, where both core and shell have different transition temperatures and interact elastically through their common elastic interface.

5.1.1 Chapter 2

In this Chapter, we have investigated the thermodynamic properties of a spin-crossover nanocomposite made of two different spin-crossover units in the core-shell configuration. We have seen that this configuration allows an efficient mechanical coupling between the two spin-crossover materials since they influence the thermodynamic properties of each other. Due to this mechanical coupling, the thermal dependence of the total nanocomposite is far from the sum of each of its constituents. To describe this phenomenon, we have adapted our electro-elastic model to the case of a nanocomposite made of two elastically coupled SCO materials having different transition temperatures and thermal hysteresis widths. We found that the shell part's transition at low-temperature significantly affects the elastic properties of the core (and vice-versa), whose lattice parameter starts to change (precursor phenomena) long before any variation of its

spin state. We found that the interplay between the electro-elastic properties of both constituents leads to a complex distribution of pressure (or elastic energy) inside the lattice. In practice, we have demonstrated that although the thermal spin-transition of the core (in the nanocomposite) is of first-order, the growth of HS macroscopic domains is prevented by the presence of the shell, which changes this mechanism to that of homogenous ramified structures, in a similar way as those observed in the Ising models. The model results are qualitatively comparable with the available experimental results. Finally, we would like to emphasize that when the rigidities of the core and the shell are significantly different and require the use of different elastic constants and lattice parameters for the two media, we expect a less efficient core-shell mechanical coupling due to the existence of a misfit acoustic impedance. The use of SCO materials having different transition temperatures and similar elastic properties is then of interest to generate new multistabilities (two three or even more steps), which can be used as q-bit systems for memories. SCO nanocomposites made of several multilayers with different transition temperatures constitute an excellent way to design multi-stable SCO materials with high tailored performances.

5.1.2 Chapter 3

The results discussed in this chapter stems from the questions asked in the previous chapter. What does the coupling of elastic interface for two spin active SCO lattices results in, if misfit is introduced in the system? How does the nature and manner in which this misfit is included affects the outcome?

To realize this situation, for first scenario, we fixed the LS lattice parameter to 1.0 nm for both core and the shell. The HS lattice parameter of the core is set equal to 1.05 nm, and we change the HS parameter of the shell in the interval 1.00-1.05 nm. While in another case, we fixed the HS lattice parameter to 1.06 nm for both the core and the shell. The LS lattice parameter of the core is set equal to 1.0 nm, and we change the LS parameter of the shell in the interval 1.0-1.06 nm.

One of the most intriguing results emerging from the magneto-elastic interactions within the nanostructure concerns the core's reaction. Indeed, for a strong lattice parameter misfit between the shell and core in HS, the shell shows thermally-induced multistep transitions on both the HS fraction and lattice parameter. In contrast, the core exhibits a multistep transition on its lattice parameters but a simple transition on its HS fraction behavior. Similarly, when there is a strong lattice parameter misfit between the shell and core in LS, the core shows thermally-induced multistep transitions on both the HS fraction and lattice parameter. In contrast, the shell exhibits a multistep transition on its lattice parameters but a simple transition on its HS fraction behavior. The coupling and decoupling of electronic and elastic behavior depends on both values, and the misfit state is very novel and impossible to obtain on a simple lattice. Spatial self-organization of the spin states with labyrinths formation stabilizing longitudinal or transversal HS and

LS strings, anti-ferromagnetically coupled to surrounding strings, is evidenced. This type of organization of the spin states is new and deserves further investigations. Moreover, the case of a spin-crossover core-shell nanostructure, with core and shell having the same lattice parameter in the HS state and a lattice parameter misfit in the LS state, shows very intriguing features such as vortex formation and drifting and rotation of the core-shell lattice is also very interesting. This particular case is still being investigated, and the results will be submitted to publication in a separate work.

Switchable molecules have also garnered a lot of attention recently for the possibility to use them as molecular machines and actuators. To achieve this aim, one has to be able to integrate and interface the molecules with their environment in order to connect them to an external source of energy, which is then transduced by the molecules to produce useful work in a controllable manner. It will be of primary importance to study the size reduction capability of the integrated SCO layers by means of a simple nanomechanical structure before addressing more complex NEMS devices. Thus, for further applications, it is of fundamental importance to understand all the phenomena hidden in the overall macroscopic thermo-induced transformations, to achieve this aim, alongside experiments, increasingly accurate and efficient modelling will be indispensable. The aim and underlying motivation of work done in Chapter Four was derived from the aforementioned perspective.

5.1.3 Chapter 4

This study was focused on the properties of the macroscopic nucleation, growth and propagation mechanisms. The Spatio-temporal aspects of the transformation were studied as a function of the position of obstruction (length or width) and the initial state of the lattice. We have as well analyzed the effect of obstruction on thermal and structural properties of the spin crossover crystal, starting from the HS and LS states. Indeed, for length obstruction, the cooperativity is significantly reduced, which leads to gradual or incomplete transition. In contrast, in case of breadth obstruction, it seems we increase the cooperativity when we start from LS state, while reduce it when we start from HS state, and thus leading to wider and narrower hysteresis respectively. We noticed a distinct difference in the shape of the hysteresis loop of n_{HS} and avg. nn distances. Indeed, starting from the HS (resp. LS) states, a residual lattice parameter appears at low (resp. high) temperature. We studied the size effects on the thermal and mechanical properties of the spin crossover crystal. We found that the increase of the length of crystal leads to a change in the thermo-induced spin transition and shift towards lower temperatures, and we see that increase or decrease in the ratio of $N_x \times N_y$ affects the bending and total length of the lattice in different ways, and is key in understanding the lattice deformation. The Spatio-temporal arrangement of spin states is also quite important as we can see that in the cases where we have the obstruction along the breadth, and we start from the LS state, during the heating

cycle for very low bending, we obtain the occurrence of stripes (Turing like pattern), which might be helpful in explaining the origin of such patterns in many experimental works if we follow the curvature of the crystal. Similarly, for the case where we start from the HS state during the length obstruction, we see that a core-shell like structure for a spin state is formed where we have high spin states at the center of lattice while the edges are all low spin, which is interesting considering that the edges along the length are fixed to the distance that of HS and thus should be the last to make this transition. Thus we can safely assume that the frustration in this system is propagated inwards, and thus we see at the center a big domain of HS with some LS states trapped alternatively.

Such behaviors underline the crucial role of the elastic constraints in the magnetic and mechanical properties of the crystal. Interestingly, the reasoning developed here could be extended to the effect of misfit between the LS and HS phases on the nucleation, growth and propagation mechanisms.

The findings obtained within this PhD project aim to extend the knowledge and possibly open new doorways and ideas for further developments and the design of novel materials. A clear understanding of the pathway together with all the accessible intermediate electronic and structural states is both demanding and of vital importance for shaping further research in this field. This PhD work pointed out the variety and complexity of the multi-scale processes around magnetoelastic phenomena in molecular solids in this context. The “experiments” reported in the previous pages focused on the particular case of SCO molecular crystals. SCO solid systems show a large variety of phase transitions as well as different changes in their physio-chemical properties (magnetic susceptibility, color, volume, etc.).

Investigations conducted in previous chapters certainly offer some insights and perspectives to control material properties via strong and cooperative interactions and feedback effects. Some prospective that may reach conclusions from these insights will be revealed in the next section and possibly shared very soon in the form of publications.

5.2 Perspectives

5.2.1 Thermal and mechanical properties of a 3-dimensional SCO crystal in elastically bounded media:

We already discussed in detail the valuable insights and conclusions for the 2-D counterpart in Chapter Four. We would like to extend this work further to study its 3-D counterpart (Fig. 5.1), which will clearly be interesting since now SCO lattice have one more degree of freedom, so it would be logical to expect changes in flexural rigidity and thus in normal modes, and domain propagations. Understanding these effects and their origin would be helpful in addressing more

complex NEMS devices.

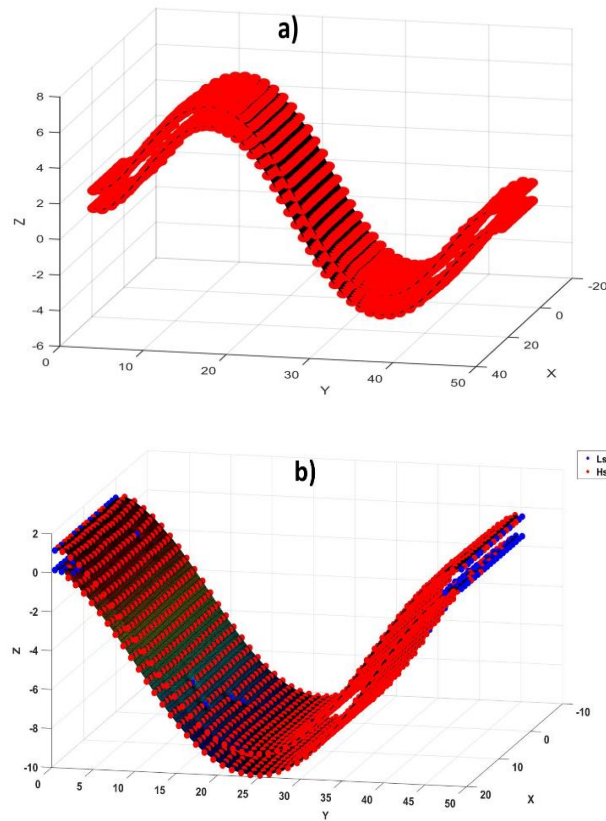


Figure 5. 1 Showing two possible orientations for a 3-D SCO doubly clamped lattice.

5.2.2 Core-Shell Architecture:

Even though two chapters have been dedicated core-shell architectures, we can always imagine new scenarios or question previous assumptions through which we viewed our previous investigations. One such question which might be asked regarding these results might be that for the previous studies, we let the interface decide what will its equilibrium distances will be during or after the transition, but it could very well be defined initially, something like in Fig. 5.2 $(\frac{R_{0,C}^{xx}+R_{0,S}^{xx}}{2})$, where R_0^{xx} is the equilibrium distances at the interfaces, something as the average of distances between core and shell counterparts for the required configuration $xx = HH, HL, LL$. So, this time, the interface has its own properties rather than flipping between core and shell equilibrium parameters. Surely, we can also choose the interface to be partial toward either shell or core. As we can see in Fig. 5.2, we have the behavior similar to the behavior which we observe in the case discussed in Chapter three with misfit in the HS state.

Another critical point is the study of the photomagnetic properties of these nanostructures and particularly the impact of the lattice misfit at the interface on the photo-induced magneto-structural properties between the core and the shell.

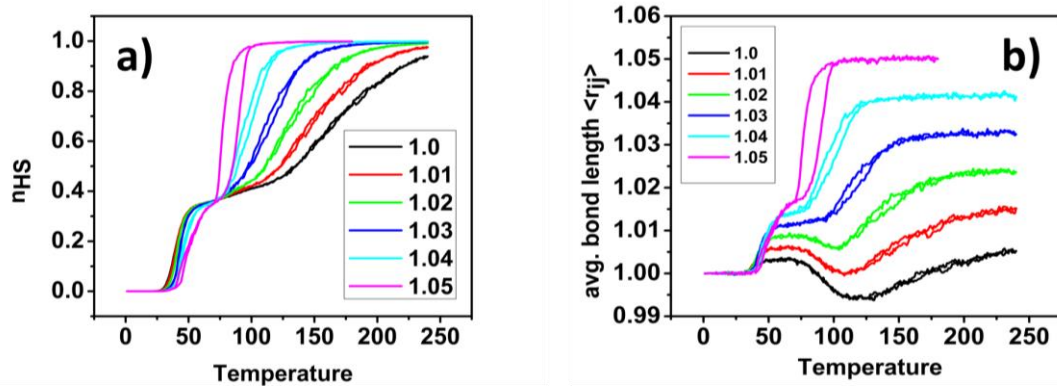


Figure 5. 2 Showing total n_{HS} fraction, and $\langle r_{i,j} \rangle$ avg. bond lengths for core-shell architecture for a predefined interface with misfit in HS state of SCO, which qualitatively is similar to what we observed and discussed in chapter 3, with some differences such as hysteresis width, transition temperature, etc.

These are just some examples, but currently, we have even more exciting questions to answers, such as investigating the origin of vortex formation, drifting and rotation of the core-shell lattice, the origin of this behavior, and how do instabilities in the lattice generate movement and how could it be harnessed to have directed movement in the SCO materials or nanocomposites. If found, it could be helpful in fields such as targeted medicine through core-shell architecture and others.

5.2.3 Metal-organic framework Spin Crossover materials:

Metal-organic frameworks (MOFs) or porous coordination polymers (PCPs) are being frequently studied nowadays due to their easily tunable adaptability (i.e. structure, composition, functionality, porosity etc.). All these characteristics find their applications in various fields such as, catalytic activity, luminescence, conductivity, magnetism, and promising applications in energy storage, gas storage, molecular separation, sensing, biomedicine, etc.

Incorporating the advantages of MOFs with the properties of SCO appears to be very appealing crossovers. As we will have one more external parameter to alter and thus more finely tune the spin transition and thus increase the horizon of application of SCO to molecular sensing, molecular sieves and many more.

It has been widely reviewed and observed experimentally that the correlation/synergy between the electronic and the structural features of SCO material are important for coupled structural phase transition. If these changes are assisted, for example, by symmetry breaking, it can induce stepped SCO behavior.

Although much is said and done about these classes of transition experimentally, a lot is yet to be determined theoretically. As a first attempt, we started to investigate the coupling between a SCO transition and an order-disorder transition arising due to anion (host-guest or ion/solvent molecules) moieties' orientation order/disorder). The following study is the first step in the direction of understanding the underlying principles for such transition and its effect on the spin transition. It will be exciting to study SCO (guest) induced guest (SCO) effect as it may lead to more control over the hysteresis and thus the properties of the SCO. In recent reported experimental studies, it has been observed that when the structural order/disorder of the lattice occurs near the spin-crossover transition, clear effects are observed on the thermal hysteresis of the SCO. As we know, in spin crossover systems generally, we have a lot of spin-inactive components such as solvents and counter anions, but during modelling of these systems, we just consider the spin-active centres, which limits us to develop a profound understanding for this phenomenon. In this paper, we will tackle this challenge by incorporating the anion lattice in the electro-elastic model.

In the previous studies, we have very well tested the robustness of this model as it has been very efficient in providing the qualitative understanding for the experimental results of the SCO materials (the macroscopic nucleation, growth and propagation of the front transformation and the reproducibility of the thermal hysteresis loop, two-step transition and mechanical relaxation at lower temperature have been well described with this model.)

5.2.3.1 Description of the model:

The Anion-SCO model accounting for the volume and structure orientation change between the spin transition units is written as a set of fictitious spins, as they mimics the 2 states of SCO (HS-LS) and anion (Right Tilt (RT) – Left Tilt (LT)) model.

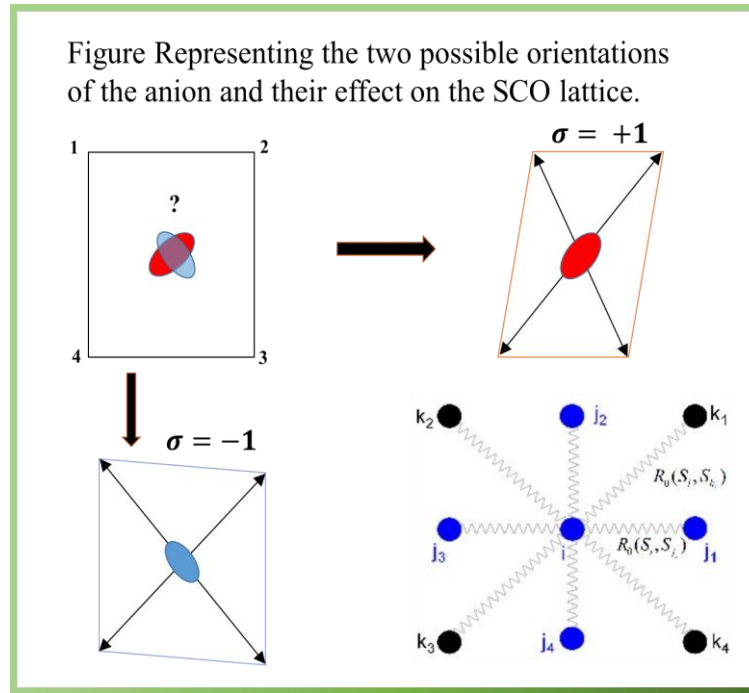


Figure 5. 3 Figurative representation of Anion-SCO model representing the two possible orientations for the anions, RT where $\sigma_i = +1$ and LT where $\sigma_i = -1$.

To simulate a SCO-Anion lattice, we consider two interpenetrated lattices with a SCO lattice (Fig. 5.3) in the center of each cell, we have an anion atom. As usual, SCO atoms may have two spin states HS or LS, while for anion atoms two states are possible either the anion elongates along the right diagonal (RT) or along the left diagonal (LT); this elongation of anion have effect on the next nearest neighbor bonds of the SCO as schematized in Fig. 5.4 . Of course, a more sophisticated model with a continuous reorientation of the anions is possible, but here we start with this simple two-state model for the anion orientation. The bond length of these next-nearest neighbors' bonds increases in the direction of elongation while decreases in the opposite direction (Fig. 5.4).

The total Hamiltonian, in 2D square symmetry, is given by

$$H_{total} = H_{electronic} + H_{elastic} + H_{anion} \quad (5.1)$$

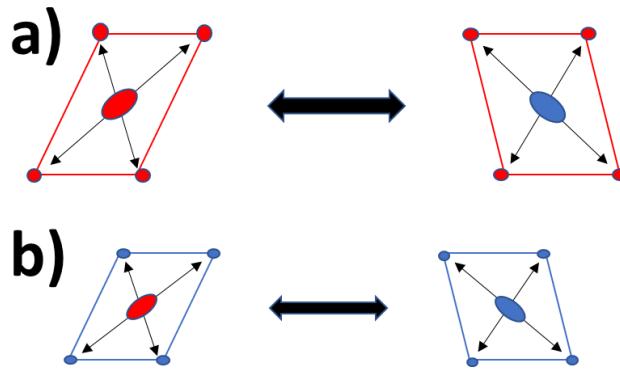


Figure 5. 4 Showing two possible states for each HS and LS state of SCO lattice due to the effect of anion orientation.

Here, $H_{electronic} + H_{elastic}$ part is the contribution from the SCO lattice, while the H_{anion} anion part is the contribution from anion lattice on further dissection of the Hamiltonian we have SCO and Anion part. As we have discussed, the anion lattice have two stable states, i.e. RT (plus) and LT (minus), but this orientation perturbs our SCO lattice as SCO atoms want the lattice to be square symmetric, while orientation freedom of the anion atom leads to stretch in one diagonal direction while shrink in other. This stretching and shrinking depend on their orientation, for example: $\sigma_i = +1$ (RT) wants to stretch along the right diagonal while shrink along the left diagonal and vice versa for $\sigma_i = -1$ (LT). This conflict of symmetries between the SC lattice and Anion lattice generates a new interaction and also a frustration of both sublattices. It is important to notice here that the interaction between the two subsystems is considered in the elastic part of the SCO Hamiltonian, which depends on the “orientation states” of the anions.

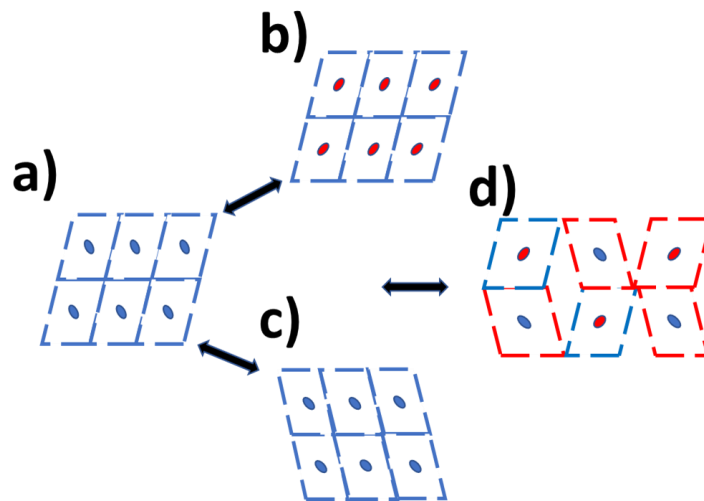


Figure 5. 5 Schematic of one such thought experiment of (a) confrontation between anion, and SCO lattice, where we begin with a SCO lattice RT but due to some external field anions have switched to LT. Either of the two (SCO, or anion) have to adapt now (i.e., (b) anions adapt to

the SCO orientation, or (c) SCO adapts to the anion preference), otherwise we might end up with situation(d) where both or either of the lattice descend to disorder.

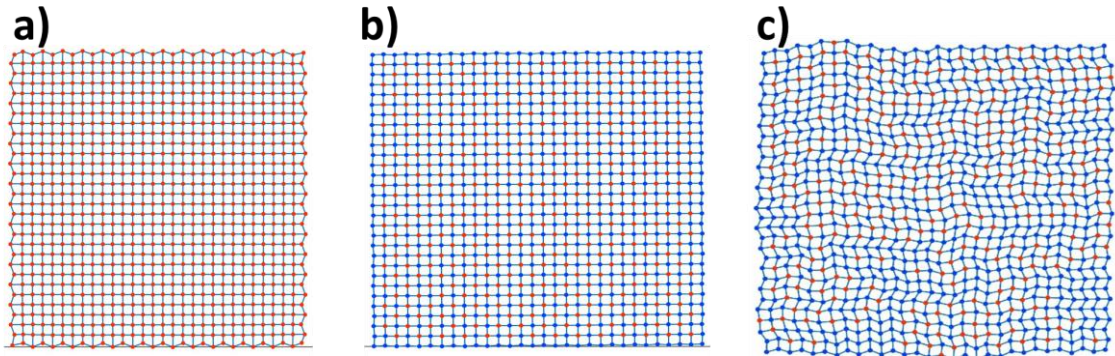


Figure 5. 6 Effect of structural and spin relaxation for SCO, and spin (i.e., orientation) relaxation for anion (as anion always remains in centre), on the structural and spin state of SCO lattice (a) showing the formation of ridges at the boundaries of SCO lattice, but no changes in its spin state (i.e., it remains in HS state). (b) Change in both structural and spin orientation for SCO lattice, but as we can see lattice is still relatively ordered. (c) Changes in spin and structural orientation of SCO lattice, also major deformations and many interesting orientations of structural ordering can be observed.

Indeed, we can imagine many exciting situations (Fig. 5.5), among which the case of anti-ferro interactions between the anions which leads to frustrate the SCO sublattice (Fig. 5.5d), and preliminary investigations on the mechanical and spin-state relaxations shows some intriguing (Fig. 5.6) and promising results like self-organized structural deformations (Fig. 5.6c). However, a more detailed study regarding the nature of SCO thermal hysteresis due the order-disorder transition of the anion lattice has to be conducted in order to shed more light on the coupling between these two transitions.

With all of these fascinating results and insights now discussed, this thesis is submitted with the understanding that it only scratches the surface. Deep underlying connections that intertwine various complex phenomena that may appear unrelated at first, but gradually unraveling these connections in any of these systems may reveal profound insights in another or a better footing and understanding in the behavior of emergent phenomena as a whole. Thus, in the hope that the work done will be useful/insightful or relevant to a large community of researchers and students.

